Phenomenology of New Physics in the Neutrino Sector

Zur Erlangung des akademischen Grades eines
DOKTORS DER NATURWISSENSCHAFTEN (Dr. rer. nat.)

von der KIT-Fakultät für Physik des
Karlsruher Instituts für Technologie (KIT)
angenommene

DISSERTATION

von

BSc (Adv. Maths) Honours I and Medal (Physics),
Zhou, Albert
IAP, KIT

Tag der mündlichen Prüfung: 01. Juli 2022
1. Referent: Prof. Thomas Schwetz-Mangold
2. Korreferent: Prof. Felix Kahlhöfer

Abstract

This PhD thesis covers my work done at the KIT under the supervision of Prof. Thomas Schwetz-Mangold, in the field of neutrino-oscillation phenomenology. I first give an historical overview of neutrino physics, covering the Standard Model of particle physics, how the neutrino was discovered, and the experimental developments that led to the discovery of the neutrino, and subsequent experimental developments. Then I cover the latest analysis of the three-neutrino oscillation parameters with all relevant experimental data, which was done as a part of the NuFit collaboration. The global dataset contains opposing tendencies, which have low statistical significance, but may develop into a serious tension with future exposure.

Then I cover my work undertaking a statistically rigorous analysis of the sterile-neutrino hypothesis, using data from terrestrial experiments, as well as solar data with a focus on the recent claimed evidence of sterile neutrinos from the Neutrino-4 and BEST experimental collaborations. The significant statistical tensions within the datasets are also evaluated, as the solar data constrains the sterile-neutrino hypothesis.

Finally, I consider the so-called neutrino dipole portal, where a neutrino interacts with a new heavy neutral particle via a magnetic interaction. This interaction was proposed to explain an observed excess at MiniBooNE. I consider this type of interaction with the different flavours of neutrino at the future experiment DUNE, which will use new liquid-argon detector technology, which will be able to distinguish electron and photon tracks. I find that DUNE is well placed to probe the neutrino dipole portal at currently unconstrained parameter space, and will be competitive with other proposed experiments such as SHiP.

Contents

List of Figures

List of Tables

Acknowledgments

I would like to thank the Doctoral School “Karlsruhe School of Elementary and Astroparticle Physics: Science and Technology (KSETA)” for financial support through the GSSP program of the German Academic Exchange Service (DAAD).

I would like to thank my supervisor, Thomas, for supporting me throughout the PhD, and for his time and energy working with my, as well as all my collaborators, whom I had the pleasure of working with. I would also like to thank my parents for their support and my office mates for being lovely people.

Finally I would like to thank my mentor, Ulrich Nierste, for all his support, particularly during the beginning of the PhD.

Chapter 1

Introduction

Corpora sunt porro partim primordia rerum,
partim concilio quae constant principiorum.
sed quae sunt rerum primordia, nulla potest vis
stinguere; nam solido vincunt ea corpore demum.

TITI LVCRETI CARI *DE RERVM NATVRA*
LIBER PRIMVS

Bodies, again,
Are partly primal germs of things, and partly
Unions deriving from the primal germs.
And those which are the primal germs of things
No power can quench; for in the end they conquer
By their own solidness;

Translation, courtesy of Tufts University [1]

Lucretius describes in his poem *On the Nature of Things* (*circa* 50 B.C.) the atomic hypothesis: that matter is composed of indivisible, elementary particles called atoms (from the Greek word $\alpha\tau o\mu o\varsigma$, "uncuttable"). The atomic hypothesis has its origins in the fifth-century B.C. from the Greek philosophers Leucippus and Democritus, who hailed from the coast of Thrace [2], and whose works we have lost. The atomic hypothesis marks one of the earliest attempts to investigate the nature of matter; a quest that still intrigues many scientists today.

Whilst the atomic hypothesis is millennia old, even as late as 1897, the idea of matter being a continuous field (like electricity) was defended by Lord Kelvin [3,4]. The first empirical evidence for the atomic hypothesis comes from J. J. Thomson's experiments, which demonstrated a fixed charge-to-mass ratio of the charge carriers of electricity, suggesting a particle interpretation [2]. Thomson went on to hypothesise, from the wavelength of optical light, that atoms had a radius of roughly one Angstrom, and hypothesised that the equilibrium electronic configurations determined the chemical properties of the elements. By using a physical magnetic analogue, he deduced a shell model of electronic states, qualitatively similar to the hydrogenic wave functions [4].

It is a testament to the reductive hypothesis, that Thomson could have gleaned such an accurate qualitative picture of the microscopic components of ordinary matter from such a humble starting point. Indeed, his investigations may be seen as the precursor to quantum chemistry. His discovery was also the origin of elementary particle physics, and kicked off a series of investigations that birthed modern physics: the particle interpretation of light and the successful explanation of the UV catastrophe with black-body radiation by Planck; the invention of quantum mechanics, which accurately described atomic phenomena like hydrogen's absorption lines; and the discovery of radioactivity, accurately described by Fermi's effective four-point interaction.

Further study of cosmic rays revealed that there were several mesons, whose production and decay, it was correctly reasoned, occurred via different interactions: one weak and one strong.[1] The investigation into the nature of mesons, the organisation of the zoo of particles, led to the quark hypothesis and the formulation of quantum chromodynamics; whereas the study of their decay and the nature of radioactivity led to the development of electroweak theory. With the technical developments of non-abelian gauge theory, we now have the highly theoretically and phenomenologically successful Standard Model of particle physics.

The success of the symmetry principles that led to chiral perturbation theory, quantum chromodynamics, and the pursuit of unification of forces that led to electroweak theory emboldened theoretical particle physicists to hypothesise the unification of lepton and hadron number, and also grand unified theories, where all interactions could be described by a single Lie group. The discovery of a new space-time symmetry, namely supersymmetry, was hypothesised to resolve fine-tuning problems like the hierarchy problem, or the cosmological-constant problem.

However, precision electroweak tests and the absence of new heavy resonances at the LHC outside of the Higgs have pushed the scale of symmetry restoration to energies that are difficult to explore experimentally, or excluded the "natural" space of parameters (although the triggers of collider searches prohibit constraining long-lived particles). This has led to growing interest in weakly coupled, light new physics; this thesis will focus on this particularly in the context of neutrino physics.

One of the most interesting phenomena in neutrino physics is their flavour oscillations. Due to the weakly interacting nature of neutrinos, the confirmation of neutrino oscillations, which started from the solar-neutrino deficit, took decades. And as evidence in favour of the deficit grew, the question of how to generate its mass generated much theoretical activity to construct models, at first in relation to unified theories and spontaneous CP violation, and later in the context of minimal extensions of the Standard Model, which hypothesise new scalars or sterile neutrinos. Nowadays, there is a plethora of neutrino mass-generation models, and experimental data searching for oscillations. There are also numerous outstanding anomalies in these data, such as the MiniBooNE anomaly and the gallium anomaly, which may be indications of new physics in the neutrino sector.

The plethora of data from different experiments, which sometimes lead to contradictory conclusions, some indicating new physics, others not, as well as the difficulty accumulating statistics, due to the weakly interacting nature of the neutrino, make it important to do global statistical analyses, to obtain the maximum usage of available data

---

[1] For a succinct but broad summary of these historical developments, which I have relied on, see chapter one of [5].

and to determine the true significance of anomalies, as well as their compatibility with other experiments. In this work, I cover my work done during my PhD at KIT, under the supervision of Prof. Thomas Schwetz-Mangold, in which I was involved with the global fits of the three-neutrino oscillation parameters, a global Feldman-Cousins Monte-Carlo statistical analysis of the sterile-neutrino hypothesis, and probing the neutrino dipole portal at the future neutrino experiment DUNE.

In chapter 2, I give an historical introduction to the neutrino. I first give an overview of the Standard Model in section 2.1, and then give an introduction into the formulation of electroweak theory and the neutrino in section 2.2. In section 2.3, I give an historical overview of neutrino mass models, and then in the following sections 2.4 to 2.6, I give an historical overview of the establishment of the phenomenon of neutrino oscillations. Then in section 2.7, I overview the early evidence of a light sterile neutrino, and I conclude in section 2.8 with a brief overview of topics in neutrino astrophysics and cosmology.

In chapter 3, I present a review of the current status of the three-neutrino oscillation parameters, and my contribution to the latest NuFit results, updating the reactor analysis with new data from Neutrino 2020 conference; this chapter also provides the foundations of the simplified simulation for neutrino phenomenology and the basic statistical tools. In chapter 4, I cover my work in the statistical analysis of the sterile-neutrino hypothesis, which is more involved due to the inapplicability of Wilks' theorem, and requires much more computationally involved Monte Carlo simulations. I not only constructed my own fast χ^2 routines for individual experiments, but highly optimised the routines from other collaborators, including the multidimensional pull minimisation for STEREO; auxiliary details are presented in appendix A. Finally, in chapter 5, I cover my work investigating the neutrino dipole portal at DUNE; the dipole portal was originally considered to resolve the MiniBooNE anomaly, and we found that the dipole portal can be well probed at DUNE.

This thesis is based on the following publications:

- I. Esteban, M. Gonzalez-Garcia, M. Maltoni, T. Schwetz, and **A. Zhou**, *The fate of hints: updated global analysis of three-flavor neutrino oscillations*, J. High Energy Phys. **2020** 178 (Sep, 2020), [arXiv:2007.14792]

- J. M. Berryman, P. Coloma, P. Huber, T. Schwetz, and **A. Zhou**, *Statistical significance of the sterile-neutrino hypothesis in the context of reactor and gallium data*, J. High Energy Phys. **2022** 55 (Feb, 2022), [arXiv:2111.12530]

- T. Schwetz, **A. Zhou**, and J.-Y. Zhu, *Constraining active-sterile neutrino transition magnetic moments at DUNE near and far detectors*, JHEP **2021** 200 (July, 2020), [arXiv:2105.09699].

Chapter 2

An Historical Introduction to Neutrino Physics

In this chapter, I first give an overview of the Standard Model with a focus on the neutrino sector in section 2.1; then in section 2.2, I review the origins of the neutrino and the development of the theory of its oscillation, as well as the electroweak model for leptons; in section 2.3, I review the historically significant neutrino mass models and the seesaw mechanism, which ends the theory part of my introduction.

In section 2.4, I review the discovery of the solar neutrino deficit and the history of the confirmation of solar oscillations; then in section 2.5, I review how atmospheric oscillations were discovered. In section 2.6 I give the early history of determining the oscillation parameters quantitatively and a brief overview of the statistical methods. In section 2.7 I touch upon some evidence for a light sterile neutrino, and I conclude this chapter with some aspects of neutrino cosmology and astrophysics in section 2.8.

2.1 Overview of the Standard Model

The Standard Model is a quantum field theory described by the gauge group $\mathrm{SU}(3)_\mathrm{C} \otimes \mathrm{SU}(2)_\mathrm{L} \otimes \mathrm{U}(1)_\mathrm{Y}$. I will not cover the Standard Model at the quantum level; technical aspects of the quantisation of non-abelian, chiral gauge theories, ghosts, Feynman rules *etc.* can be found in the standard texts [6–8]. The colour group $\mathrm{SU}(3)_\mathrm{C}$ describes the strongly coupled force of the gluon. The form of perturbation theory of the S-matrix with asymptotically free quark fields, is only valid above the confinement scale, where at high energies the coupling constant is small. Below that, the quarks are bound in colourless states like mesons or nucleons. Interactions between leptons and hadrons can be factorised into a perturbative leptonic part, which can be calculated using perturbative methods, and a hadronic part, which is phenomenologically parameterised into form factors.

The $\mathrm{SU}(2)_\mathrm{L}$ gauge group operates only on the left-handed fields, the charges of which are called weak isospin. The $\mathrm{U}(1)_\mathrm{Y}$ describes hypercharge interactions, which acts on both left- and right-handed fields, albeit with different charges. The left-handed fields transform as isospin doublets

$$L \mapsto \exp\left[\mathrm{i}\theta_a(x) I_a + \mathrm{i}\eta(x)\frac{Y_\mathrm{L}}{2}\right] L, \qquad \text{where} \qquad I_a \equiv \frac{\sigma_a}{2} \tag{2.1}$$

Generation:	1	2	3	I	I_3	Y
left-handed lepton $L =$	$\begin{pmatrix}\nu_e \\ e_\mathrm{L}\end{pmatrix}$	$\begin{pmatrix}\nu_\mu \\ \mu_\mathrm{L}\end{pmatrix}$	$\begin{pmatrix}\nu_\tau \\ \tau_\mathrm{L}\end{pmatrix}$	$\frac{1}{2}$	$+\frac{1}{2}$ $-\frac{1}{2}$	-1
left-handed quark $Q =$	$\begin{pmatrix}u_\mathrm{L} \\ d_\mathrm{L}\end{pmatrix}$	$\begin{pmatrix}c_\mathrm{L} \\ s_\mathrm{L}\end{pmatrix}$	$\begin{pmatrix}t_\mathrm{L} \\ b_\mathrm{L}\end{pmatrix}$	$\frac{1}{2}$	$+\frac{1}{2}$ $-\frac{1}{2}$	$\frac{1}{3}$
right-handed lepton $\ell_\mathrm{R} =$	e_R	μ_R	τ_R	0	0	-2
right-handed quark $q_\mathrm{R} =$	u_R d_R	c_R s_R	t_R b_R	0	0	$+\frac{4}{3}$ $-\frac{2}{3}$

Table 2.1: Charges of the three generations of fermion fields.

are the generators for SU(2), whilst the right-handed fields transform as

$$\psi_\mathrm{R} \mapsto \exp\left[\mathrm{i}\eta(x)\frac{Y_\mathrm{R}}{2}\right]\psi_\mathrm{R}. \tag{2.2}$$

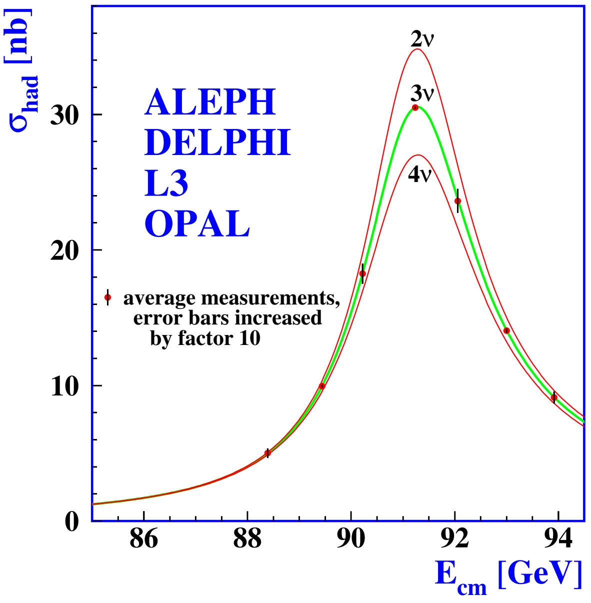

Figure 2.1: The cross section for hadron production at the Z resonance for two, three and four neutrino species, compared to data; courtesy of [9].

The three generations of fermion fields and their charges are given in table 2.1. The electric charge is given by $Q = I_3 + Y/2$ (for a kind of derivation of the electroweak gauge group, see [6, §11]). Whilst there are no theoretical constraints on the number of generations, precise measurement of the Z resonance from electron-positron colliders constrain the number of light neutrino flavours with electroweak couplings to be three [9].

As per gauge theory, electroweak interactions are determined by the covariant derivative

$$\psi_\mathrm{L}^\dagger\left(\mathrm{i}\sigma^\mu\mathrm{D}_\mu\right)\psi_\mathrm{L} + \psi_\mathrm{R}^\dagger\left(\mathrm{i}\overline{\sigma}^\mu\mathrm{D}_\mu\right)\psi_\mathrm{R},$$

$$\mathrm{D}_\mu = \partial_\mu - \mathrm{i}g\boldsymbol{I}\boldsymbol{\sigma}\cdot\mathbf{A}_\mu - \mathrm{i}g'\frac{Y}{2}B_\mu, \tag{2.3}$$

where $\sigma^\mu = \begin{pmatrix}1 & \boldsymbol{\sigma}\end{pmatrix}$, $\overline{\sigma}^\mu = \begin{pmatrix}1 & -\boldsymbol{\sigma}\end{pmatrix}$, and $\mathbf{A}_\mu$ are the gauge fields for the $\mathrm{SU}(2)_\mathrm{L}$ group, and B_μ is the gauge field for the $\mathrm{U}(1)_\mathrm{Y}$ group. For one lepton generation, the interaction term for the charged-current interactions may be written

$$\mathcal{L}_\mathrm{int}^{(CC)} \ni \frac{g}{\sqrt{2}}\left(\nu_e^\dagger\sigma^\mu e_\mathrm{L}W_\mu^+ + e_\mathrm{L}^\dagger\sigma^\mu\nu_e W_\mu^-\right), \qquad \text{where} \qquad W_\mu^\pm \equiv \frac{A_\mu^1 \mp \mathrm{i}A_\mu^2}{\sqrt{2}}. \tag{2.4}$$

The neutral-current interactions are determined by the diagonal components of the covariant derivative (in weak-isospin space),

$$\mathcal{L}_{\text{int}}^{(NC)} \ni -\mathrm{i}\psi_{\mathrm{L}}^{\dagger}\sigma^{\mu}\psi_{\mathrm{L}}\left(gI_3A_{\mu}^3 + g'\frac{Y_{\mathrm{L}}}{2}B_{\mu}\right) - \mathrm{i}\left(\psi_{\mathrm{R}}^{\dagger}\overline{\sigma}^{\mu}\psi_{\mathrm{R}}\right)g'\frac{Y_{\mathrm{R}}}{2}B_{\mu}. \tag{2.5}$$

We will see below, when we introduce the Higgs, that the mass spectrum for the neutral gauge bosons is

$$A_{\mu}^{\mathrm{EM}} = \sin\theta_{\mathrm{W}}A_{\mu}^3 + \cos\theta_{\mathrm{W}}B_{\mu}, \qquad Z_{\mu} = \cos\theta_{\mathrm{W}}A_{\mu}^3 - \sin\theta_{\mathrm{W}}B_{\mu}, \tag{2.6}$$

where $\tan\theta_{\mathrm{W}} \equiv g/g'$ is the weak mixing angle. By defining $Q_{\mathrm{EM}} \equiv I_3 + Y_{\mathrm{L}}/2 = Y_{\mathrm{R}}/2$, we can write the neutral-current term as

$$\mathcal{L}_{\text{int}}^{(NC)} \ni -\mathrm{i}\frac{g}{\cos\theta_{\mathrm{W}}}\left[\left(\psi_{\mathrm{L}}^{\dagger}\sigma^{\mu}\psi_{\mathrm{L}}\right)I_3Z_{\mu} + \left(\overline{\psi}\gamma^{\mu}\psi\right)\sin\theta_{\mathrm{W}}Q_{\mathrm{EM}}B_{\mu}\right], \tag{2.7}$$

where one must make the substitution $B_{\mu} = \cos\theta_{\mathrm{W}}A_{\mu}^{\mathrm{EM}} - \sin\theta_{\mathrm{W}}Z_{\mu}$. For neutral leptons like the neutrino, the heavy neutral current is purely left-handed, however for charged leptons, it will have both left- and right-handed couplings.

The Higgs field $\Phi \sim (\frac{1}{2}, 1)$ is a scalar $\mathrm{SU}(2)_{\mathrm{L}}$ doublet, with $I = \frac{1}{2}$, and hypercharge $Y = 1$, whose Lagrangian contains the famous Mexican-hat potential,

$$|\mathrm{D}_{\mu}\Phi|^2 - V\left(\Phi^{\dagger}\Phi\right), \qquad V\left(\Phi^{\dagger}\Phi\right) \equiv -\mu^2|\Phi|^2 + \lambda|\Phi|^4, \qquad \Phi \equiv \begin{pmatrix}\phi^+ & \phi^0\end{pmatrix}^{\mathrm{T}}. \tag{2.8}$$

The potential determines the symmetry-breaking Higgs vacuum $\langle\Phi\rangle_0$, which in the unitary gauge adopts the form $\begin{pmatrix}0 & v/\sqrt{2}\end{pmatrix}^{\mathrm{T}}$, where v is a real number. The other degrees of freedom (ϕ^+ and $\Im\phi^0$) are transferred to the gauge bosons in the unitary gauge. The gauge-boson masses then come from the covariant derivative,

$$|\mathrm{D}_{\mu}\langle\Phi\rangle_0|^2 = \frac{v^2}{4}\left[g^2W_{\mu}^+W^{-\mu} + \frac{1}{2}\left(gA_{\mu}^3 - g'B_{\mu}\right)^2\right]. \tag{2.9}$$

The first term defines the W-boson mass as $M_W = gv/2$, whereas the second defines the mass matrix, which is diagonalised by eq. (2.6)

$$\frac{v^2}{8}\begin{pmatrix}A_{\mu}^3 & B_{\mu}\end{pmatrix}\begin{pmatrix}g^2 & -gg' \\ -gg' & g'^2\end{pmatrix}\begin{pmatrix}A^{3\mu} \\ B_{\mu}\end{pmatrix} = \frac{1}{2}\left(Z_{\mu}, A_{\mu}^{\mathrm{EM}}\right)\begin{pmatrix}M_Z^2 & 0 \\ 0 & 0\end{pmatrix}\begin{pmatrix}Z^{\mu} \\ A_{\mathrm{EM}}^{\mu}\end{pmatrix}, \tag{2.10}$$

where $M_Z^2 = v^2(g^2 + g'^2)/4$. Since perturbation theory is done in the mass basis, where the propagator $\sim (p^2 - m^2)^{-1}$ is well-defined, the eigenstates of the mass matrix define the physical basis of propagating particles.

Fermion masses are generated by Yukawa couplings

$$\sum_{i,j=1,2,3}\left[Y_{ij}^uQ_{\mathrm{L}}^{i\dagger}\widetilde{\Phi}u_{\mathrm{R}}^j + Y_{ij}^dQ_{\mathrm{L}}^{i\dagger}\Phi d_{\mathrm{R}}^j + Y_{ij}^{\ell}L^{i\dagger}\Phi\ell_{\mathrm{R}}^i + \mathrm{h.\,c.}\right], \qquad \text{where} \qquad \widetilde{\Phi} \equiv \mathrm{i}\sigma_2\Phi^*. \tag{2.11}$$

Note that the up-type quarks have two units of hypercharge more than the down-type quarks, which is why we need $\widetilde{\Phi}$, which transforms as $Y = -1$,

$$\widetilde{\Phi} \mapsto \mathrm{i}\sigma_2\exp\left[-\mathrm{i}\frac{\theta_a(x)\sigma_a^* + \eta(x)}{2}\right]\Phi^* = \exp\left[\mathrm{i}\frac{\theta_a(x)\sigma_a - \eta(x)}{2}\right]\widetilde{\Phi}, \tag{2.12}$$

where we have used the relation $\sigma_2\sigma_a^*\sigma_2 = -\sigma_a$. In the unitary gauge, the hypercharge conjugate $\widetilde{\Phi}$ flips the top and bottom components, so that the VEV v can connect with the top components of the quark doublet. Note how we have not written a neutrino mass term $L^\dagger\widetilde{\Phi}\nu_{\mathrm{R}}$, as there is, by definition, no right-handed neutrino.

Note how the fermionic mass term is not diagonal. Since particles propagate as mass states (see the discussion on coherence in section 2.2), we must diagonalise the mass matrix $M_{ij}^\Psi \equiv Y_{ij}^\Psi v/\sqrt{2}$, via biunitary transformations $\Psi_{\mathrm{L}} \mapsto V_{\mathrm{L}}^\Psi \Psi_{\mathrm{L}}$, $\Psi_{\mathrm{R}} \mapsto V_{\mathrm{R}}^\Psi \Psi_{\mathrm{R}}$,

$$M_{ij}^u \mapsto \left(V_{\mathrm{L}}^{u\dagger}\right)_{ik} m_k^u \left(V_{\mathrm{R}}^u\right)_{kj} = V_{\mathrm{L}}^{u\dagger}\,\mathrm{diag}(m_u, m_c, m_t) V_{\mathrm{R}}^u \tag{2.13}$$

$$M_{ij}^d \mapsto \left(V_{\mathrm{L}}^{d\dagger}\right)_{ik} m_k^d \left(V_{\mathrm{R}}^d\right)_{kj} = V_{\mathrm{L}}^{d\dagger}\,\mathrm{diag}(m_d, m_s, m_b) V_{\mathrm{R}}^d \tag{2.14}$$

$$M_{ij}^\ell \mapsto \left(V_{\mathrm{L}}^{\ell\dagger}\right)_{ik} m_k^\ell \left(V_{\mathrm{R}}^\ell\right)_{kj} = V_{\mathrm{L}}^{\ell\dagger}\,\mathrm{diag}(m_e, m_\mu, m_\tau) V_{\mathrm{R}}^\ell \tag{2.15}$$

(for a proof that this is possible, see [10, §4]). Since neutral interactions are diagonal in weak-isospin space, the left- and right-handed currents are invariant under such transformations, $\Psi_{\mathrm{L,R}}^\dagger \Psi_{\mathrm{L,R}} \mapsto \Psi_{\mathrm{L,R}}^\dagger V_{\mathrm{L,R}}^{\Psi\dagger} V_{\mathrm{L,R}}^\Psi \Psi_{\mathrm{L,R}} = \Psi_{\mathrm{L,R}}^\dagger \Psi_{\mathrm{L,R}}$. (We have ignored gamma/Pauli matrices because they only act on spinor indices, not flavour indices.) However charged-current interactions mix flavours of quarks and leptons,

$$u_{\mathrm{L}}^{i\dagger}\sigma^\mu d_{\mathrm{L}}^i W_\mu^+ \mapsto \left(V_{\mathrm{L}}^{u\dagger} V_{\mathrm{L}}^d\right)_{jk} u_{\mathrm{L}}^{j\dagger}\sigma^\mu d_{\mathrm{L}}^k W_\mu^+, \qquad \nu_{\mathrm{L}}^{i\dagger}\sigma^\mu \ell_{\mathrm{L}}^i W_\mu^+ \mapsto \left(V_{\mathrm{L}}^\ell\right)_{ij} \nu_{\mathrm{L}}^{i\dagger}\sigma^\mu \ell_{\mathrm{L}}^j W_\mu^+. \tag{2.16}$$

For the quarks, we have intergenerational couplings like the up-strange charged-current coupling, which induce kaon oscillations, given by the *CKM matrix* $U_{\mathrm{CKM}} \equiv V_{\mathrm{L}}^{u\dagger} V_{\mathrm{L}}^d$. If neutrinos were massless, we could absorb V_{L}^ℓ by the transformation $\nu_{\mathrm{L}}^i \mapsto \left(V_{\mathrm{L}}^\ell\right)_{ij} \nu_{\mathrm{L}}^j$, however since we know that neutrinos do have mass, there will be a similar *PMNS matrix* $U_{\mathrm{PMNS}} \equiv V_{\mathrm{L}}^{\nu\dagger} V_{\mathrm{L}}^\ell$, which can be parameterised as

$$\begin{pmatrix} 1 & 0 & 0 \\ 0 & c_{23} & s_{23} \\ 0 & -s_{23} & c_{23} \end{pmatrix} \begin{pmatrix} c_{13} & 0 & s_{13}e^{-i\delta_{\mathrm{CP}}} \\ 0 & 1 & 0 \\ -s_{13}e^{i\delta_{\mathrm{CP}}} & 0 & c_{13} \end{pmatrix} \begin{pmatrix} c_{12} & s_{12} & 0 \\ -s_{12} & c_{12} & 0 \\ 0 & 0 & 1 \end{pmatrix} \begin{pmatrix} e^{i\alpha_1} & 0 & 0 \\ 0 & e^{i\alpha_2} & 0 \\ 0 & 0 & 1 \end{pmatrix}, \tag{2.17}$$

where $s_{ij} \equiv \sin\theta_{ij}$ and $c_{ij} \equiv \cos\theta_{ij}$. The last term are the Majorana phases, which have no physical meaning for Dirac neutrinos, due to the lepton-number symmetry $\nu_i \mapsto e^{-\mathrm{i}\varphi_i}\nu_i$. (The reason for there only being two is that only phase differences matter in physical quantities.) The CP-violating phase δ_{CP} cannot be transformed away, and determines the amount of CP violation, with $\delta_{\mathrm{CP}} = 0, \pi$ restoring CP in the neutrino sector.

Due to the lightness of the neutrinos, they are emitted in charged-current interactions as a coherent quantum superposition of mass eigenstates (for a discussion on coherence see section 2.2),

$$|\nu_\alpha\rangle = U_{\alpha 1}^* |\nu_1\rangle + U_{\alpha 2}^* |\nu_2\rangle + U_{\alpha 3}^* |\nu_3\rangle\,. \tag{2.18}$$

In the simplified derivation (although see the discussion on coherence for a list of caveats), the neutrino mass states are assumed to be plane waves with equal momentum, whence the oscillation probability is

$$\begin{aligned} P\left(\nu_\alpha \to \nu_\beta\right) &= \left|\langle \nu_\beta(t) \,|\, \nu_\alpha(0)\rangle\right|^2 = \left|U_{\beta j} e^{\mathrm{i}E_j t} U_{\alpha j}^*\right|^2 \\ &= \sum_{i,j} U_{\alpha i} U_{\alpha j}^* U_{\beta i}^* U_{\beta j} \exp\left(-\mathrm{i}\frac{\Delta m_{ij}^2 L}{2E}\right), \end{aligned} \tag{2.19}$$

where we have made the approximations $E_i - E_j = \frac{\Delta m_{ij}^2}{2E}$ and $t = L$, which are valid in the ultra-relativistic limit. In the two-flavour approximation, the only non-zero parameters are θ_{12}, Δm_{12}^2 and one obtains the oscillation probabilities

$$P_{e\mu} = \sin^2 2\theta \cdot \sin^2 \left(\frac{\Delta m^2}{4E_\nu} L \right), \qquad P_{ee} = 1 - P_{e\mu}. \tag{2.20}$$

The quantity $L_{\text{osc}} \equiv \frac{\pi}{2} \frac{4E_\nu \hbar c}{\Delta m^2}$ is called the *oscillation length*, which is the distance of maximum oscillation. Terrestrial experiments tune their neutrino energy and source-to-detector distance to be at this maximum.

There are important phenomenological differences when oscillations occur in matter, rather than vacuum. Neutrinos will coherently scatter off the electrons, protons and neutrons via charged- and neutral-current scattering. This scattering induces an effective potential in the wave-function picture of neutrino propagation (for a derivation, see [10, §9] and [11, §8]), which in flavour space is the diagonal matrix $V \equiv \sqrt{2} G_F \operatorname{diag}\left(N_e - \frac{1}{2} N_n, -\frac{1}{2} N_n, -\frac{1}{2} N_n \right)$, where $N_{e,n}$ is the electron, neutron number density, respectively. The neutron number density appears due to the flavour-blind neutral-current scattering, and can be transformed away by a flavour-blind phase rotation. This results in the equations of propagation in matter,

$$\mathrm{i} \frac{\mathrm{d}}{\mathrm{d}t} \begin{pmatrix} \nu_e \\ \nu_\mu \end{pmatrix} = \begin{pmatrix} -\frac{\Delta m^2}{4E} \cos 2\theta + \sqrt{2} G_F N_e & \frac{\Delta m^2}{4E} \sin 2\theta \\ \frac{\Delta m^2}{4E} \sin 2\theta & \frac{\Delta m^2}{4E} \cos 2\theta \end{pmatrix} \begin{pmatrix} \nu_e \\ \nu_\mu \end{pmatrix}. \tag{2.21}$$

In the case of constant density, two-flavour oscillations in matter can be understood as replacing the vacuum angle and oscillation length with its matter values

$$\sin^2 2\theta_{\mathrm{m}} = \frac{S^2}{\left(C - \sqrt{2} G_F N_e \right)^2 + S^2}, \quad \text{where} \quad S = \frac{\Delta m^2}{2E} \sin 2\theta, \quad C = \frac{\Delta m^2}{2E} \cos 2\theta, \tag{2.22}$$

$$\text{and} \quad L_{\text{osc}}^{\mathrm{m}} = \frac{2\pi}{\sqrt{\left(C - \sqrt{2} G_F N_e \right)^2 + S^2}}. \tag{2.23}$$

When $\sqrt{2} G_F N_e = C$, the matter mixing is maximal $\sin^2 2\theta_{\mathrm{m}} = 1$ and is called the MSW resonance, after Mikheev, Smirnov and Wolfenstein. If the electron density slowly varies with propagation, then the matter mixing (*i.e.* the propagation eigenstates) adiabatically varies; this adiabatic rotation basis also has significant consequences for oscillation phenomenology, as flavour transitions are then driven by the slowly varying electron density, rather than quantum-mechanical oscillations ($\theta_{\mathrm{m}}(t) : 0^\circ \mapsto 90^\circ$ adiabatically during evolution). For more details, see the relevant sections of [10, 11].

If the matter density is extremely high, then it may become opaque to neutrinos (the scattering length becomes small), which occurs for the Earth at extremely high neutrino energies. Furthermore, if the neutrino density is extremely large (*dense neutrino gas*), which can occur in a supernova, collective oscillations can take place, whereby neutrinos can themselves generate a matter potential, and the density-matrix formalism is needed (see [12]). We will not address this, as it is not relevant for this work.

2.2 The Birth of the Neutrino and their Oscillations

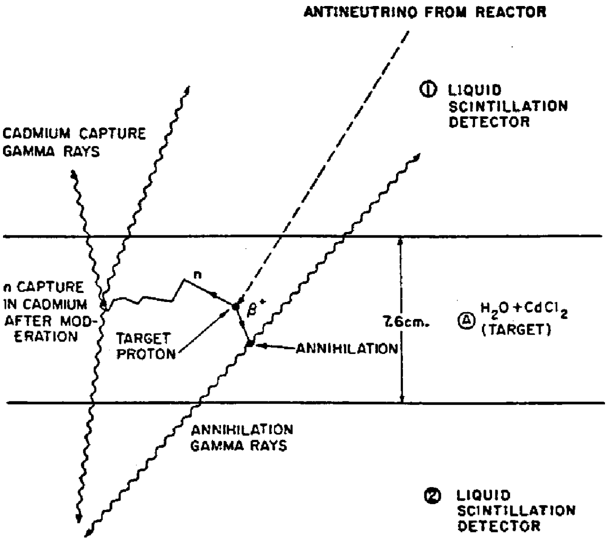

Figure 2.2: Sketch of the prompt and delayed scintillation signal, used in the experiment that detected the neutrino; from [13].

Whilst most accounts credit Wolfgang Pauli for the invention of the neutrino, his original suggestion in his now-famous 1930 letter (with the title “Dear radioactive ladies and gentlemen”) connected the problem of the continuous beta spectrum with the need for additional constituents of the nucleus to obey the spin-statistics relation; indeed he originally called this neutral particle a neutron, which he hypothesised had a mass similar to the electron and resided in the nucleus. (My presentation of this history follows [14].) It was Fermi in 1934 who coupled a neutrino-electron vector bilinear (which he saw analogous to the photon vector field), to a proton-neutron current, in analogy to quantum electrodynamics [15, 16]: in what could be called the first (successful) application of effective field theory.[1] One crucial observation, which was essentially the generalisation of the fundamental ideas of quantum electrodynamics, was that the number of neutrinos and electrons need not be constant, but could create and destroy one another:

“Die totale Anzahl der Elektronen, sowie der Neutrinos, ist nicht notwendigerweise konstant. Elektronen (oder Neutrinos) können entstehen und verschwinden. . . . , dass jedem Übergang von Neutron zu Proton das Entstehen eines Elektrons und eines Neutrinos zugeordnet ist. Dem umgekehrten Prozess, Verwandlung eines Protons in ein Neutron, soll dagegen das Verschwinden eines Elektrons und eines Neutrinos zugeordnet sein. Man bemerke, dass hierdurch die Erhaltung der Ladung gesichert ist.” [15]

The first detection of an antineutrino occurred in the first reactor antineutrino experiment by Reines, Cowan, *et al.*, using liquid scintillation and a delayed coincident signal. This signal, a prompt pair of 511 keV gammas from positron annihilation and then scintillation from neutron capture, allowed excellent discrimination from cosmic-ray backgrounds [13, 17], and is still used for reactor experiments today (see fig. 2.2). The results of the 1953 experiment were reported in 1956. Shortly afterwards, Lee and Yang suggested, based on meson-decay observations, that parity was not conserved in weak interactions, despite being conserved in electromagnetic and strong ones [18], which was confirmed by Wu *et al.* in 1957 [19].

There were many attempts to describe a universal theory of the Fermi interaction based on symmetry principles (see [10, §1] for a list of references, and whose detailed historical overview I have relied on), however one crucial step was the introduction of lepton-number conservation by Konopinski and Mahmoud in 1953 [20], which explained the non-observation of certain lepton-number-violating decays. With the evidence that

---

[1] Fermi does not even assume the equations of motion for the “heavy” particles: the proton and neutron; he merely assumed they can be described by a wave function.

parity was not conserved, Salam [21], Landau [22], and Lee & Yang [23] simultaneously suggested in 1957 that this was due to a two-component theory of a massless neutrino, where the handedness of the neutrino was fixed; later that year, the Majorana formulation of the neutrino, where a small mass was allowed, was published by Case [24]. (A few months prior, McLennan had noted that there are no differences between a massless Majorana neutrino and the two-component theory [25].)

The Lorentz structure of the coupling (vector minus axial vector) was elucidated in 1958 by Sudarshan & Marshak [26], and Sakurai [27] by symmetry principles, and also Feynman & Gell-Mann [28] based on other arguments; the left-handedness of the neutrino was confirmed experimentally in 1958 by Goldhaber, Grodzins and Sunyar [29], by indirectly measuring the neutrino polarisation in the electron-capture decay of ^{152}Eu to a metastable state of ^{152}Sm.

During these developments, Pontecorvo suggested that, in analogy to K^0 oscillations, neutrinos and antineutrinos could also mix and oscillate [30]. Although this would violate lepton number (or neutrino charge, as he put it) Pontecorvo was motivated by a rumour, which turned out to be false, that Davis had observed a lepton-number violating process [31]. (Davis would later use this experimental technique to pioneer his famous Homestake experiment, which was the first evidence for neutrino oscillations.)

Since Pontecorvo did not know about the flavours of neutrino, he could not postulate flavour oscillations. In 1962, in the first neutrino accelerator experiment [32], electron-like events were searched for in an off-axis muon-neutrino beam (created by colliding accelerated protons on a beryllium target). The absence of electron-like events confirmed the hypothesis that electron and muon neutrinos were different particles. This was important for the "intermediate-meson theory" (the existence of the W boson), which would have otherwise incorrectly predicted $\mu \to e\gamma$ decay, as pointed out by Feinberg in 1958 [33].

Simultaneously in 1962, Maki, Nakagawa and Sakata proposed flavour oscillations under the two-neutrino hypothesis [34], although they did not pursue the idea in depth. However, by 1968, Davis would report the first results of his experiment to detect solar neutrinos: an upper bound on the solar-neutrino flux, which was smaller than theoretical predictions [35].[2] The indication of such a deficit prompted Gribov and Pontecorvo in 1969 to suggest that the cause of this deficit might be due to almost-massless neutrinos undergoing flavour oscillations, with frequency $\Delta = (m_1^2 - m_2^2)/(2p)$ [38].

Simultaneous to these developments was the unification of the electromagnetic and weak interactions. An important technical development in 1954 was the invention of Yang-Mills theory by generalising gauge theory to non-abelian groups [39]. In 1957, Schwinger suggested that the two charged vector bosons of SU(2) gauge theory generated the weak force, and the neutral boson generated the electromagnetic force [40]. Later in 1961, Sheldon Glashow noticed that the neutral boson of SU(2) did not couple to the charged leptonic currents. He argued that using a principle of partial symmetry (in analogy with the partially conserved axial current), to allow for gauge-violating mass terms for the vector bosons, there should be a new neutral boson (which we now call the Z boson), which could mix with the photon [41].

Although it was generally accepted that gauge invariance necessitated massless gauge

---

[2] John N. Bahcall's contribution seems to have been overlooked when Davis was awarded the Nobel Prize in 2002, despite Bahcall's pioneering efforts predicting the solar neutrino flux, crucial to the claim of a deficit [36] and his involvement in proposing the Homestake experiment [37].

bosons, and a theory of massive gauge bosons would not be renormalisable, doubt first came in 1962 in an article by Schwinger suggesting a loop-hole [42]. The first explicit realisations of a massive gauge boson in a Lorentz-invariant theory came in 1964, by two independent papers: one by Higgs [43], which only dealt with classical field theory; another by Englert and Brout [44], which also considered leading-order quantum corrections. Only a few months later, Guralnik, Hagen and Kibble published another similar paper [45]. This mechanism was incorporated into Glashow's model by Weinberg and Salam by 1968 [46, 47], however the crucial question of renormalisability was still open, and was addressed only as conjecture by Weinberg and Salam. This issue was finally resolved by 't Hooft and Veltman in 1972, where they introduced dimensional regularisation as a way to renormalise non-abelian gauge theories that also respects Ward identities (gauge invariance or positivity) [48].[3] The existence of neutral-current neutrino interactions, as predicted by the electroweak theory, was discovered first in the Gargamelle experiment at CERN in 1973 [49] and then Fermilab in 1974 [50]. The discovery and confirmation of a third heavy lepton a few years later, which Martin Perl called the tau, and the inference of its associated neutrino, completed the Standard Model leptonic sector [51, 52].

Coherence In 1976, Nussinov addressed an important conceptual issue for neutrino oscillations [53]. Since oscillations are due to mass differences, each neutrino mass state will travel at a different speed — after long enough propagation, the wave packets of the different states will physically separate and cease to oscillate. Nussinov's treatment was merely heuristic, but in 1981, Kayser fleshed out the wave-packet formalism for neutrino oscillations, and also realised that kinematic coherence was crucial [54], *i.e.* there has to be enough momentum uncertainty in the parent particle and other decay products like charged leptons, so that individual neutrino mass eigenstates cannot be kinematically resolved.

The early history of neutrino oscillations was dominated by the solar neutrino deficit, which I review in section 2.4. It took decades for the deficit to gain credibility, due to the complexity of solar modelling and important phenomenology that needed to be discovered, like matter oscillations and the MSW resonance. For this reason it was not until the 90s that theorists began to examine the foundations of neutrino oscillations. There was much confusion over the assumptions made to derive the neutrino-oscillation formula: for example the original derivation of the formula by Gribov and Pontecorvo assumes that the mass states have equal energy. This condition is not Lorentz invariant, and will be violated in different frames. This caused many authors to propose alternative oscillation formulae (for a review of this history as well as the various theoretical issues, see the review by Beuthe [55]). This issue is also nicely highlighted in Winter's 1981 derivation of neutrino oscillations from electron-capture decay [56], where energy-momentum conservation fixes the neutrino kinematics.

Another important theoretical aspect, pointed out by Giunti, Kim and Lee in 1992 [57], was the problem of creating a Fock space for the weak eigenstates. Since the propagators of quantum field theory have a definite mass $i/(\not{p} - m)$, it is impossible to use weak eigenstates for perturbation theory. In 1993, Giunti, Kim, Lee and Lee proposed a

---

[3] I omit a discussion of the technical details of chiral non-abelian gauge theory such as anomaly cancellation and the BRST formalism. I refer the reader to the references in §§9, 11 of [6]; see also [7, §16].

prescription in quantum field theory [58], in which neutrinos were internal lines of a Feynman diagram and the amplitudes of the different mass states were summed coherently (fig. 2.3). External particles, however, were described as wave packets. (There would still be confusion due to the arbitrariness of the form of the external wave packet, which was eventually resolved in 2002 by Beuthe [59].)

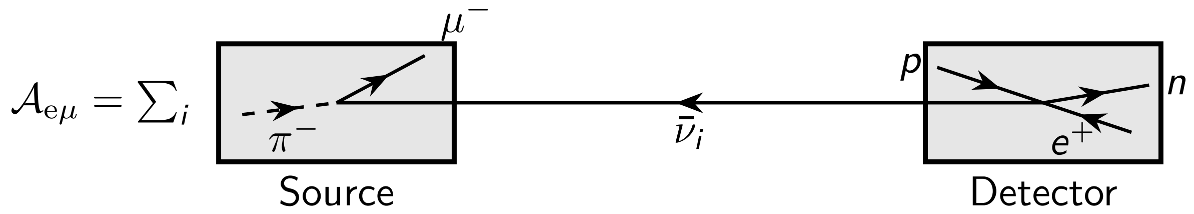

Figure 2.3: Feynman diagram for muon-to-electron neutrino flavour oscillation.

Thus, we see that neutrino oscillations are an explicitly quantum-mechanical phenomenon on a macroscopic scale. Whilst (partial) macroscopic coherency is also exhibited in systems such as a toroidal Josephson junction, (see for example the seminal Caldeira-Leggett model [60]), where the magnetic flux through the torus is quantised, neutrinos are perhaps unique in that they exhibit perfect coherence over thousands of kilometres. For a more recent discussion on issues such as Lorentz invariance of neutrino oscillations, on whether charged leptons can oscillate, see Akhmedov and Smirnov's articles [61–63]. Whilst these discussions are purely academic for SM neutrinos, the issue of coherence does become relevant for a fourth, light sterile neutrino of mass 1–10 eV.

2.3 Neutrino-Mass Models

Introduction Recall that in the chiral representation, a four-component spinor $\psi = \begin{pmatrix} L & R \end{pmatrix}^{\mathrm{T}}$ transforms under $\mathrm{SU}(2)_{\mathrm{L}} \otimes \mathrm{SU}(2)_{\mathrm{R}}$ in the following way

$$L \mapsto \exp\left[-\frac{\boldsymbol{\sigma}}{2} \cdot (\mathrm{i}\boldsymbol{\theta} + \boldsymbol{\phi})\right] L \qquad R \mapsto \exp\left[-\frac{\boldsymbol{\sigma}}{2} \cdot (\mathrm{i}\boldsymbol{\theta} - \boldsymbol{\phi})\right] R, \tag{2.24}$$

where L, R are two-component spinors, $\boldsymbol{\theta}$ are the parameters for spinor rotations, and $\boldsymbol{\phi}$ are for spinor boosts. (Throughout this section I use two-component spinors unless otherwise stated.) Since the rotations have the same sign, whilst the boosts have opposite signs for left and right spinors, the simplest Lorentz scalar must mix the left and right two-component spinors L, R,

$$m_D(L^\dagger R + R^\dagger L). \tag{2.25}$$

This is thoroughly dissatisfying as a theory of neutrino mass, as one must introduce three SM singlets ν_{R} for each neutrino flavour, which have no interactions apart from the Higgs. Furthermore, there is no explanation for why the neutrino is almost massless. Fortunately, there is an alternative to Dirac's formulation of spinors, first developed by Majorana [64]. We shall not need its quantum theory, which is covered in [24] and [10, §6.2]. We shall merely note that, with the aid of the relation $\sigma_2\sigma_i^{\mathrm{T}}\sigma_2 = -\sigma_i$, we can write down the

Majorana mass

$$m_M(L^{\mathrm{T}}\mathrm{i}\sigma_2 L + L^{\dagger}\mathrm{i}\sigma_2 L^*) = m_M\bar{\chi}\chi, \qquad \text{where} \qquad \chi \equiv \begin{pmatrix} L & \mathrm{i}\sigma_2 L^* \end{pmatrix}^{\mathrm{T}} \tag{2.26}$$

is called a (four-component) Majorana spinor. Note that the antiparticle of L is $L^c \equiv \mathrm{i}\sigma_2 L^*$, which is derived in most textbooks when determining the charge-conjugation operator $C \equiv \mathrm{i}\gamma_2$. Thus, we can understand the four-component Majorana spinor χ as using the antiparticle of the left-handed component to generate the right-handed component.

To explain neutrino mass, we need a model that induces one of these mass terms, and which preferably explains why it is almost massless. In the so-called Standard-Model Effective Field Theory, neutrino masses can be generated by the non-renormalisable electroweak-invariant dimension-five operator, first published by Weinberg in 1979 [65],

$$\frac{y_\nu}{\Lambda}\left(L^{\mathrm{T}}\mathrm{i}\sigma_2\boldsymbol{\sigma}L\right)\cdot\left(H^{\mathrm{T}}\mathrm{i}\sigma_2\boldsymbol{\sigma}H\right). \tag{2.27}$$

In eq. (2.34), I demonstrate that $\Psi^{\mathrm{T}}\mathrm{i}\sigma_2\boldsymbol{\sigma}\Psi$ transforms as the adjoint representation.

The seesaw mechanism Already in the first quantitative discussion of neutrino oscillations by Gribov and Pontecorvo in 1969 [38], Majorana mass terms for the electron and muon neutrinos were explicitly introduced to induce oscillations — however they did not address how to generate them in a way that respected electroweak gauge invariance. When Pati and Salam first introduced their grand unified theory (GUT), with left-right symmetry, they found in 1974 that neutrino masses could naturally arise from it [66]. This idea was followed up in 1975 by Mohapatra and Pati [67], who developed a GUT, whose CP violation was naturally suppressed by the parameter $(m_{W_{\mathrm{L}}}/m_{W_{\mathrm{R}}})^2 \sin 2\theta_{\mathrm{R}}/\sin 2\theta_{\mathrm{L}}$, where $m_{W_{\mathrm{L}}}$ is the mass of the Standard-Model W boson, and $m_{W_{\mathrm{R}}}$ is the mass of a new heavy gauge boson that couples to right-handed currents. This suppression due to the ratio of a lighter and heavier scale is the essence of the seesaw mechanism, and indeed they even mentioned in the introduction

"We conjecture that a qualitative link between [the] breakdown of CP invariance and tiny but nonzero neutrino masses may emerge in such an extended scheme, which may be considered elsewhere."

Another precursor to the seesaw mechanism came later that year, in a footnote by a paper by Fritzsch, Gell-Mann and Minkowski [68] and was followed up in more detail by Cheng in 1976 [69], who sought to explain the lightness of the neutrino by setting its bare mass to zero, and inducing a small Majorana mass term through radiative corrections with a heavy Majorana neutrino N_M (he did not take this to be sterile, but was motivated by emerging evidence of a new heavy charged lepton, which we now know as the tau, and took N_M to be its doublet partner). He also considered inducing a small mixing between the SM neutrino and the new Majorana one, $\nu_e + \epsilon N_M$ for small ϵ, to explain the hierarchy of masses between neutrinos and electrons; this was based off analogous earlier work to explain the mass hierarchy in the quark sector by Zee in 1974 and 1976 [70, 71]. In 1977, Cheng and Li [72, 73] showed that such a lepton-flavour-violating Majorana mass term did not contradict bounds on processes like $\mu \to e\gamma, 3e$ *etc.*, due to a suppression similar to the GIM mechanism (1970) in the quark sector [74].

In 1977, Peter Minkowski first wrote down the *type-I seesaw mechanism* [75], which was popularised by Gell-Mann, Ramond and Slansky [76] and Yanagida [77, 78] in the context of $SO(10)$ GUT. Mohapatra and Senjanović also discussed it in 1980 by [79] in the context of a left-right symmetric model with gauge group $\mathrm{SU}(2)_{\mathrm{L}} \otimes \mathrm{SU}(2)_{\mathrm{R}} \otimes \mathrm{U}(1)$. (I personally find their suggestion particularly elegant, as they connect the smallness of the neutrino mass with the suppression of right-handed currents. The neutrino mass is suppressed by $m_e/m_{W_{\mathrm{R}}}$, and in the limit of an infinitely heavy W_{R}, the neutrino is massless and there is maximal parity violation.)

In type-I seesaw, a new electroweak-singlet (sterile), right-handed, two-component neutrino N_{R} is introduced, with a Majorana mass term, whose mass is connected with the UV scale of new physics; the Lagrangian also contains a Dirac mass term, generated by the SM Higgs in the same way as the charged leptons:

$$\begin{aligned}\mathcal{L}_{\text{mass}} &= -m_{\mathrm{EW}} N_{\mathrm{R}}^{\dagger} \nu_{\mathrm{L}} - M_{\mathrm{UV}} \frac{1}{2} N_{\mathrm{R}}^{\dagger} \mathrm{i}\sigma_2 N_{\mathrm{R}}^{*} + \mathrm{h.\,c.} \\ &= -\frac{1}{2} \begin{pmatrix} \nu_{\mathrm{L}}^{\dagger} & [N_{\mathrm{R}}^{c}]^{\dagger} \end{pmatrix} \hat{C}^{-1} \begin{pmatrix} 0 & m_{\mathrm{EW}} \\ m_{\mathrm{EW}} & M_{\mathrm{UV}} \end{pmatrix} \begin{pmatrix} \nu_{\mathrm{L}} \\ N_{\mathrm{R}}^{c} \end{pmatrix} + \mathrm{h.\,c.},\end{aligned} \tag{2.28}$$

where $\hat{C} \equiv \mathrm{i}\gamma_2\gamma_0 = (\mathrm{i}\sigma_2)_{\mathrm{L}} \otimes (-\mathrm{i}\sigma_2)_{\mathrm{R}}$ is the particle-antiparticle conjugation operator, and $\overline{\psi^c} \equiv \psi^{\mathrm{T}} \hat{C}^{-1}$. Expanding to leading order in $\varepsilon \equiv m_{\mathrm{EW}}/M_{\mathrm{UV}}$, the mass eigenstates and there masses become

$$\begin{aligned}(\nu_{\text{light}})_{\mathrm{L}} &= \nu_{\mathrm{L}} - \varepsilon \nu_{\mathrm{R}}^{c}, \quad m_{\text{light}} = \varepsilon \cdot m_{\mathrm{EW}} \\ (\nu_{\text{heavy}})_{\mathrm{L}} &= \varepsilon \nu_{\mathrm{L}} + \nu_{\mathrm{R}}^{c}, \quad m_{\text{heavy}} = M_{\mathrm{UV}}.\end{aligned} \tag{2.29}$$

One can formulate the theory of Majorana neutrinos with the four-component Majorana spinors $\chi_\alpha = \begin{pmatrix} (\nu_\alpha)_{\mathrm{L}} & (\nu_\alpha)_{\mathrm{L}}^{c} \end{pmatrix}^{\mathrm{T}}$, where $\alpha =$ light, heavy.

As it is expected that the new-physics scale, which I call M_{UV}, is many orders of magnitude larger than the electroweak scale, ε is expected to be very small, thus naturally explaining the smallness of the neutrino mass. (And if one takes the electroweak Yukawa coupling to be small, so $m_{\mathrm{EW}} \sim$ electron mass, then $M_{\mathrm{UV}} \sim$ TeV.) If the Majorana mass is generated by the spontaneous breaking of global lepton-number symmetry, the (very weakly coupled) massless Nambu-Goldstone mode is called the majoron, which was first considered in 1980 by Chikashige, Mohapatra and Peccei [80].

In type-II seesaw, a Majorana mass for the left-handed SM neutrino is generated directly. This can be achieved via a Higgs triplet $\boldsymbol{\Delta} \sim (-1, 2)$, which, to the best of my knowledge, was first discussed in the context of lepton-number violation by Konetschny and Kummer in 1977 [81],

$$\begin{aligned}\mathcal{L}_{\text{mass}} &= y_{\Delta} \left(\overline{L^c} \mathrm{i}\sigma_2 \boldsymbol{\sigma} L \right) \cdot (U \boldsymbol{\Delta}) + \mathrm{h.\,c.} \\ &= -\sqrt{2} y_{\Delta} \left(\overline{\nu_{\mathrm{L}}^{c}} \nu_{\mathrm{L}} \Delta^{0} + \overline{e_{\mathrm{L}}^{c}} e_{\mathrm{L}} \Delta^{++} + \sqrt{2}\, \overline{\nu_{\mathrm{L}}^{c}} e_{\mathrm{L}} \Delta^{+} \right) + \mathrm{h.\,c.},\end{aligned} \tag{2.30}$$

where $\boldsymbol{\sigma}$ is the vector of Pauli matrices, whose second component is σ_2, and

$$U \equiv \begin{pmatrix} -\frac{1}{\sqrt{2}} & 0 & \frac{1}{\sqrt{2}} \\ \frac{\mathrm{i}}{\sqrt{2}} & 0 & \frac{\mathrm{i}}{\sqrt{2}} \\ 0 & 1 & 0 \end{pmatrix}, \qquad \boldsymbol{\Delta} \equiv \begin{pmatrix} \Delta^{0} \\ \Delta^{+} \\ \Delta^{++} \end{pmatrix}, \qquad L \equiv \begin{pmatrix} \nu_{\mathrm{L}} \\ e_{\mathrm{L}} \end{pmatrix}; \tag{2.31}$$

the superscripts on Δ reflect their electric charge. Note that the Pauli matrices operate in weak-isospin space, whereas the conjugate $\overline{L^c} \equiv L^{\mathrm{T}} \hat{C}^{-1}$ operates on the Lorentz indices.

To see that $\left(\overline{L^c}\mathrm{i}\sigma_2\boldsymbol{\sigma}L\right) \sim (-1,-2)$, we note that since L has hypercharge -1, it's clear that the combination has hypercharge -2. To see how it transforms under $\mathrm{SU}(2)_{\mathrm{L}}$, first discard $\hat{C}$, which only operates on spinor indices, and then apply an infinitesimal transformation

$$L^{\mathrm{T}}\mathrm{i}\sigma_2\sigma_i L \mapsto L^{\mathrm{T}}\left(1+\frac{\mathrm{i}}{\epsilon_a}\sigma_a^{\mathrm{T}}\right)\mathrm{i}\sigma_2\sigma_i\left(1+\frac{\mathrm{i}}{2}\epsilon_a\sigma_a\right)L. \tag{2.32}$$

One can move the σ_2 left by conjugating $\sigma_2\sigma_a^{\mathrm{T}}\sigma_2 = -\sigma_a$, whence one obtains

$$L^{\mathrm{T}}\mathrm{i}\sigma_2\left(1-\frac{\mathrm{i}}{2}\epsilon_a\sigma_a\right)\sigma_i\left(1+\frac{\mathrm{i}}{2}\epsilon_a\sigma_a\right)L = L^{\mathrm{T}}\mathrm{i}\sigma_2\left(\sigma_i-\frac{\mathrm{i}}{2}[\sigma_a,\sigma_i]\right)L. \tag{2.33}$$

Recall from representation theory, that the adjoint representation is defined by the action of the commutator, that is $A_a(\frac{\sigma_b}{2}) = [\frac{\sigma_a}{2},\frac{\sigma_b}{2}] = \mathrm{i}\varepsilon_{abc}\frac{\sigma_c}{2}$. Therefore, we have the transformation (with a sign flip from swapping the indices of A_a)

$$L^{\mathrm{T}}\mathrm{i}\sigma_2\sigma_i L U_{im} \mapsto L^{\mathrm{T}}\mathrm{i}\sigma_2\sigma_j L\left(\mathbb{1}+\mathrm{i}\epsilon_a A_a\right)_{ji}U_{im}. \tag{2.34}$$

Inserting $UU^\dagger = \mathbb{1}$, and noting that $U^\dagger A_a U = T_a$, where T_a is the triplet representation of $\mathfrak{su}(2)$, we see $L^{\mathrm{T}}\mathrm{i}\sigma_2\boldsymbol{\sigma}LU$ manifestly transforming as a triplet under $\mathrm{SU}(2)_{\mathrm{L}}$.

The triplet will develop a VEV like the Higgs (with associated Majoron [82]; see [83] for a more recent analysis with a sterile neutrino),

$$\langle\boldsymbol{\sigma}\cdot U\boldsymbol{\Delta}\rangle \equiv \begin{pmatrix} \langle\Delta^+\rangle & \sqrt{2}\,\langle\Delta^{++}\rangle \\ -\sqrt{2}\,\langle\Delta^0\rangle & -\langle\Delta^+\rangle \end{pmatrix} = \begin{pmatrix} 0 & 0 \\ \sqrt{2}v_\Delta & 0 \end{pmatrix}, \tag{2.35}$$

thereby generating a tree-level Majorana mass for the neutrino. However, since one is now modifying the electroweak sector, one has to consider constraints from, for example, the electroweak parameter $\rho \equiv M_W^2/(M_Z\cos\theta_W)^2$, due to the contribution from the new scalar (see [84] for an early discussion).

In 1980, Zee proposed a neutrino-mass model of type II, where the neutrino mass is generated at the one-loop level and is calculable [85]. (This suppression of the neutrino mass due to it being generated radiatively is not possible for the triplet [84].) A scalar h is introduced, which has electric charge, but is a singlet under $\mathrm{SU}(2)_{\mathrm{L}}$. (This can be well motivated from $\mathrm{SU}(5) \to \mathrm{SU}(3)\otimes\mathrm{SU}(2)_{\mathrm{L}}\otimes\mathrm{U}(1)_{\mathrm{Y}}$, GUT-to-SM symmetry breaking.) Since it is charged, it cannot attain a VEV due to gauge invariance, so one must have two Higgs doublets to introduce a trilinear scalar interaction (here my presentation follows [84]), with Lagrangian

$$\mathcal{L}_{\text{mass}} = y_{ab}L_a^{\mathrm{T}}\hat{C}^{-1}\mathrm{i}\sigma_2 L_b h + f_{12}H_1^{\mathrm{T}}\mathrm{i}\sigma_2 H_2 h + \mathrm{h.\,c.} \tag{2.36}$$

Notice that since $\mathrm{i}\sigma_2$ is antisymmetric, the operators for diagonal couplings y_{11} and f_{11} vanish, such that only couplings off-diagonal in flavour space are permitted. Further note that $\hat{C}^{-1}$ makes the first term a Lorentz scalar, and that $(\psi^{\mathrm{T}}\mathrm{i}\sigma_2\psi) \sim (0,2)$ for $\psi \sim \left(\frac{1}{2},1\right)$, whence $h \sim (0,-2)$.

In 1980 Cheng and Li also discussed [84] using a doubly charged singlet scalar (coupled to the right-handed leptons) to induce a neutrino mass at the two-loop level (see fig. 2.4), however they did not investigate the model in detail. (Konetschny and Kummer discussed both the singly and doubly charged scalar, but in the context of lepton-number violation,

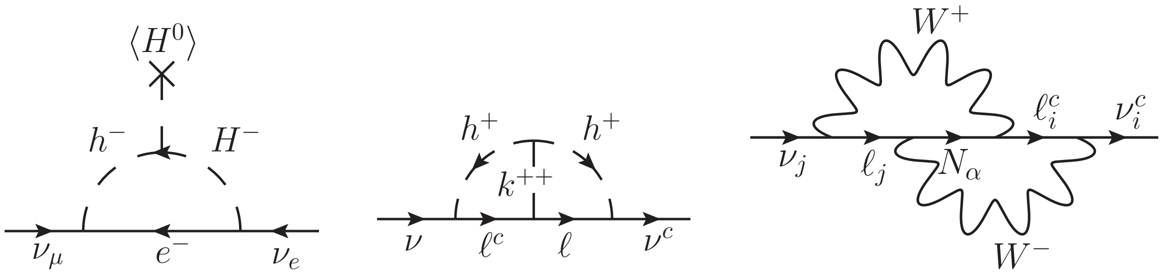

Figure 2.4: Left: one-loop diagram, which generates the neutrino mass in Zee's model. Middle two-loop diagram, which generates the neutrino mass à la Cheng & Li, and Babu. Right: two-loop diagram that induces neutrino mass by Petcov and Toshev.

not neutrino mass.) Later in 1988 Babu investigated this suggestion as a realistic mass model in more depth [86], albeit with a singly charged singlet instead of a multiplet like Cheng & Li's original suggestion.

In addition to these scalar extensions, it is possible to extend only the fermionic lepton sector to induce a radiative Majorana mass, one of the first examples being that of Petcov and Toshev in 1984 [87] (later rediscovered by Babu and Ma in 1988 [88]). By introducing a fourth heavy neutrino with both Dirac and Majorana masses, which mixes with the light SM neutrinos, two-loop Majorana masses for the SM neutrinos can be induced by double W-boson exchange fig. 2.4. The diagram is proportional to the mass of the central neutrino m_α, which is why a heavy neutral lepton is needed, otherwise the neutrino mass is protected (multiplicatively renormalisable; see [89] for an instructive overview).

The models discussed above were historically important, but since then various other radiative models with one-, two- and three-loop diagrams involving new scalars or leptoquarks have been proposed. For a review, see [90]; see also the references of [91, §1].

Another novel extension of the fermionic lepton sector, which can induce tree-level neutrino masses, was considered by Foot *et al.* in 1989 [92], but see also [93, 94]. (This is called type-III seesaw by some [95, 96], however for others type-III seesaw means something different [97–99]. The former epithet is due to a complete classification of tree-level realisations of the dimension-5 effective operator, which generates neutrino mass [100].) An hyperchargeless ($Y = 0$), $\mathrm{SU}(2)_\mathrm{L}$ triplet of right-handed (two-component) leptons $\boldsymbol{\Sigma}_\mathrm{R}$ is introduced,

$$\boldsymbol{\sigma}\cdot U\boldsymbol{\Sigma}_\mathrm{R} = \begin{pmatrix} \Sigma^0_\mathrm{R} & \sqrt{2}\Sigma^+_\mathrm{R} \\ -\sqrt{2}\Sigma^-_\mathrm{R} & -\Sigma^0_\mathrm{R} \end{pmatrix}, \quad \text{where} \tag{2.37}$$

$$\begin{aligned} \mathcal{L}_\Sigma &= \sum_{\alpha=e,\mu,\tau} y_\alpha \phi^\mathrm{T} \mathrm{i}\sigma_2 \boldsymbol{\sigma}\cdot U\boldsymbol{\Sigma}^\dagger_\mathrm{R} L_\alpha - \frac{1}{2}\operatorname{Tr}\left(M_\Sigma \boldsymbol{\Sigma}^\mathrm{T}_\mathrm{R}\hat{C}^{-1}\boldsymbol{\Sigma}_\mathrm{R}\right) + \mathrm{h.\,c.} \\ &= -\sum_{\alpha=e,\mu,\tau} y_\alpha \left[\sqrt{2}\phi^0\left(\Sigma^+_\mathrm{R}\right)^\dagger e_\mathrm{L} + \phi^0\left(\Sigma^0_\mathrm{R}\right)^\dagger \nu_\mathrm{L} + \phi^+\left(\Sigma^0_\mathrm{R}\right)^\dagger e_\mathrm{L} + \sqrt{2}\phi^+\left(\Sigma^-_\mathrm{R}\right)^\dagger \nu_\mathrm{L}\right] \\ &\quad - \frac{1}{2}\operatorname{Tr}\left(M_\Sigma \boldsymbol{\Sigma}^\mathrm{T}_\mathrm{R}\hat{C}^{-1}\boldsymbol{\Sigma}_\mathrm{R}\right) + \mathrm{h.\,c.} \end{aligned} \tag{2.38}$$

Recall that $L \sim \left(\frac{1}{2}, -1\right)$, $\phi^\mathrm{T} \sim \left(\frac{1}{2}, +1\right)$, so in the first term, the SM fields $\phi^\mathrm{T}\mathrm{i}\sigma_2\boldsymbol{\sigma}L_\alpha$ form a hypercharge singlet, isospin triplet. Note that in Foot *et al.*'s original paper, they use $\boldsymbol{\Sigma}^c_\mathrm{L}$ instead of $\boldsymbol{\Sigma}_\mathrm{R}$. Upon electroweak symmetry breaking, a Dirac mass term between Σ^0_R

and ν_L is generated, leading to a mass matrix like type-I seesaw.

For a modern review on the seesaw mechanism in the context of GUTs, see [99, §§6,7]. For a comprehensive early review, see [101].

Dirac vs. Majorana As already pointed out by Case in 1957 [24], novel effects due to the Majorana nature of a fermion are suppressed by factors $(m/E)^2$, for Majorana mass m and where E is the characteristic energy scale for a relevant process. Case already recognised that double β decay was a crucial observable for the differentiation between the Dirac or Majorana nature of the neutrino, noting that,

> *"The only experimental conclusion that follows from the [Majorana] theory is that a maximum degree of nonconservation of parity [*i.e. *massless neutrinos] implies a minimum probability of double β decay while conservation of parity implies a maximum probability of double β decay. Loosely speaking, this says that "parity nonconservation" and "double β decay" are conjugate variables."*

(He credits [25] for first noting this.) Since neutrino oscillations do not violate the total lepton number, they cannot distinguish between Dirac or Majorana masses, either in vacuum [102, 103], or matter [104], although lepton-number violating processes like $\nu \leftrightarrow \overline{\nu}$, like those originally considered by Pontecorvo, may be sensitive to Majorana phases [105]. For an overview of neutrinoless double-beta decay, see [10, §14.3].

The existence of Dirac neutrinos is determined by whether the Lagrangian has a global U(1) symmetry; if no such symmetry exists, then lepton number (the charge of the U(1) symmetry) is violated, and we have Majorana neutrinos. However, this cannot be determined by simply inspecting the mass term, as identified by Wolfenstein in 1981 [106] (see [107] for a discussion with arbitrary number of generations). Wolfenstein considered the case of pseudo-Dirac neutrinos, where the mass matrix has a global U(1) symmetry, however the charge of the symmetry is not the same as the lepton number of the weak sector. Namely, it is possible to write the mass term in the Dirac form only, but in a basis that is not the weak-flavour basis. Therefore, there is no global U(1) symmetry of the whole Lagrangian, and a small Majorana mass is generated by radiative corrections.

2.4 Solar Oscillations

The oscillations of solar neutrinos were the first kind of neutrino oscillations to be observed. Whilst the notion of neutrino oscillations seems natural to us today, at the time there was much scepticism of Davis's experiment; furthermore, enormous effort was needed in both nuclear-physics experiments and solar-physics simulations to create what is now known as a standard solar model (for an historical overview with relevant references, upon which I have relied, I refer the reader to the scientific biography of John Bahcall [108]; also see the appendix of [109]). Numerous alternative solutions to the solar neutrino problem were also put forward, which we shall briefly review here.

The foundations of any prediction for the solar neutrino flux lie in stellar nucleosynthesis. Ions in the plasma of the sun collide with each other, with the collision energy determined by the Maxwell-Boltzmann distribution with the local thermodynamic parameters (temperature, density, pressure, *etc.*). Some of those collisions will result in quantum-tunneling ions and nuclear fusion (the physics of Coulomb-barrier tunneling was first worked out by Gamow: see §10.1 of [10] for relevant references).

The primary source of solar neutrinos comes from the *pp* chain, where protons collide to make deuteron, which again collides with protons to make isotopes of helium, which collide to make beryllium and also boron. The cross section of each relevant nuclear reaction has to be measured in laboratory experiments. (One important historical development was the measurement of the $^3\mathrm{He}(\alpha,\gamma)^7\mathrm{Be}$ cross section, which was one thousand times larger than expected [110]; another is the calculation by Bahcall in 1964 that showed the capture of ^{8}B neutrinos by ^{37}Cl was enhanced by 18 times due to transitions to excited states of ^{37}Ar [111].) These along with observations of the surface composition, opacity, equation of state and age, are input parameters for a detailed, computationally sophisticated simulation of the sun.

The first realistic calculation of the solar neutrino flux by Bahcall, Fowler, Iben and Sears [36] was crucial for the design of the Homestake experiment. (This is because the neutrino-capture cross section increases sharply with energy, so the neutrinos from ^{8}B contribute the most, despite it being the least common reaction in the sun — and therefore the most difficult to predict). The complicated procedure for predicting the neutrino flux, and the dependence of the model on input parameters, meant that Bahcall would continue refining the solar model for the rest of his career. (§1.17 of [109] gives a taste of some of the scepticism that solar modelling could be accurate enough for the purpose of neutrino physics.) His efforts eventually bore fruit, as his standard solar model could independently reproduce the precise measurements of solar helioseismology [112].

A list of non-neutrino solutions to the solar neutrino problem can be found in §5 of [109]. Whilst most involve modifying solar physics to reduce the ^{8}B flux (to explain the Homestake deficit), there are some more exotic suggestions, such as a black hole in the solar core [114], and WIMPs altering solar physics in its core [115–117]. Other non-oscillation solutions were also suggested: electron-neutrino decay by Bahcall in 1972 [118] (see also §9.4 of [109]), spin precession (via solar magnetic fields into the right-handed sterile state) from a neutrino magnetic moment by Cisneros and Werntz in 1971 [119] (see also §9.3 of [109]), and violation of the equivalence principle (flavour-dependent gravitational couplings) by Gasperini in 1988 [120].

An important development for the solar neutrino problem was the consideration of matter effects. It was Wolfenstein in 1978 who first considered how off-diagonal, coherent forward scattering (analogous to kaon oscillations), could induce oscillation in the case of massless neutrinos, and how they modified oscillations from massive neutrinos [121]. Further investigation of the effect of matter on solar neutrino propagation by Mikheyev and Smirnov in 1986 led them to discover that the varying electron density of the sun could lead to resonant oscillations within the sun, for a wide range of neutrino oscillation parameters, including small mixing [122]. They also noted that in some regions of parameter space, the resonance effect would only affect high-energy ^{8}B neutrinos. The physics of the resonance, its analysis as adiabatic conversion in the form of a two-level crossing and its analogy with the Landau-Zener transition was immediately made by Bethe [123], Parke [124] and Haxton [125].

The resonance in matter, called the MSW effect, was a turning point for the solar neutrino problem. Since the deficit of observed neutrinos was ~ 3 times less, mixing parameters between all three neutrinos would need to be maximal to explain the deficit, which was viewed as unattractive [126]. (Indeed in 1988, Bahcall, Davis and Wolfenstein

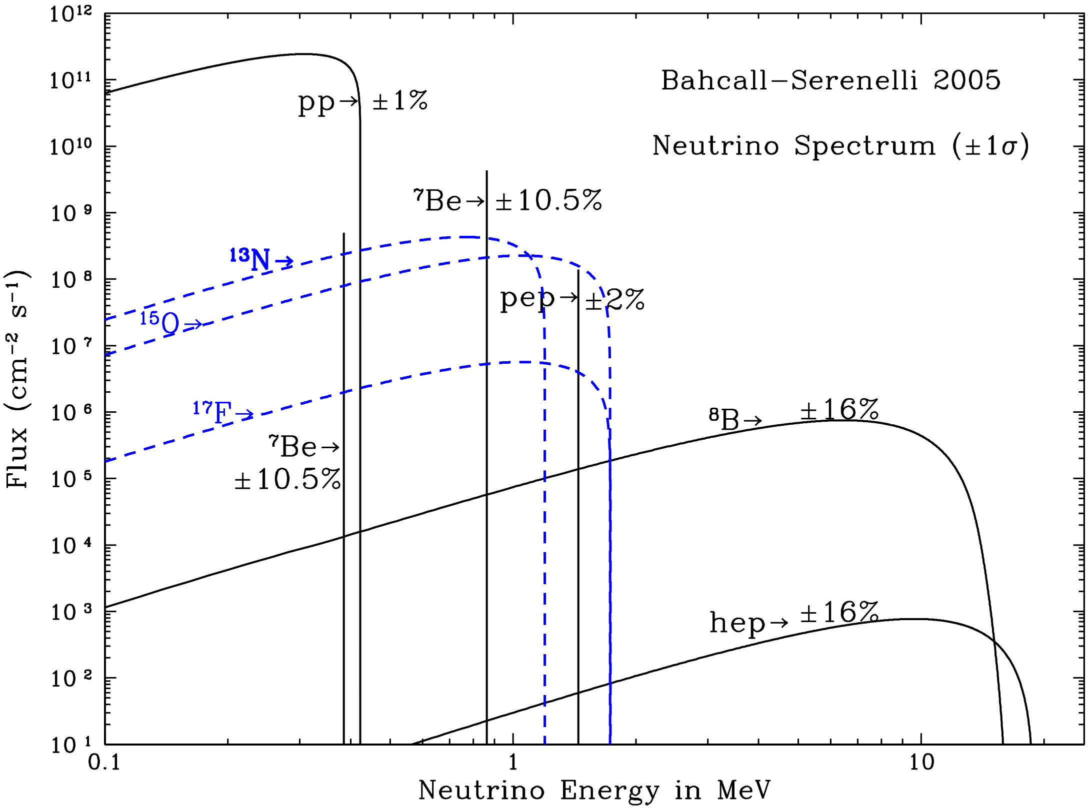

Figure 2.5: Solar neutrino flux, as calculated by Bahcall, Serenelli and Sarbani in 2005 [113] (a PDF version can be found at `www.sns.ias.edu/~jnb/`).

wrote a review article in *Nature* titled *Solar neutrinos: a field in transition* [127].) In 1986, using only a two-neutrino framework, Rosen and Gelb identified two possible solutions to the solar neutrino problem: one with small and the other with large vacuum mixing angles [128]. Large mixing angles were seen to be unattractive at the time (Rosen and Gelb state that the solution with small mixing angles was *"a most attractive solution"*), particularly as the other example of flavour mixing in the quark sector had small mixing parameters. (Bahcall and Bethe would write a paper in 1990 predicting the small mixing angle would prevail [129].)

During these theoretical developments, other experiments were proposed to confirm the deficit observed by Homestake. The second experiment to observe solar neutrinos was Kamiokande-II. This experiment was original proposed as a nucleon decay experiment at a mine in the mountain Kamioka, Japan — hence the acronym KamiokaNDE — by observing 3000 tonnes of water with photomultiplier tubes, to detect any anomalous decays of protons, as predicted by grand unified theories. The experiment was upgraded to observe elastic scattering of solar neutrinos on electrons, by observing the Cerenkov radiation of a scattered electron.

Kamiokande-II was able to infer the direction (and energy spectrum) of the incoming neutrinos, thereby correlating the signal to the sun, and timing information was also used, for example to observe the day-night asymmetry, when solar neutrino propagation through the Earth at night can regenerate electron neutrinos [130]. However, the scattering cross section is much smaller than the absorption cross section so the event rate was much lower than Homestake. This required much effort to reduce backgrounds from radioactive species in water; furthermore, since any light high-energy particle can mimic the Cerenkov-radiation signal, this technique has poor particle identification — another problem for background reduction. (See [131] and §13.2 of [109] for details.) This meant that K-II had a high energy threshold for neutrino events, and was only sensitive to ^{8}B neutrinos — but it confirmed the deficit by Homestake and unequivocally determined the origin of the neutrinos in 1989 [132]. (It was also fortunate to have been operating during the famous SN1987A neutrino burst [133], which still provide relevant constraints on new physics in the neutrino sector.)

During these developments, another radiochemical neutrino experiment, similar to the original Homestake one was under development. First suggested by Kuzmin in 1965 [134], the experiment used ^{71}Ga as a neutrino target (instead of ^{37}Cl). Thus one can measure *pp* neutrinos, the most intense neutrino flux, owing to the low energy threshold of gallium. Two such experiments were undertaken: one at Gran Sasso called GALLEX (Gallium European Experiment) and another at Baksan Valley called SAGE (Soviet American Gallium Experiment). Both were very ambitious, as at the time of development, the required amount of gallium needed was several times the total annual production [127]. The European group used gallium in solution, whereas the Soviet group used metallic gallium; both used a similar method of radiochemical extraction, calibrated by injecting a low artificial amount of ^{71}Ge which was then extracted; the detector efficiency is calibrated with an intense ^{51}Cr source (see [109, §11] and references therein for a detailed overview of the experimental technique).

SAGE first published confirmation of the solar-neutrino deficit in 1991 [135]; GALLEX followed in 1992 [136, 137], which bolstered confidence that the deficit was not due to an error in the calculations of Bahcall, as the *pp* neutrinos were directly related to solar luminosity, therefore being insensitive to the details of the internal dynamics of the sun.

The final proof that solar neutrinos were oscillating (instead of more exotic physics), came from the Sudbury Neutrino Observatory (SNO), which aimed to observe all solar neutrinos using the flavour-blind neutral-current disintegration of the deuterium nucleus by a neutrino, as proposed by Chen in 1985 [139]. The neutron emitted from the disintegrated nucleus would be captured by deuterium in the detector and release a 6.25 MeV photon. In 2002, SNO confirmed a total neutrino flux, consistent with Bahcall's calculations as well as other solar neutrino observatories, thereby unequivocally proving that solar neutrinos oscillated [140].

2.5 Atmospheric Oscillations

Atmospheric neutrinos are produced in the same manner as accelerator neutrinos:

$$\begin{aligned} p(\text{cosmic ray}) + \text{air} \to \pi^\pm(K^\pm) \quad &+ \quad X \\ \pi^\pm(K^\pm) \quad \to \quad &\mu^\pm + \nu_\mu/\overline{\nu}_\mu \\ &\mu^\pm \to e^\pm + \nu_e/\overline{\nu}_e + \overline{\nu}_\mu/\nu_\mu, \end{aligned} \tag{2.39}$$

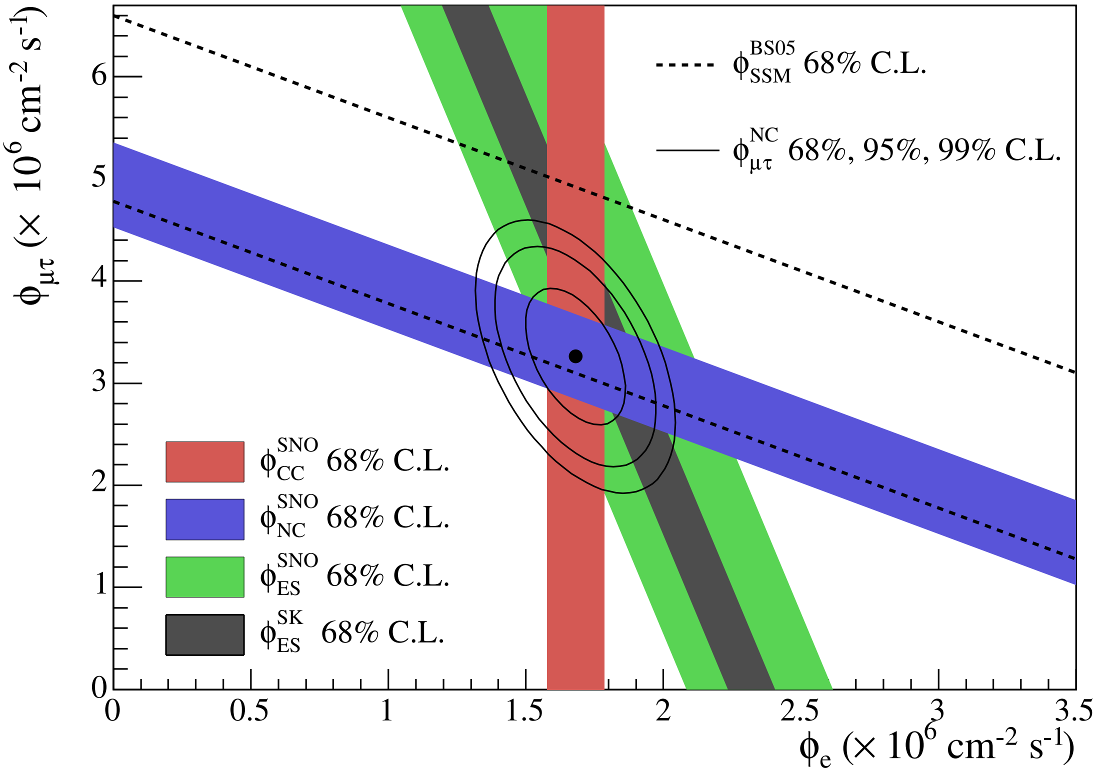

Figure 2.6: SNO charged-current (red), neutral-current (blue), electronic recoil (green) and the Super Kamiokande electronic recoil (grey) measurements, and their combination (solid contours), compared with the Standard Solar Model prediction (dotted contour); courtesy of [138].

high-energy cosmic protons (and heavier nuclei) smash onto target nuclei in the atmosphere, creating mesons (mostly pions and kaons), which decay into muons and neutrinos. The basic detection technique, using a large water Cerenkov detector, with a veto layer to discard Cerenkov radiation from passing cosmic muons, was suggested already in the early 1960s [141, 142]. The first (indirect) detection of atmospheric neutrinos occurred in the Kolar Gold Field Mine, South India, in 1965, which used plastic scintillator plates to detect horizontal muons, produced from charged-current interactions of the muon neutrino with rock [143, 144] (the direction of the muon excludes the possibility that it was produced from cosmic rays, as muons do not have such a long penetration depth through rock — the mine acted as a veto); and also in the East Rand Proprietary Gold Mine, South Africa, also in 1965, using walls of mineral-oil liquid scintillators [145].

Similar experiments were undertaken in the decades following, with some reporting deficits compared to Monte Carlo calculations (see the references in [10, §11], from which I draw much of the history), most notably the nucleon-decay experiments in the late ’80s and early ’90s: Kamiokande [146] and IMB [147, 148], for whom the atmospheric neutrinos were merely a background. This was called the *atmospheric neutrino anomaly*. However other experiments based on scintillating iron plates like NUSEX [149, 150] and

Fréjus [151,152] observed no deficit. The parameters relevant for solar neutrino oscillation were not relevant for the energies and propagation lengths of neutrinos created from cosmic rays in the atmosphere, leading to the possibility that a deficit be due to $\nu_\mu \leftrightarrow \nu_\tau$ oscillations — furthermore, no experiment observed a deficit of electron neutrinos.

Atmospheric oscillations were definitively confirmed by the Super Kamiokande experiment, a much larger 50 kiloton version of Kamiokande, located in the same mine, with more than 11 000 photomultiplier tubes. In 1998, SuperK published its results, where they could successfully explain the angular dependence of the neutrino flux by oscillations. Since the propagation length depends on the zenith angle the could also demonstrate sinusoidal dependence of the atmospheric neutrino flux with L/E_ν [153]. The MACRO experiment at Gran Sasso, which consisted of a box of ten layers of concrete sandwiched between thin tracking layers, surrounded by liquid scintillators [154], simultaneously released similar results, albeit at a much lower significance [155].

The deficit was also confirmed in 1999 by Soudan 2, Soudan Minnesota, [156], a 963-ton fine-grained tracking calorimeter; the detector consisted of tubes of argon gas sandwiched between high-voltage copper-foil electrodes and corrugated steel sheets. Charged particles ionised the argon gas, and the ions would drift to the electrodes, registering a signal [157,158]. Later in 2003 it also observed a zenith-angle dependence of the neutrino flux, and oscillations in L/E_ν [159].

2.6 Entering the Precision Era of Neutrino Oscillations

As one has seen from the history, it took many decades to establish that neutrinos do indeed oscillate. Because they interact so weakly, large detectors with long exposure times need to be built. Since neutrino experiments are generally statistics limited, it is crucial to combine the datasets of different experiments to determine the oscillation parameters (of the standard PMNS parameterisation eq. (2.17)) most precisely. Already in 1980, there were attempts to combine data from nuclear reactors (which are an intense source of antineutrinos) [160], as well as reconciling their data with those from the deep-mine experiments that measured atmospheric neutrinos, and Homestake's solar-neutrino data [161,162].

As more and more data from different experiments accumulated, it became possible to make quantitative statements on the oscillation parameters. To do so, one introduces a parameter χ^2 with known statistical properties, in order to characterise how well a model reproduces data. In the early 1990s, an approximate two-flavour oscillation probability was used, with the two parameters Δm^2 and $\sin^2 2\theta$. When there was no spectral information on the solar neutrinos, the statical parameter was defined as

$$\chi^2(\Delta m^2, \sin^2 2\theta) = \sum_{ij} (R^i_{\text{data}} - R^i_{\text{pred}}) V^{-1}_{ij} (R^j_{\text{data}} - R^j_{\text{pred}}), \tag{2.40}$$

where the indices i, j run over the three observations from the Homestake, Gallium and Kamioka experiments. The covariance matrix V determines the correlated statistical properties of the ratios R^i, due to statistics, experimental systematics, and theoretical systematics of the solar model. Under certain conditions, the quantity $\Delta\chi^2 \equiv \chi^2 - \chi^2_{\text{min}}$,

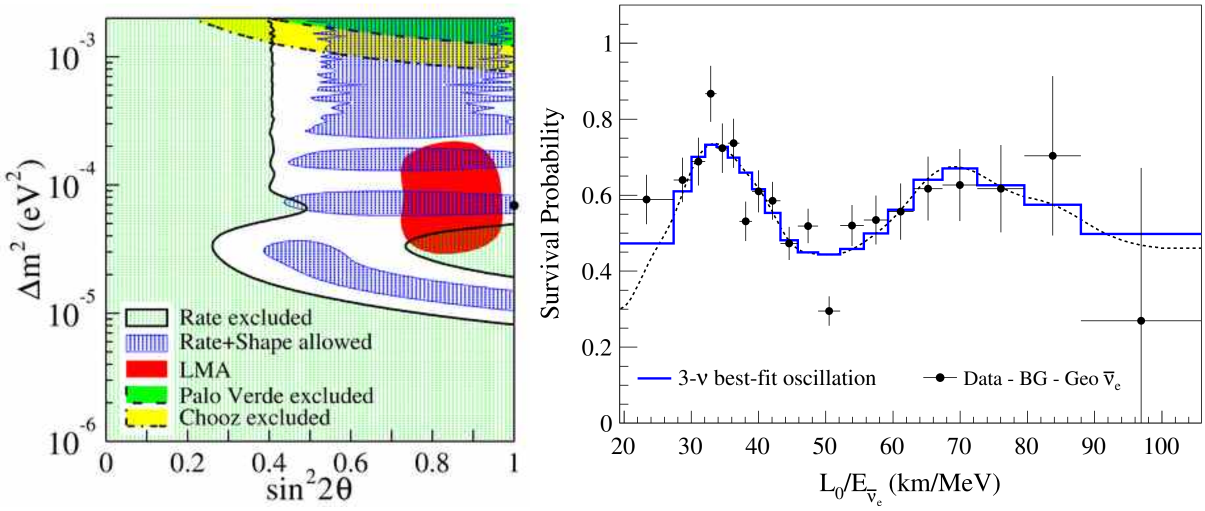

Figure 2.7: KamLAND confirms the large-angle MSW solution in 2003 [166] with KamLAND allowed regions in blue and solar data in red (left); and latest 2013 data from KamLAND showing neutrino oscillations [167] (right). Note that KamLAND was the first experiment to measure geoneutrinos, which are emitted from naturally occurring ^{238}U and ^{232}Th [168].

will be distributed as the chi-squared distribution with two degrees of freedom (known as Wilks' theorem [163]), although a more detailed discussion of the nuances of statistics is dealt in chapter 4. In 1994, for a mass-squared splitting $\Delta m^2_{\text{sol}} \sim 10^{-5}\,\text{eV}^2$, both small- and large-angle solutions could explain the data [164]; furthermore, if the mass splitting were to be extremely small, the MSW resonance would cease to operate, and one could obtain the vacuum-oscillation solution for $\Delta m^2_{\text{sol}} \sim 10^{-10}\,\text{eV}^2$ and $\sin^2 2\theta \sim 1$ [165].

Due to the large propagation distance, it is not possible to observe actual oscillations in energy of the solar neutrino spectrum, which is why the solar data was so ambiguous. To observe spectral oscillations, the Kamioka Liquid scintillator Anti-Neutrino Detector (KamLAND) was proposed. At the site of the Kamioka observatory it observed neutrinos from 53 nuclear power plants in Japan (as well as a few outside Japan) at distances from 80–800 km, and an average distance of $\sim$ 180 km. By 2003, KamLAND confirmed the large-angle MSW solution [166], and since then has seen oscillations in L/E_ν fig. 2.7 (right).

Due to the wide energy range and propagation lengths of atmospheric neutrinos, the Super Kamiokande data was much richer and could determine the oscillation parameters roughly, with a best fit (χ^2 minimum) at $\Delta m^2_{\text{atm}} = 2.2 \cdot 10^{-3}\,\text{eV}^2$, $\sin^2 2\theta = 1$, in the two-neutrino $\nu_\mu \leftrightarrow \nu_\tau$ oscillation framework. The long-baseline accelerator experiment K2K (KEK to Kamiokande) [169] was designed to confirm these oscillations, using neutrinos generated from the KEK laboratory. At KEK, a 12 GeV proton beam is focused onto an aluminium target. The resulting mesons are allowed to decay until a beam dump of iron and concrete, which stops all charged particles except muons with $E > 5.5\,\text{GeV}$. The resulting muon beam is monitored to check its direction, which is important because the far detector (Super Kamiokande) is located 250 km away; a precision of 0.01 mrad is required for the beamline, which was achieved using GPS, and the muon beam itself must have milliradian stability. A near detector is located 300 m away, shielded from non-neutrino beam products by 70 m of dirt. The near detector is a smaller one-kiloton version of the SuperK water Cerenkov detector, equipped with 680 photomultiplier tubes. The neutrino beam resulting from muon decay has an average energy of 1.3 GeV. Since neutrino interactions at GeV energies depend on the complex nuclear structure (due to the larger four-momentum transfer), the near detector must be used to calibrate the Monte Carlo prediction for the far detector. Analysis of the data during the first phase of SuperK was reported in 2003 [170], which was consistent with atmospheric oscillations. During the upgrade of SuperK, an implosion destroyed a majority of photomultiplier tubes, which resulted in reduced coverage for SuperK II [171]. The analysis of the final data was published in 2005, which confirmed atmospheric oscillations at the 4σ level, with a best-fit at $\Delta m^2_{\text{atm}} = 2.2 \cdot 10^{-3}\,\text{eV}^2$, $\sin^2 2\theta = 1$ [172].

MINOS was a follow-up experiment, which used higher-energy protons of 120 GeV on graphite at the NuMI beam at Fermilab to produce a 1–3 GeV muon-neutrino beam. It had a near detector 1 km away, as well as a 5.4 kton far detector 735 km away, located in the Soudan mine, where the original atmospheric-neutrino experiment was hosted. MINOS first reported results in 2007 [173] and operated until 2013 [174], providing very precise measurements of the atmospheric oscillation parameters.

Due to the lower energies, MINOS and K2K were only able to observe a deficit of muon-neutrino events at their far detectors, as the tau neutrinos can only be observed with the production of a heavy tau. The OPERA experiment, which first started operation in 2006 [175], aimed to do this, using 400 GeV protons from the CERN SPS beam on a graphite target to produce a ν_μ beam of average energy 17 GeV. The detector, located 730 km away at the Gran Sasso Laboratory, comprised of two 900 ton super modules, made of alternating layers of lead and emulsion film, called an emulsion cloud chamber. OPERA reported its first candidate event in 2010 [177], and published its final analysis of the 2008 – 2012 data in 2015 [178], reporting five candidate events, corresponding to a $5\,\sigma$ discovery of tau neutrinos in a muon-neutrino beam due to oscillations.

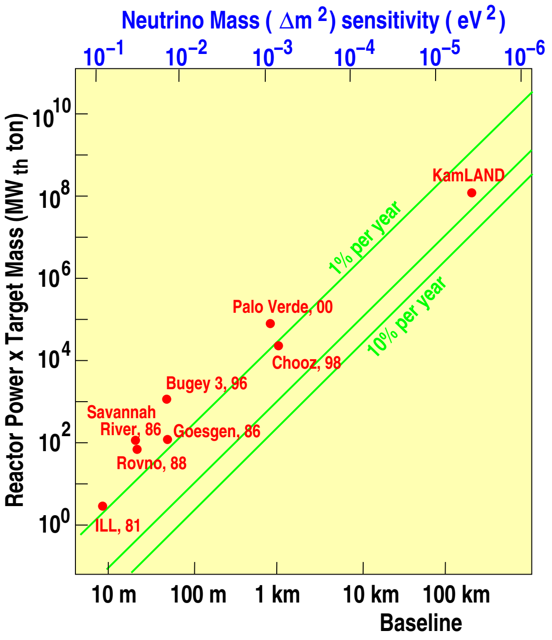

Figure 2.8: Reactor experiments plotted against their exposure and baseline — note how the short-baseline experiments have a reduced exposure, as it is difficult to build large detectors very close to the reactor; courtesy of [176].

The CHOOZ and Palo Verde experiments were reactor experiments proposed to test $\nu_\mu \leftrightarrow \nu_e$ oscillations at $\Delta m^2_{\text{atm}} \sim 10^{-3}\text{eV}^2$ with a baseline of $L \sim 1\,\text{km}$, which translates to a bound on θ_{13} in the three-flavour framework. CHOOZ operated in France near its border with Belgium, and reported its first bound in 1998 [179], whilst Palo Verde operated in Arizona of the United States and reported its first bound in 2000 [180]. Many other short-baseline experiments operated during this time, probing smaller baselines

Figure 2.9: Visual representations of the two mass hierarchies.

and Δm^2, which are shown in fig. 2.8. See [10, §12.2] and the references therein for an overview of these reactor experiments. The efforts to pin down θ_{13} would be carried on by the reactor experiments Daya Bay (China) [181], Double Chooz (France) [182] and RENO (Korea) [183], which all announced in 2012 observations of non-zero θ_{13}. I shall cover the current status of the global fit of three-neutrino oscillations in chapter 3.

The history I have just outlined focused exclusively on the two-flavour framework, which is adequate for analysing the results of a single experiment. However, in order to combine results to obtain a consistent global fit of all parameters, one needs the full three-flavour framework. Because of the hierarchy $\Delta m^2_{\text{sol}} \ll \Delta m^2_{\text{atm}}$, the mass states mainly involved solar oscillations have much more similar masses than the third mass state: fig. 2.9. One typically makes the identifications $\Delta m^2_{\text{sol}} = \Delta m^2_{21}$, $\Delta m^2_{\text{atm}} = |\Delta m^2_{32}| \approx |\Delta m^2_{31}|$, where the sign of Δm^2_{31} depends on the mass ordering. It is possible to understand analytically how the different mixings probed by experiments in the two-flavour scheme relate to one another, by exploiting the hierarchy of mass-squared splittings. These details are examined in chapter 3, which details my contribution to the NuFit project of global fits to neutrino-oscillation parameters.

Direct mass measurements Oscillation experiments are not sensitive to the absolute neutrino mass, and in particular, there is no lower bound for the lightest state: it could be massless. Two types of experiments are being performed to probe the absolute neutrino mass: precise measurements of the end-point of the beta-decay spectrum; and attempts to observe neutrinoless double beta decay. The distortion of the end-point spectrum of beta decay due to the neutrino mass, and the possibility of measuring the neutrino mass with it, was discussed in Fermi's seminal 1934 paper,

“Wir wollen zuerst diskutieren, wie diese Form [des kontinuierlichen β-Spektrums] von der Ruhemasse μ des Neutrinos abhängt, um von einem Vergleich mit den empirisichen Kurven diese Konstante zu bestimmen.” [15]

The principle is quite simple: the maximum kinetic energy of the electron if the neutrino is massless is the Q-value for the decay, *i.e.* the mass difference of the initial and final nuclear state and electron mass, $T_{\text{max}} = Q_\beta \equiv M_i - M_f - m_e$. If the neutrino is massive, it will shift to $T_{\text{max}} = Q_\beta - m_\nu$. For the case of multiple mass eigenstates, the differential decay spectrum is

$$\frac{\mathrm{d}\Gamma}{\mathrm{d}T} \propto \sum_i |U_{ei}|^2 E_\nu \sqrt{E_\nu^2 - m_i^2} \approx E_\nu \sqrt{E_\nu - m_\beta^2}, \quad \text{where} \quad m_\beta^2 = \sum_i |U_{ei}|^2 m_i^2 \tag{2.41}$$

and $E_\nu \equiv Q_\beta - T$. (The sum is incoherent over the mixing U_{ei}, as in the diagram for the decay rate, the neutrino is a final-state asymptotic particle.) Working on the foundations of the Troitsk (1982–1998) [184] and Mainz (1991–2001) [185], the KATRIN experiment at Karlsruhe has published world-leading bounds on the absolute neutrino mass scale of $m_\nu < 0.8\,\text{eV}$ (90% CL) by measuring the end-point spectrum of tritium beta-decay [186]. Tritium was chosen for its low Q-value of 18.574 keV. The electron kinetic-energy spectrum is measured with a MAC-E-filter, which uses a strong magnetic field to collimate the emitted electrons, and an electrostatic field to filter out low-energy electrons. This method can also be used to constrain light sterile neutrinos, by scanning the spectrum at energies $Q_\beta - m_4$, which will be discussed in chapter 4.

If neutrinos have Majorana masses, then the lepton-number violating, neutrinoless double-beta decay is allowed (fig. 2.10). A Majorana mass allows one to connect the opposite-helicity neutrinos emitted in a $2\nu2\beta$ decay. Searches are made by choosing radioactive elements, for whom single-beta decay is energetically forbidden. Therefore, the only SM background is $2\nu2\beta$ decay, which can be distinguished from the spectrum of the total kinetic energy of the emitted electrons being continuous, rather than a line. The Majorana phases enter into the relation between the effective decay mass $m_{2\beta} \propto \sum_i U_{ei}^2 m_i$. For more details, see [10, §14.3]. Due to the process being second-order in G_F, lifetimes are very long $\sim 10^{19}$ years.

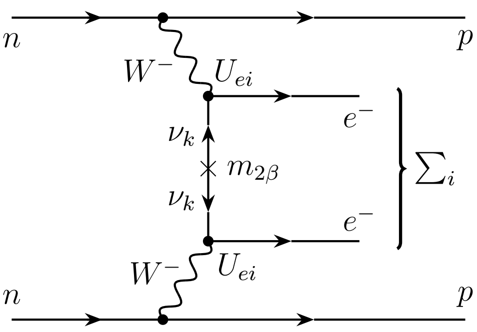

Figure 2.10: A Feynman diagram for neutrinoless double-beta ($0\nu2\beta$) decay. Without the Majorana-mass insertion, two neutrinos would be emitted.

2.7 Light Sterile Neutrino

The early studies of both solar and atmospheric oscillations considered the possibility that oscillations could occur between SM neutrinos and a light sterile neutrino (a SM singlet, so as to not disturb the measurement of the invisible Z width). A host of short-baseline accelerator experiments were undertaken starting from the 1980s (see the references in [10, Table 12.1]), which were sensitive to larger Δm^2 oscillations, which must come from a light sterile neutrino. In the LSND experiment (1993–1998), an excess of electron-like events was detected in a muon-neutrino beam, generated by a 0.8 GeV proton beam on varying targets; the excess, interpreted as $\bar{\nu}_\mu \to \bar{\nu}_e$ oscillations, was marginally compatible with other experiments [188]. A subsequent experiment, MiniBooNE (2002–2019) was undertaken to verify the anomaly, using 8 GeV protons on a beryllium target to create a muon-neutrino beam; MiniBooNE also saw an excess at high significance, consistent with oscillations for $\Delta m^2 < 1\,\mathrm{eV}^2$ [189]. However, if there were new oscillations for muon neutrinos, one should also see a deficit in data from MINOS and IceCube, which observe the disappearance channel $\nu_\mu \to \nu_\mu$; no such evidence was found, contradicting the neutrino-oscillation interpretation of the LSND+MiniBooNE anomaly (see fig. 2.11) [187].

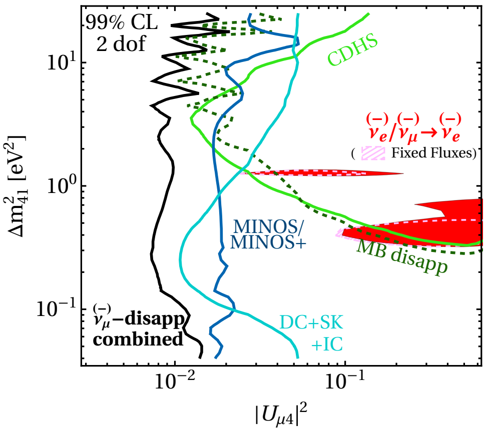

Figure 2.11: Constraint from ν_μ disappearance data (black) and allowed region by LSND (red), courtesy of [187].

Alternative explanations to the MiniBooNE were proposed, such as that by Gninenko in 2009 [190], which exploited the poor particle discrimination of MiniBooNE to explain the excess as single-photon emission from a decaying heavy neutral lepton generated from neutrino upscattering — the so-called neutrino dipole portal. The MicroBooNE experiment was proposed, which uses a liquid-argon time projection chamber, which can reconstruct tracks of neutrino interactions with high resolution, thereby allowing excellent particle discrimination. Whilst MicroBooNE disfavours the electron-like nature of the MiniBooNE excess [191–194], issues regarding background modelling do not yet rule it out [195]. In chapter 5, we examine how the neutrino dipole portal can be tested at DUNE, the upcoming long-baseline accelerator experiment.

In addition to the experimental anomalies in the short-baseline accelerator experiments, there have also been anomalies present in the short-baseline reactor experiments, as well as radiochemical experiments, originating from the gallium solar-neutrino experiments. The *gallium anomaly* originates from the calibration of the solar-neutrino experiments GALLEX (1994–1995) [196] and SAGE (1994–1995) [197], which exposed their gallium detectors to an artificial ^{51}Cr source, whose activity was calibrated via calorimetric measurements. Chromium-51 was chosen for its simple decay scheme, which allows a simple conversion from calorimetric to neutrino activity. Chromium-51 decays to the ground or excited state of vanadium-50; the excited state decays into the ground state via the emission of a 320 keV gamma ray, which is the main source of heat. These decays are associated with Auger electrons and X-rays due to the alteration of the electronic energy levels as the nuclear charge changes. These measurements (in addition to a later measurement using ^{37}Ar by SAGE in 2004 [198]) yielded a deficit compared to the expected number from the capture cross section of gallium, which could be interpreted as evidence for a sterile neutrino [199, 200]. Most recently, the Baksan Experiment on Sterile Transitions (BEST) has confirmed the gallium anomaly with very high significance [201], and will be addressed in chapter 4.

The efforts to measure θ_{13} at short-baseline reactor experiments led to major theoretical efforts to calculate the reactor antineutrino spectrum. Two approaches were published in 2011 by Mueller *et al.* [202] and Huber [203]. Nuclear fuel contains four main isotopes involved in the burning process: ^{235}U, ^{238}U, ^{239}Pu and ^{241}Pu, whose abundances vary over time. Each isotope has thousands of decay branches, into hundreds of possible final states. Whilst Mueller *et al.* use all branches directly to get a prediction, Huber phenomenologically parameterises the decay spectrum of each isotope with 30 virtual branches. Both methods yield similar results, and crucially resulted in a 6% deficit compared to the measured reactor flux (fig. 2.12), which was dubbed the *reactor antineutrino anomaly* [204], and could be interpreted as evidence for a sterile neutrino. The Huber-Mueller predictions used data from various measurements at the Institute Laue-Langevin during the 1980s, which also determined the relative normalisation of the flux from the different isotopes. Since then, efforts have been made to determine whether the origin of the anomaly comes from some mismodelling of the isotopic neutrino flux, including a remeasurement of the ratio between the ^{235}U and ^{239}Pu flux [205] and improved flux models (see [206] for a recent analysis). For a more in-depth overview, with relevant references of important developments, see the reviews [207, 208].

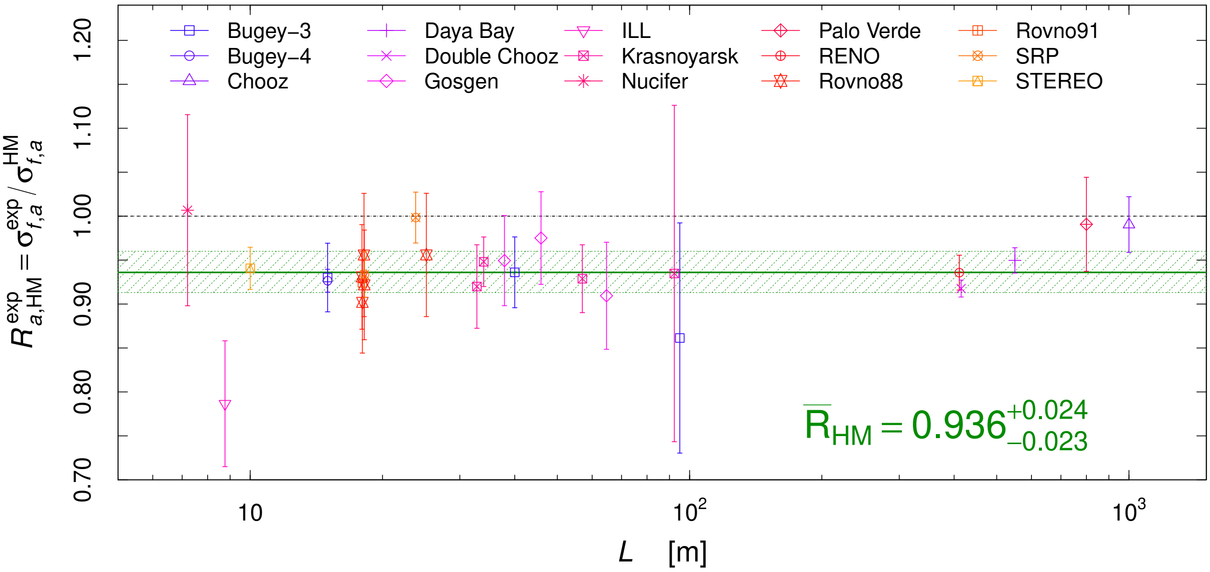

Figure 2.12: The reactor antineutrino anomaly from the Huber-Mueller flux, from [206].

2.8 Neutrinos in Cosmology and Astrophysics

Neutrinos play an important role in the cosmology of the early universe, as they formed a large portion of the relativistic (and total) energy density in the early universe. For temperatures $T_\nu \gtrsim 1.5\,\mathrm{MeV}$, neutrinos are in thermal equilibrium with the primordial plasma via weak interactions (muon and tau neutrinos decouple earlier), after which they decouple, free streaming and cooling; for an overview of cosmology see [209, 210]. The first discussions of cosmic relic neutrinos dates back to Marx and Menyhárd in 1960 [211], who discussed their detection in the context of the steady-state universe, and Pontecorvo, Smorodinskii and Zel'dovich in 1962 [212, 213], who discussed them in the context of an expanding universe. With the discovery of the *cosmic microwave background* (CMB), with a temperature $\sim 3\,\mathrm{K}$, by Penzias & Wilson in 1965 [214, 215], Gamow's 1946 suggestion that the early universe was hot and facilitated *big-bang nucleosynthesis* (BBN) — the creation of light nuclei in the early universe — was vindicated [216]. Based on these developments, Gershtein and Zel'dovich in 1966 calculated the relic number density of cosmic neutrinos, and using upper limits on the cosmic energy density derived an upper bound for a neutrino mass state of 400 eV [217]. (Their bound was weak partly because their age of the universe was estimated lower than today's value [218].) BBN is also sensitive to the number of light neutrinos, first observed by Hoyle and Tayler in 1964 [219], although serious bounds would have to wait till the modern era. For an historical and thorough review of neutrino cosmology, see Dolgov's 2002 report [218].

The second source of extraterrestrial neutrinos to be detected was SN1987A, a supernova burst in the Large Magellanic Cloud that was first detected optically on 24 February 1987. Kamiokande had only recently been upgraded, so it was very fortunate to find neutrino events, whose directions and timing were consistent with the SN1987A source [133]. The length of the neutrino burst can be used to determine the energy released, which can in turn be used to constrain weakly interacting particles, which can be emitted during the burst and increase energy loss if they do not scatter with the imploding matter [220, 221].

IceCube is a dedicated ice Cerenkov neutrino observatory, built in the Antarctic by drilling into the ice and installing strings of photomultiplier tubes. The distance between strings was chosen to optimise the volume of $1\,\mathrm{km}^3$ and sensitivity to high-energy neutrinos, with energies $>$ TeV. IceCube began operating in 2007, and in 2013 they published their first $E_\nu \sim 1\,\mathrm{PeV}$ events, which were highly likely to be of astrophysical origin [222]. By today, IceCube has definitively established the existence of an all-sky high-energy neutrino flux of unknown extraterrestrial origin and has measured parts of its spectrum [223]. Furthermore, in 2021 IceCube published the observation of a 6 PeV event, consistent with the Glashow resonance, where a neutrino creates an on-shell W boson via electron scattering, which then decays hadronically [224].

Two other sources of neutrinos that have not been measured are the diffuse neutrino supernova background, which is the weak MeV glow of the accumulation of neutrinos from all supernovae in our past light cone [225], which could be detected at the next-generation experiments: DUNE (United States), Hyper-Kamiokande (Japan) and JUNO (China) [226]; and thermally emitted keV solar neutrinos (like Bremsstrahlung for neutrinos) [227]. The entire spectrum of neutrinos from meV to EeV is sometimes called the *grand unified neutrino spectrum* [228].

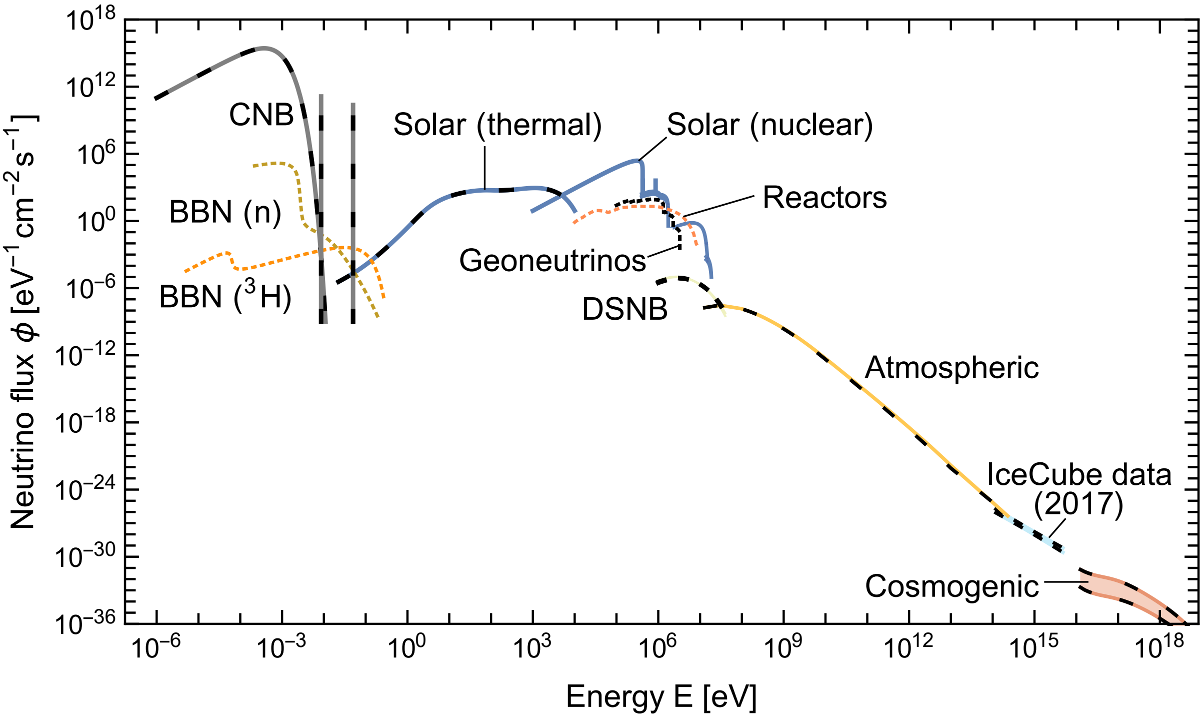

Figure 2.13: Grand unified neutrino spectrum at Earth, courtesy of [228].

Chapter 3

Status of Global Three-Neutrino Fit

In the previous chapter 2, I presented a cursory overview of the Standard Model and neutrino oscillations, presenting historical developments of both electroweak theory and neutrino oscillations as well as mass models, and the gradual build-up of evidence for solar and atmospheric oscillations in the two-flavour framework.

In this chapter, I will present the current status of the Standard Model neutrino-oscillation parameters in the three-flavour framework, based on the global analysis presented in [229]. This work was done as a part of the NuFit collaboration[1], as such a venture is most efficiently pursued via teamwork. My contribution to the global fit focused on updating the reactor analysis, building on the code base by the previous PhD candidate Álvaro Hernández-Cabezudo [230].

3.1 Three-Neutrino Oscillation Phenomenology

From eq. (2.19), by noting that swapping i and j is equivalent to taking the complex conjugate of the summand, and adding and subtracting $\sum_{i,j} U^*_{\alpha i} U_{\alpha j} U_{\beta i} U^*_{\beta j}$, one can deduce the expression for flavour transitions $\nu_\alpha \to \nu_\beta$

$$\begin{aligned} P_{\alpha\beta}(L,E) = \delta_{\alpha\beta} &- 4 \sum_{i>j} \Re\left[U^*_{\alpha i} U_{\alpha j} U_{\beta i} U^*_{\beta j}\right] \sin^2\left(\frac{\Delta m^2_{ij} L}{4E}\right) \\ &+ 2 \sum_{i>j} \Im\left[U^*_{\alpha i} U_{\alpha j} U_{\beta i} U^*_{\beta j}\right] \sin\left(\frac{\Delta m^2_{ij} L}{2E}\right), \end{aligned} \tag{3.1}$$

and the expression for $\bar{\nu}_\alpha \to \bar{\nu}_\beta$ can be obtained by making the transformation $E \mapsto -E$. The second term describes CP violation, as it is the only term that flips sign under the $\nu \mapsto \bar{\nu}$ transformation; this term is determined up to sign by the Jarlskog invariant, which under the parameterisation eq. (2.17) is,

$$J \equiv \left|\Im\left(U^*_{\alpha i} U_{\alpha j} U_{\beta i} U^*_{\beta j}\right)\right| = s_{12} c_{12} s_{13} c^2_{13} s_{23} c_{23} \sin\delta_{\text{CP}} \qquad (\alpha \neq \beta). \tag{3.2}$$

The CP-violating phase δ_{CP} is the least determined oscillation parameter, and is being sought after by current experiments. Furthermore notice how the second term is not sensitive to the mass ordering, as it is invariant under the transformation $\Delta m^2_{3j} \mapsto -\Delta m^2_{3j}$.

---

[1] `http://www.nu-fit.org/`

For this reason, the mass ordering is still undetermined, like δ_{CP} — particularly because a background of matter (which contains no antimatter) can mimic CP violation.

Solar oscillations The (vacuum) survival probability in the three-flavour framework for electron neutrinos and antineutrinos is

$$P_{ee} = 1 - c_{13}^4 \sin^2 2\theta_{12} \sin^2 \Delta_{21} - \sin^2 2\theta_{13} \left[c_{12}^2 \sin^2 \Delta_{31} + s_{12}^2 \sin^2 \Delta_{32}^2 \right], \tag{3.3}$$

where, $\Delta_{ij} \equiv \frac{\Delta m_{ij}^2 L}{4E}$. For terrestial experiments sensitive to Δ_{21} oscillations, the oscillations in Δ_{3j} will be smeared out by the finite energy resolution (see section 3.2 for a discussion), and so $\sin^2 \Delta_{3j} \mapsto \frac{1}{2}$. By using the relation $1 = (s_{13}^2 + c_{13}^2)^2$, we can write

$$P_{ee}^{12} = c_{13}^4 P_{12} + s_{13}^4, \qquad \text{where} \qquad P_{12} \equiv 1 - \sin^2 2\theta_{12} \sin^2 \Delta_{21} \tag{3.4}$$

is the effective two-flavour probability. Thus, we see the three-flavour framework vertically shifts and scales the two-flavour probability with θ_{13}, which is known to be small. This can be used to constrain θ_{13} with experiments sensitive to Δ_{21} oscillations, like KamLAND [231]. Since effects due to θ_{13} are small, one should also take into account matter effects; for a reactor experiment like KamLAND, one can expand to leading order, ignoring effects due to both matter and θ_{13}, in that one only considers matter effects on θ_{12} by using the two-flavour framework with constant density for P_{12}, however replacing the electron density with $N_e \cos^2 \theta_{13}$ (see [232, eq. 22]).

For oscillations of solar neutrinos, matter effects are significant due to the MSW resonance. The survival probability must be modified to include the mixing parameters in matter, discussed briefly in the two-flavour framework at the end of section 2.1. With the assumption of adiabaticity (that the solar density varies slowly), the survivial probability of solar neutrinos is [242]

$$\begin{gathered} P_{ee}^{\mathrm{sol}} = \sum_j \left| U_{ej}^m(n_0) \right|^2 \left| U_{ej} \right|^2 = c_{13}^2 \left(c_{13}^m \right)^2 P_2^{\mathrm{ad}} + s_{13}^2 \left(s_{13}^m \right)^2, \\ \text{where} \quad P_2^{\mathrm{ad}} = s_{12}^2 + \cos 2\theta_{12} \left(c_{12}^m \right)^2, \end{gathered} \tag{3.5}$$

where we have ignored the neutrino phases, due to loss of coherence; $U_{ej}^m(n_0)$ is the mixing angle at the production point, with electron density n_0; and s_{13}^m, c_{13}^m, c_{12}^m are the sine and cosine of the mixing angles in matter with electron density n_0. The explicit expressions for the matter mixings can be found in [242, eqs. 16 − 19]. Thus, similar bounds on θ_{13} can also be made using solar neutrinos, taking into account the matter mixings [231,232].

Atmospheric oscillations Because there is a degeneracy of the two other splittings $\Delta m_{31}^2 \approx \Delta m_{32}^2 \approx \Delta m_{\mathrm{atm}}^2$, the relation between the two- and three-flavour framework is more complicated for atmospheric oscillations than solar oscillations. Following [233], define the effective mass-squared splitting as a weighted average between Δm_{31}^2 and Δm_{32}^2: $\Delta m_{\alpha\alpha}^2 = (1-x)\Delta m_{31}^2 + x\Delta m_{32}^2 = \Delta m_{31}^2 - x\Delta m_{21}^2$. The survival probability in the three-neutrino framework takes the form

$$P_{\alpha\alpha} = 1 - 4 \left| U_{\alpha 3} \right|^2 U_{\alpha 1} \right|^2 \sin^2 \Delta_{31} - 4 \left| U_{\alpha 3} \right|^2 \left| U_{\alpha 2} \right|^2 \sin^2 \Delta_{32} - 4 \left| U_{\alpha 2} \right|^2 \left| U_{\alpha 1} \right|^2 \sin^2 \Delta_{21}. \tag{3.6}$$

Using the relations $\Delta_{31} = \Delta_{\alpha\alpha} + x\Delta_{21}$, $\Delta_{32} = \Delta_{\alpha\alpha} + (x-1)\Delta_{21}$ and $\sin^2(a+b) = \sin^2 a + \cos 2a \cdot \sin^2 b + \sin 2a \cdot \sin 2b/2$, we have the exact relation

$$\begin{aligned} P_{\alpha\alpha} = 1 &- 4\left|U_{\alpha 3}\right|^2\left(1-\left|U_{\alpha 3}\right|^2\right)\sin^2\Delta_{\alpha\alpha} \\ &-4\left|U_{\alpha 3}\right|^2\left[\left\{\left|U_{\alpha 1}\right|^2\sin^2\left(x\Delta_{21}\right)+\left|U_{\alpha 2}\right|^2\sin^2\left((x-1)\Delta_{21}\right)\right\}\cos 2\Delta_{\alpha\alpha}\right. \\ &\qquad\left.+\frac{1}{2}\left\{\left|U_{\alpha 1}\right|^2\sin\left(2x\Delta_{21}\right)+\left|U_{\alpha 2}\right|^2\sin\left(2(x-1)\Delta_{21}\right)\right\}\sin 2\Delta_{\alpha\alpha}\right] \\ &- 4\left|U_{\alpha 2}\right|^2\left|U_{\alpha 1}\right|^2\sin^2\Delta_{21}. \end{aligned} \tag{3.7}$$

By choosing

$$x = \frac{1}{2\Delta_{21}}\arctan\left(\frac{\left|U_{\alpha 2}\right|^2\sin 2\Delta_{21}}{\left|U_{\alpha 1}\right|^2+\left|U_{\alpha 2}\right|^2\cos 2\Delta_{21}}\right) = \frac{\left|U_{\alpha 2}\right|^2}{1-\left|U_{\alpha 3}\right|^2} + \mathcal{O}\left(\Delta_{21}^2\right), \tag{3.8}$$

the coefficient of $\sin 2\Delta_{\alpha\alpha}$ is zero and the coefficient of $\cos 2\Delta_{\alpha\alpha}$ is minimised. For atmospheric oscillations, we can expand in the small parameter Δ_{21},

$$P_{\alpha\alpha}^{\text{atm}} = 1 - 4\left|U_{\alpha 3}\right|^2\left(1-\left|U_{\alpha 3}\right|^2\right)\sin^2\Delta_{\alpha\alpha} + \mathcal{O}\left(\Delta_{21}^2\right), \tag{3.9}$$

where

$$\Delta m_{\alpha\alpha}^2 = \Delta m_{31}^2 - \frac{\left|U_{\alpha 2}\right|^2}{1-\left|U_{\alpha 3}\right|^2}\Delta m_{21}^2 = m_3^2 - \frac{\left|U_{\alpha 2}\right|^2 m_2^2 + \left|U_{\alpha 1}\right|^2 m_1^2}{\left|U_{\alpha 1}\right|^2+\left|U_{\alpha 2}\right|^2}. \tag{3.10}$$

The second equality above gives us physical insight into the effective splitting: it is the mass-squared difference between m_3 and a flavour-weighted average of the first and second mass eigenstates.

For the atmospheric neutrinos and long-baseline accelerator experiments, oscillations are observed via a deficit of muon neutrinos,

$$P_{\mu\mu}^{\text{atm}} = 1 - c_{13}^2\left(1+s_{13}^2 t_{23}^2\right)\sin^2 2\theta_{23}\cdot\sin^2\Delta_{\mu\mu}, \tag{3.11}$$

where $t_{ij} \equiv \tan\theta_{ij}$ and

$$\Delta m_{\mu\mu}^2 = \Delta m_{31}^2 + \left(\cos\delta_{\text{CP}} s_{13} t_{23}\sin 2\theta_{12} - c_{12}^2\right)\Delta m_{21}^2. \tag{3.12}$$

For a realistic analysis, matter effects should also be taken into account, whose effects are larger than effects from Δm_{21}^2: see [234] for an early example of a three-neutrino analysis of atmospheric neutrino data from SuperK.

Reactor experiments, which are sensitive to electron-neutrino disappearance due to oscillations from Δm_{3j}^2, can also provide another measurement of Δm_{atm}^2 (in addition to a precise measurement of θ_{13}). The vacuum survival probability in the atmospheric regime is

$$P_{ee}^{\text{atm}} = 1 - \sin^2 2\theta_{13}\sin^2\Delta_{ee}, \qquad \text{where} \qquad \Delta m_{ee}^2 = \Delta m_{31}^2 - s_{12}^2\Delta m_{21}^2. \tag{3.13}$$

The two different measurements of Δm_{atm}^2 (from reactors via $\bar{\nu}_e$ disappearance, and via accelerators or atmospheric neutrinos from $\bar{\nu}_\mu$ disappearance) is actually sensitive to the mass ordering, as first recognised by [233]. Since the magnitude of Δm_{31}^2 dominates Δm_{21}^2, the sign of Δm_{31}^2 will determine the sign of Δm_{ee}^2 and $\Delta m_{\mu\mu}^2$. So,

$$|\Delta m_{\mu\mu,\,ee}^2| = +\Delta m_{\mu\mu,\,ee}^2 \quad (\text{NO}), \qquad |\Delta m_{\mu\mu,\,ee}^2| = -\Delta m_{\mu\mu,\,ee}^2 \quad (\text{IO}), \tag{3.14}$$

whence,

$$|\Delta m_{ee}^2| - |\Delta m_{\mu\mu}^2| = \pm\Delta m_{21}^2\left(\cos 2\theta_{12} - \cos\delta_{\text{CP}} s_{13} t_{23}\sin 2\theta_{12}\right), \tag{3.15}$$

where the positive sign is for the normal ordering (NO) case, and the negative sign for the inverted ordering (IO) case. This synergy between reactor and accelerator experiments is important for the global three-neutrino fit, as it provides an independent method (in addition to the appearance channel of the long-baseline accelerator experiments, covered below) to determine the mass ordering. (On a technical note, other effective mass-squared splittings were suggested, which have L/E dependence, which is compared in [235]; they are all equivalent in the regime when atmospheric oscillations dominate.)

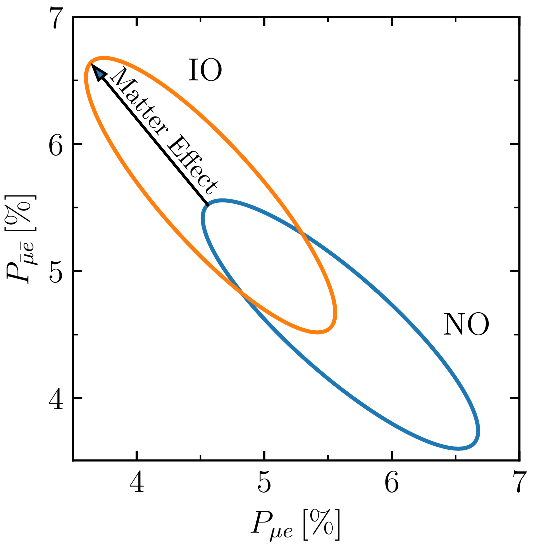

Figure 3.1: A schematic example of the so-called *bievent plot*. Each point on an oval of a mass ordering represents predictions for a specific δ_{CP} value.

CP violation and matter effects The previous discussion focused on vacuum oscillation, which is adequate for short-baseline experiments like reactor neutrinos. However the long-baseline accelerator experiments (particularly NOνA), which are the leading experiments to determine the CP-violating phase, are sensitive to matter effects. The long-baseline accelerator experiments T2K and NOνA measure electron-neutrino appearance in a muon-neutrino beam. To understand how this oscillation channel affects the three-neutrino parameters, we use the analytic approximations developed in the past [236–238], expanding the probability of $\nu_\mu \to \nu_e$ oscillations to second order in s_{13} and $\alpha \equiv \Delta m^2_{21}/\Delta m^2_{31}$ assuming constant electron density,

$$\begin{aligned} P_{\mu e} &= \alpha^2 \sin^2 2\theta_{12}\, c_{23}^2\, \frac{\sin^2(\Delta A)}{A^2} + 4 s_{13}^2 s_{23}^2\, \frac{\sin^2[\Delta(A-1)]}{(A-1)^2} \\ &+2\alpha\, s_{13}\, \sin 2\theta_{12}\, \sin 2\theta_{23}\, \cos\left(\Delta + \delta_{\text{CP}}\right)\, \frac{\sin(\Delta A)}{A}\, \frac{\sin[\Delta(A-1)]}{A-1}, \end{aligned} \tag{3.16}$$

where $A \equiv 2E_\nu \left(\sqrt{2} G_F N_e\right)/\Delta m^2_{31}$ and $\Delta \equiv \Delta_{31}$. To obtain the probability for the antineutrino channel, one makes the transformation $A \mapsto -A$ and $\Delta \mapsto -\Delta$. Following [239], let us make the approximation, appropriate for the long-baseline experiments T2K and NOνA, that we are near the oscillation maximum, $\Delta = \pi/2 + \delta\Delta$ and expand to first order in A, ignoring solar oscillations $\alpha^2\Delta^2 = \Delta^2_{21}$ (noting that $\alpha^2 < s_{13}\alpha$),

$$\begin{aligned} P_{\mu e} &\approx 4 s_{13}^2 s_{23}^2 (1+2A) - C(1+A)\sin\left(\delta_{\text{CP}} + \delta\Delta\right), \\ P_{\bar{\mu}\bar{e}} &\approx 4 s_{13}^2 s_{23}^2 (1-2A) + C(1-A)\sin\left(\delta_{\text{CP}} - \delta\Delta\right), \end{aligned} \tag{3.17}$$

where $C \equiv \Delta_{21} \sin 2\theta_{12} \sin 2\theta_{13} \sin 2\theta_{23}$, and where I have used $2s_{13} \approx \sin 2\theta_{13}$ to first order to be consistent with our publication [229]. In the plane $(P_{\mu e}, P_{\bar{\mu}\bar{e}})$, for each mass ordering, an oval is drawn as δ_{CP} is varied; the sign of A determines the mass hierarchy, and shifts the centre of the oval; an example is shown in fig. 3.1.

Due to the large amount of data from the new accelerator experiments, the atmospheric data does not have a significant impact on the global fit , however the impact of matter effects on atmospheric neutrinos and the oscillating parameters can be found in [240, 241]. Analytical simplifications are more involved due to the wide range of energies and baselines that atmospheric neutrinos probe (both for the disappearance and appearance channels).

3.2 Overview of Experiments and their Simulation

At the Neutrino 2020 conference, new data for the most relevant neutrino-oscillation experiments were presented, which prompted a major update for the NuFit global analysis. A full list of the data used in the latest NuFit global fit can be found in [229]. Data from solar experiments, reviewed in section 2.4, (Homestake, GALLEX, SAGE, SuperK, SNO) as well as from the most recent running Borexino experiment provide the strongest constraint on θ_{12}, whereas KamLAND provides the best constraint of Δm^2_{21}. The solar sector was handled by Michele Maltoni, and the details of the evolution of the neutrinos through the sun and then the Earth can be found in his 2016 article with Smirnov [242].

The parameters of the atmospheric sector are constrained mainly by two sets of terrestrial experiments: medium-baseline reactor experiments (Daya Bay, Double Chooz and RENO), and long-baseline accelerator experiments (MINOS, NOνA and T2K). The principles underlying reactor experiments are the same as reviewed in section 2.2. The current accelerator experiments use an off-axis beam, where the far detector is displaced from the beam axis, which yields a neutrino beam sharply peaked around a specific energy (see fig. 3.2). (For an explanation see [10, §12.3.3].) Due to the difficulty describing meson-production cross sections from proton scattering on a nucleus, a near detector is used to measure the neutrino flux [243, 244].

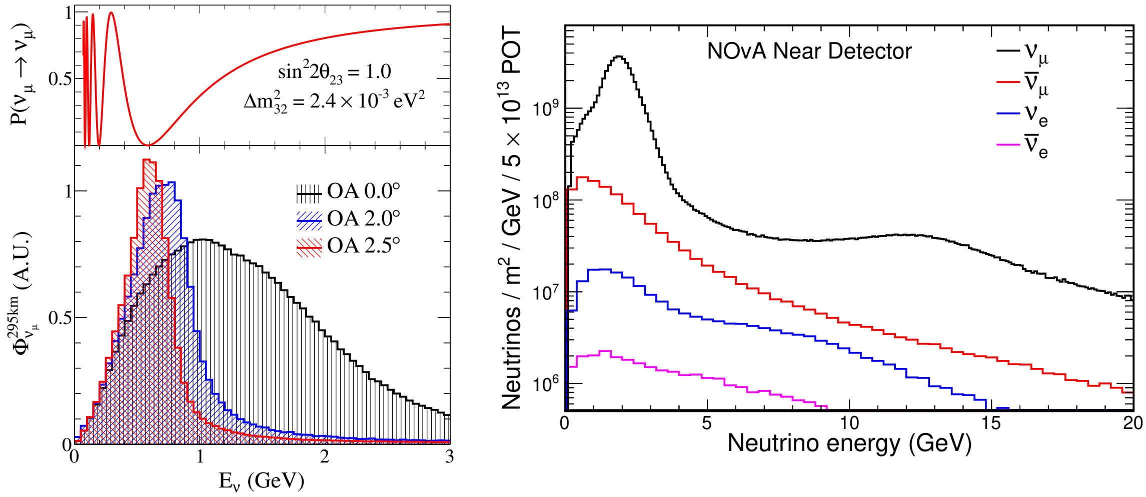

Figure 3.2: Left: demonstration of the off-axis effect, tuning and sharpening the energy spectrum to the oscillation maximum; courtesy of [243]. Right: Neutrino flux at NOνA, including other flavours intrinsic to the beam from rare meson decays; from [245].

At the reactor experiments, a near detector is also used to avoid assuming the absolute flux, which had a long-standing anomaly (see discussion on the reactor anomaly in section 2.7), and unexplained features such as the 5 MeV bump (first reported by RENO [246, 247] and subsequently by the other θ_{13} experiments Daya Bay [248] and Double Chooz [249]). The bump persists till today (see fig. 3.3), although various possible explanations have been proposed, and the origin of the bump, whether it is due to all or a single isotope, is also being investigated (see [250] and the references therein for a non-exhaustive list).

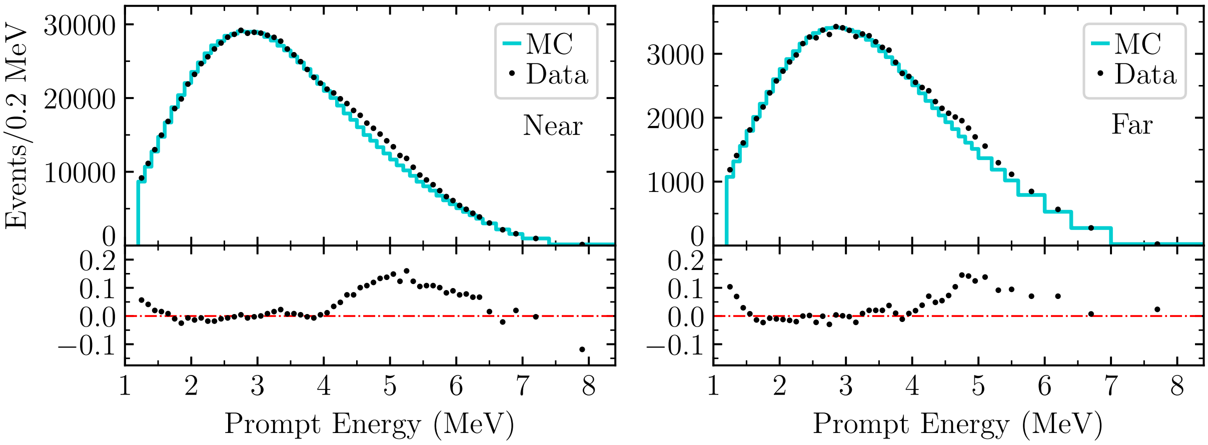

Figure 3.3: Most recent RENO data (2900 days), demonstrating the anomalous 5 MeV bump; data extracted from [251].

The experimental collaborations' analyses of their data is a complicated process. The accelerator experiments require involved Monte Carlo simulations, which are tuned with near-detector data, due to, *e.g.,* the complexity of hadronic physics for neutrino-nucleus scattering at GeV energies. The calibration of the detector, which are complicated devices, is also very involved, and collaborations make various cuts of the data, whereby events that do not satisfy some metric are removed, to reduce background. These complexities, which members outside the collaboration are not privy to, can be simplified into a reconstruction matrix $R\left(E_{\rm rec};E_\nu\right)$, which determines the probability density of reconstructing the energy of a neutrino event to be $E_{\rm rec}$, if the energy of the neutrino is E_ν, which is taken to be a normal distribution,

$$R\left(E_{\rm rec};E_\nu\right)\equiv\frac{1}{\sqrt{2}\sigma_E\left(E_\nu\right)E_\nu}\exp\left[-\frac{1}{2\sigma_E^2\left(E_\nu\right)}\left(\frac{E_\nu-E_{\rm rec}}{E_\nu}\right)^2\right], \tag{3.18}$$

where $\sigma\left(E_\nu\right)$ is the detector energy resolution at energy E_ν, which is normally given by the collaboration. The detector does not usually detect events with different energies with the same efficiency, so the detector efficiency $\varepsilon\left(E_\nu\right)$ is also needed.

Data from the collaboration are usually presented as events binned in energy intervals $[E_{i-1},E_i]$. Our simplified prediction for bin i with flavour type α takes the form

$$N_i^\alpha=N_i^{\rm bkg}+\int_{E_{i-1}}^{E_i}{\rm d}E_{\rm rec}\int_0^\infty{\rm d}E_\nu\;R\left(E_{\rm rec};E_\nu\right)\varepsilon\left(E_\nu\right)\sum_\beta\frac{{\rm d}\Phi^\beta}{{\rm d}E_\nu}P_{\nu_\beta\to\nu_\alpha}\left(E_\nu\right)\sigma_\alpha\left(E_\nu\right), \tag{3.19}$$

where $N_i^{\rm bkg}$ are the predicted background events (as determined by the collaboration), $\sigma_\alpha\left(E_\nu\right)$ is the cross section for neutrino flavour α on the detector, and ${\rm d}\Phi^\beta/{\rm d}E_\nu$ is the flux for neutrino flavour β. The possible flavours for accelerator experiments are $\alpha, \beta \in \{\nu_e, \nu_\mu, \bar{\nu}_e, \bar{\nu}_\mu\}$; the flux and cross sections are supplied by the collaboration, which are based on tuned Monte Carlo models. The oscillation terms in the probability have the form $\sin^2\left(\frac{\Delta m^2 L}{4E_\nu}\right) = \frac{1}{2} - \frac{1}{2}\cos\left(\frac{\Delta m^2 L}{2E_\nu}\right)$. In the event that the phase is very large, the cosine term will average out to zero, in that by making the transformation $\frac{\Delta m^2 L}{2E_\nu} = \omega x - 2n\pi$, where $\omega \equiv 2n\pi \equiv \frac{\Delta m^2 L}{2E_\nu^{(n)}}$, splitting the energy integration into the intervals $\left[E_\nu^{(n)}, E_\nu^{(n+1)}\right]$, the integral takes the form

$$\int_0^{\frac{2\pi}{\omega}} f(\omega x + 2n\pi)\cos(\omega x)\mathrm{d}x = \int_0^{\frac{1}{n}} f(2n\pi)\cos(\omega x)\mathrm{d}x + \mathcal{O}\left(\frac{1}{n}\right) = \mathcal{O}\left(\frac{1}{n}\right). \tag{3.20}$$

Thus we see that the oscillations average out for large $\frac{\Delta m^2 L}{2E_\nu}$.

The analysis of accelerator experiments was handled by the then PhD candidate Iván Esteban [252]. Since this thesis will focus on reactor neutrinos, I will focus on this case, where $\alpha = \beta = \bar{\nu}_e$. For reactor neutrinos, the differential cross section is given by the calculation by Vogel & Beacom [253], which is an expansion in the inverse nucleon mass $1/M$, and includes the zeroth- and first-order terms; integrating the angular distribution given in [253] over $\cos\theta$ yields the total cross section for inverse beta decay as a function of neutrino energy. The flux is given by the Huber-Mueller model [202, 203], which parameterises the flux of each isotopic component of the nuclear fuel as,

$$\frac{\mathrm{d}\Phi}{\mathrm{d}E_\nu} = \sum_{\text{iso}} f^{\text{iso}} \phi^{\text{iso}}(E_\nu), \qquad \text{where} \qquad \phi^{\text{iso}}(E_\nu) \equiv \sum_{k=0}^{5} \alpha_k^{\text{iso}} E_\nu^k \tag{3.21}$$

and iso $\in \{{}^{235}\mathrm{U}, {}^{239}\mathrm{Pu}, {}^{238}\mathrm{U}, {}^{241}\mathrm{Pu}\}$; the time-averaged effective fission fractions f^{iso} are provided by the collaboration: for RENO they can be found in [254]; for Daya Bay and RENO, non-equilibrium corrections are also applied to the Huber-Mueller model, as detailed in [255, §2.6].

The detector for RENO, which is similar to Daya Bay and Double Chooz, is shown in fig. 3.4 (right) and consists of four cylindrical layers. The innermost layer is a vessel made of transparent acrylic plastic, containing gadolinium-doped liquid scintillator; the positron from an inverse-beta-decay event loses energy by emitting scintillation photons until pair annihilation on an electron, whilst the neutron is captured on a Gd nucleus. The next layer is the γ catcher, which is a liquid scintillator contained in another acrylic vessel, which is meant to catch any 511 keV gammas, which escape the inner layer. The buffer layer contains photomultiplier tubes immersed in non-scintillating mineral oil, whilst the veto layer helps reject events due to external radiation (cosmic rays, neutrons from radiative decays in the rock). The whole device is surrounded by 40 cm concrete. For more information, see [256, §3].

The term *prompt energy*, as labelled in fig. 3.3, refers to the total recorded photon energy from pair-annihilation photons, which is (assuming perfect detection of the photons) $E_{\text{pr}} = 2m_e + T_{e^+}$, where T_{e^+} is the kinetic energy of the positron. (Here we assume that the electron, on which the positron decays, is stationary.) If we had a perfect detector, the prompt energy can be easily related to the neutrino energy, as $T_{e^+} = E_{\bar{\nu}_e} + m_p - E_n - m_e$, where m_p is the proton mass, and E_n is the neutron energy. Since the neutron mass $\sim 1\,\text{GeV}$ is orders of magnitude larger than nuclear energies $\mathcal{O}(\text{MeV})$, we can assume the neutron is non-relativistic, and therefore ignore its kinetic energy (typically $\sim 10\,\mathrm{keV}$). However, the energy deposited by the gamma rays has a non-linear relation with its emitted energy [257], due to quenching of the photon energy in the liquid scintillator; we denote this effect by the function $f(\,\cdot\,)$. In practice we use the non-linear detector response provided by the Daya Bay collaboration [258] for both RENO and Daya Bay, as RENO does not provide their absolute energy calibration; this still reproduces adequate results for RENO: see fig. 3.5. Then the relation between the prompt energy and reconstructed neutrino energy is

$$E_{\bar{\nu}_e} = f(E_{\mathrm{pr}}) + m_n - m_p - m_e. \tag{3.22}$$

The energy resolution is taken from [257, fig. 11].

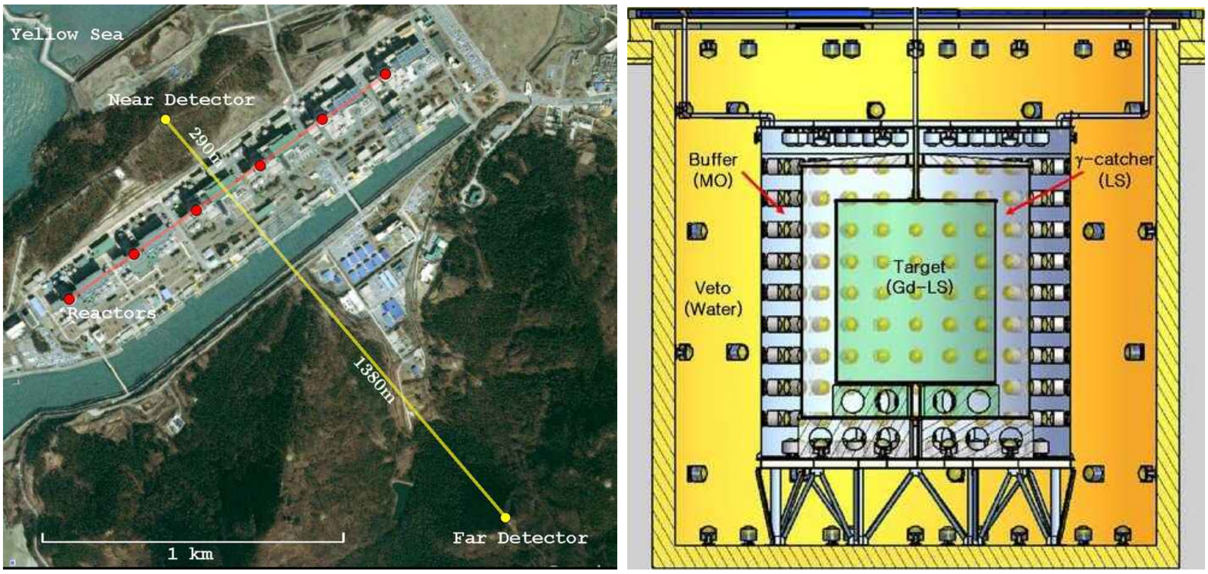

Figure 3.4: Left: layout of RENO reactors and detectors, modified from [256, fig. 1.2]. The six reactors span an array of 1280 m. Right: sketch of the RENO detector, consisting of four cylindrical layers; courtesy of *ibid.* fig. 1.9.

The Daya Bay and RENO experiments use multiple reactors at different distances as neutrino sources; since only the oscillation probability has baseline dependence in the integrand, we need to make the substitution

$$P_{\nu_\beta \to \nu_\alpha}(E_\nu) \mapsto \sum_r \frac{1}{L_r^2} P_{\nu_\beta \to \nu_\alpha}(E_\nu, L_r)\,, \tag{3.23}$$

where r labels the reactor sources. At RENO, six reactors in roughly a line act as neutrino sources, in the geometry shown in fig. 3.4. The baselines for each detector-reactor pair was taken from [256, tab. 1.2]. The integrals are then normalised to reproduce the total number of Monte Carlo events from the collaboration. The integrals are precomputed for each bin, on a discrete grid of the parameter $\Delta m^2 L$, noting that we can decompose the integral into a sum of terms like $\mathrm{const} \times \int \sum_L f(E) \sin^2 \frac{\Delta m^2 L}{4E} \mathrm{d}E$, where we have extracted the mixing angles from the integrals. Noting that only the reconstruction matrix $R(E_{\mathrm{rec}}; E_\nu)$ participates in the integral over E_{rec}, this integral is converted into the error function.

3.3 Construction of the Test Statistic

Due to the aforementioned anomalies in the reactor spectrum, we construct our test statistic as a function of the far-to-near ratio $\mathcal{R}_i \equiv (N_i - N_i^{\text{bkg}})_{\text{far}}/(N_i - N_i^{\text{bkg}})_{\text{near}}$, which is insensitive to the normalisation of the total reactor flux. The ratio also has the advantage of being less sensitive to defects due to detector mismodelling; for example, if an error in the reconstruction matrix caused us to overestimate events in a bin, we would expect this to occur in both near and far detectors (which have identical design), resulting in partial cancellation in the ratio. Specifically, denoting $S_i \equiv N_i - N_i^{\text{bkg}}$ as shorthand for the signal (3.19),

$$\mathcal{R}_i = \frac{(S_i + \epsilon)_{\text{far}}}{(S_i + \epsilon)_{\text{near}}} = \mathcal{R}_i \left[1 + (\epsilon_{\text{far}} - \epsilon_{\text{near}}) + \mathcal{O}\left(\epsilon^2\right)\right], \tag{3.24}$$

whence the first-order corrections cancel (albeit not exactly). If we ignore systematic errors, the test statistic for an experiment is defined

$$\chi^2_{\text{no syst}} = \sum_{i,j} (O_{\mathcal{R}} - \mathcal{R})^i \, V_{ij}^{\text{stat}} \, (O_{\mathcal{R}} - \mathcal{R})^j \,, \tag{3.25}$$

where the sum occurs over the bins, and $O_{\mathcal{R}}$ defines the ratio calculated from the observed data. The covariance matrix of statistical correlations V^{stat}, is defined under the assumption that bin events N_i are distributed normally (which is valid in the limit of large numbers, *c.f.* the central limit theorem), using the Poissonian variance N_i,

$$V_{ij}^{\text{stat}} = \sum_i \sum_{d=\text{near,far}} \frac{\partial \mathcal{R}_i}{\partial N_i^d} \frac{\partial \mathcal{R}_j}{\partial N_i^d} N_i^d. \tag{3.26}$$

The global test statistic without systematics would be the sum of the $\chi^2_{\text{no syst}}$ for each experiment. Each experiment, however, has its own set of systematics that must be implemented individually. In the reactor sector, only the RENO experiment needed updating from new data at NU2020, so I will concentrate on that. Details on Daya Bay and the other experiments can be found in the appendices of [259] and the theses [230,252].

Systematic errors Systematic errors occur due to a lack of knowledge on certain quantities in the experiment. There are three types of systematics for RENO, which were implemented by the previous PhD candidate Álvaro Hernández-Cabezudo: uncertainty on the relative detection efficiency $\varepsilon^{\text{far}}/\varepsilon^{\text{near}}$, uncertainty on the energy scale, and uncertainty on the ^{9}Li-^{8}He background. (Other systematics can be neglected; for a total list, see [260].) The systematic for relative detection efficiency is implemented with the simple substitution $\mathcal{R}_i \mapsto (1+\varepsilon)\mathcal{R}_i$. The energy-scale uncertainty refers to systematic errors related to the reconstructed energy, implemented by rescaling $E_{\text{rec}} \mapsto (1+\eta_d)\, E_{\text{rec}}$, where the near and far detectors have independent rescaling $d \in \{\text{near}, \text{far}\}$. Its effect is to change the integration limits in eq. (3.19), $E_i \mapsto (1+\eta_d)\, E_i$.

Cosmic muons scattering on carbon in dirt can create the radioactive isotopes ^{8}He and ^{9}Li, which decay into an electron and neutron, which results in an irreducible background for reactor detectors [256, §6.6.3]. The production cross section for cosmogenic helium and lithium is not precisely known; this uncertainty modifies the background $N_{d,i}^{\text{bkg}} \mapsto$

$N^{\mathrm{bkg}}_{d,i} + \beta_d N^{\mathrm{LH}}_{d,i}$, where $N^{\mathrm{LH}}_{d,i}$ is the ^{9}Li-^{8}He background component. Note that its effect in the χ^2 expression eq. (3.25) is in changing $O_{\mathcal{R}}$,

$$O^{\mathrm{syst}}_{\mathcal{R}} = \frac{O^{\mathrm{far}}_i - N^{\mathrm{bkg}}_{\mathrm{far},i} - \beta_{\mathrm{far}} N^{\mathrm{LH}}_{\mathrm{far},i}}{O^{\mathrm{near}}_i - N^{\mathrm{bkg}}_{\mathrm{near},i} - \beta_{\mathrm{near}} N^{\mathrm{LH}}_{\mathrm{near},i}}, \tag{3.27}$$

where O^d_i are the observed number events in bin i for detector d. Additional *pull terms* are added to the test statistic, which penalise non-zero systematics (for more information about the pull method see [261]). The test statistic is defined as,

$$\begin{aligned}\chi^2_{\mathrm{syst}} = \min_{\boldsymbol{\beta},\boldsymbol{\eta},\varepsilon} \sum_{i,j} \left[O_{\mathcal{R}}(\boldsymbol{\beta}) - (1+\varepsilon)\mathcal{R}(\boldsymbol{\eta})\right]^i V^{\mathrm{stat}}_{ij} \left[O_{\mathcal{R}}(\boldsymbol{\beta}) - (1+\varepsilon)\mathcal{R}(\boldsymbol{\eta})\right]^j \\ + \left(\frac{\varepsilon}{\sigma_\varepsilon}\right)^2 + \sum_d \left[\left(\frac{\beta^d}{\sigma^d_\beta}\right)^2 + \left(\frac{\eta^d}{\sigma_\eta}\right)^2\right],\end{aligned} \tag{3.28}$$

where $\boldsymbol{\beta} \equiv \begin{pmatrix}\beta_{\mathrm{far}} & \beta_{\mathrm{near}}\end{pmatrix}^{\mathrm{T}}$, $\boldsymbol{\eta} \equiv \begin{pmatrix}\eta_{\mathrm{far}} & \eta_{\mathrm{near}}\end{pmatrix}^{\mathrm{T}}$, and $\sigma_\varepsilon = 0.22\%$, $\sigma^{\mathrm{far,near}}_\beta = 5.61\%, 3.26\%$, $\sigma_\eta = 0.15\%$ are the uncertainties for each systematic, taken from [260]. I tuned some of the central values and uncertainties of the systematics to match the collaboration's χ^2 contours, namely $1+\varepsilon \mapsto 1.001+\varepsilon$, $\sigma_\varepsilon \mapsto 1.6\sigma_\varepsilon$, and $\sigma_\eta \mapsto 0.45\sigma_\eta$. By Wilks' theorem, χ^2_{syst} is distributed as a chi-squared with $n-p$ degrees of freedom, where n is the number of bins, and p is the number of systematics.

Denoting the summand of the first term in eq. (3.28) as $f_{ij}(\varepsilon, \boldsymbol{\beta}, \boldsymbol{\eta})$, the minimisation is done by expanding f_{ij} to first order in all systematics. The first-order partial derivative in ε, $\beta_{\mathrm{far,near}}$ is relatively straightforward; for the energy-scale systematic, we note that

$$\frac{\partial}{\partial\eta} \int_{(1+\eta)E_{i-1}}^{(1+\eta)E_i} \mathrm{d}E_{\mathrm{rec}} R(E_{\mathrm{rec}}, E_\nu) \bigg|_{\eta=0} = R(E_i, E_\nu)E_i - R(E_{i-1}, E_\nu)E_{i-1}, \tag{3.29}$$

using the Leibniz integral rule. A comparison of my $\Delta\chi^2$ contours, compared with the results from RENO as presented at NU2020 [251] is presented in fig. 3.5.

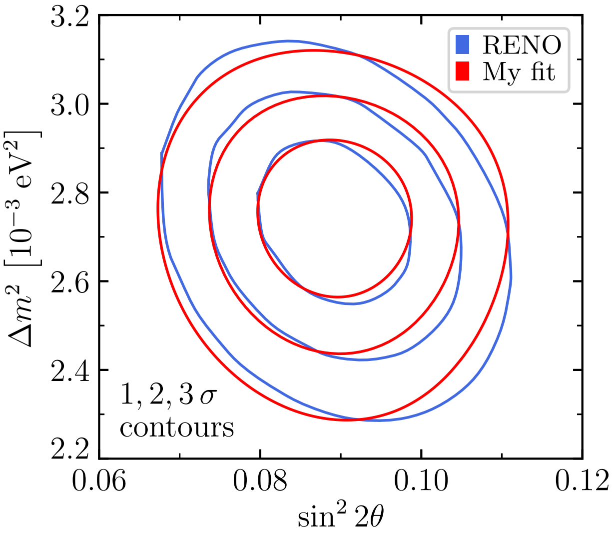

Figure 3.5: A comparison of my contours (red) compared to the collaboration's results (blue), extracted from [251].

3.4 Results

In this section, I present the results of our global analysis. These were obtained, by constructing χ^2 tables for each experiment, and using them as input in a pre-written routine for NuFit, which was done by others. In fig. 3.6, an overview of the 2σ contours of the main experiments are shown in the parameter space they are most sensitive to. In the left panels, the accelerator experiments T2K, NOνA and MINOS, as well as atmospheric neutrino data from IceCube (DeepCore) and SuperK are shown in the space of atmospheric oscillation parameters, $(s_{23}^2, \Delta m_{31}^2)$ for normal ordering, and $(s_{23}^2, \Delta m_{32}^2)$ for inverted ordering. For the normal ordering, Δm_{31}^2 is the mass-squared splitting between the heaviest and lightest neutrino mass state; therefore, in inverted ordering, the corresponding splitting would be Δm_{32}^2, as ν_2 becomes the heaviest mass state (see fig. 2.9). A prior is included on θ_{13} for the non-global analysis, and θ_{13} is marginalised over. In the right panels, the reactor experiments Daya Bay, Double Chooz and RENO are shown in the $(s_{13}^2, \Delta m_{3\ell}^2)$ plane are shown, where $\ell = 1$ for NO and $\ell = 2$ for IO. For all experiments, the contours are defined with respect to the global minimum of both orderings, and solar and KamLAND data is included to constrain Δm_{21}^2 and s_{12}^2.

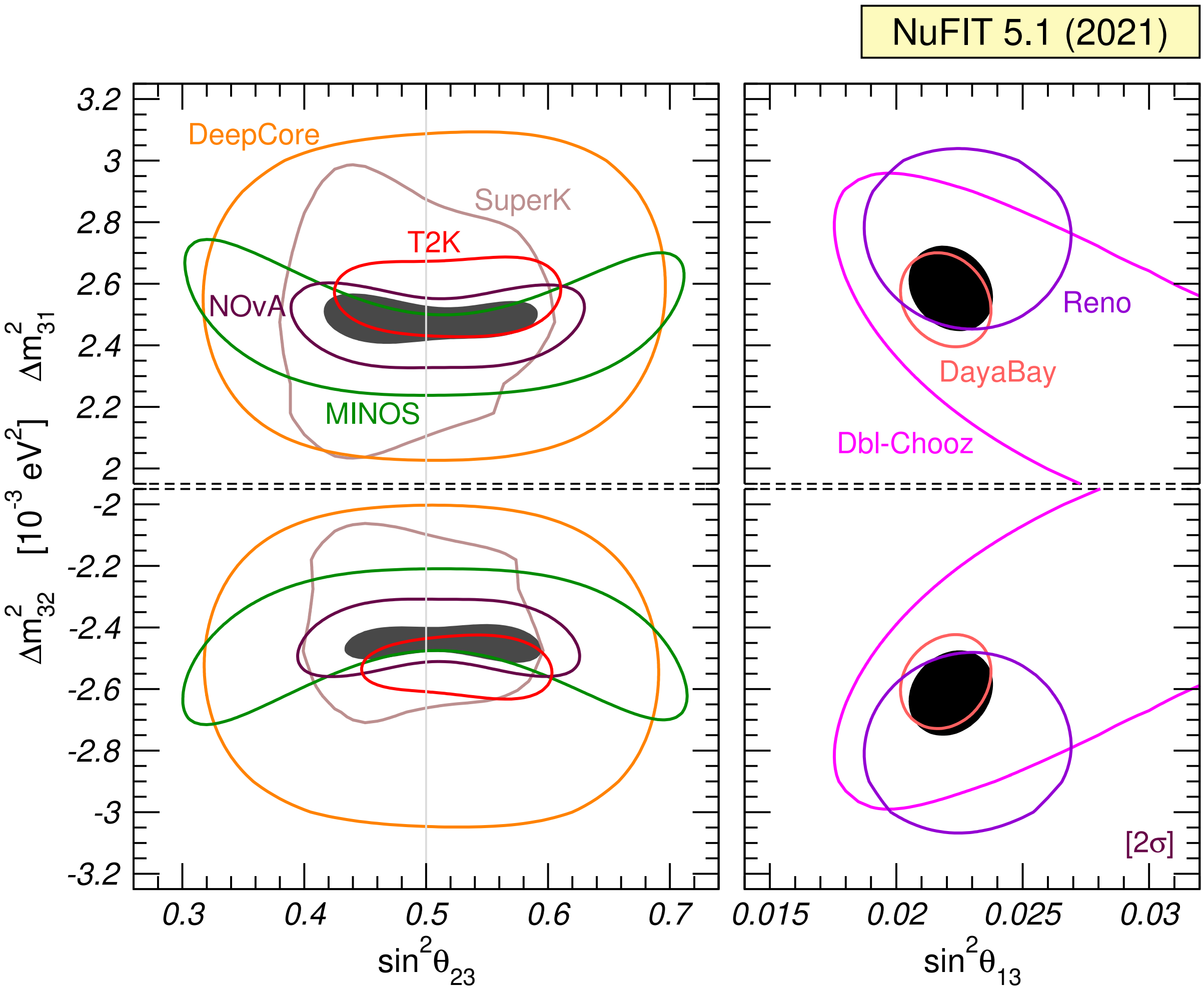

Figure 3.6: Overview of 2σ contours for experiments sensitive to atmospheric oscillations with their combination in dark grey, and reactor experiments sensitive to s_{13} with their combination in black, courtesy of [229]. See text for details.

For the SuperK atmospheric data, a neural network was used for their event reconstruction, which was designed to boost SuperK's sensitivity to the mass ordering and CP violation. Due to the lack of public information, it is not possible to reproduce their analysis (see [262, §3.3] for a discussion). Our analysis uses the χ^2 map provided by the collaboration [263], which emerged after the publication of [229].

CP violation and mass ordering In fig. 3.7, we see the $\Delta\chi^2$ profile as a function of δ_{CP}, where the other oscillation parameters have been left free. As explained in section 3.1, the appearance channel of neutrinos and antineutrinos for atmospheric oscillations can be sensitive to the mass ordering and CP violation. In the top panels, only accelerator data is used, with a prior on θ_{13}. We can see that T2K data (red) has a slight preference for normal ordering, and in both orderings strongly prefers $\delta_{\mathrm{CP}} \sim 3\pi/2$. On the other hand, we can see that NOνA data does not have strong preference for either ordering, but disfavours $\delta_{\mathrm{CP}} \sim 3\pi/2$ in the normal ordering and favours it in the inverted ordering. In dotted and dashed lines we have also plotted the $\Delta\chi^2$ profile using only the NOνA data from neutrinos and antineutrinos, respectively. We can see that the NOνA neutrino appearance data dominates $\Delta\chi^2$ at $\delta_{\mathrm{CP}} \sim 3\pi/2$, and leads to a slight tension with T2K at normal ordering. The combined data (blue) shows that the accelerator data prefers inverted ordering and $\delta_{\mathrm{CP}} \sim 3\pi/2$, due to the tension in δ_{CP} in normal ordering.

As explained in section 3.1, the interplay between the disappearance measurement of the atmospheric mass-squared splitting in the muon flavour $\Delta m^2_{\mu\mu}$, via accelerator data, and in the electron flavour Δm^2_{ee}, via reactor neutrinos, is sensitive to the mass ordering. The lower panels of fig. 3.7 show $\Delta\chi^2(\delta_{\mathrm{CP}})$ when we include reactor data in the fit. The result is that inverted ordering is disfavoured by the inclusion of reactor data, and the global minimum occurs at $\delta_{\mathrm{CP}} \sim \pi$ at NO, avoiding the tension from NOνA data at $\delta_{\mathrm{CP}} \sim 3\pi/2$.

Statistical consistency Given the opposing tendencies of the various data sets in the global fit, an important question becomes whether the data sets are consistent with one another. An internal inconsistency in the global fit would make it invalid, as the best-fit values for the oscillation parameters would merely be a result of the fit attempting to resolve a tension between two sets of data, indicating that something is wrong with the physical model of our data.

The classic goodness-of-fit test is simply χ^2, which is distributed as a chi-squared with $n - p$ degrees of freedom, where n is the number of bins and p are the number of systematics. This is used by experimental collaborations to determine whether their detector models and calibrations correctly describe their data. However, in a global fit we do not wish to determine whether our fit is good at the level of individual bins, but at the level of statistically independent datasets (*i.e.* the different experiments). The *parameter goodness-of-fit* test statistic χ^2_{PG} was first introduced in [264] to do precisely this job. It is defined as the difference between the χ^2 at the global minimum and the sum of the χ^2 minima of the individual datasets,

$$\chi^2_{\mathrm{PG}} = \chi^2_{\text{global min}} - \sum_{\text{dataset}} \chi^2_{\text{dataset min}}, \tag{3.30}$$

and is distributed as a chi-squared with

$$n = \sum_{\text{dataset}} n_{\text{dataset}} - n_{\text{global}} \tag{3.31}$$

degrees of freedom (see [265] for a proof). Here, n_{dataset} is the number of oscillation parameters of χ^2_{dataset}, and likewise for n_{global}.

data sets	NO			IO		
	χ^2_{PG}/n	p-value	$\#\sigma$	χ^2_{PG}/n	p-value	$\#\sigma$
T2K vs. NOνA (θ_{13} free)	6.7/4	0.15	1.4	3.6/4	0.46	0.7
T2K vs. React.	0.3/2	0.87	0.2	2.5/2	0.29	1.1
NOνA vs. React.	3.0/2	0.23	1.2	6.2/2	0.045	2.0
T2K vs. NOνA vs. React.	8.4/6	0.21	1.3	8.9/6	0.18	1.3
T2K vs. NOνA (θ_{13} fixed)	6.5/3	0.088	1.7	2.8/3	0.42	0.8
T2K vs. NOνA vs. React.	7.8/4	0.098	1.7	7.2/4	0.13	1.5

Table 3.1: The values of the parameter goodness-of-fit test statistic χ^2_{PG} and the corresponding statistical significance for various combinations of data sets. "React" refers to Daya Bay, RENO and Double Chooz. Both combinations in the last two lines have fixed θ_{13}. Solar parameters are fixed in all cases; courtesy of [229].

The results of the parameter goodness-of-fit test for various combinations of datasets is shown in table 3.1. We have separated the normal and inverted orderings into two cases, such that the χ^2 minimisation is restricted to a given ordering. Furthermore, the solar parameters are fixed to their global best-fit values. For the last two lines of the table, both combinations have $s^2_{13} = 0.0224$ fixed. The purpose of fixing s^2_{13} is to prevent a large reduction of tension between the T2K and NOνA datasets due to a large fluctuation of s^2_{13}. As can be seen, there is no significant tension, with the most significant occurring between NOνA and the reactor datasets in inverted ordering.

Solar sector In the previous NuFit paper [259], there was a $\sim 2\sigma$ tension between the KamLAND value of Δm^2_{21} and that of the solar data. The origin of this tension is visualised in fig. 3.8; the green data points from SuperK cause there to be a preference for lower Δm^2_{21}. The day-night variation also played a role in driving the tension. With the update from NU2020, the new SuperK data is no longer in tension with KamLAND, as shown in fig. 3.9.

Summary The best-fit values and 3σ ranges for the three-neutrino oscillation parameters, both with and without the tabulated SuperK atmospheric χ^2 map (364.8 kton years) are shown in table 3.2. We show the global $\Delta\chi^2$ profiles for each oscillation parameter (marginalising over the others) in fig. 3.10.

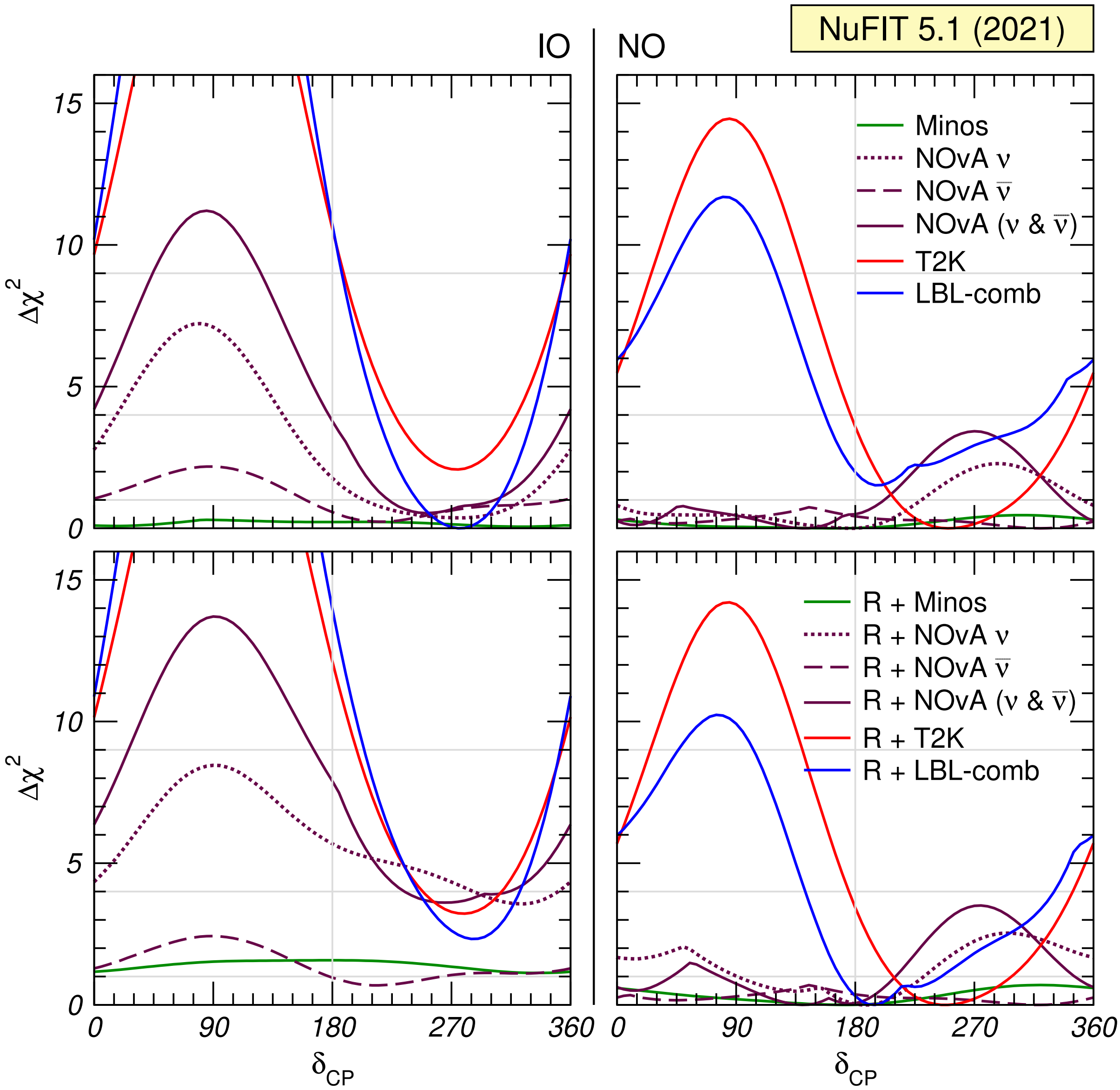

Figure 3.7: The top panels show $\Delta\chi^2(\delta_{\rm CP}))$ for long-baseline (LBL) accelerator data and their combination for inverted and normal ordering (left and right) with a prior for θ_{13}; the bottom panels show the same, but including reactor data; courtesy of [229].

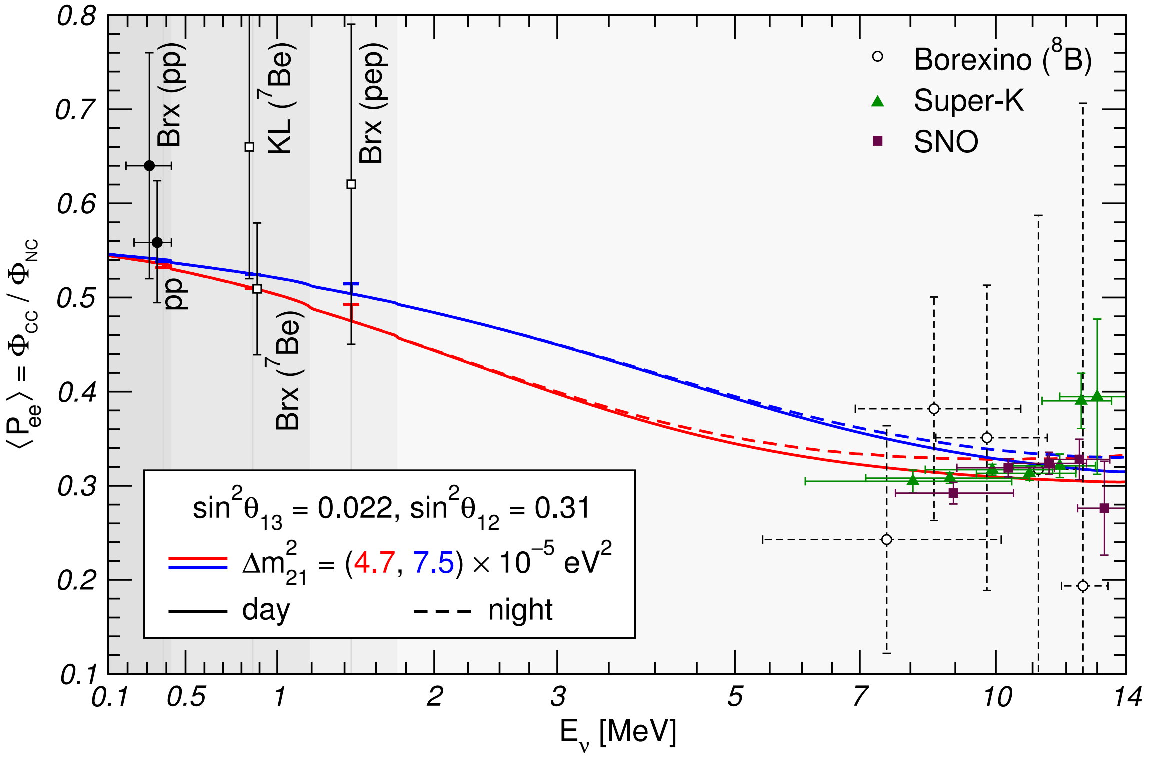

Figure 3.8: Figure, courtesy of [242], visualising data from KamLAND (KL), Borexino (Brx) and SuperK. The green data points cause a preference for lower Δm^2_{21}.

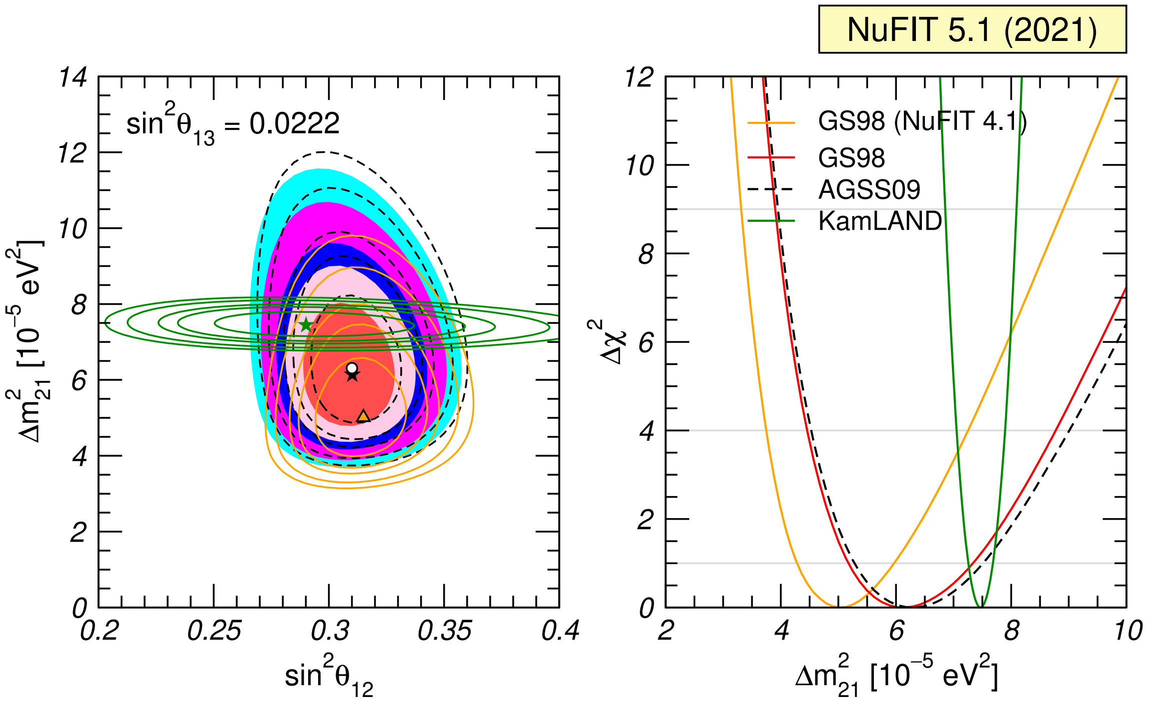

Figure 3.9: Solar sector of the global fit; left shows allowed 1, 2, 3σ regions with fixed $s^2_{13} = 2.22 \times 10^{-3}$ for KamLAND (green), solar data with the GS98 model (coloured regions) and the AGSS09 model (dashed lines), with the previous NuFit v4.1 in orange. Right shows the $\Delta\chi^2(\Delta m^2_{21})$ profiles, marginalising over s^2_{12}; courtesy of [229].

NuFIT 5.1 (2021)

		Normal Ordering (best fit)		Inverted Ordering ($\Delta\chi^2 = 2.6$)	
		bfp $\pm 1\sigma$	3σ range	bfp $\pm 1\sigma$	3σ range
without SK atmospheric data	$\sin^2\theta_{12}$	$0.304^{+0.013}_{-0.012}$	$0.269 \to 0.343$	$0.304^{+0.012}_{-0.012}$	$0.269 \to 0.343$
	$\theta_{12}/^\circ$	$33.44^{+0.77}_{-0.74}$	$31.27 \to 35.86$	$33.45^{+0.77}_{-0.74}$	$31.27 \to 35.87$
	$\sin^2\theta_{23}$	$0.573^{+0.018}_{-0.023}$	$0.405 \to 0.620$	$0.578^{+0.017}_{-0.021}$	$0.410 \to 0.623$
	$\theta_{23}/^\circ$	$49.2^{+1.0}_{-1.3}$	$39.5 \to 52.0$	$49.5^{+1.0}_{-1.2}$	$39.8 \to 52.1$
	$\sin^2\theta_{13}$	$0.02220^{+0.00068}_{-0.00062}$	$0.02034 \to 0.02430$	$0.02238^{+0.00064}_{-0.00062}$	$0.02053 \to 0.02434$
	$\theta_{13}/^\circ$	$8.57^{+0.13}_{-0.12}$	$8.20 \to 8.97$	$8.60^{+0.12}_{-0.12}$	$8.24 \to 8.98$
	$\delta_{\rm CP}/^\circ$	194^{+52}_{-25}	$105 \to 405$	287^{+27}_{-32}	$192 \to 361$
	$\dfrac{\Delta m^2_{21}}{10^{-5}\ \text{eV}^2}$	$7.42^{+0.21}_{-0.20}$	$6.82 \to 8.04$	$7.42^{+0.21}_{-0.20}$	$6.82 \to 8.04$
	$\dfrac{\Delta m^2_{3\ell}}{10^{-3}\ \text{eV}^2}$	$+2.515^{+0.028}_{-0.028}$	$+2.431 \to +2.599$	$-2.498^{+0.028}_{-0.029}$	$-2.584 \to -2.413$
		Normal Ordering (best fit)		Inverted Ordering ($\Delta\chi^2 = 7.0$)	
		bfp $\pm 1\sigma$	3σ range	bfp $\pm 1\sigma$	3σ range
with SK atmospheric data	$\sin^2\theta_{12}$	$0.304^{+0.012}_{-0.012}$	$0.269 \to 0.343$	$0.304^{+0.013}_{-0.012}$	$0.269 \to 0.343$
	$\theta_{12}/^\circ$	$33.45^{+0.77}_{-0.75}$	$31.27 \to 35.87$	$33.45^{+0.78}_{-0.75}$	$31.27 \to 35.87$
	$\sin^2\theta_{23}$	$0.450^{+0.019}_{-0.016}$	$0.408 \to 0.603$	$0.570^{+0.016}_{-0.022}$	$0.410 \to 0.613$
	$\theta_{23}/^\circ$	$42.1^{+1.1}_{-0.9}$	$39.7 \to 50.9$	$49.0^{+0.9}_{-1.3}$	$39.8 \to 51.6$
	$\sin^2\theta_{13}$	$0.02246^{+0.00062}_{-0.00062}$	$0.02060 \to 0.02435$	$0.02241^{+0.00074}_{-0.00062}$	$0.02055 \to 0.02457$
	$\theta_{13}/^\circ$	$8.62^{+0.12}_{-0.12}$	$8.25 \to 8.98$	$8.61^{+0.14}_{-0.12}$	$8.24 \to 9.02$
	$\delta_{\rm CP}/^\circ$	230^{+36}_{-25}	$144 \to 350$	278^{+22}_{-30}	$194 \to 345$
	$\dfrac{\Delta m^2_{21}}{10^{-5}\ \text{eV}^2}$	$7.42^{+0.21}_{-0.20}$	$6.82 \to 8.04$	$7.42^{+0.21}_{-0.20}$	$6.82 \to 8.04$
	$\dfrac{\Delta m^2_{3\ell}}{10^{-3}\ \text{eV}^2}$	$+2.510^{+0.027}_{-0.027}$	$+2.430 \to +2.593$	$-2.490^{+0.026}_{-0.028}$	$-2.574 \to -2.410$

Table 3.2: Three-neutrino oscillation parameters from our global fit. The left column column represents the best-fit values relative to the global minimum at normal ordering, and the right-column relative to the local minimum at inverted ordering. For NO $\Delta m^2_{3\ell} \equiv \Delta m^2_{31} > 0$ and for IO $\Delta m^2_{3\ell} \equiv \Delta m^2_{32} < 0$. The upper part of the table excludes SuperK atmospheric data, whereas the lower part includes it.

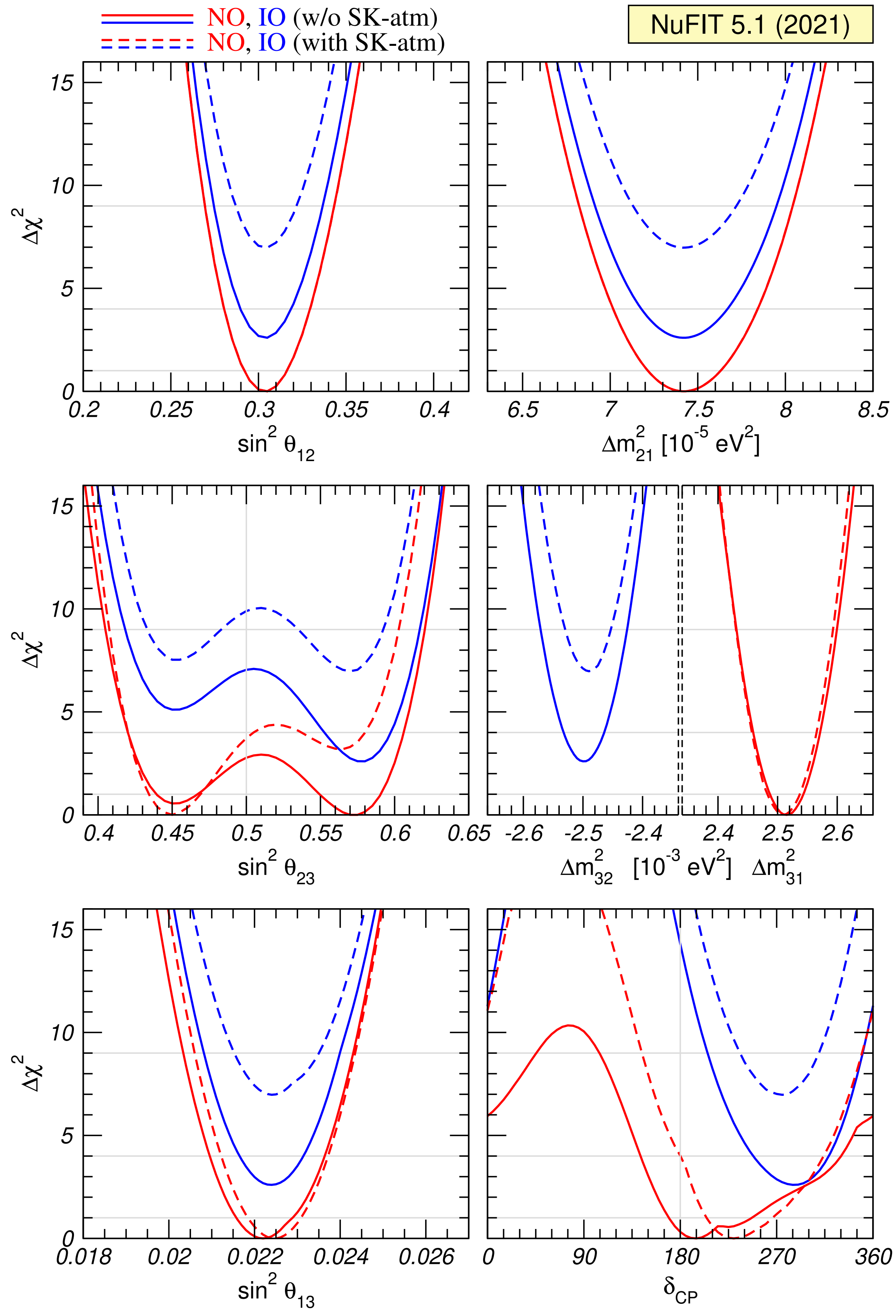

Figure 3.10: Profiles of global $\Delta\chi^2$ for each parameter in NO (red) or IO (blue), including (dashed) and excluding (solid) SuperK atmospheric data, courtesy of [229].

Chapter 4

Reactor Experiments and a Fourth, Sterile Neutrino

As reviewed in chapter 2, the idea of oscillations between a Standard Model neutrino and a fourth, light, sterile neutrino state, has a long history, with this being an alternative hypothesis to the solar and atmospheric neutrino anomaly during their early days. With advancements in the prediction of the reactor spectrum revealing a deficit between prediction and experiments figs. 2.8 and 2.12, including the gallium anomaly, numerous studies have investigated the global significance of the interpretation of this deficit as neutrino oscillations [266–271].

This chapter is based on my work published in [272], which builds on previous global analyses of the evidence for sterile oscillations. The work was sparked by the announcement by Neutrino-4 of evidence for neutrino oscillations at NU2020 [273], and later, the confirmation of the gallium anomaly by the Baksan Experiment on Sterile Transitions (BEST) [201], which provided further impetus for our work. When Neutrino-4 announced its results at NU2020, they claimed evidence for sterile oscillations at $> 3\sigma$. However this was based on Wilks' theorem, which is inapplicable for sterile-oscillation searches. The intuitive reason for this is that one can always fit a high-frequency low-amplitude pattern to random noise (Neutrino-4's best-fit point occurred at relative large $\Delta m^2 \sim 7\,\mathrm{eV}^2$) leading to a bias due to a false signal (see also the discussion in [274]). Using Monte Carlo simulations to derive the correct distribution of χ^2, Coloma, Huber and Schwetz derive only 2.6σ evidence for new oscillations [274]. A reevaluation of the analysis by the collaboration also found a statistical significance of 2.7σ [275].

Using a robust statistical method is important for correctly interpreting the bounds and signals found in reactor experiments. The correct way to construct exclusion curves, particularly for our case, in which a parameter like $\sin^2 2\theta$ is bounded in the interval $[0, 1]$, is to use the prescription developed by Feldman and Cousins in 1998 [276]. In such a prescription, the statistical distribution of χ^2 is calculated via the Monte Carlo method for each point in parameter space. This is computationally expensive, but gives statistically correct results. In this chapter, I cover the details of my work constructing fast χ^2 routines for the relevant reactor experiments, which needed to be written in the programming language C^{++} and heavily optimised; I also cover the details of the FCMC (Feldman-Cousins Monte-Carlo) statistical analysis, which needed the high-performance computing facilities at the KIT for reasonable computation times.

4.1 Reactor Experiments

In this section I will give an overview of the relevant reactor experiments that we used in the global analysis, and an overview of our implementation of each experiment's χ^2 routine. (For a concise overview of the relevant reactor experiments, see [277]). All the experiments have extremely short baselines, 10 – 20 m, and as mentioned previously, this provides numerous challenges for such an experiment, limiting the detector size and in addition to safety concerns due to the radiation from the reactor itself; because of the close proximity to the reactor, some detectors cannot use a liquid scintillator. Furthermore, due to the small size of the detector, there will be more complicated detector physics regarding energy reconstruction, due to escaping gamma rays, and also finite-size effects of the source and detector. For all experiments, I am grateful to the GNU Scientific Library [278], whose routines I have benefited from.

4.1.1 DANSS

The DANSS (Detector of AntiNeutrino based on Solid Scintillator) experiment, is a 1 m^3 highly segmented plastic-scintillator detector at the Kalinin Nuclear Power Plant, located between Moscow and St Petersburg [279]. The detector does not use a liquid scintillator, due to safety concerns regarding the proximity to the reactor, which has a thermal power of 3.1 GW. The detector's plastic scintillator strips are coated with gadolinium for neutron capture, as well as to contain scintillation light. The detector is mounted on a movable platform underneath the industrial reactor at Kalinin (fig. 4.1).

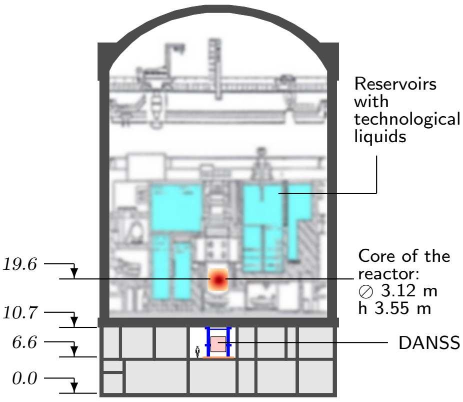

Figure 4.1: Sketch of nuclear reactor and DANSS detector, courtesy of [279].

The detector measured the neutrino flux over five years (2016 – 2021) at three baselines: bottom, middle and top, $\lambda \equiv \mathrm{B}, \mathrm{M}, \mathrm{T}$, at distances 10.9, 11.9 and 12.875 m [280, p. 24].[1] Their data [280, p. 17] is reported with the ratios

$$R_1^i \equiv \frac{n_\mathrm{B}^i}{n_\mathrm{T}^i} \qquad R_2^i \equiv \frac{n_\mathrm{M}^i}{\sqrt{n_\mathrm{B}^i n_\mathrm{T}^i}}, \qquad \text{where} \qquad n_\lambda^i \equiv \frac{N_\lambda^i - B_\lambda^i}{\Delta t_\lambda} \tag{4.1}$$

and i labels the energy bin; N_λ^i, B_λ^i labels the absolute number of events, background, respectively, and Δt_λ is the exposure period, extracted from [280, p. 12]. The reconstruction matrix is taken to be of form eq. (3.18), with energy resolution taken from [281, fig. 5], but increased by 10% (to better match the results of the collaboration),

$$\frac{\sigma_E(E_\nu)}{E_\nu} = 0.352 + 2.44 \cdot 10^{-2} \frac{E_\nu}{\mathrm{MeV}} - 0.148 \cdot \sqrt{\frac{E_\nu}{\mathrm{MeV}}} + \frac{4.04 \cdot 10^{-2}}{\sqrt{E_\nu/\mathrm{MeV}}}. \tag{4.2}$$

Because the baseline is so short, the finite size of the reactor core and detector needs to be taken into account, as opposed to the medium-baseline experiments like RENO

---

[1] However, I added 0.05 m to all baselines to better match the collaboration's results.

and Daya Bay, where the assumption of a point-like neutrino detector and source was sufficient. To simplify the calculation, I make the assumption that the neutrino source is a collimated beam, and neutrinos are produces homogeneously throughout its volume, thus reducing the geometry to one dimension. The detector is assumed to be a $1\,\mathrm{m}^3$ cube [279], and the relevant reactor size is taken to be $4.5\,\mathrm{m}$, which is set slightly higher than the value quoted in [280] to better match the results of the collaboration. I assume that this is due to diagonally travelling neutrinos having a longer path length. Then, the no-oscillation prediction is

$$N^i_{0,\lambda} = \int_{L_\lambda-0.5}^{L_\lambda+0.5} \mathrm{d}\ell \int_{\ell-2.25}^{\ell+2.25} \frac{\mathrm{d}L}{L^2} \int_{E_{i-1}}^{E_i} \mathrm{d}E^{\mathrm{rec}} \int_0^\infty \mathrm{d}E_\nu\, \sigma(E_\nu) \frac{\mathrm{d}\Phi}{\mathrm{d}E_\nu} R(E_\nu, E^{\mathrm{rec}}). \tag{4.3}$$

As previously mentioned, the baselines are $L_\lambda \equiv 10.95,\ 11.95$ and $12.925\,\mathrm{m}$, for $\lambda = \mathrm{B}, \mathrm{M}$ and T, respectively. The integral over E_ν is restricted to $[E_{i-1} - 3\sigma(E_{i-1}), E_i + 3\sigma(E_i)]$, and the integral over the $1/L^2$ geometric suppression is done analytically. The fission fractions for the flux can be found in [280, p. 5]. The predicted number of events with oscillations is

$$N^i_\lambda = N^i_{0,\lambda}\left[1 - \sin^2 2\theta \cdot \Omega^i_\lambda\left(\Delta m^2\right)\right], \tag{4.4}$$

where

$$\begin{aligned}\Omega^i_\lambda\left(\Delta m^2\right) \equiv \frac{1}{N^i_{0,\lambda}} \int_{L_\lambda-0.5}^{L_\lambda+0.5} \mathrm{d}\ell \int_{\ell-2.25}^{\ell+2.25} \mathrm{d}L \int_{E_{i-1}}^{E_i} \mathrm{d}E^{\mathrm{rec}} \int_0^\infty \mathrm{d}E_\nu \\ \left[\sigma(E_\nu) \frac{\mathrm{d}\Phi}{\mathrm{d}E_\nu} R(E_\nu, E^{\mathrm{rec}}) \frac{\sin^2 \frac{\Delta m^2 L}{4E}}{L^2}\right]\end{aligned} \tag{4.5}$$

is the oscillating part of the integral; I tabulate Ω^i_λ on a grid of Δm^2 values for fast χ^2 evaluation. Note that by integrating the $\sin^2 x/x^2$ term by parts, the L integral is converted to trigonometric functions and the special function $\mathrm{Si}(x) = \int_0^x \sin(t)/t$ (also known as the Sine integral).

My prediction for the ratios is defined by rescaling the collaboration's no-oscillation prediction, extracted from [280, p. 17],

$$P^i_1 = R^{3\nu}_1 \frac{\rho^i_{\mathrm{B}}}{\rho^i_{\mathrm{T}}}, \quad P^i_2 = R^{3\nu}_2 \frac{\rho^i_{\mathrm{M}}}{\sqrt{\rho^i_{\mathrm{B}}\rho^i_{\mathrm{T}}}}, \quad \text{where} \quad \rho^i_\lambda \equiv \frac{N^i_\lambda}{N^i_{0,\lambda}}. \tag{4.6}$$

For each energy bin i, the two ratios have statistical correlations, defined by the 2×2 covariance matrix (with indices $a, b \in [1, 2]$),

$$V^i_{ab} \equiv \sum_{\lambda=B,M,T} \frac{\partial R^i_a}{\partial N^i_\lambda} \frac{\partial R^i_b}{\partial N^i_\lambda} \sigma^2_{N^i_\lambda} = \sum_{\lambda=B,M,T} \frac{\partial R^i_a}{\partial n^i_\lambda} \frac{\partial R^i_b}{\partial n^i_\lambda} \frac{n^i_\lambda}{\Delta t_\lambda}, \tag{4.7}$$

where I have neglected the background for simplicity. (This will have the effect of increasing the statistical significance, however since the background only represents $\sim 2\%$ of the events, its effect is small.) The full expression of the covariance matrix is given in appendix A.1.1.

There are two pulls, $\kappa_{1,2}$, which represent the systematic uncertainty of the relative efficiencies of each ratio $R^i_{1,2}$, which have a common error $\sigma_{\text{sys}} \equiv 0.2\%$ [280, p. 18]. The χ^2 function for DANSS is then defined as

$$\chi^2_{\text{DANSS}} = \min_{\kappa_1,\kappa_2} \left\{ \sum_{i=1}^{36} \sum_{a,b=1}^{2} \left[D^i_a - (1+\kappa_a) P^i_a \right] (V^i)^{-1}_{ab} \left[D^i_b - (1+\kappa_b) P^i_b \right] + \frac{\kappa_1^2 + \kappa_2^2}{\sigma^2_{\text{sys}}} \right\}. \quad (4.8)$$

The 36 energy bins used in the analysis span energies between 1.5 − 6 MeV; here D^i_a denotes the observed ratios, from the data in [280, p. 17]. The minimisation over the pulls is done analytically, as outlined in appendix A.1.2. In fig. 4.2, I compare my χ^2 map with the collaboration's.

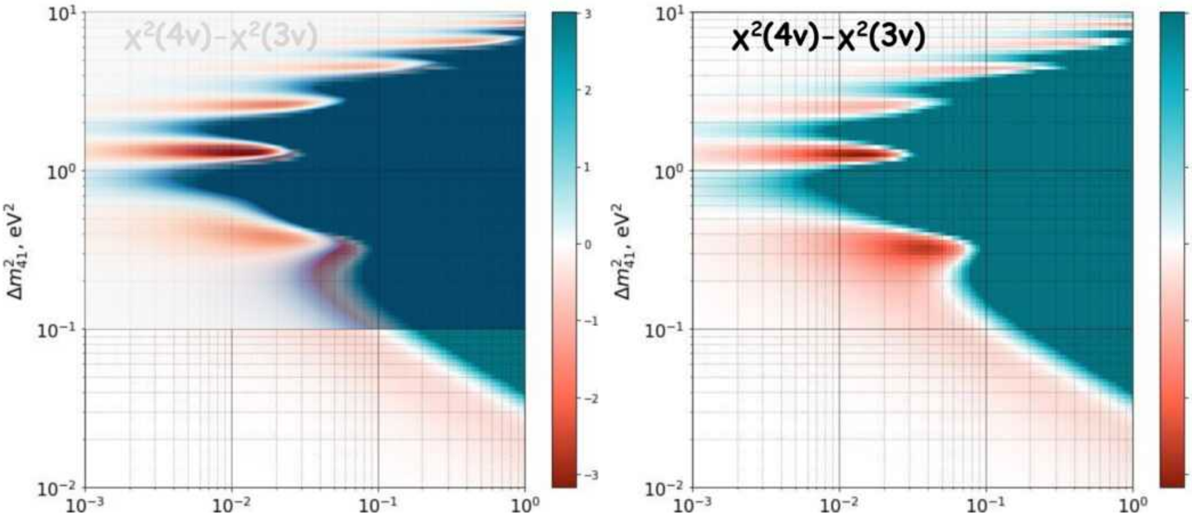

Figure 4.2: Left: our $\chi^2(4\nu) - \chi^2(3\nu)$ map plotted with the same colour scale, overlaid on the collaboration's results [280]. Right: the collaboration's results.

4.1.2 NEOS

The NEOS experiment is located in reactor unit five of the Hanbit Nuclear Power Complex, in Yonggwang, Korea, which is part of the same reactor complex used by RENO. The reactor core has an active size of 3.1 m in diameter and 3.8 m in height, and a thermal power of 2.8 GW. The detector is a cylindrical tank of 1008 L, filled with 0.5% Gd-doped liquid scintillator, with photomultiplier tubes at the ends of the tank. The detector is placed at a distance of roughly 23.7 m away from the detector. The detector operated for 180 days with the reactor on and 46 days with the reactor off, with data being recorded in the years 2015 − 2016. NEOS measured 1976.7 ± 3.4 events/day (with prompt energies between 1 − 10 MeV) during the reactor-on period, and 85.1 ± 1.4 events in the reactor-off period. Their data is reported in [282, fig. 3a]; the black points are assumed to be background subtracted, normalised to the quoted total signal rate, 1976.7 − 85.1 = 1891.6 events/day. *Note:* this number does not include the last 3 MeV-wide energy bin; it is the signal rate for 1 − 7 MeV.

The analysis for NEOS is complicated by the fact that they do not have a movable detector or near detector, and the small size of their detector, which complicates the energy reconstruction[2]. Because of the anomalies in the reactor spectrum, NEOS uses the reactor antineutrino spectrum, weighted by cross section, extracted from the Daya Bay experiment [255], and applies corrections due to the different isotopic fission fractions of the nuclear fuel with the Huber-Mueller flux, namely

$$\left[\sigma\frac{\mathrm{d}\Phi}{\mathrm{d}E_\nu}\right]^{3\nu}_{\mathrm{NEOS}} = \left[\sigma\frac{\mathrm{d}\Phi}{\mathrm{d}E_\nu}\right]^{3\nu}_{\mathrm{DB}} + \sigma(E_\nu)\sum_{\mathrm{iso}}\left(f^{\mathrm{iso}}_{\mathrm{NEOS}} - f^{\mathrm{iso}}_{\mathrm{DB}}\right)\phi^{\mathrm{iso}}(E_\nu). \tag{4.9}$$

The superscript 3ν denotes that the Daya Bay weighted flux was extracted assuming three-neutrino oscillations; since Daya Bay is sensitive to three-neutrino oscillations, these had to be folded out (along with energy-reconstruction effects). However, under the assumption of four-neutrino oscillations, the folding-out procedure should be modified. The baselines of Daya Bay range between $350-2000\,\mathrm{m}$, at which any oscillations due to a fourth eV-scale neutrino will average out. Therefore, to remove sterile oscillations, it is enough to divide the Daya Bay weighted flux by $1-(\sin^2 2\theta)/2$. In order to disentangle the mixing from the mass-squared splitting, I ignore the fact that the Huber-Mueller correction should not be divided by this. Explicitly, for $m_4 \sim \mathcal{O}(1\,\mathrm{eV})$

$$\begin{aligned}\left[\sigma\frac{\mathrm{d}\Phi}{\mathrm{d}E_\nu}\right]^{4\nu}_{\mathrm{DB}} &= \left(1-\frac{\sin^2 2\theta}{2}\right)^{-1}\left[\sigma\frac{\mathrm{d}\Phi}{\mathrm{d}E_\nu}\right]^{3\nu}_{\mathrm{DB}} \implies \\ \left[\sigma\frac{\mathrm{d}\Phi}{\mathrm{d}E_\nu}\right]^{4\nu}_{\mathrm{NEOS}} &\approx \left(1-\frac{\sin^2 2\theta}{2}\right)^{-1}\left[\sigma\frac{\mathrm{d}\Phi}{\mathrm{d}E_\nu}\right]^{3\nu}_{\mathrm{NEOS}}.\end{aligned} \tag{4.10}$$

Due to the smallness of the baseline, we have to consider the finite size of the reactor and detector. Fortunately, the distribution of baselines $\rho(L)$ is provided by the collaboration in [284, p. 8]. As previously mentioned, this requires us to define a baseline-averaged neutrino-oscillation probability

$$\left\langle\frac{P_{ee}}{L^2}\right\rangle(\sin^2 2\theta, \Delta m^2, E_\nu) = \int_{L_{\min}}^{L_{\max}} P_{ee}\left(\sin^2 2\theta, \frac{\Delta m^2 L}{E_\nu}\right)\frac{\rho(L)}{L^2}\mathrm{d}L\,. \tag{4.11}$$

Another complication is in the reconstruction matrix. As mentioned previously, we need to consider the non-linear response of the detector. Since NEOS does not publish this information, I use the following based on Daya Bay's non-linear response $f(\,\cdot\,)$, from the supplementary material of [258],

$$E_p = 1.01\cdot E_{e^+} f(0.41\cdot E_{e^+} - 0.05), \qquad \text{where} \qquad E_{e^+} = E_\nu - \Delta_{np} + m_e, \tag{4.12}$$

m_e is the electron mass, and Δ_{np} the neutron-proton mass difference. This form was established by making the *ansatz* $aE_{e^+}f(bE_{e^+}+c)$, and tuning the parameters a, b, c, to match the results of the collaboration.

The reconstruction matrix consists of two contributions, due to two important physical effects. The first I take from [250] which takes the standard normal distribution, and

---

[2] Whilst RENO published a re-analysis using RENO data as an additional baseline [283], alleged in-fighting in the collaboration resulted in the decision not to follow this work. The preprint remains unpublished at the time of writing this thesis.

modifies it to taken into account escaping positrons, which only deposit energy due to scintillation and do not have a prompt signal from pair annihilation,

$$R_{e^+}(E_\text{rec}, E_\nu) = \begin{cases} Z + \left(\dfrac{1}{\sqrt{2\pi}\sigma(E_p)} - Z\right) \exp\left\{-\dfrac{(E_\text{rec} - E_p)^2}{2\sigma^2(E_p)}\right\} & \text{if } E_\text{rec} < E_p\,, \\ \dfrac{1}{\sqrt{2\pi}\sigma(E_p)} \exp\left\{-\dfrac{(E_\text{rec} - E_p)^2}{2\sigma^2(E_p)}\right\} & \text{if } E_\text{rec} > E_p\,, \end{cases} \tag{4.13}$$

where $Z = 0.01$. The second contribution is due to escaping 511-keV gamma rays after pair annihilation, with a relative height of 0.5, as per [284, p. 15],

$$R_\gamma(E_\text{rec}, E_\nu) = 0.5 \times \frac{1}{\sqrt{2\pi}\sigma(E_p)} \exp\left\{-\frac{(E_\text{rec} + m_e - E_p)^2}{2\sigma^2(E_p)}\right\}. \tag{4.14}$$

The energy resolution is taken from [285, fig. 3], which I parameterised as

$$\sigma_E(E) = \sqrt{2 \cdot 10^{-2} + 1.2 \cdot 10^{-3} \frac{E}{\text{MeV}} + 2 \cdot 10^{-4} \left(\frac{E}{\text{MeV}}\right)^2}\,. \tag{4.15}$$

The final reconstruction matrix $R(E_\text{rec}, E_\nu)$ is the sum of the two contributions eqs. (4.13) and (4.14). However, I found that this approach does not reproduce the last bin, as the reconstruction matrix shown in the inset of [282, fig. 3a] shows different behaviour for the last bin. For the last bin, I estimate the reconstruction matrix as a piecewise constant (as a function of E_ν), so that the ratio in the last bin of [282, fig. 3c] is correctly reproduced. As per previous sections, the integral over E_rec is done with the error function,

$$\mathcal{R}_i(E_\nu) = \int_{E_{i-1}}^{E_i} R\left(E_\text{rec}, E_\nu\right) \mathrm{d}E_\text{rec}\,. \tag{4.16}$$

My prediction is then defined as

$$\text{Pred}_i\left(\sin^2 2\theta, \Delta m^2\right) = \left(1 - \frac{\sin^2 2\theta}{2}\right)^{-1} \int \mathcal{R}_i(E_\nu) \left[\sigma \frac{\mathrm{d}\Phi}{\mathrm{d}E_\nu}\right]^{3\nu}_\text{NEOS} \left\langle \frac{P_{ee}}{L^2} \right\rangle \mathrm{d}E_\nu. \tag{4.17}$$

However due to all the unknown details of detector effects, I rescale the collaboration's no-oscillation prediction $\text{NEOS}_i^{3\nu}$ using my prediction, to minimise the effect of detector mismodelling,

$$P_i \equiv \text{NEOS}_i^{3\nu} \frac{\text{Pred}_i\left(\sin^2 2\theta, \Delta m^2\right)}{\text{Pred}_i\left(\sin^2 2\theta = 0\right)}. \tag{4.18}$$

To construct the test statistic, I first define the covariance matrix, following [282], as $V_{ij} = V_{ij}^\text{stat} + V_{ij}^\text{syst}$; the first term V^stat accounts for statistical errors,

$$V_{ij}^\text{stat} = \delta_{ij} \left[\frac{D_i + B_i}{\Delta t_\text{on}} + \frac{B_i}{\Delta t_\text{off}}\right], \tag{4.19}$$

where δ_{ij} is the Kronecker delta symbol; D_i is the background-subtracted events/day for bin i obtained from data (the black points in [282, fig. 3a]), measured during the reactor-on period of Δt_on days; B_i corresponds to the background events/day (the yellow bars of *ibid.*), measured during the reactor-off period of Δt_{off} days. In eq. (4.19) the first term is the Poisson error for the event rate, and the second is the Poisson error of the measured background rate, which is not known exactly.

The second contribution to the covariance matrix V^{syst} accounts for systematic errors from the Daya Bay weighted flux; the covariance matrix for the weighted flux $V_{\mathrm{DB}}(E_\nu, E'_\nu)$ is provided in [255, tab. 13]. I make the simplifying assumption that experimental uncertainties dominate the Daya Bay covariance matrix, such that I do not need to do any rescaling to remove sterile oscillations in the covariance matrix. (In fact, due to the unfolding procedure, it is impossible to separate theoretical and experimental uncertainties, the former being sensitive to the oscillation model.) I make V_{DB} a continuous function by bicubic interpolation; then I fold in the NEOS energy response,

$$V_{ij}^{\mathrm{syst}} = \mathcal{N}^2 \iint V^{\mathrm{DB}}(E_\nu, E'_\nu)\mathcal{R}_i(E_\nu)\mathcal{R}_j(E'_\nu)\, \mathrm{d}E_\nu \mathrm{d}E'_\nu\,, \tag{4.20}$$

where the normalisation is determined to be

$$\mathcal{N} = \frac{\sum_i \mathrm{NEOS}_i^{3\nu}}{\sum_i \mathrm{Pred}_i\,(\sin^2 2\theta = 0)} \int_{L_{\mathrm{min}}}^{L_{\mathrm{max}}} \frac{\rho(L)}{L^2} \mathrm{d}L\,. \tag{4.21}$$

The χ^2 function is defined as

$$\chi^2_{\mathrm{NEOS}} = \min_{\xi} \sum_{i,j=1}^{61} (D_i - \xi P_i) V_{ij}^{-1} (D_j - \xi P_j), \tag{4.22}$$

where the sum runs over the 61 energy bins. The free normalisation ξ does not have a pull term, as the NEOS analysis seeks to be independent of the flux normalisation. As mentioned previously, we make the simplifying assumption that V^{syst} is dominated by experimental uncertainties, which should be independent of the flux normalisation ξ. The minimisation is done analytically, and the relevant formulae are detailed in appendix A.2.

In fig. 4.3 (left), I compare 90% exclusion curve (red) with the collaboration's (blue), which was calculated by the raster-scan method (see [282] for details, particularly eq. (4)). This method assumes that the unnormalised probability distribution for a fixed Δm^2 is $\exp(-\Delta\chi^2/2)$. My curve has extremely good agreement in the range $1-2\,\mathrm{eV}^2$, but at lower Δm^2 my oscillations are smaller than the collaboration's, and at larger Δm^2 they are larger. I attribute this to mismodelling the detector response. I tuned my detector response $aE_{e^+} f(bE_{e^+} + c)$ until it reproduced the $\chi^2(3\nu)$ value, and the quasi-degenerate islands at $(\Delta m^2_{41}, \sin^2 2\theta_{14}) = (0.05, 1.73\,\mathrm{eV}^2)$ and $(0.04, 1.30\,\mathrm{eV}^2)$ as best possible. Away from them, the deviations are expected to be larger (due to say quadratic corrections in the argument of $f(\,\cdot\,)$). The position of my global minimum also differs from NEOS', but my χ^2_{min} value is similar to the collaboration's (7.4 vs. 6.5). Whilst the collaboration reports two degenerate minima at $(\Delta m^2, \sin^2 2\theta) = (0.05, 1.73\,\mathrm{eV}^2)$ and $(0.04, 1.30\,\mathrm{eV}^2)$, my $\Delta\chi^2$ map has more such islands (see fig. 4.3 (right)). At NEOS' two degenerate minima, my fit yields a higher χ^2 by approximately two units, see table 4.1. I assume this to be due to the unknown detector response, combined with the impact of systematic uncertainties (*e.g.,* energy scale), which are technically difficult to implement outside the collaboration.

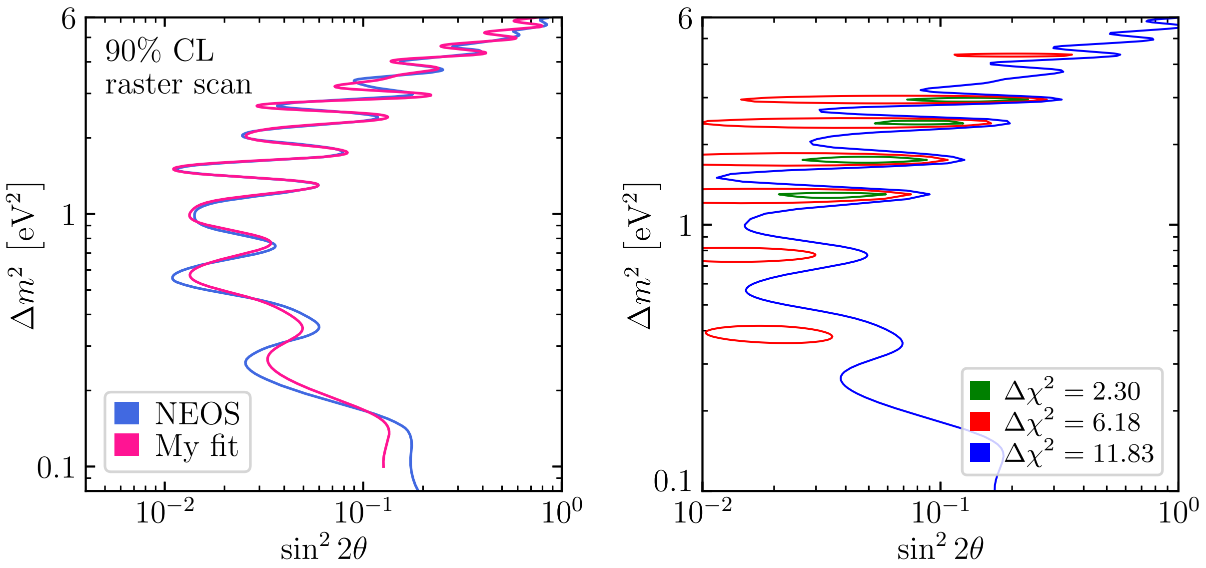

Figure 4.3: Left: a comparison of my exclusion curve (red) with the collaboration's (blue), extracted from [282]. Right: my $\Delta\chi^2$ map, showing multiple quasi-degenerate islands.

NEOS	My Fit χ^2	Collab. χ^2	Δm^2	$\sin^2 2\theta$
Minimum 1	59.73	$\sim$ 57.5	1.30 eV^2	0.04
Minimum 2	59.60	57.5	1.73 eV^2	0.05

Table 4.1: Comparison of our χ^2 to the values obtained by the collaboration at their quasi-degenerate global minima.

4.1.3 PROSPECT

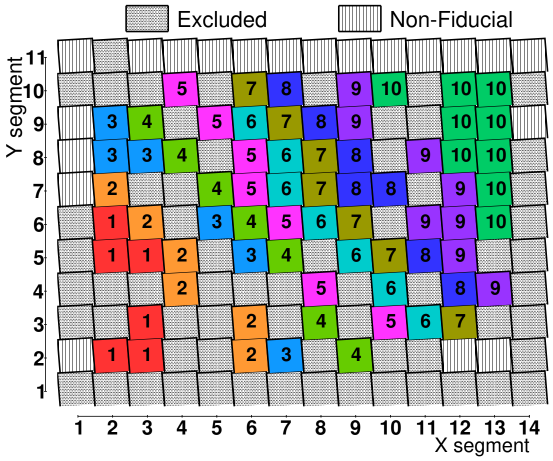

Figure 4.4: Map of detector segments, both operable and inoperable, and the groupings of the operable ones; courtesy of [286].

PROSPECT (the Precision Reactor Oscillation and Spectrum Experiment) is located at the Oak Ridge National Laboratory, using a research reactor with 85 MW of thermal power, consisting of highly enriched ^{235}U (> 99% fission fraction). The detector, located 7.9 m away, consists of four tons of liquid scintillator, doped with ^{6}Li at a mass fraction of 0.08%. The scintillator is divided into 154 14.5 cm × 14.5 cm × 117.6 cm segments arranged in a 11 × 14 grid (fig. 4.4), optically isolated by reflecting panels. We used data from the supplementary material of [286], which corresponds to 183 days of data taking, 105 days with the reactor on, and 78 with the reactor off, collected in 2018. The resulting exclusion curve is not as strong as those from the commercial-reactor experiments, due to the much lower thermal power, but also because the PROSPECT detector had defects: 64 of 154 detector segments were inoperable, resulting in a loss of 42% of the detector volume (most of which is fiducial).

As shown in fig. 4.4, the segments are grouped into ten clusters of similar baseline. The data is reported as ten energy spectra (one for each cluster), with sixteen energy bins from $1-7\,\mathrm{MeV}$. The χ^2 routine was developed by Jeffrey Berryman with the `GLoBES` software [287, 288]. In the supplementary material of [286], the collaboration publishes segment-level efficiencies ϵ_s and detector-response matrices R^s_{ij}, where s labels the detector segment, i labels the reconstructed prompt energy, and j labels the true neutrino energy (binned in 82 0.1-MeV intervals from $1.8-10\,\mathrm{MeV}$). For the prediction, the segment-level detector properties were converted into baseline-level objects, labelled by $l \in \{1 \dots 10\}$. Within `GLoBES`, the detector mass (defined in the Abstract Experiment Definition Language (AEDL) file), associated with baseline l, is set to the sum of the relative efficiencies of the segments contained in that baseline. The baseline distribution $\rho_s(L)$ for each segment s is constructed by randomly selecting points in the reactor core and detector segment to form a density histogram (the segment map provided by the collaboration determines the detector geometry, while the reactor core is modelled as a cylinder of height 51 cm and radius 22 cm). The effective baseline is then calculated by adding the contribution of each segment, weighted by its relative efficiency $w_s = \frac{\epsilon_s}{\sum_s \epsilon_s}$,

$$\left\langle \frac{1}{L^2} \right\rangle_l = \sum_s w_s \left\langle \frac{1}{L^2} \right\rangle_s , \qquad \text{with} \qquad \left\langle \frac{1}{L^2} \right\rangle_s = \int \mathrm{d}L\, \frac{\rho_s(L)}{L^2} . \tag{4.23}$$

The four-neutrino oscillation probability for a given bin l and neutrino energy E_ν is computed as

$$P^l_{ee}\left(\sin^2\theta, \frac{\Delta m^2}{4E_\nu}\right) = 1 - \sin^2 2\theta \cdot \Pi_l\left(\frac{\Delta m^2}{4E_\nu}\right) , \tag{4.24}$$

where for each baseline bin l we define

$$\Pi_l(q) = \left[\sum_s w_s \left\langle \frac{\sin^2(qL)}{L^2} \right\rangle_s\right] \Big/ \left\langle \frac{1}{L^2} \right\rangle_l \tag{4.25}$$

with

$$\left\langle \frac{\sin^2(qL)}{L^2} \right\rangle_s = \int \mathrm{d}L\, \frac{\rho_s(L)\sin^2(qL)}{L^2} . \tag{4.26}$$

The effective detector-response matrix R^l_{ij} for bin l is given by

$$R^l_{ij} = \sum_s W_s R^s_{ij}, \qquad \text{where} \qquad W_s = \frac{w_s \left\langle L^{-2} \right\rangle_s}{\left\langle L^{-2} \right\rangle_l} . \tag{4.27}$$

The weights W_s account for the relative expected rates in the segments. In principle, these vary as a function of the sterile-neutrino parameters, but we assume that these differences are negligible. At a given baseline bin l and energy bin i, the predicted event rate for a set of oscillation parameters is proportional to

$$\mathrm{Pred}_{l,i}\left(\sin^2 2\theta, \Delta m^2\right) = \sum_j R^l_{ij} \int_{E_{j-1}}^{E_j} \mathrm{d}E_\nu\, \sigma(E_\nu) \frac{\mathrm{d}\Phi_{^{235}\mathrm{U}}}{\mathrm{d}E_\nu} \cdot P^l_{ee}\left(\sin^2 2\theta, \frac{\Delta m^2}{4E_\nu}\right) . \tag{4.28}$$

Following eq. (4.18), we define our prediction by rescaling the collaboration's three-neutrino prediction,

$$P_{l,i} \equiv \mathrm{PROSPECT}^{3\nu}_{l,i} \frac{\mathrm{Pred}_{l,i}\left(\sin^2 2\theta, \Delta m^2\right)}{\mathrm{Pred}_{l,i}\left(\sin^2 2\theta = 0\right)}. \tag{4.29}$$

We calculate χ^2 as per [286, eq. (11)],

$$\chi^2_{\mathrm{PROSPECT}} = \sum_{l,m=1}^{10} \sum_{i,j=1}^{16} \left(D_{l,i} - P_{l,i} \frac{D_i}{P_i} \right) V^{-1}_{(l,i)(m,j)} \left(D_{m,j} - P_{m,j} \frac{D_j}{P_j} \right), \tag{4.30}$$

where V is the 160×160 covariance matrix provided by the collaboration, which includes both statistical and systematic uncertainties; and we define

$$D_i \equiv \sum_l D_{l,i} \quad \text{and} \quad P_i \equiv \sum_l P_{l,i}\,. \tag{4.31}$$

In fig. 4.5, I compare our exclusion curve with the collaboration's. The curve is calculated using the $\mathrm{CL_s}$ method (see [289]). This method requires creating two additional $\Delta\chi^2$ maps: one labelled H_0 uses the three-flavour prediction as pseudo data and the four-flavour prediction as the prediction, and another labelled H_1, which uses the four-flavour prediction as pseudo data and the three-flavour prediction as the prediction. These are then used in eq. (33) of *ibid.* (see also [286, eq. (17)]) to construct $\mathrm{CL_s}$ and the exclusion curve defined by $\mathrm{CL_s} < 0.05$.

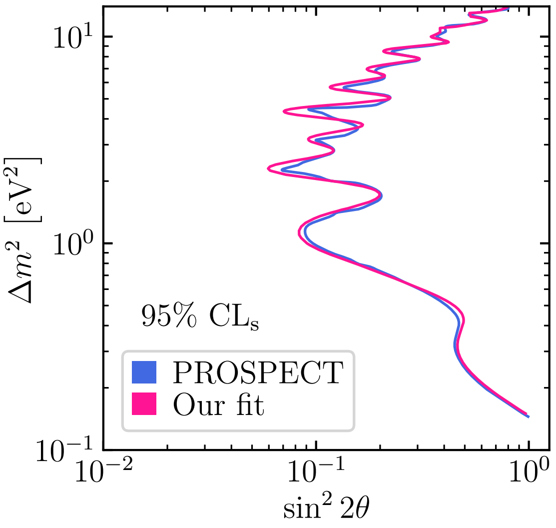

Figure 4.5: A comparison of my exclusion curve (red) with the collaboration's (blue), extracted from [286, fig. 45].

4.1.4 STEREO

The STEREO experiment is an experiment similar to PROSPECT, located at the Institut Laue-Langevin in Grenoble, France. It uses a research reactor with 58 MW of thermal power consisting of highly enriched ^{235}U (93% fission fraction). The detector, located 10 m away, consists of six optically isolated 369 mm × 892 mm × 918 mm cells filled with Gd-doped liquid scintillator, corresponding to a total volume of roughly 1800 L, and is surrounded by a gamma catcher, to detect gamma rays escaping the fiducial volume (fig. 4.6). We used the data published with [290] (available at [291]), corresponding to 179 reactor-on days, and 235 reactor-off

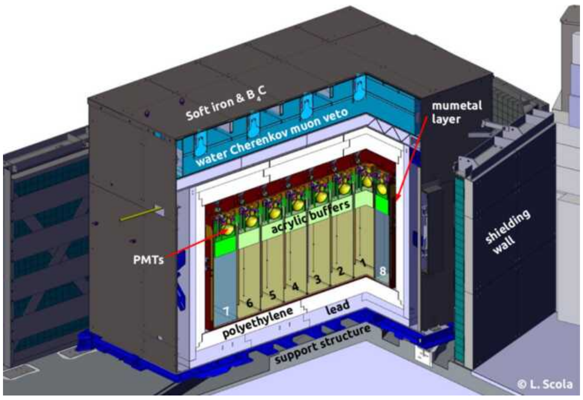

Figure 4.6: A cross section of the STEREO detector, showing the six cells, bookended by gamma catchers; from [290, fig. 2].

days, collected during the years 2016 – 2018. The data is divided into two phases, between which the reactor underwent maintenance: for each cell, phase-I data are reported with ten 0.5-MeV energy bins between prompt energies of 1.625 – 6.625 MeV, while phase-II data are reported with eleven 0.5-MeV bins between 1.625 – 7.125 MeV. The collaboration publishes the event rates normalised to their three-neutrino prediction (after minimisation over their pulls). We follow this procedure to calculate our prediction, using the pull values from [290, fig. 31].

The prediction routine was implemented by Jeffrey Berryman like PROSPECT in `GLoBES`. However, the STEREO analysis uses forty pulls, which needed to be highly optimised for the FCMC analysis; the optimisation of the χ^2 routine was done by myself. For each cell $l \in \{1 \ldots 6\}$, we calculate the effective baseline and oscillation probability in a similar fashion to PROSPECT (described in section 4.1.3), according to the geometry described in [290]. We assume each cell is perfectly isolated and independent from one another, ignoring any possible leakage of light from one cell to another. The detector response matrix $R_{l,\lambda}$ is distinct for each phase $\lambda = \mathrm{I}, \mathrm{II}$ and cell l. We take them be normally distributed with energy resolution extracted from [292, fig. 2.19] for phase I, and from [290, fig. 11] for phase II, parameterised as

$$\frac{\sigma_\lambda(E)}{E} = a_\lambda + \frac{b_\lambda}{E/\mathrm{MeV}}, \quad \text{where} \quad \begin{array}{ll} a_I = 0.031, & b_I = 0.059; \\ a_{II} = 0.043, & b_{II} = 0.050; \end{array} \tag{4.32}$$

and the non-linear detector response $E_p = E_{e^+}\left[1 + f_l^\lambda(E_{e^+})\right]$, extracted from the same references, as

$$f_l^\lambda(E) = c_l^\lambda + d_l^\lambda \frac{E}{\mathrm{MeV}} + e_l^\lambda \left(\frac{E}{\mathrm{MeV}}\right)^2 , \tag{4.33}$$

where the coefficients can be found in table 4.2. The response matrix $R_{ij}^{\lambda,l}$ is built from

	Phase I			Phase II		
l	c_l^I [%]	d_l^I [%]	e_l^I [%]	c_l^{II} [%]	d_l^{II} [%]	e_l^{II} [%]
1	2.2	−0.97	0.092	−0.23	0.25	−0.029
2	1.7	−0.98	0.10	−0.054	0.043	−0.010
3	1.1	−0.69	0.074	−0.11	0.22	−0.027
4	1.65	−0.96	0.01	0.15	−0.076	0.0026
5	2.0	−0.99	0.10	−0.10	0.095	−0.020
6	1.2	−0.70	0.070	0.35	−0.38	0.022

Table 4.2: STEREO non-linearity coefficients (eq. (4.33) for each cell l, as obtained from a quadratic fit to the points shown in ref. [292, fig. 2.19] for phase I, and from ref. [290, fig. 10] for phase II.

the normal distribution, using the energy resolution and non-linear response functions, where i labels the energy bin (integrated over prompt energy), and j labels true neutrino energy, binned in 70 intervals between 1.85 – 7.95 MeV.

The predicted event rate is proportional to

$$\mathrm{Pred}_{l,i}^\lambda\left(\sin^2 2\theta, \Delta m^2\right) = \sum_j R_{ij}^{\lambda,l} \int_{E_\nu^j}^{E_\nu^{j+1}} \mathrm{d}E_\nu \, \sigma(E_\nu) \frac{\mathrm{d}\Phi_{^{235}\mathrm{U}}}{\mathrm{d}E_\nu} P_{ee}^l \left(\sin^2 2\theta, \frac{\Delta m^2}{4E_\nu}\right) . \tag{4.34}$$

As already mentioned, the collaboration normalised their rates with their three-neutrino prediction, minimised over the pulls. Two types of pulls are introduced for each baseline and phase: one for energy-scale uncertainty η_l^λ, and another for normalisation uncertainty ζ_l^λ. In addition to these two, a cell-correlated pull ξ^λ for energy-scale uncertainty is also introduced. The implementation of the energy-scale uncertainty is discussed in appendix A.3.6. Our prediction, then, is

$$P_{l,i}^\lambda = \frac{\left(1+\zeta_l^\lambda\right) \mathrm{Pred}_{l,i}^\lambda \left[\eta_l^\lambda + \xi^\lambda\right]}{\left(1+\widetilde{\zeta}_l^\lambda\right) \mathrm{Pred}_{l,i}^\lambda \left(\sin^2 2\theta = 0\right) \left[\widetilde{\eta}_l^\lambda + \widetilde{\xi}_l^\lambda\right]}, \tag{4.35}$$

where $\widetilde{\eta}_l^\lambda, \widetilde{\xi}_l^\lambda, \widetilde{\zeta}_l^\lambda$ are provided in [290, fig. 31]. , The χ^2 function for STEREO is computed by adding the contributions from the two phases. Following [290, eqs. (15, 19)], we introduce a set of free flux normalisations for each energy bin, ϕ_i, common to the two phases (eleven in total), as well as a relative normalisation uncertainty for the first phase, Φ^{I}, common to all bins, to account for a possible difference in reactor power, or baseline difference, after the reactor maintenance. Therefore, we have

$$\begin{aligned} \chi^2_{\mathrm{STEREO}} = \min_{\substack{\eta_l^{\mathrm{I,II}},\, \xi^{\mathrm{I,II}},\\ \zeta_l^{\mathrm{I,II}},\, \phi_i,\, \Phi^{\mathrm{I}}}} \Bigg\{ & \sum_{l=1}^{N_{\mathrm{cells}}} \sum_{i=1}^{N_{\mathrm{Ebins}}^{\mathrm{I}}} \left(\frac{D_{l,i}^{\mathrm{I}} - \Phi^{\mathrm{I}} \phi_i P_{l,i}^{\mathrm{I}}(\eta_l^{\mathrm{I}} + \xi^{\mathrm{I}}, \zeta_l^{\mathrm{I}})}{\sigma_{l,i}^{\mathrm{I}}} \right)^2 \\ & + \sum_{l=1}^{N_{\mathrm{cells}}} \sum_{i=1}^{N_{\mathrm{Ebins}}^{\mathrm{II}}} \left(\frac{D_{l,i}^{\mathrm{II}} - \phi_i P_{l,i}^{\mathrm{II}}(\eta_l^{\mathrm{II}} + \xi^{\mathrm{II}}, \zeta_l^{\mathrm{II}})}{\sigma_{l,i}^{\mathrm{II}}} \right)^2 \\ & + \sum_{\substack{l=1\\ \lambda=\mathrm{I,II}}}^{N_{\mathrm{cells}}} \left[\left(\frac{\eta_l^\lambda}{\sigma_\eta^\lambda} \right)^2 + \left(\frac{\zeta_l^\lambda}{\sigma_\zeta^\lambda} \right)^2 \right] + \sum_{\lambda=\mathrm{I,II}} \left(\frac{\xi^\lambda}{\sigma_\xi^\lambda} \right)^2 \Bigg\}, \end{aligned} \tag{4.36}$$

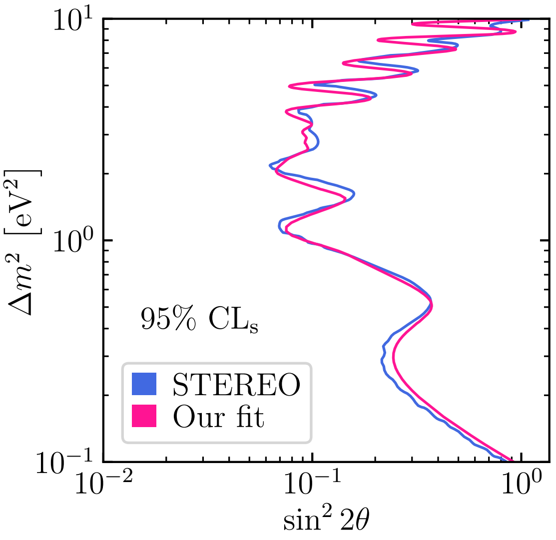

Figure 4.7: Our CL$_\mathrm{s}$ exclusion curve (red) vs the collaboration's (blue), from [290].

where $D_{l,i}^\lambda$ is the data, and $\sigma_{l,i}^\lambda$ its statistical errors, obtained from [291]; and the systematic errors for the pulls are:

$$\begin{aligned} \sigma_\eta^{\mathrm{I}} &= 1.06\%, & \sigma_\eta^{\mathrm{II}} &= 1.02\%, \\ \sigma_\xi^{\mathrm{I}} &= 0.35\%, & \sigma_\xi^{\mathrm{II}} &= 0.30\%, \\ \sigma_\zeta^{\mathrm{I}} &= 1.18\%, & \sigma_\zeta^{\mathrm{II}} &= 1.18\%. \end{aligned} \tag{4.37}$$

(Note that the first phase only has ten bins, so ϕ_{11} only enters the second-phase sum.) In order to optimise the minimisation procedure, we make the following transformations,

$$\begin{aligned} \alpha_l^\lambda &= \eta_l^\lambda + \xi^\lambda, \\ \Phi^I \left(1 + \zeta_l^I\right) &= 1 + \beta_l^I, \end{aligned} \tag{4.38}$$

and for consistency $\beta_l^{\mathrm{II}} = \zeta_l^{\mathrm{II}}$. This isolates the dependence of ξ^λ, Φ^I in the quadratic pull terms, which we can analytically minimise. We numerically minimise the remaining pulls with a non-linear conjugate-gradient algorithm [293]. The details of the minimisation procedure is covered in appendix A.3. In fig. 4.8 I compare the $\Delta\chi^2$ contours of our fit and the collaboration, and in fig. 4.7, I compare our 95% $\mathrm{CL_s}$ exclusion curve with the collaboration's.

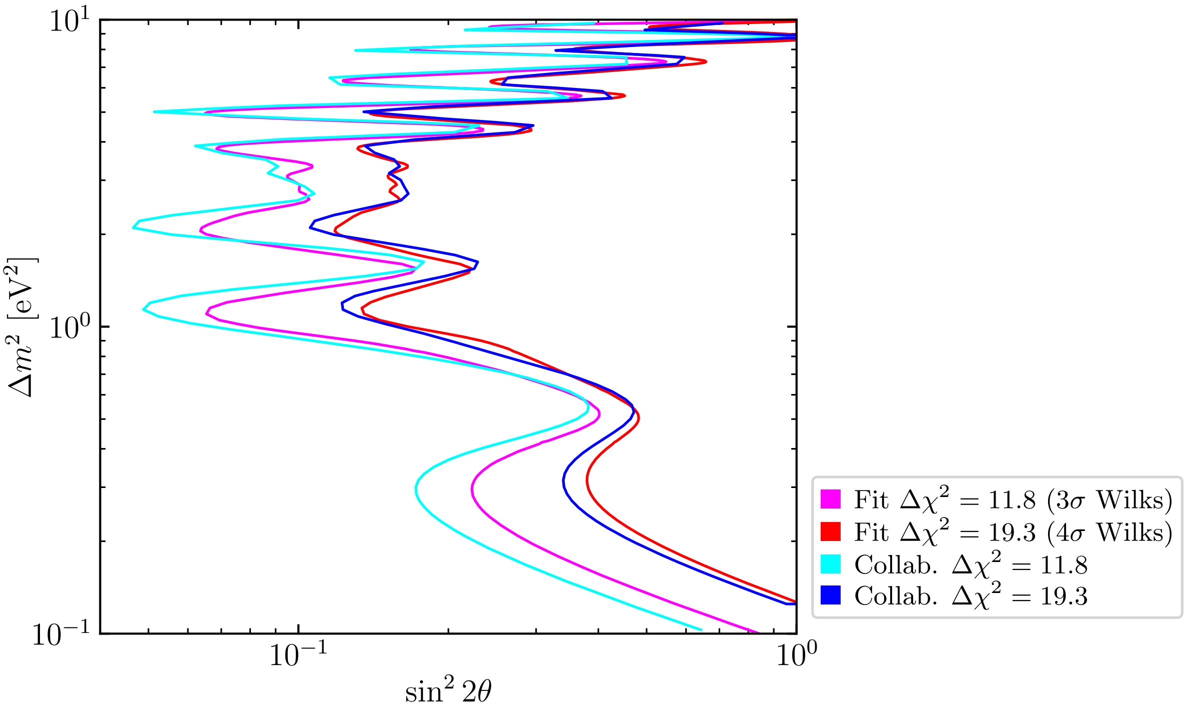

Figure 4.8: I compare our fit's $\Delta\chi^2 = 11.8, 19.3$ curves (corresponding to 3 and $4\,\sigma$ significance under Wilks' theorem with two degrees of freedom) with the collaboration's, from their χ^2 map provided by [291].

4.1.5 Neutrino-4

The Neutrino-4 experiment is conducted at Dimitrovgrad, Russia, using a highly compact research reactor with 90 MW of thermal power, consisting of highly enriched ^{235}U, and a 1.8 m^3 detector, consisting of 5×10 225 mm × 225 mm × 850 mm segments, filled to a height of 70 cm with liquid scintillator with 0.1% gadolinium [294]. The first and last rows of the ten rows (each containing five segments) are used as veto, with the resulting fiducial volume being 1.42 m^3. The detector is mounted on a movable platform, which allows the baseline to be adjusted between $6-12$ m. The experiment collected data with the reactor on for 720 days between June 2016 to July 2019, after which the reactor was turned off and the background was measured. We use the data presented in fig. 47 of the second version of the arXiv preprint of [275] with 417 days of the reactor off, however the published version of the article uses reactor-off data until October 2020, corresponding to 860 days. The reason for the discrepancy is due to a long review process, due to criticism of not only their statistical method (as already mentioned) but also concerns due to background (lack of pulse-shape discrimination) and their treatment of energy resolution [295, §4] (see also [296]), as well as concerns regarding the finite-size of the detector (baseline smearing) and escaping gamma photons due to the small size of the detector [297, 298]. Our Neutrino-4 analysis is based on the previous work done by co-authors Pilar Coloma, Patrick Huber and Thomas Schwetz [274], which was finished before the publication of the finalised Neutrino-4 results, which is why we follow the older version of the Neutrino-4 analysis, albeit accounting for the various criticisms.

Neutrino-4 bins their data into nine 0.5-MeV energy bins and twenty-four 0.235-m baseline bins from 6.25 − 11.89 m. The resulting 24×9 bins in L/E are used to form the ratios, following [275, eq. (2)],

$$R_{ik}^{\mathrm{obs}} = \frac{N_{ik} L_k^2}{\sum_{k=1}^{24} N_{ik} L_k^2 / 24} \qquad \text{and} \qquad R_{ik}^{\mathrm{pred}} = \frac{\left\langle \frac{\mathrm{d}\Phi_{^{235}\mathrm{U}}}{\mathrm{d}E_\nu} P_{ee}(L_k/E_\nu) \right\rangle_i}{\sum_{k=1}^{24} \left\langle \frac{\mathrm{d}\Phi_{^{235}\mathrm{U}}}{\mathrm{d}E_\nu} P_{ee}(L_k/E_\nu) \right\rangle_i \Big/ 24}, \tag{4.39}$$

where N_{ik} denotes the observed number of events in energy bin i and baseline bin k; and where R_{ik}^{pred} denotes the prediction, with implicit dependence of the survival probability P_{ee} on Δm^2 and $\sin^2 2\theta$, and where the average $\langle\,\cdot\,\rangle_i$ is over the energy bin $[E_{i-1}, E_i)$. Note that the prediction does not include any response matrix, which is one of the criticisms of the collaboration's analysis. Following the collaboration, we make the assumption that the energy dependence of the flux can be neglected in the average $\langle\,\cdot\,\rangle_i$, whence the flux $\mathrm{d}\Phi_{^{235}\mathrm{U}}/\mathrm{d}E_\nu$ cancels in the ratio. Our prediction is therefore

$$\mathrm{Pred}_{ik} = \frac{1 - \sin^2\theta \left\langle \sin^2 \frac{\Delta m^2 L_k}{4E_\nu} \right\rangle_i}{1 - \sum_{i=1}^{24} \sin^2\theta \left\langle \sin^2 \frac{\Delta m^2 L_k}{4E_\nu} \right\rangle_i \Big/ 24}, \qquad \text{where} \tag{4.40}$$

$$\left\langle \sin^2 \frac{\Delta m^2 L_k}{4E_\nu} \right\rangle_i = \int_{-\Delta E/2}^{+\Delta E/2} \sin^2 \left[\frac{\Delta m^2 L_k}{4\left(E_i + \delta E_\nu\right)} \right] \frac{\mathrm{d}\left(\delta E_\nu\right)}{\Delta E}. \tag{4.41}$$

This is only an approximation, as a realistic detector response matrix is not available, which would involve a normally distributed energy response with an energy resolution that depends on the true neutrino energy. Furthermore, we approximate the baseline smearing by increasing ΔE to the effective value

$$\Delta E_{\mathrm{eff}} = E\sqrt{(\Delta L/L)^2 + (\Delta E/E)^2}, \tag{4.42}$$

where $\Delta E = 0.5\,\mathrm{MeV}$ and $\Delta L = 0.48\,\mathrm{m}$.

The integral in eq. (4.41) can be transformed via integration by parts to

$$\left\langle \sin^2 \frac{\Delta m^2 L_k}{4E_\nu} \right\rangle_i = E_i^+ \sin^2 \omega_i^+ - E_i^- \sin^2 \omega_i^- - \frac{\Delta m^2 L_k}{4} \left[\mathrm{Si}\left(\omega_i^+\right) - \mathrm{Si}\left(\omega_i^-\right) \right], \tag{4.43}$$

where $E_i^\pm = E_i \pm \Delta E/2$ and $\omega_i^\pm = \Delta m^2 L_k / (4E_i^\pm)$. The values of L_k/E_i are then arranged in increasing order, $L_{k_1}/E_{i_1} < L_{k_2}/E_{i_2} < \cdots < L_{k_{216}}/E_{i_{216}}$, and then the data and prediction are then averaged over groups of consecutive eight bins, leading to a total of 27 data points,

$$D_j = \sum_{n=8j-7}^{8j} \frac{R_{i_n k_n}^{\mathrm{obs}}}{8} \qquad \text{and} \qquad P_j = \sum_{n=8j-7}^{8j} \frac{\mathrm{Pred}_{i_n k_n}}{8}, \tag{4.44}$$

although in our analysis we only use the 19 blue-triangle data points in fig. 47 of the version-two arXiv preprint. The χ^2 function is then

$$\chi^2_{\text{Neutrino-4}} = \sum_{j=1}^{19} \left(\frac{D_j - P_j}{\sigma_j} \right)^2 , \tag{4.45}$$

where the statistical uncertainties are extracted from the same fig. 47 of *ibid.* A comparison of our results with the collaboration is shown in fig. 4.9.

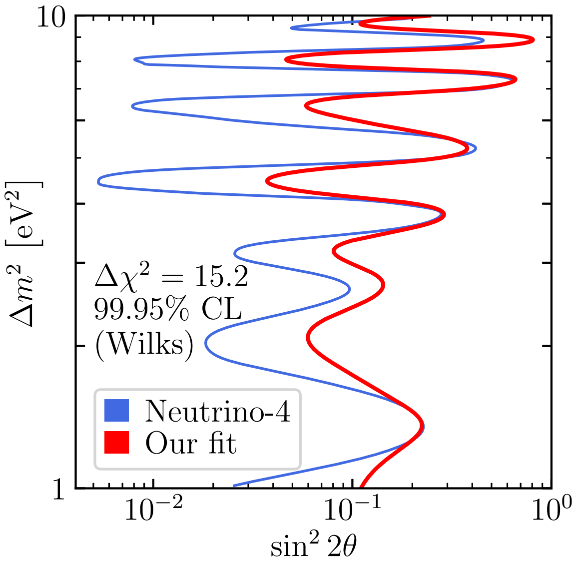

Figure 4.9: The $\Delta\chi^2 = 15.2$ contour of our fit (red) compared with the collaboration's (blue), extracted from fig. 45 from the version-two arXiv preprint of [275].

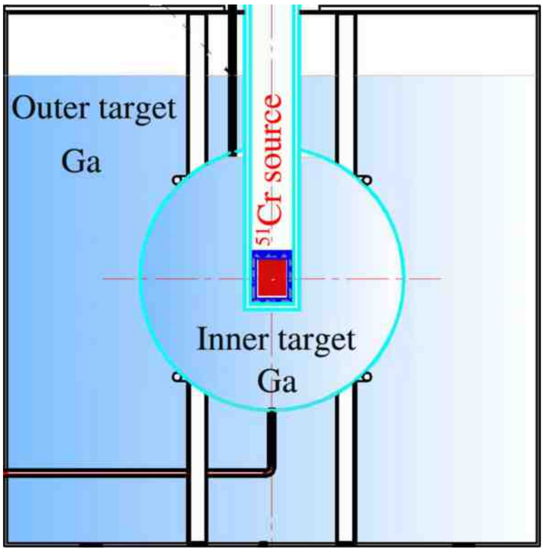

Figure 4.10: Two-zone gallium vessel of BEST with the chromium-51 source at the centre, taken from [201].

4.2 Gallium and Solar Data

In this section, I will overview the analysis of data from the gallium experiments and solar-neutrino observations. The χ^2 routines were initially implemented by my supervisor, Thomas Schwetz, which I then optimised using modern C^{++} features.

4.2.1 Gallium data

As already mentioned in section 2.7, calibration measurements for the solar-neutrino experiments GALLEX and SAGE using ^{51}Cr (and one measurement by SAGE using ^{37}Ar) found a deficit compared to the theoretical prediction (using the Bahcall cross section) [196–198, 299], which had a combined significance of $3\,\sigma$ [200].

The BEST experiment recently confirmed this anomaly at very high $> 5\,\sigma$ significance [201]. The experiment uses an artificial, highly intense, 3.4-MCi ^{51}Cr neutrino source, manufactured by exposing ^{50}Cr to thermal neutrons from a reactor, whose heat output is precisely measured [300, 301]. The calorimetric measurement of heat is converted to neutrino activity, by using the nuclear tables, containing the decay channels and branching ratios [302]. The source was chosen due to its simple electron-capture decay scheme, allowing for a simple conversion between thermal power and neutrino activity (unlike reactor sources, whose set of possible decays is enormous). The source was then placed in a cylindrical vessel, shielded with 3-cm-thick tungsten alloy, which is located in a two-zone vessel containing liquid gallium. The vessel contains an inner spherical volume with 7.5 t of Ga, and an outer cylindrical volume with 40 t of Ga (fig. 4.10). Exposure to the neutrino source began in July, 2019, and after nine-day intervals, the ^{71}Ge, produced from charged-current neutrino scattering, was extracted, purified and its radioactivity measured. At the beginning of each exposure period, $\approx 250\,\mu$g of Ge carrier was artificially added to the gallium volume, which ensured the validity of the extraction procedure.

Following [201], the rate of germanium production can be written as

$$r = n\sigma A \iiint_V \frac{\sum_i f_i P_{ee}\left(\sin^2 2\theta, \frac{\Delta m^2 |\vec{r}|}{4E_i}\right)}{4\pi|\vec{r}|^2} \mathrm{d}\vec{r}, \tag{4.46}$$

where n is the gallium number density, σ is the neutrino cross-section on gallium, A is the source activity, $\iiint_V$ is an integral over the detector volume, i denotes the neutrino line with branching ratio f_i, and E_i is the energy of the emitted neutrino. The analysis is done in terms of the capture rate, normalised to the no-oscillation prediction,

$$D = \frac{r^{\mathrm{obs}}}{r\left(\sin^2 2\theta = 0\right)} \qquad \text{and} \qquad P = \frac{r\left(\sin^2 2\theta\right)}{r\left(\sin^2 2\theta = 0\right)}. \tag{4.47}$$

Note that the denominator in both ratios are predictions, so the analysis is not flux free, unlike in the reactor experiments. There are multiple calculations for the cross section, and the ratios D obtained from the collaborations are reported using the 1997 Bahcall calculation [303], however we also considered more recent calculations by Kostensalo *et al.* [304] and Semenov [305], which requires the ratios for each experiment D to be rescaled. In tables 4.3 and 4.4, I reproduce the table of D and cross sections from our paper [272].[3]

GALLEX [299]	GALLEX [299]	SAGE [197]	SAGE [197]	BEST [201] (inner)	BEST [201] (outer)
0.953 ± 0.11	0.812 ± 0.10	0.95 ± 0.12	0.791 ± 0.084	0.791 ± 0.044	0.766 ± 0.045

Table 4.3: The ratios of the observed-to-expected production rates for the gallium experiments. The quoted $1\,\sigma$ errors include statistical and uncorrelated experimental errors. The SAGE measurement [198] in the fourth column uses an ^{37}Ar source; all other measurements are from a ^{51}Cr source. The ratios are based on the Bahcall cross section [303].

The neutrino branches for the source can be found in [306]. (Note how we have implicitly made the approximation of using the same effective cross section for each branch in eq. (4.46), which is justified as the cross section between branches is very similar.) The detector geometry for GALLEX can be found in [307], which we model as a cylinder

---

[3] Note that there is a technical inconsistency in the quoted ground-state cross section for Kostensalo *et al.* ; see our paper [272] for details.

Reference	σ(Cr)	$\sigma_{\text{g.s.}}$(Cr)	σ(Ar)	$\sigma_{\text{g.s.}}$(Ar)
Bahcall [303]	58.1 ± 2.1	55.2	70.0 ± 4.9	66.2
Kostensalo *et al.* [304]	56.7 ± 1.0	55.3 ± 0.7	68.0 ± 1.2	66.2 ± 0.9
Semenov [305]	59.38 ± 1.16	55.39 ± 0.19	71.69 ± 1.47	66.25 ± 0.23

Table 4.4: Cross section for ν_e scattering on gallium, weighted by the branching ratios for the neutrino branches of the source, chromium-51 or argon-37, for three cross-section models. Units are 10^{-46}cm^2. The ground-state contribution is also displayed.

of height 5 m and radius 1.9 m, with the source located at a height of 2.7 m; note the second GALLEX experiment located their source 32 cm lower [196]. The SAGE detector geometry is taken to be a cylinder of radius 0.7 m and height 1.47 m, with the source located at height 0.72 m [306]. For both SAGE and GALLEX the source size (regulating the integral for small $|\vec{r}|$) is taken to be 1 cm (specifically, we set the minimum radius in cylindrical coordinates to be 1 cm). For BEST, the geometry is taken from [201], the inner vessel being a sphere of radius 66.75 cm and the outer vessel being a cylinder of height 2.345 m and radius 1.09 m, with the source at the centre, having a radius of 4.3 cm.[4]

We define the χ^2 function as $\chi^2_{\text{gall}} =$

$$\min_{\xi}\left\{\sum_{j=1}^{6}\frac{[D_j - f(\xi)P_j]^2}{\sigma_j^2} + \xi^2\right\}, \quad (4.48)$$

where the sum j runs over the experimental ratios of table 4.3, from which the uncertainties σ_j are taken with relevant rescaling. The systematic ξ is associated with the uncertainty in the cross section, which is fully correlated across experiments. The function $f(\xi)$ is defined to take into account that the ground-state contribution of the cross-section is known more precisely than the total cross-section, and the exited-state contribution can only increase the cross section, so that when $f(\xi)\sigma < \sigma_{\text{g.s.}}$, we use the ground-state cross section's uncertainty,

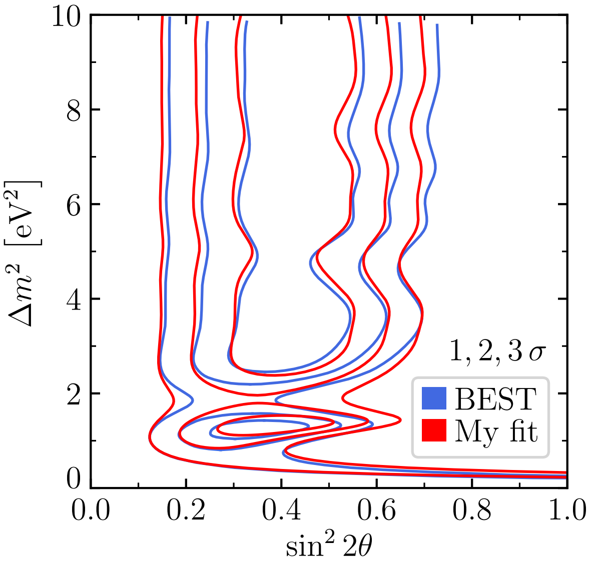

Figure 4.11: The 1, 2, 3 σ (Wilks 2 dof) contours of our fit (red) compared with (blue), extracted from fig. 3 of [201].

$$f(\xi) = \begin{cases} 1 + \varepsilon\xi & \text{if } \xi \geq \xi^* \\ \sigma_{\text{g.s.}}/\sigma + \varepsilon_{\text{g.s.}}(\xi - \xi^*) & \text{otherwise} \end{cases}, \quad \text{where} \quad (1 + \varepsilon\xi^*)\,\sigma = \sigma_{\text{g.s.}}, \quad (4.49)$$

$\varepsilon \equiv \Delta\sigma/\sigma$, $\varepsilon_{\text{g.s.}} \equiv \Delta\sigma_{\text{g.s.}}/\sigma$, and $\Delta\sigma$ and $\Delta\sigma_{\text{g.s.}}$ are the error of the total cross section σ and ground-state contribution $\sigma_{\text{g.s.}}$, respectively, given in table 4.4. Note that both ε and $\varepsilon_{\text{g.s.}}$ are defined relative to the *total* cross section. In fig. 4.11 I compare our results with the collaboration's.

---

[4] Note that the integral for the outer vessel excludes the inner vessel.

4.2.2 Solar data

The solar χ^2 is based on a simplified analysis of solar data that my supervisor constructed in collaboration with Michele Maltoni [308]. The idea is that the solar data (see fig. 3.8) are clustered in the low-energy ($\lesssim 1\,\text{MeV}$) and high-energy ($\gtrsim 7\,\text{MeV}$) regions, where the effective survival probability is approximately constant in energy. Therefore, the analysis is done in terms of the effective probabilities

$$\left(P_{ee}^{\text{LE}}, P_{ee}^{\text{HE}}, \ P_{ex}^{\text{LE}}, \ P_{ex}^{\text{HE}}\right), \tag{4.50}$$

where $P_{ex} = P_{e\mu} + P_{e\tau}$, and

$$\begin{aligned} P^{\text{LE}} &\equiv P\left(E_\nu \to 0\right), \\ P^{\text{HE}} &\equiv P\left(E_\nu \to \infty\right). \end{aligned} \tag{4.51}$$

Assuming that the neutrino states arrive incoherently, so that all phase information is lost, the prediction is defined as

$$P_{e\alpha} = \sum_{k=1}^{4} |U_{ek}^{m}|^2 |U_{\alpha k}|^2, \qquad \text{where} \qquad U = \begin{pmatrix} c_{14} & 0 & 0 & -s_{14} \\ 0 & 0 & 0 & 0 \\ 0 & 0 & 0 & 0 \\ s_{14} & 0 & 0 & c_{14} \end{pmatrix} U_{\text{PMNS}}^{3\nu}, \tag{4.52}$$

and $U_{\text{PMNS}}^{3\nu}$ is the SM three-flavour mixing matrix but with an extra row and column of zeroes appended. We have made the approximation that $\theta_{24} = \theta_{34} = 0$, and we define

$$s_{12}^{\text{m}} = s_{12} \ \text{(low energy)} \qquad \text{and} \qquad s_{12}^{\text{m}} = 1 \ \text{(high energy)}, \tag{4.53}$$

to take into account the energy-dependent nature of the MSW resonance. In the analysis, we fix s_{13} to the global best-fit value. See [308] for more details.

The observed values D_j of the effective probabilities, their uncertainties and correlation matrix are reproduced in table 4.5 from [308], which are tuned to reproduce the full global solar-neutrino fit. The correlation matrix includes both experimental and theoretical systematics from the solar model; we use the GS98 solar model, which is less constraining then the AGSS09 model [309].

	D_j	σ_j	correlation matrix			
P_{ee}^{LE}	0.5585	0.0440	+1.000	+0.104	−0.635	+0.475
P_{ee}^{HE}	0.3444	0.0397	+0.104	+1.000	+0.296	+0.498
P_{ex}^{LE}	0.6512	0.2233	−0.635	+0.296	+1.000	−0.274
P_{ex}^{HE}	0.7526	0.1116	+0.475	+0.498	−0.274	+1.000

Table 4.5: Effective solar-data values for the observations D_j, their 1σ uncertainty σ_j, and their correlation matrix ρ, corresponding to the GS98 solar model [309].

The χ^2 function is defined as

$$\chi^2\left(s_{12}^2, s_{14}^2\right) = \sum_{i,j=1}^{4} (D_i - P_i) V_{ij}^{-1} (D_j - P_j), \tag{4.54}$$

where the sum is over the four probabilities in eq. (4.50) and

$$V_{ij}^{-1} = \frac{S_{ij}^{-1}}{2}\left[\frac{1}{D_i}\frac{1}{D_j} + \frac{1}{P_i}\frac{1}{P_j}\right], \quad \text{where} \quad S_{ij} = \rho_{ij}\frac{\sigma_i}{D_i}\frac{\sigma_j}{D_j} \quad \text{(no sum over indices)} \tag{4.55}$$

and S^{-1} is the matrix inverse of S.

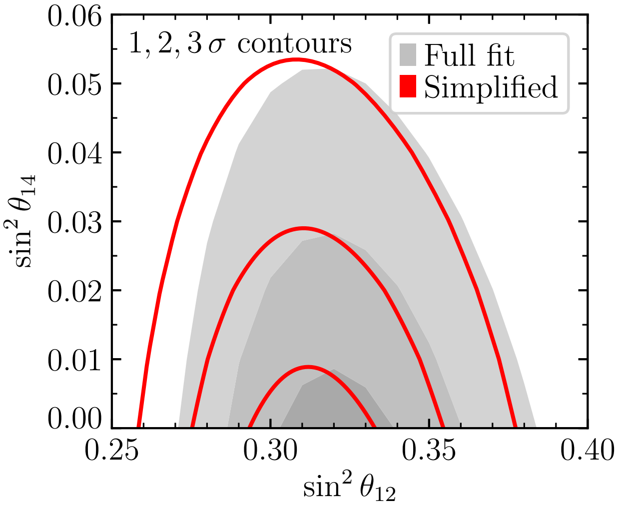

Figure 4.12: A comparison of our four-point solar fit with the full solar fit.

This definition is in fact merely an approximation of the correct covariance matrix $V_{ij} = S_{ij}/2 \cdot (D_i D_j + P_i P_j)$, whose full inverse depends on the oscillation parameters, which is computationally expensive. A Δm^2-independent constraint on s_{14}^2 can be obtained by using

$$\chi^2_{\text{solar}} = \min_{s_{12}^2} \chi^2(s_{12}^2, s_{14}^2). \tag{4.56}$$

A comparison of our simplified four-point fit with the full solar fit is shown in fig. 4.12. Note that in this subsection, we have used the parameter s_{14}^2 instead of $\sin^2 2\theta_{14}$, which is what we used for the other terrestrial experiments and for the next sections. As can be seen from fig. 4.12, the best-fit value of s_{12}^2 does not change significantly as a function of s_{14}^2, so we fix $s_{12}^2 = 0.3125$ in the global FCMC analysis. I checked that this does not change the FCMC bounds on s_{14}^2 for the solar analysis.

4.3 Feldman-Cousins Analysis

As already mentioned, Wilks' theorem breaks down when searching for new neutrino oscillations, which prompted Feldman and Cousins to develop a more rigorous statistical approach [276]. The reasons given by Feldman and Cousins for the breakdown are:

1. the bounded nature of the physical region for $\sin^2 2\theta \in [0, 1]$; considering χ^2 values outside this region, it is possible for a minimum to occur outside the interval $[0, 1]$, which violates the assumptions of Wilks' theorem;

2. the oscillatory nature of the χ^2 contours, which can cause a global minimum to occur in a local island, which does not contain the true oscillation parameters;

3. non-constant degrees of freedom: for some regions in parameter space, the degrees of freedom become one, *e.g.* $\sin^2 2\theta = 0$, or for large Δm^2, when oscillations average out and χ^2 is only sensitive on the mixing $\sin^2 2\theta$.

Therefore, for each point in parameter space, we calculate the statistical distribution of $\Delta\chi^2\,(\sin^2 2\theta, \Delta m^2)$ via Monte Carlo simulations. The procedure for this, roughly, is to use the prediction as the mean for the statistical distribution of the binned data, and to inject statistical fluctuations on top of the mean using the relevant distribution provided by the collaboration: the covariance matrix and relevant pulls. Using this *pseudo data*, we then calculate the quantity

$$\Delta\chi^2\left(\sin^2 2\theta, \Delta m^2\right) = \chi^2\left(\sin^2 2\theta, \Delta m^2\right) - \chi^2_{\text{min}}. \tag{4.57}$$

We then repeat this process with pseudo data with new fluctuations for a large number of iterations, until a large dataset of $\Delta\chi^2$ values is obtained, whose histogram gives an estimate for its true statistical distribution.

4.3.1 Pseudo-data generation

For the pulls with a given uncertainty, we generate normally distributed fluctuations with the given uncertainty on top of the mean value as reported by the collaboration. For the free flux normalisations, we set them to the values that provide the best fit to the real data. (In this scheme we are treating the two systematics differently, as the free normalisations are introduced merely to make our analysis independent on absolute normalisation; whereas setting the constrained pulls to their best-fit value would yield a biased χ^2, which would not reproduce Wilks' theorem for non-pathological cases). For a discussion on these assumptions, see appendix B.1,3 of our paper [272]. The procedure I used to generate pseudo is (reproduced from our paper):

(i) choose the parameters Δm^2, $\sin^2 2\theta$ for the hypothesis of new oscillations;

(ii) calculate the free flux normalisations $\{\eta^{\text{min}}\}$, which provide the best fit to the observed data for the assumed hypothesis;

(iii) generate fluctuations for the pulls,

$$\xi_k^{\text{pseudo}} = \overline{\xi}_k + \sigma_{\xi_k}\delta_k\,, \tag{4.58}$$

where δ_k are standard-normal fluctuations and $\overline{\xi}_k$ is the mean value provided by the collaboration;

(iv) compute the prediction for the assumed hypothesis, applying the fluctuated nuisance parameters and calculated flux normalisations, and set this as the mean for the generation of pseudo data,

$$\overline{D}_i^{\text{pseudo}} = P_i\left(\Delta m^2, \sin^2 2\theta; \{\xi^{\text{pseudo}}\}, \{\eta^{\text{min}}\}\right)\,; \tag{4.59}$$

(v) if the χ^2 function contains a covariance matrix V, first recalculate it (if necessary) by replacing all data with $\overline{D}_i^{\text{pseudo}}$ in V;

(vi) calculate the Cholesky decomposition L of V^{pseudo} (note if χ^2 does not contain a covariance matrix, then L is diagonal with the standard deviations of each bin as the diagonal entries);

(vii) inject fluctuations around the pseudo-data mean with L, *i.e.,*

$$D_i^{\text{pseudo}} = \overline{D}_i^{\text{pseudo}} + \sum_j L_{ij}\delta_j, \tag{4.60}$$

where δ_j are standard-normal fluctuations.

Remarks on individual experiments For DANSS, we generate the pseudo data not at the level of ratios, but at the level of the absolute rates for each baseline. However, the predicted ratios are used to set the pseudo-data mean,

$$\left\langle n_T^i \right\rangle = n_T^{i,\mathrm{obs}}, \quad \left\langle n_M^i \right\rangle = n_T^{i,\mathrm{obs}} P_2^i \sqrt{P_1^i}, \quad \left\langle n_B^i \right\rangle = n_T^{i,\mathrm{obs}} P_1^i, \tag{4.61}$$

where $P_{1,2}^i$ are given in eq. (4.6). The statistical fluctuations are then normally distributed with standard deviation $\sigma_\lambda^i = \sqrt{\langle n_\lambda^i \rangle / \Delta t_\lambda}$.

For NEOS, I merely remark that the pseudo data replaces D_i in V^{stat} in eq. (4.19). For STEREO, since the uncertainties of some bins are large, this introduces occasional negative values after statistical fluctuations. If this occurs for a dataset per phase, I throw away the dataset for that phase and redraw fluctuations. Negative values only occur for the last or penultimate bin, for which $D_{l,i}^\lambda / \sigma_{l,i}^\lambda \sim 2.2$. For the solar analysis, I merely remark that in the case of generation of pseudo data, we use the covariance matrix $V_{ij} = \rho_{ij}\sigma_i\sigma_j$, which is based on its original definition, given below eq. (4.55).

In fig. 4.13, I compare our Feldman-Cousins exclusion curves with the curves provided by PROSPECT and STEREO. Possible reasons for some of the deviations in the case of STEREO are given in appendix A.4 of our paper [272]. Furthermore, sometimes my grid spacing does not resolve the peaks in the exclusion curve for STEREO. In fig. 4.14, I compare the distribution of my best-fit points with the collaboration for STEREO.

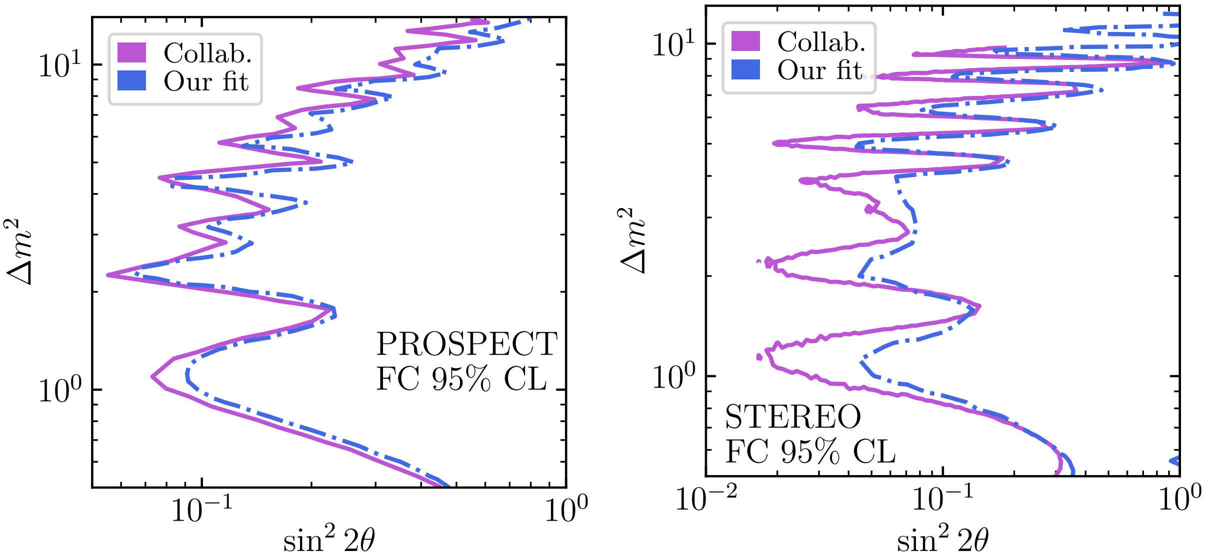

Figure 4.13: Comparison of our 95% FC curve for PROSPECT (left) and STEREO (right) to the collaboration [286,291], evaluated with 10^4 pseudo experiments; from [272].

4.3.2 Minimisation algorithm

An important part of the FCMC analysis is computational speed. After optimising the χ^2 routines for each experiment (for which the tools `perf` and `valgrind` are very useful), and using useful compilation flags such as `-O3 -ffast-math -funroll-loops`

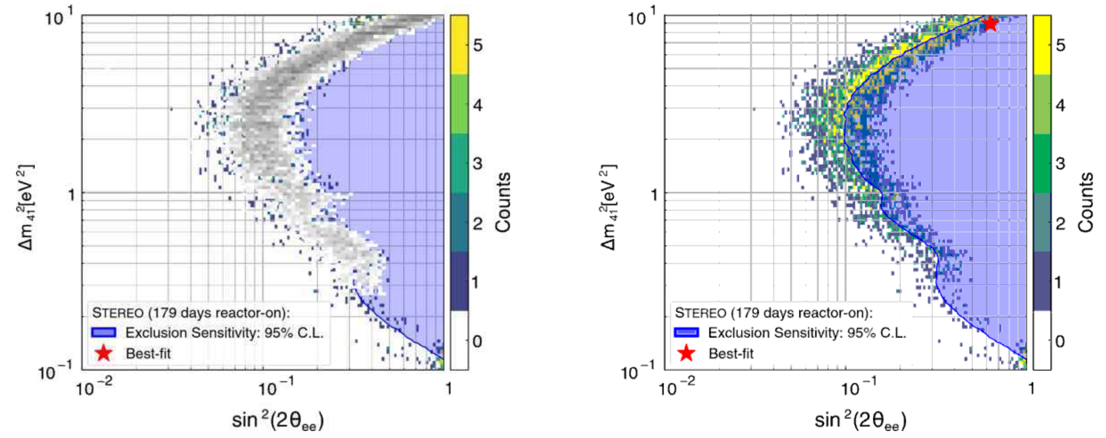

Figure 4.14: My fit's distribution of null-hypothesis best-fit points overlaid ($2 \cdot 10^4$ runs) on the collaboration's (left) and the collaboration's distribution ($5 \cdot 10^3$ runs) (right).

`-march=cascadelake`[5] as well as multithreading, I tuned the algorithm to find the minimum for a given pseudo dataset, which is a leading factor determining computing time.

The first part of the strategy to find the minimum was to exploit the fact that χ^2 profiles for fixed Δm^2 (as a function of $\sin^2 2\theta$) have a parabolic shape and a unique minimum. The algorithm to minimise $\chi^2(\sin^2 2\theta)$ for a fixed Δm^2 was to use repeated parabolic interpolation, with occasional bisections, and is detailed in appendix A.4.

The second part of the minimisation algorithm was to take into consideration the oscillatory nature of the χ^2 profile once minimised over $\sin^2 2\theta$, *i.e.*

$$\min_{\sin^2 2\theta}[\chi^2(\sin^2 2\theta, \Delta m^2)].$$

An example profile is shown in fig. 4.15, which shows the existence of multiple parabolic-like minima. We also see noise-like features, which are probably numerical artefacts due to the imperfect pull-minimisation procedure for STEREO. The profile is flat for $\Delta m^2 > 10\,\mathrm{eV}^2$.

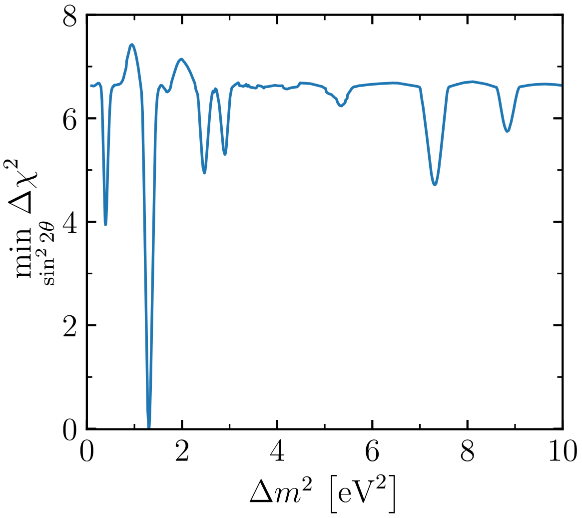

Figure 4.15: Plot of $\Delta\chi^2$ profile, minimised over $\sin^2 2\theta$, as a function of Δm^2. The χ^2 function used is the sum of reactor experiments and the solar analysis (I do not include gallium for this plot).

Recall that the Δm^2 dependence of the prediction, and therefore the χ^2 function, is discretised on a grid. This grid is made to be very fine, with intervals of $10^{-3}\,\mathrm{eV}^2$ for $\Delta m^2 \in [0.1, 1)\,\mathrm{eV}^2$, $10^{-2}\,\mathrm{eV}^2$ for $\Delta m^2 \in [1, 10)\,\mathrm{eV}^2$, and $0.1\,\mathrm{eV}^2$ for $\Delta m^2 \in [10, 30]\,\mathrm{eV}^2$; the result is a total of 2000 grid points. In order to optimise minimisation, I do not

---

[5] The last of these options is specific to the computing cluster I worked on, whose CPU architecture was Intel Cascadelake. This architecture had in-built vector operations, which allowed for multiple scalar operations to be executed in a single CPU instruction.

scan every single grid point, but rather use larger steps (which are tuned depending on whether we include gallium or not) and use parabolic interpolation on the discrete grid when I encounter a local minimum. More details can be found in appendix A.4.

4.4 Results

In this section, I present the results of our FCMC analysis, which can also be found in our paper [272]. The results in this section are based on computations on the KIT Kalinka5 cluster, which contains several Intel Xeon Gold 6230 processors. Each processor contains twenty cores and can run forty threads. Using $100-200$ threads, I could obtain results for a full parameter-space scan on a grid with roughly 6000 points in $10-20$ hours.

4.4.1 Best-fit points and p_0 value

In table 4.6, I show a comparison of our fit's best-fit points with the collaborations' in the middle three columns, which show reasonable agreement in all cases. (The discrepancy for the best-fit parameters for NEOS and our fit is explained in section 4.1.2; see also table 4.1.) Note that for NEOS and PROSPECT, there is a different number of degrees of freedom between our analysis and the collaborations', due to the different number of pulls used. In the last four columns, I show the $\Delta\chi^2$ value for the null hypothesis ($\sin^2 2\theta = 0$) of our fit and the collaborations (again with good agreement); also shown is p_0: the p value for the null hypothesis, calculated from Monte Carlo simulations of the test statistic $\Delta\chi^2_{3\nu}$. Because of the high significance of gallium, the p_0 value could not be calculated via MC simulations, and instead an estimated range of its value was calculated. The estimated range is based on two extrapolations of the survival function, which is explained in the next section 4.4.2.

In the last two columns, I show the number of standard deviations of a standard normal distribution that corresponds to p_0, and also the number of standard deviations when assuming Wilks' theorem, *i.e.* assuming $\Delta\chi^2_{3\nu}$ is distributed like $\chi^2(2\text{ dof})$. As can be seen, Wilks' theorem consistently overestimates the significance by $0.6-1.1\,\sigma$, and the global reactor data is compatible with the hypothesis of no new oscillations.

4.4.2 Null-hypothesis $\Delta\chi^2$ distribution

In this section, I present the distributions of the $\Delta\chi^2$ test statistic at the null hypothesis for the different combinations of datasets. In fig. 4.16, I show the $\Delta\chi^2_{3\nu}$ probability distribution function (PDF) and the survival function (SF) for $\sqrt{\Delta\chi^2_{3\nu}}$, for the combination of all reactor experiments, as well as the same functions for the $\chi^2(2\text{ dof})$ distribution. It is clear that Wilks' theorem does not hold, and the $\chi^2(2\text{ dof})$ distribution drastically underestimates the p_0 value.

In fig. 4.16 (left), I have also plotted the maximum-Gauss distribution, which was introduced in the paper by the coauthors Coloma, Huber and Schwetz [274], as a semi-analytic approximation for the $\Delta\chi^2_{3\nu}$ distribution of. As previously mentioned, one can always fit a high-frequency oscillating signal to a set of normally distributed residuals. The Fourier transform of a set of normally distributed random variables is also normally

	$\chi^2_{\rm min}/\mathrm{dof}$	$\Delta m^2_{\rm min}$	$\sin^2 2\theta_{\rm min}$	$\Delta\chi^2_{3\nu}$	p_0	$\#\sigma$	$\#\sigma^{(W)}$
DANSS		1.3 eV^2	0.014	3.2			1.3
Our Fit	77.6/70	1.32 eV^2	0.011	3.6	43.8%	0.8	1.4
NEOS	57.5/59	1.73 eV^2	0.05	6.5	22%	1.2	2.1
Our Fit	59/58	2.95 eV^2	0.16	7.4	19.4%	1.3	2.2
PROSPECT	119.3/142	1.78 eV^2	0.11	4.0	57%	0.6	1.5
Our Fit	118.1/158	1.75 eV^2	0.11	4.3	63.3%	0.5	1.6
STEREO	128.4/112	8.95 eV^2	0.63	9.0	9%	1.7	2.5
Our Fit	128.6/112	8.72 eV^2	0.59	7.8	15.8%	1.4	2.3
Nu-4	14.7/17	7.26 eV^2	0.38	15.3			3.5
Our Fit	16.1/17	7.31 eV^2	0.38	12.6	1.5%	2.4	3.1
REACTORS	428/421	8.86 eV^2	0.26	7.3	27.4%	1.1	2.2
W/ Solar	432/425	1.30 eV^2	0.014	6.6	17.8%	1.3	2.1
W/ Gallium	433/427	8.86 eV^2	0.32	38.8	$(0.14 \to 1.4)\times 10^{-7}$	5.7 → 5.3	5.9

Table 4.6: Comparison of our fit results with the collaborations' (where available) for DANSS [280, p. 17], NEOS [282], PROSPECT [286, §VIII.C], STEREO [290, table 5] and Neutrino-4 [275, §21 of v2 of arXiv preprint]; reproduced from [272]. The middle three columns contain the global-minimum χ^2 value, and the corresponding oscillation parameters. The last four columns contain the $\Delta\chi^2$ value of the null hypothesis, the p value of the null hypothesis calculated from MC simulations (p_0), and its equivalent number of normal standard deviations, $\#\sigma$. In the last column is the number of standard deviations when Wilks' theorem is assumed (with two degrees of freedom). We also show our combined results for all reactors, as well as reactors with solar, and reactors with gallium data. The gallium analysis uses the Kostensalo *et al.* cross section [304]. Due to the very low p_0 value for gallium, the range given is an estimate (see section 4.4.2).

distributed, and the maximum value of the Fourier-transformed variables will determine the pseudo-signal strength of the pseudo oscillations. Therefore, the test statistic

$$T \equiv \left(\max_k \; a_k\right)^2, \qquad \text{where } \; k \in \{1 \ldots n\}, \tag{4.62}$$

and its distribution, which I denote as $\mathrm{Gau}_{\text{„max}}(n)$, approximates $\Delta\chi^2_{3\nu}$ and its distribution. The parameter n is an effective number of degrees of freedom, which is tuned to match the MC distribution. Deviation from maximum Gauss, which assumes that bins are statistically independent, can be traced to correlations between bins in the reactor dataset, as well as other simplifying assumptions such as equal bin size of all data.

In fig. 4.17, I show the survival function (at the null hypothesis) for $\sqrt{\Delta\chi^2_{3\nu}}$ for the reactor data combined with solar as well as with gallium. The functions are almost identical, implying that the reactor data dominates and determines the null-hypothesis distribution. The two extrapolations shown as dotted dashed lines, a linear one in cyan and a maximum-Gauss one in purple, are used to estimate the p_0 value, given in table 4.6.

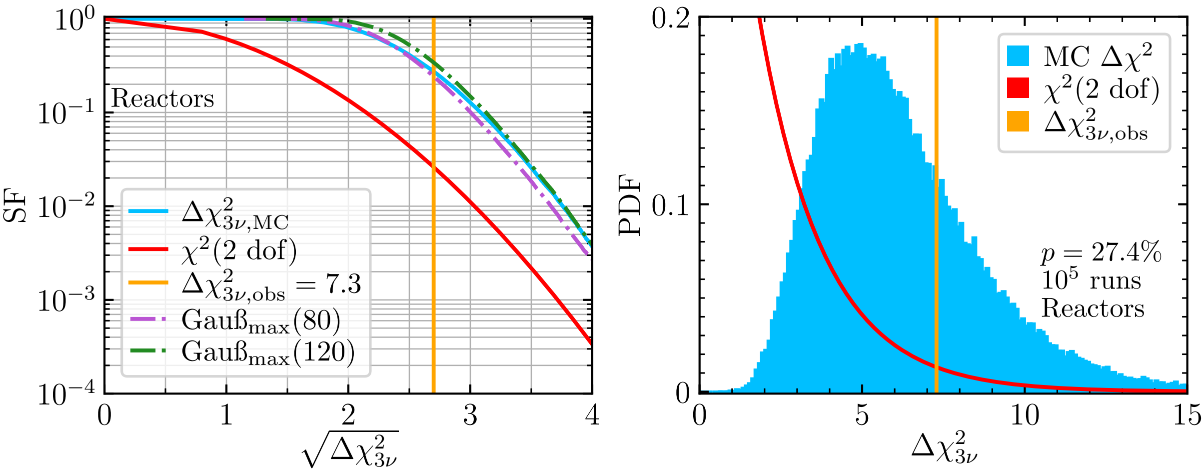

Figure 4.16: Survival function (SF, left) and probability distribution function (PDF, right) of $\sqrt{\Delta\chi^2_{3\nu}}$, and $\Delta\chi^2_{3\nu}$, respectively, for all reactor experiments for 10^5 simulations (blue), compared with the χ^2(2 dof) SF and PDF (red), as well as the maximum-Gauss distribution for $n = 80, 120$, see text for details; reused from [272].

The linear extrapolation is based on fitting a line to the tail of the survival function, and represents an upper limit for p_0, as the survival function has negative curvature. The maximum-Gauss extrapolation is tuned using n as the free parameter to roughly match the survival function in the interval $\sqrt{\Delta\chi^2_{3\nu}} \in [3.5, 4.5]$. As can be seen from figs. 4.16 and 4.17, the maximum-Gauss distribution generically decays faster than the MC distribution, and so the maximum-Gauss extrapolation represents a lower limit on p_0. The Gau„$_{\text{max}}$(60) curve, extended to $\sqrt{T} \sim 6.5$ was calculated on four NVIDIA Tesla K40c GPUs using CUDA, using $1.15 \cdot 10^{10}$ simulations, taking roughly one to two hours.

4.4.3 FCMC exclusion curves

In fig. 4.18, I show the FCMC exclusion curves for each individual reactor experiment, as well as their combination, as bands. The corresponding curves under the assumption of Wilks' theorem with two degrees of freedom are also plotted with thin lives. Comparing the bands with lines of the same colour, we see that the true significance is reduced by roughly one standard deviation, similar to the null-hypothesis case.

The bands signify the 99% confidence spread due to statistical fluctuations of the MC simulations. Namely, for N MC trials, the number n of pseudo datasets with $\Delta\chi^2_{\mathrm{pseudo}} > \Delta\chi^2_{\mathrm{obs}}$ is distributed as a binomial distribution, with parameters N and p, where p is the true p value. We can define the distribution of p values calculated via Monte Carlo simulations as $f(q) = N \cdot B(n; N, p)$, where $q = n/N$ is the MC-calculated p value, and $B(\,\cdot\,; \cdot\,, \cdot\,)$ is the binomial PDF. The $\alpha = 99\%$ confidence interval $[q_0, q_1]$ is estimated using $f(\,\cdot\,)$ by using the obtained p value via MC simulations as an estimate for the true p value in $f(\,\cdot\,)$, and defining $q_{0,1}$ to satisfy

$$\frac{F(p) - F(q_0)}{F(p) - F(0)} = \alpha, \qquad\qquad \frac{F(q_1) - F(p)}{F(1) - F(p)} = \alpha, \tag{4.63}$$

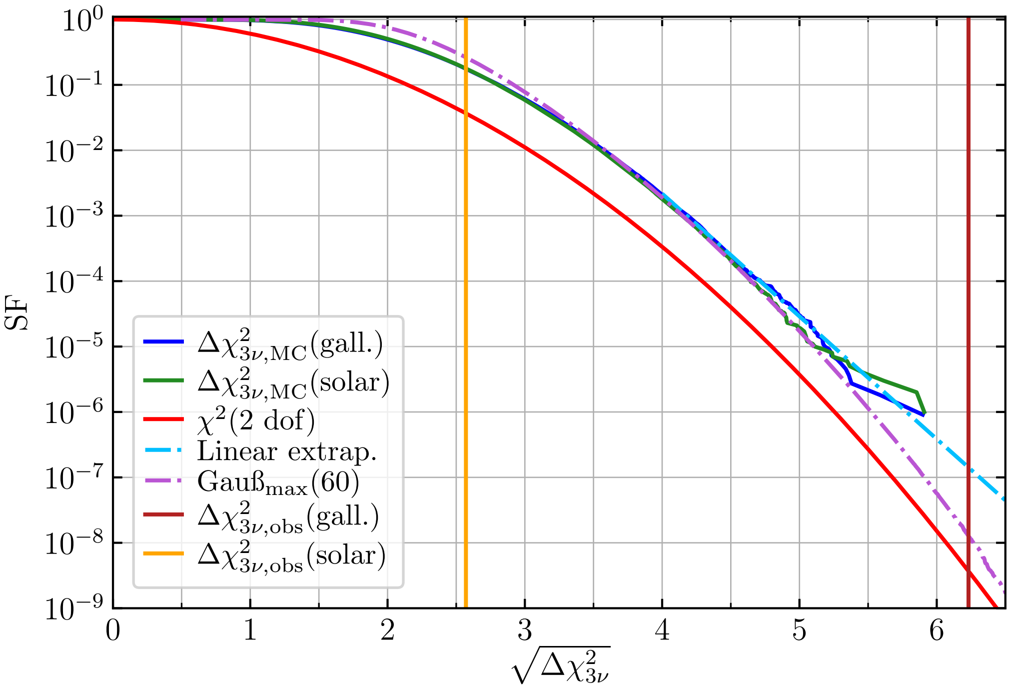

Figure 4.17: The survival function of $\sqrt{\Delta\chi^2_{3\nu}}$ for reactor data combined with solar (green) or with gallium (blue), for 10^6 runs, from [272]. The corresponding distribution for χ^2(2 dof) is shown for comparison (red), as well as extrapolations with a line (cyan) and the max-Gauss distribution (purple) with $n = 60$, which are used to estimate p_0.

where $F(\,\cdot\,)$ is the CDF of $f(\,\cdot\,)$ and $p \equiv n_{\mathrm{MC}}/N$. Note that for very small p values, the distribution $f(\,\cdot\,)$ is highly skewed. Parameter points that lie in a band of confidence level p_{CL} are defined so that p_{CL} lies in the confidence interval $[q_0, q_1]$ at that parameter point.

In fig. 4.19 (left), I show the results for our gallium analysis, which combines the data from GALLEX, SAGE and BEST. Because the relevant regions for gallium lie far away from the boundaries of parameter space, and because of their high significance, the Feldman-Cousins analysis does not significantly differ from the equivalent contours under Wilks' theorem, shown in dash dotted. In fig. 4.19 (right), the $2\,\sigma$ regions for gallium, reactor data, solar data are shown, as well as from other data such as ν_e scattering on ^{12}C from LSND and KARMEN [310, 311], as well as from KATRIN [312]. (Note that I have updated the KATRIN curve to the latest 2022 data, whereas our publication uses the old 2020 data.) The LSND and KARMEN limits come from searching for charged-current electron-neutrino scattering in a muon-neutrino beam; whereas the KATRIN bound comes from searching for spectral distortions in the near-endpoint spectrum of tritium decay. As can be seen, gallium is compatible with all data except for the solar data, whose tension will be quantified in section 4.4.4. Note that the LSND and KARMEN data is only marginally relevant for $\Delta m^2 \leq 10\,\mathrm{eV}^2$, where most of the parameter space is already excluded by reactor data. Also note that for the KATRIN curve, the collaboration ignores the lightest neutrino mass; marginalising over this would lead to slightly less stringent bounds.

Because of the gallium-solar tension, it is statistically unsound to combine the two datasets, as explained in section 3.4. Therefore, I only show the reactor+solar (left) and reactor+gallium (right) combined FCMC confidence regions in fig. 4.20. Whereas for the reactor+solar data, the best-fit is at $\Delta m^2 \sim 1\,\text{eV}^2$ and $\sin^2 2\theta \sim 10^{-2}$, the gallium data drastically changes the confidence regions, with a best-fit at $\Delta m^2 \sim 9\,\text{eV}^2$, which is determined by the Neutrino-4 data, and large mixing $\sin^2 2\theta \sim 0.3$, determined by the gallium data.

4.4.4 Quantifying the gallium-solar tension

Similar to the three-neutrino global fit in section 3.4, we use the parameter goodness-of-fit test statistic, χ^2_{PG}, defined in eq. (3.30) to quantify the gallium-solar tension. In table 4.7, the χ^2_{PG} values for the different combinations of the datasets (reactors, solar and gallium), as well as the number of degrees of freedom n, as defined by eq. (3.31). As proven in [265], under certain conditions, χ^2_{PG} is distributed as $\chi^2(n \text{ dof})$, which I also refer to as Wilks' theorem. In table 4.7, I also provide the p value and equivalent normal standard deviations under the assumption of Wilks' theorem, as well as a p value calculated from MC simulations, where the pseudo data is generated with mean defined by the prediction at the best-fit point of the combined dataset. Note that a truly rigorous p value would consider its value at all parameter points (calculated using MC simulations) and take the maximum value, which would yield the most conservative result. Since this is too computationally expensive, taking the best-fit point to be the parameter point of least tension is intuitively a reasonable approximation.

Data set	χ^2_{PG}/ dof	$p^{(W)}$	$\#\sigma^{(W)}$	$p_{\text{b.f.}}$	$\#\sigma_{\text{b.f.}}$
Reactor vs Solar	0.65/1	0.42	0.8	0.39	0.9
Reactor vs Gallium	1.4/2	0.50	0.67	0.62	0.5
Solar vs Gallium	13.0/1	$3.1 \cdot 10^{-4}$	3.6	$1.6 \cdot 10^{-3}$	3.2
Reactor vs Solar vs Gallium	15.6/3	$1.4 \cdot 10^{-3}$	3.2	$5.1 \cdot 10^{-3}$	2.8

Table 4.7: In the second column are the values of the parameter goodness-of-fit test statistic and its number of degrees of freedom, for different combinations of the datasets. In the middle columns, its significance is evaluated under the assumption of Wilks' theorem. The final two columns show its significance derived from MC simulations, generating pseudo-data fluctuations around the best-fit (b.f.) prediction. Courtesy of [272].

We can see that the significance of the χ^2_{PG} test statistic is less than one sigma for the reactor and solar datasets, as well as the reactor and gallium datasets. However the solar and gallium datasets are in tension at the $\sim 3\,\sigma$ level, and the total dataset of reactors, solar, and gallium, also has a tension slightly less than $3\,\sigma$.

4.5 Discussion of the Gallium-Solar Tension

In this section I will discuss possibilities that I considered to alleviate the tension between the gallium and solar data. The two possibilities presented are, firstly, the possibility of experimental errors or unknown systematics in the technique of the gallium experiment; and secondly the possibility of introducing new physics to evade the solar bound. Unfortunately, neither options look promising, which is why they were never published, however perhaps others may find inspiration.

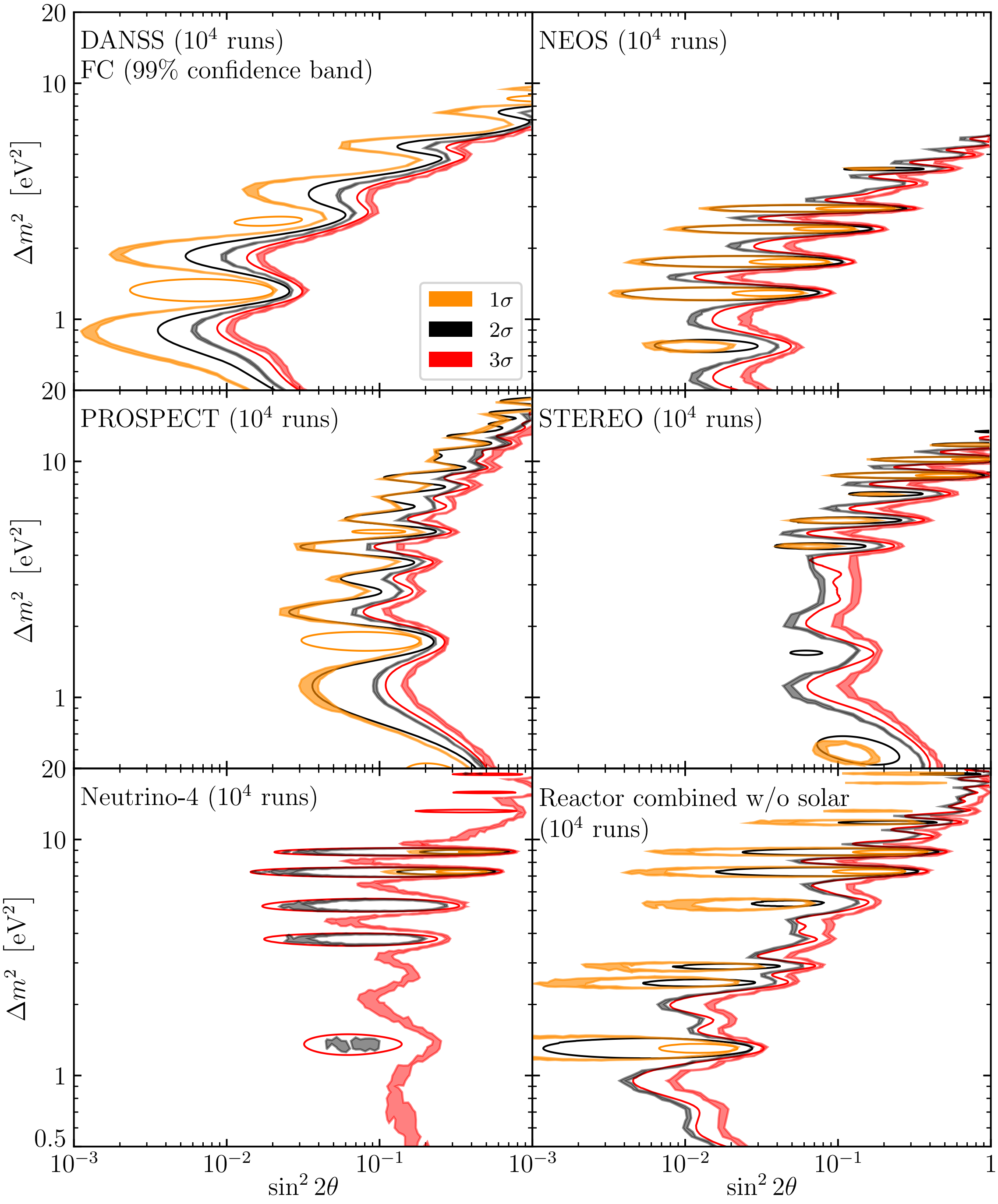

Figure 4.18: Confidence regions at 68.27%, 95.45%, 99.73% CL (1, 2, 3 σ, respectively) for the individual reactor experiments, and all reactors combined (bottom right), from [272]. The bands correspond to the Feldman-Cousins analysis, where their width indicates the 99% confidence spread due to statistical fluctuations from MC simulations (see text). The thin curves correspond to Wilks' theorem with two degrees of freedom.

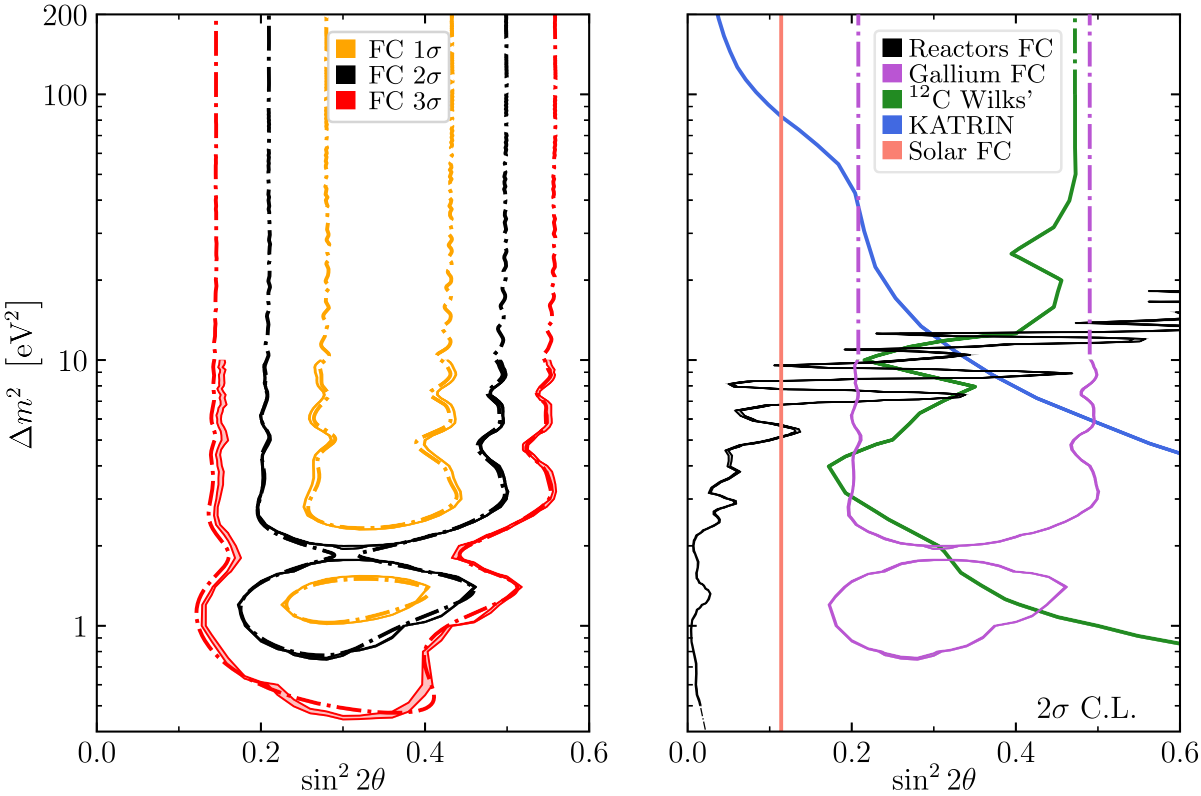

Figure 4.19: Left: confidence regions at 68.27%, 95.45%, 99.73% CL (1, 2, 3 σ, respectively) for the Feldman-Cousins analysis (bands), where the bands indicate the 99% confidence spread of the contour (see text), for 10^5 runs, from [272]. Dash-dotted curves are obtained under the assumption of Wilks' theorem with two degrees of freedom. Right: FC confidence regions for gallium, reactor, and solar data at 2 σ. (Dash-dotted lines are extrapolations assuming constant sensitivity in the mixing.) In addition, the 95% exclusion limit from the KATRIN collaboration [312] is shown (this curve fixes the lightest neutrino mass to zero) and the Wilks' 95% exclusion limit (2 dof) from ν_e-^{12}C scattering from the LSND and KARMEN experiments [310, 311], taken from [267].

4.5.1 Gallium systematics

It is difficult to envisage explaining the deficit from the detection side of the experiment. This is because the germanium-extraction technique has been highly developed over decades, with the miniscule amount of artificially added carrier germanium being able to be extracted to validate the extraction procedure. Furthermore, the ground-state cross section on gallium provides a lower bound on the production rate, and this component is constrained by experimental data — theoretical uncertainties on the calculated excited-state contribution cannot explain a deficit.

There is a slim possibility that there are unknown systematics regarding the source calibration. The conversion from heat output to neutrino activity requires precise knowledge of the amount of heat released per decay. For the source ^{51}Cr, the electron-capture decay scheme is quite simple: the nucleus can decay into the ground state of ^{51}V, with branching ratio 90.09%; or it can decay into its excited state, after which the nucleus

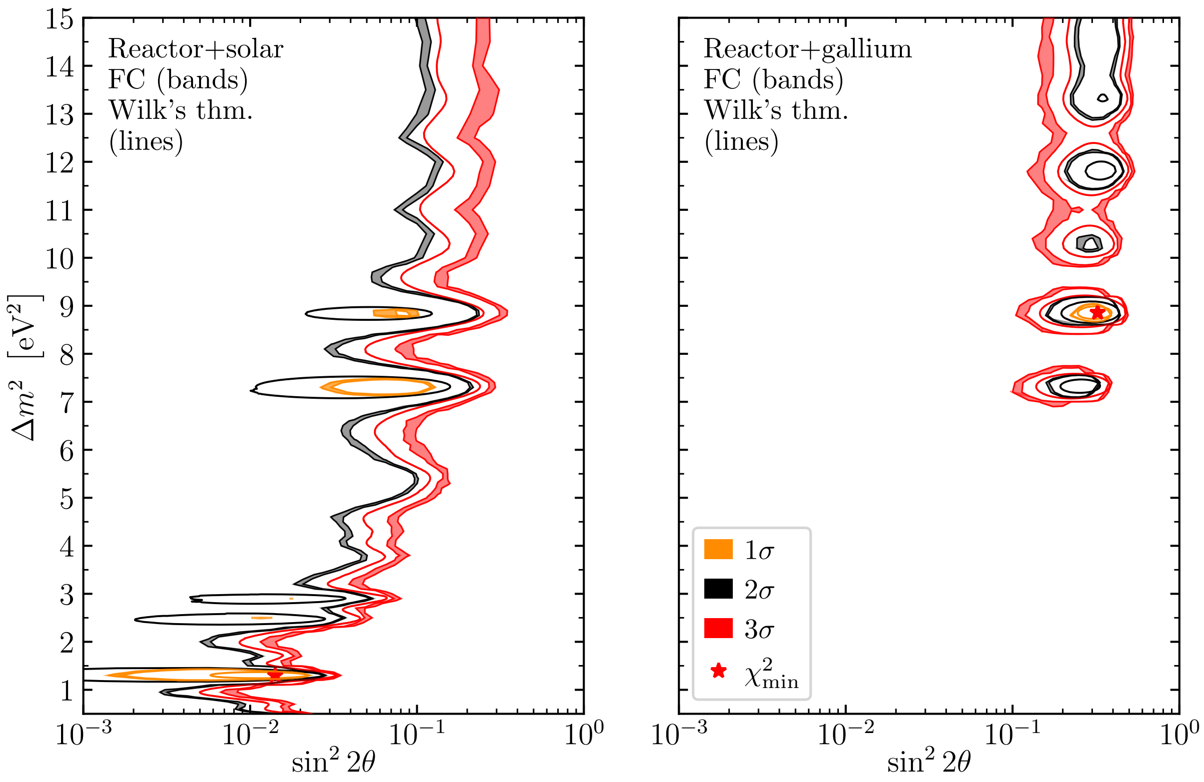

Figure 4.20: Confidence regions at 68.27%, 95.45%, 99.73% CL (1, 2, 3σ, respectively) for reactor+solar data (left), and reactor+gallium data (right), from [272]. The bands correspond to the Feldman-Cousins analysis, where the width of the bands indicates the 99% confidence spread of the contour for 10^4 runs (see text). The thin curves are obtained under the assumption of Wilks' theorem.

decays to its ground state via the emission of a 320 keV gamma ray, with branching ratio 9.91%. Thus, on average, the gamma rays contribute 32 keV of heat per decay. After the nuclear decay, the electronic energy levels change, leading to Auger electrons and X-rays, which contribute roughly 5 keV to the heat. For a full list, see [300, tab. 1].

Since the subleading excited-state decay contributes the majority of heat, a 1% absolute change in its branching ratio would yield a 10% shift in expected production rate. (Measurement of the photon spectrum of ^{51}Cr eliminates the possibility of a new decay channel with a branching ratio of 1% and high-energy gamma-ray emission [301, fig. 10].) The different measurements of the excited-state branching ratio can be found in the commentary of the nuclear table for ^{51}Cr [313]. Of the modern experiments (after 1980), there is an outlier (with a larger branching ratio), which turns out to be the only modern measurement using neutron counting instead of measuring the Auger electrons, done by Fisher and Herschberger in 1984 [314]. The authors remark on the discrepancy,

"Since the earlier ^{7}Be *and* ^{51}Cr *measurements were both made by looking at Auger electrons, a possible conclusion that may be drawn is that there is a systematic difference between these recent measurements and those which look at Auger electrons."*

I was not able to find any follow-up measurements using neutron counting for ^{51}Cr. If neutron-counting measurements consistently yield larger branching ratios, this would put into question the significance of the gallium anomaly. However, the measurement by Fisher & Herschberger only yields a branching ratio of 10.30%, which is only marginally larger.

Most of the modern measurements, *e.g.* [315, 316], use the $4\pi(\mathrm{X},\mathrm{A})$-$\gamma$ coincident counting method to determine the absolute activity (instead of neutron counting). The coincidence method is used because the efficiencies of the detector are not known. Following [317], consider a radioactive source whose decay emits an electron and gamma photon simultaneously. Then, assuming the efficiency of measuring a coincident electron and photon is simply the product of the efficiencies of measuring each particle individually, the radioactive-source activity A can be measured without knowing the efficiencies,

$$A = \frac{N_\beta \cdot N_\gamma}{N_\mathrm{c}}, \tag{4.64}$$

where N_β is the electron count, N_γ is the photon count, and N_c is the number of coincident events. In the decay scheme for ^{51}Cr, every decay emits an Auger electron or X-ray, but only P_γ proportion of events emit a 320-keV photon. This idea can be extended, but it requires one to evaluate $N_\mathrm{XA} N_\gamma / N_\mathrm{c}$ at different efficiencies, and extrapolating the result to large efficiency (see [318]). For some non-chromium examples, see [319]. I could not find any such extrapolation curves for ^{51}Cr. Whilst the examples in [319] show a high degree of precision, given that the method requires extrapolation, the possibility of hidden systematic effects seem plausible. However, such a systematic effect would require a 10% shift in order to affect the gallium result by 10%, as it would change the absolute normalisation of the branching ratio.

I also found an old 1985 paper from an analytical biochemistry journal [320], which reported anomalous liquid scintillation for a ^{51}Cr solution, like that used for the absolute activity measurement. However, the effect only becomes significant after a few days.

4.5.2 Relaxing the solar constraint

Another option to reduce the gallium-solar tension is to introduce new neutrino interactions to relax the solar constraint. Here I will consider neutrino decay, such that the heavier fourth neutrino decays back into Standard Model neutrinos during propagation from the Sun to the Earth.

Neutrino decay in the context of the Majoron model was considered in the 1980s as a possible solution to the solar-neutrino deficit; in this model, neutrinos interact with a complex scalar like $\bar{\nu}_s \nu_s \phi$. (Interactions with the other weak eigenstates are forbidden by gauge invariance). However, it was noticed in 1989 that decay from neutrino to anti-neutrino is permitted [321]. Nowadays, solar data can constrain this scenario due to the absence of a sizeable anti-neutrino signal [322].

The authors of [322] considered parity-violating scalar interactions in order to forbid the decays of neutrinos to anti-neutrinos. Parity violation occurs at the level of the mixing matrices $V_\mathrm{L} \neq V_\mathrm{R}$, by choosing

$$\nu_s^\mathrm{R} = \nu_1^\mathrm{R} \qquad \text{and} \qquad \nu_s^\mathrm{L} = \cos\vartheta \left|\nu_4\right\rangle - \sin\vartheta \left|\nu_e^{3\nu}\right\rangle, \tag{4.65}$$

where

$$\left|\nu_e^{3\nu}\right\rangle = c_{13}\left[c_{12}\left|\nu_1\right\rangle - s_{12}\left|\nu_2\right\rangle\right] - s_{13}\left|\nu_3\right\rangle. \tag{4.66}$$

The states $\nu_i^{\mathrm{L,R}}$ are the chiral mass eigenstates, where $V_{\mathrm{L,R}}$ diagonalise the Dirac mass term. The scalar interactions are

$$\mathcal{L} = g_\phi \sum_{i=1}^{4} (V_{\mathrm{L}})^*_{si} \left(\bar{\nu}_i P_{\mathrm{R}} \nu_1\right) \phi + \mathrm{h.\,c.} \tag{4.67}$$

In order to avoid producing anti-neutrinos from ϕ decay, I will assume that m_ϕ is small enough to ignore decays of ϕ.

It turns out that energy threshold effects are important. For simplicity, I will use Borexino's energy thresholds [323] of $0.19\,\mathrm{MeV}$ – $2.93\,\mathrm{MeV}$ for the low-energy neutrinos and $3.2\,\mathrm{MeV}$ – $16\,\mathrm{MeV}$ for the high-energy neutrinos. Based on [324, tab. 6], we see that for the low-energy neutrinos, the dominant contributions are *pp* and ^{7}Be, and for high-energy neutrinos ^{8}B dominates. The ^{7}Be neutrinos are emitted as lines due to electron capture on beryllium. There are two lines due to the two possible final states: ground- and exited-state of lithium, the former having the larger energy, with probabilities 89.56% and 10.44%, respectively [325, 326].

The differential decay width in the relativistic limit can be written as [327]

$$\frac{\mathrm{d}\Gamma}{\mathrm{d}E_1} = \Gamma_{\mathrm{tot}} \frac{E_1}{E_4^2}, \qquad \text{where} \qquad \Gamma_{\mathrm{tot}} = \frac{m_4^2 g_\phi^2 \sin^2\vartheta}{32\pi}. \tag{4.68}$$

Assuming that $E_4 \leq E_{\mathrm{thresh}}^{\mathrm{high}}$, the proportion of final-state SM neutrinos with energies larger than the lower threshold $E_1 > E_{\mathrm{thresh}}^{\mathrm{low}}$ is

$$1 - \left(\frac{E_{\mathrm{thresh}}^{\mathrm{low}}}{E_4}\right)^2. \tag{4.69}$$

For ^{8}B neutrinos, the peak of the flux distribution occurs at $\sim 6.4\,\mathrm{MeV} = 2E^{\mathrm{low}}$, which means that there is actually a suppression of $\sim 75\%$ due to neutrinos decaying to an energy below the experimental threshold. Define

$$\begin{aligned}\mathcal{I}(m_4 g_{\mathrm{eff}}) = \int_{E_{\mathrm{low}}}^{E_{\mathrm{high}}} \sum_a \frac{\mathrm{d}\Phi_a}{\mathrm{d}E_4} \left(1 - e^{-\Gamma\cdot 1\,\mathrm{AU}}\right) \left[1 - \left(\frac{E_{\mathrm{low}}}{E_4}\right)^2\right] \mathrm{d}E_4 \\ \bigg/ \left(\int_{E_{\mathrm{low}}}^{E_{\mathrm{high}}} \sum_a \frac{\mathrm{d}\Phi_a}{\mathrm{d}E_4} \mathrm{d}E_4\right),\end{aligned} \tag{4.70}$$

to be the proportion of neutrinos which decay into energies above the threshold, where $g_{\mathrm{eff}} = g_\phi \sin\vartheta$. Similarly, define

$$\mathcal{J}(m_4 g_{\mathrm{eff}}) = \int_{E_{\mathrm{low}}}^{E_{\mathrm{high}}} \sum_a \frac{\mathrm{d}\Phi_a}{\mathrm{d}E_4} e^{-\Gamma\cdot 1\,\mathrm{AU}} \mathrm{d}E_4 \bigg/ \left(\int_{E_{\mathrm{low}}}^{E_{\mathrm{high}}} \sum_a \frac{\mathrm{d}\Phi_a}{\mathrm{d}E_4} \mathrm{d}E_4\right), \tag{4.71}$$

to be the neutrinos which do *not* decay. Then,

$$P_{ee} = \sum_{k=1}^{3} |U_{ek}^m|^2 |U_{ek}|^2 + |U_{e4}^m|^2 \left(\mathcal{I}|U_{e1}|^2 + \mathcal{J}|U_{e4}|^2\right) \tag{4.72}$$

$$P_{ex} = \sum_{k=1}^{3} |U_{ek}^m|^2 \sum_{\alpha=\mu,\tau} |U_{\alpha k}|^2 + |U_{e4}^m|^2 \left(\mathcal{I} \sum_{\alpha=\mu,\tau} |U_{\alpha 1}|^2 + \mathcal{J} \sum_{\alpha=\mu,\tau} |U_{\alpha 4}|^2\right), \tag{4.73}$$

however note that $U_{\alpha 4} = 0$ for $\alpha = \mu, \tau$. Explicitly,

$$P_{ee}^{\mathrm{LE}} = \cos^4\vartheta \cdot P_{ee}^{\mathrm{SM}} + \sin^2\vartheta \left(\cos^2\vartheta \cdot c_{12}^2 c_{13}^2 \cdot \mathcal{I}_{\mathrm{LE}} + \sin^2\vartheta \cdot \mathcal{J}_{\mathrm{LE}}\right), \tag{4.74}$$

$$P_{ee}^{\mathrm{HE}} = \cos^4\vartheta \left(s_{12}^2 c_{13}^4 + s_{13}^4\right) + \sin^2\vartheta \left[\cos^2\vartheta \cdot c_{12}^2 c_{13}^2 \cdot \mathcal{I}_{\mathrm{HE}} + \sin^2\vartheta \cdot \mathcal{J}_{\mathrm{HE}}\right], \tag{4.75}$$

$$P_{ex}^{\mathrm{LE}} = \cos^2\vartheta \left(1 - P_{ee}^{\mathrm{SM}}\right) + \sin^2\vartheta \left(1 - c_{12}^2 c_{13}^2\right) \mathcal{I}_{\mathrm{LE}}, \tag{4.76}$$

$$P_{ex}^{\mathrm{HE}} = \cos^2\vartheta \left(1 - s_{12}^2 c_{13}^4 - s_{13}^4\right) + \sin^2\vartheta \left(1 - c_{12}^2 c_{13}^2\right) \mathcal{I}_{\mathrm{HE}}. \tag{4.77}$$

To do the calculation, I parameterise the dependence of $\mathcal{I}$ on model parameters like so

$$\begin{aligned} \Gamma \cdot (1\,\mathrm{AU}) &= 0.754 \left(\frac{g_{\mathrm{eff}}}{10^{-5}}\right)^2 \left(\frac{m_4}{\mathrm{eV}}\right)^2 \bigg/ \frac{E_4}{\mathrm{MeV}} \\ &= \frac{0.754 \times x}{E_4/\mathrm{MeV}}, \end{aligned} \tag{4.78}$$

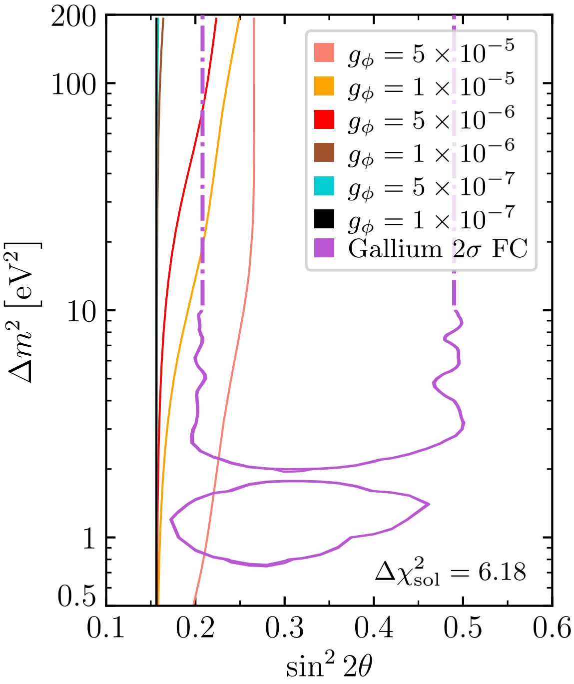

Figure 4.21: Solar exclusion curve under the partial-decay model for Wilks significance $2\,\sigma$ for two degrees of freedom compared to the gallium curve at $2\,\sigma$ using the Feldman-Cousins procedure.

where $x \equiv (g_{\mathrm{eff}}/10^{-5})^2\,(m_4/\mathrm{eV})^2$. I tabulated $\mathcal{I}$, $\mathcal{J}$ on discrete points of x.

Results

Results for different values of g_ϕ compared to the $2\,\sigma$ FC gallium curve are shown in fig. 4.21. Note that the solar results will now depend on $\Delta m_{41}^2 \approx m_4^2$, so the degrees of freedom are two. This is why I compare the gallium curve to $\Delta\chi^2_{\mathrm{sol}} = 6.18$, which is $2\,\sigma$ under Wilks' theorem. One can see the effect of decay saturating for $g_\phi = 5 \cdot 10^{-5}$ and $\Delta m^2 > 20\,\mathrm{eV}^2$ in fig. 4.21. The combined best-fit point for $g_\phi = 5 \cdot 10^{-5}$ is still at low Δm^2: $(\Delta m^2, \sin^2 2\theta) = (1.2\,\mathrm{eV}^2, 0.23)$, and the test statistic for parametric goodness of fit is $\chi^2_{\mathrm{PG}} = 9.1 \sim 2.6\sigma$. Regrettably, taking the gallium-solar tension from Wilks' theorem, this is only a $1\,\sigma$ reduction in tension.

Unfortunately, cosmology sets extremely stringent constraints on $g_\phi \sin\vartheta$. This is because the Majoron model introduces neutrino self-interactions, which violates the free streaming of the neutrino fluid. Because the free streaming allows neutrino perturbations to travel at the speed of light, and faster than the speed of sound, at which perturbations in the tightly coupled baryon-photon fluid travel, there is a unique phase shift of the CMB acoustic oscillations [328], which provides extremely stringent constraints [329, 330],

$$g_\phi \sin\vartheta \lesssim 10^{-7} – 10^{-6}. \tag{4.79}$$

Thus, it is clear that any such mild relaxation of the solar bound via neutrino decay will be in severe tension with cosmology.

4.5.3 Conclusion

In conclusion, I have presented my FCMC analysis of global reactor spectral data, in combination with gallium data and solar data, separately. Due to the low sensitivity for $\Delta m^2 \sim 9\,\mathrm{eV}^2$, the Neutrino-4 results are not in tensions with the other reactor experiments. Reactor data alone do not shown any preference of new oscillations. When combined with the gallium data, there is a strong preference for new oscillations, with the mass-squared splitting being determined by Neutrino-4, and the mixing by gallium data. However, this is in tension $(3.2\,\sigma)$ with the solar data. It is difficult to find any possibility of experimental errors to reduce the gallium anomaly, or new neutrino interactions to reduce the solar bound. The gallium anomaly, therefore, remains a puzzling result, with the Neutrino-4 result making it particularly intriguing.

Chapter 5

Testing the Neutrino Dipole Portal at DUNE

In this chapter, I cover the work that I did investigating the neutrino dipole portal at DUNE. The project started as an investigation of a signal from tau-sterile mixing at DUNE and T2HK with then Masters student, Mahmoud Al-Awashra, for which there is an unexcluded region in parameter space at low mass and large mixing (see [331, fig. 3]). Such a signal, whose results can be found in our paper [332], is only marginally relevant compared to existing constraints, and uncompetitive compared to future constraints. My supervisor suggested that we then turn our attention to the neutrino dipole portal, which turned out to be more relevant. I wrote up my results in the publication [332], which I wrote with my supervisor and his postdoc Jing-Yu Zhu, the latter assisting me in some theoretical aspects of the calculation, and constructing the set of exclusion curves from other experiments. I am also grateful to the well-constructed integration routines provided by the GNU Scientific Library [278].

5.1 The Neutrino Dipole Portal

As already mentioned in section 2.4, the neutrino dipole was already considered as an explanation of the solar deficit in 1971 by Cisneros and Werntz [119]. In 1979, Kunitomo Sakurai published an article that studied possible periodic temporal variations of the neutrino flux from the eleven years of data by Homestake [333], in which he found evidence for a quasi-biennial variation in the Homestake data (see also [334, fig. 2]). Although Bahcall, Field and Press in 1987 would later do a robust statistical analysis to show that it had low statistical significance [335], Voloshin, Vysotskiĭ and Okun' [336–339] suggested that a neutrino magnetic moment could explain this variation, where a temporally varying magnetic field within the sun would cause temporally varying spin precession from left- to right-handed neutrinos. This sparked numerous investiga-

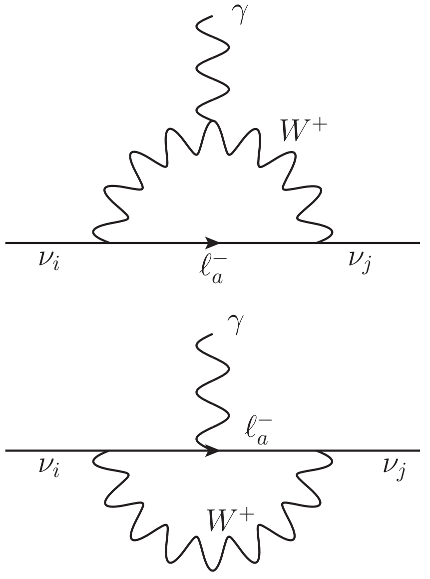

Figure 5.1: Magnetic moment of SM ν at one-loop level.

tions on how to generate large neutrino magnetic moments.

Within the Standard Model, the neutrino does in fact obtain a magnetic moment, but it is tiny due to suppression from the neutrino and W-boson mass $d \propto m_\nu/m_{\mathrm{W}}^2$ [340,341]. One suggestion by Fukugita and Yanagida in 1987 [342] simply replaces the W boson with a new charged scalar, such as that from the Zee model, which yields $d \propto m_\ell/m_\eta^2$, where m_ℓ is the mass of the associated charged lepton, and m_η is the mass of the new scalar. (Babu and Mathur also simultaneously published a similar paper, using a charged Higgs [343], and Stefanov incorporated this idea into a model that naturally suppressed the lepton-flavour violating decay $\mu \to e\gamma$ in 1988 [344].) One issue with generating a large neutrino magnetic moment, is that it can generate large neutrino masses at one-loop (recognised in 1988 by Barbieri and Fiorentini [345]); one-loop corrections to the neutrino mass in the Fukugita-Yanagida model was considered in [346]. In 1988, Voloshin hypothesised an approximate $\mathrm{SU}(2)_\nu$ symmetry, under which ν_{L} and ν_{L}^c transform as a doublet [347]; the neutrino mass term transforms as a triplet under this symmetry, whereas the magnetic moment transforms as a singlet, allowing one to give a symmetry reason for disentangling the relation between magnetic moment and mass for the neutrino. In 1989, Babu and Mohapatra implemented a version of this idea where instead of ν_{L} and ν_{L}^c, one considers ν_e and ν_μ (and therefore a transition magnetic moment between them), calling the $\mathrm{SU}(2)_{\mathrm{H}}$ an approximate horizontal symmetry [348]. More recently, these ideas have been revived by Babu, Jana and Lindner [349] by the XENON1T low-energy excess [350], which could be explained by a neutrino magnetic moment. (They also investigate explaining the muon $g-2$ anomaly [351] simultaneously [352].)

However, in this chapter we shall be concerned not with a neutrino magnetic moment, but the neutrino dipole portal, where the magnetic-moment operator connects the SM neutrino with a new heavy neutral lepton (HNL), which I call ν_4,

$$\mathcal{L} = d_\alpha \bar{\nu}_{\alpha\mathrm{L}} \sigma^{\mu\nu} \nu_4 F_{\mu\nu} + \text{h. c.} \tag{5.1}$$

Here, ν_α is a left-handed SM neutrino field of flavour $\alpha = e, \mu, \tau$, $F_{\mu\nu}$ is the photon field-strength tensor, and $\sigma^{\mu\nu} = \frac{\mathrm{i}}{2}(\gamma^\mu\gamma^\nu - \gamma^\nu\gamma^\mu)$ is the antisymmetric combination of gamma matrices. We shall be interested in the simplified scenario, where we consider the effects of one $d_{e,\mu,\tau}$ at a time, setting the others to zero. I will not discuss model building, which would require us to determine the charges of ν_4 under a larger gauge group, as well as specifying its mass generation; see [354, § IV] for some discussion. As mentioned in section 2.7, the dipole portal was considered by Gninenko in 2009 [190] to explain the MiniBooNE anomaly. His original suggestion created HNLs via mixing with muon neutrinos and neutral-current (NC) scattering, which then decayed via the dipole operator (fig. 5.2).

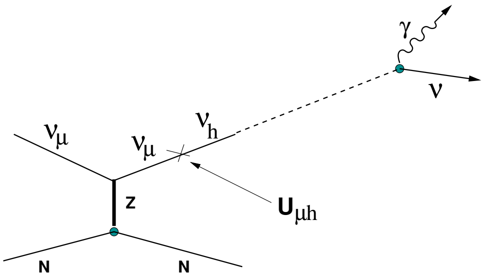

Figure 5.2: Courtesy of [190].

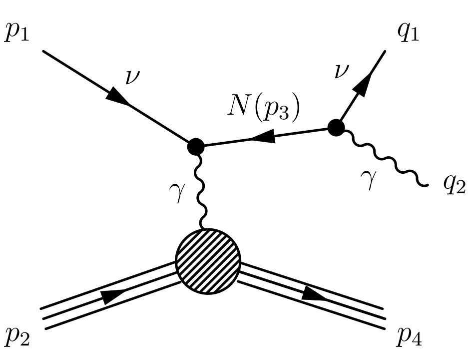

Figure 5.3: Courtesy of [353].

In 2018, Magill, Plestid, Pospelov and Tsai published a global evaluation of the neutrino dipole portal [353], as well as considering LSND and MiniBooNE. In their analysis, they use the dipole operator to produce the HNL and its decay (fig. 5.3). They analysed existing collider data, as well as the SN1987A neutrino burst to place bounds on the dipole parameter space. One important aspect of the collider bounds, which operate at energies about the electroweak symmetry-breaking scale, is that the bounds depend on the UV completion, as the dipole operator eq. (5.1) is not electroweak gauge-invariant. The low-energy dipole coupling to the photon should be a combination of couplings to the $\mathbf{A}_\mu$, B_μ fields (eq. (2.3)), which induces couplings to the W and Z bosons; but without a complete model, the exact induced couplings are not known, so there is some dependency of the collider bounds on the UV completion. They also analysed possible bounds that could be attained with SHiP, a proposed experiment at the beam dump of the CERN Super Proton Synchrotron.

In 2020, MiniBooNE published an updated analysis of its data, which reported a $4.8\,\sigma$ excess, and also studied possibilities of background mismodelling. Beam timing information and the radial distribution of events (namely the excess is less near the border of the fiducial volume) strongly disfavours the excess originating from outside the detector (second row of table 5.1). Other beam backgrounds, including π^0 emission from NC scattering, which then decays into an unresolved photon pair (mimicking single-photon emission), are mildly disfavoured compared to the oscillation hypothesis (table 5.1). However, notice that single-photon emission from the Δ resonance (first row of table 5.1) is the second-best possibility, albeit the SM prediction for Δ production must be increased by more than a factor three. The dipole-portal explanation could mimic this. Furthermore, the MicroBooNE experiment, which has excellent particle discrimination, searched for such $\Delta \to N\gamma$ events, and found no excess [355].

Hypothesis	Factor	$\chi^2/9ndf$
NC $\Delta \to N\gamma$	3.18	10.0
External Event	5.98	44.9
ν_e from K_L^0 Decay	7.85	14.8
ν_e from $K^\pm$ Decay	2.95	16.3
ν_e from $\mu^\pm$ Decay	1.88	16.1
Other ν_e & $\bar{\nu}_e$	3.21	12.5
NC π^0 Background	1.75	17.2
Best Fit Oscillations	1.24	8.4

Table 5.1: Log-likelihood shape-only fits of background to the radial distribution in neutrino mode, assuming only statistical errors, extracted from [189].

5.2 The Deep Underground Neutrino Experiment

DUNE (the Deep Underground Neutrino Experiment) is an accelerator experiment, currently under construction, whose primary goal is to measure the CP-violating phase δ_{CP} in the neutrino mixing matrix. The neutrino beam is generated at Fermilab, using a proton beam with a wide energy band of $60-120\,\text{GeV}$. The beam will deliver $1.1 \cdot 10^{21}$ POT (protons on target) per year. The near and far detectors, like MicroBooNE, will be liquid-argon time-projection chambers, whose sub-centimetre detector resolution allows for extremely good particle discrimination [356], which provides a major advantage compared to MiniBooNE, which could not distinguish photons from electrons. A comparison of tracks from MicroBooNE and NOνA is shown in fig. 5.4. As is clear, the MicroBooNE tracks can be resolved to a much higher resolution than NOνA, which allows for much better particle discrimination.

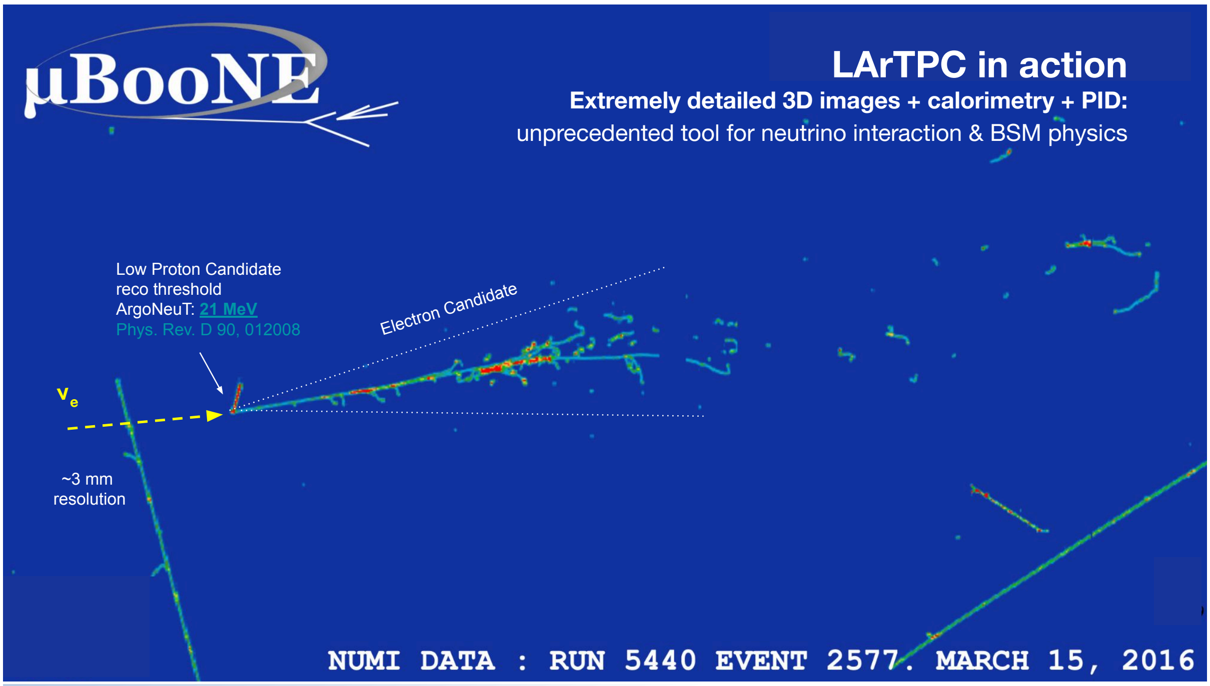

LArTPC in action

Extremely detailed 3D images + calorimetry + PID:

unprecedented tool for neutrino interaction & BSM physics

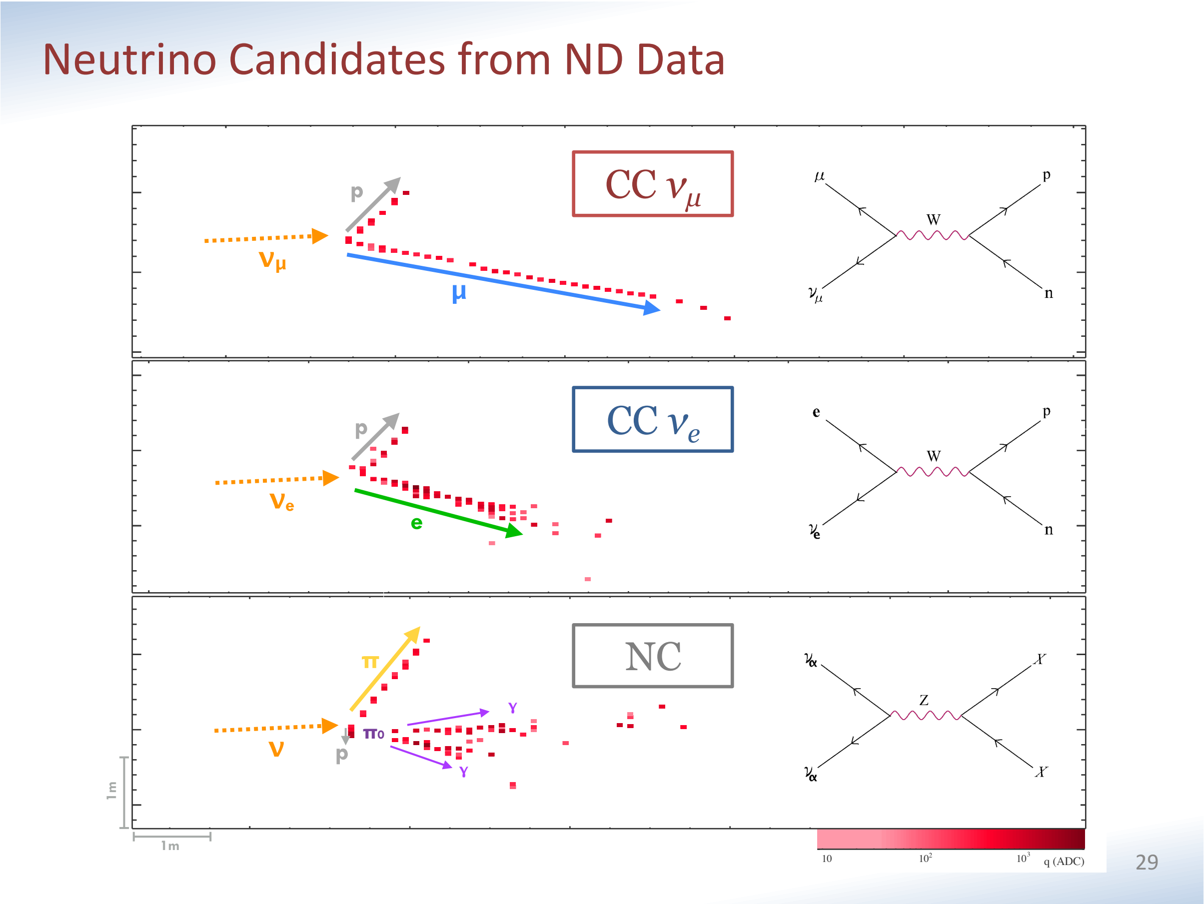

Neutrino Candidates from ND Data

Figure 5.4: Tracks from MicroBooNE (top) [357] and NOνA (bottom) [358].

In the lower panel of fig. 5.4, one can see a NC π^0 event in NOνA with two photon tracks; if the decay was highly asymmetric, such that the angle between the two photons were smaller, the photons would look like a single track, which could be misinterpreted as a single EM shower from an electron or photon. For comparison, the cell size for NOνA is 3.9 cm × 6.6 cm [245].

The DUNE far detector (FD) is planned to be in an on-axis configuration, so will be exposed to the wide-band neutrino beam. There will be four detector modules, each holding 17.5 kt of liquid argon, although the fiducial mass per module is 10 kt (40 kt total), with a size 12 m × 14 m × 58.2 m [356, tab. 3.1]. The near detector (ND) is located 574 m away from the beam target, 6 m wide, 3 m deep, and 2 m high, with a fiducial mass of 50 t [359, §2.7]. The ND layout with respect to the beam line is shown in fig. 5.5.

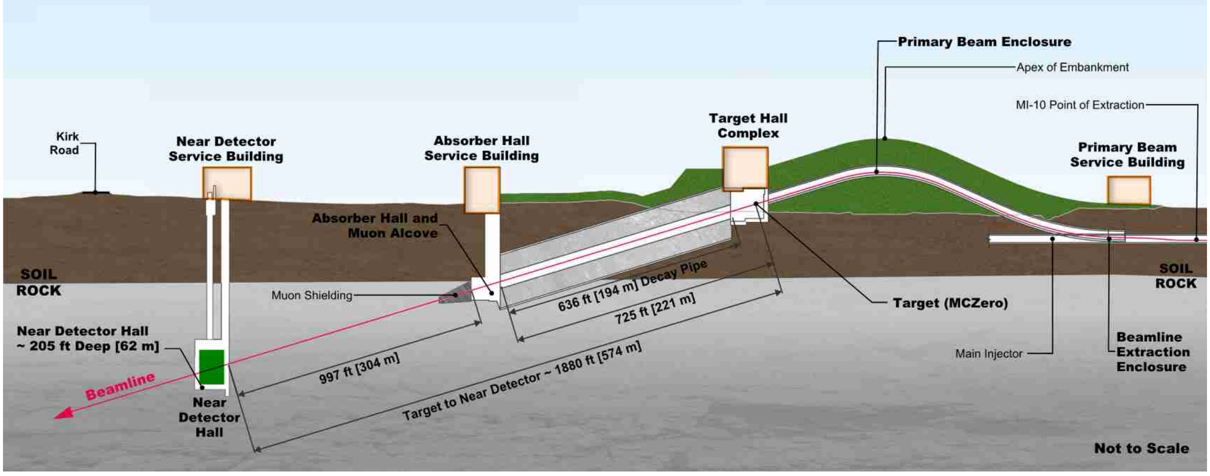

Figure 5.5: Layout of the near detector with respect to the proton beam [356, fig. 1.2].

Originally, the goal of the project was to exclude d_τ, as in general, the properties of the tau neutrino are not well constrained (like a mixing to a sterile neutrino), as it is difficult to produce an intense beam of tau neutrinos. The DUNE FD is located 1300 km away from the beam, at the Sanford Underground Research Facility in South Dakota, at the oscillation maximum for atmospheric oscillations. Thus, due to flavour oscillations, copious numbers of tau neutrinos will be present around the far detector. Later, in conversation with Ryan Plestid, who had attempted a similar calculation, I realised a similar calculation could be done at the near detector with the intrinsic muon and electron neutrinos.

5.3 Dipole-Portal Signal at the DUNE

The two classes of events for d_τ at the far detector are shown in fig. 5.6, where I have ignored the spatial separation from the beam and near detector, which is less than half a kilometre. The first class of events, which were originally the only ones considered, are the *outside events*, where tau neutrinos upscatter off target particles in the Earth's crust or upper mantle: either off individual nucleons (incoherent scattering), electrons, or off the whole nuclei, coherently. The upscattering creates an HNL, which can travel to the detector and decay inside it. The project originally only considered these outside events at the far detector, where the detector geometry can be ignored. However, I also discovered that in some areas of parameter space, this assumption was violated: in these areas, *inside events* dominate, where upscattering and decay both occur inside the detector. In conversation with Ryan Plestid, we realised that the same calculation could be done for the near detector, at which d_e and d_μ can be constrained, except without any oscillations and with a different geometry.

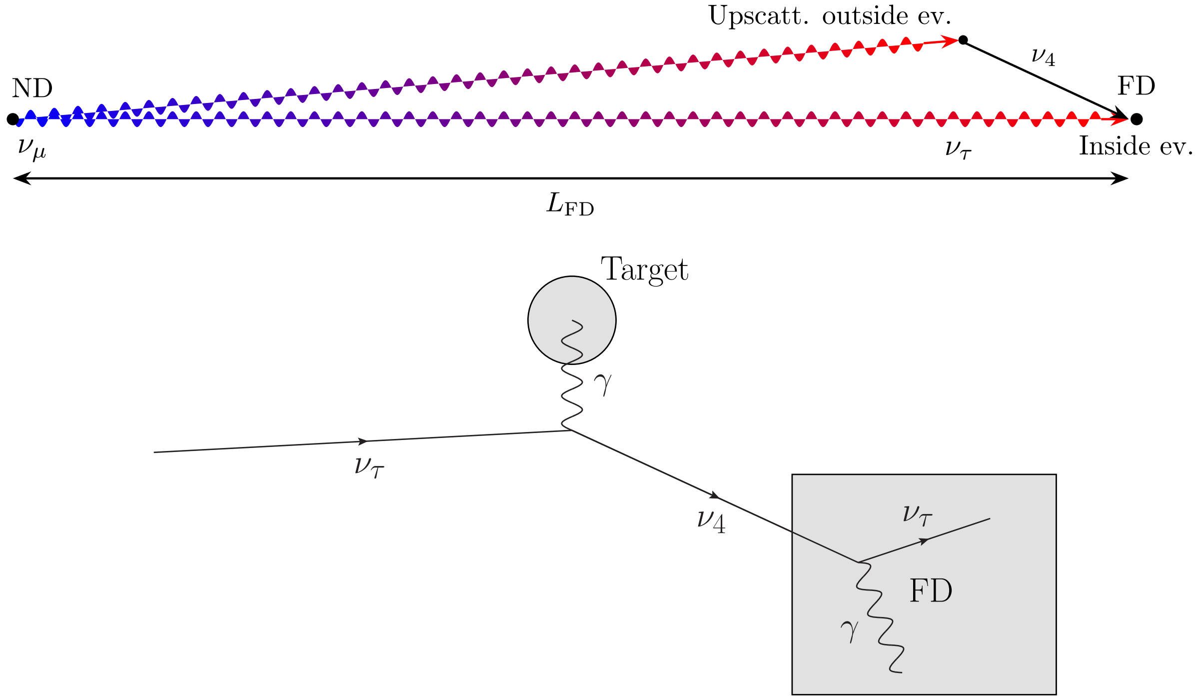

Figure 5.6: Cartoons of the upscattering production and decay signal for d_τ in the far detector, reproduced from [332].

Although in this work we will treat all events on an equal footing, in reality an experimental collaboration would have to distinguish between the different signals that would be created in the detector:

- **outside event**: since the upscattering occurs outside the detector, the signal is a single-photon event from HNL decay;
- **inside event, coherent:** the coherent scattering on the nucleus leaves a recoil of low energy, which is difficult to detect (however there have been efforts to make this possible [360, 361]); otherwise the signal is a single-photon event from HNL decay;
- **inside event, incoherent:** also called *double-bang events* [362], the incoherent scattering on the nucleon leads to a NC-like event, or a free electron if the scattering is on an electron; then a displaced single-photon event from the decay.

Neither do I do a background analysis in this work, although I shall provide a band of possible exclusion, depending on the background rate. As already mentioned, the DUNE detector has excellent particle discrimination, and so will not suffer from the inability to distinguish electrons and photons [363–365], unlike MiniBooNE. Therefore, the relevant SM backgrounds from the neutrino beam are single-photon processes like

NC1γ, and extremely asymmetric NCπ^0 decays (like MiniBooNE), where the two photons, even in DUNE, cannot be distinguished. The NC1γ cross section is negligibly small, $\sim 10^{-41}\mathrm{cm}^2$/nucleon [366–368], and so I expect the main background to be from misreconstructed NCπ^0 photons (see [364,365] for studies of NCπ^0 in liquid argon). A rigorous study would involve detector simulation, cuts of data, and background modelling, which are beyond the scope of this work, so I concentrate on predicting the signal, which I take simply to be a single photon, with reconstruction efficiency, provided in [369, fig. 4.26]. Effects such as detector resolution are ignored.

In this work, the differential event rate $\mathrm{d}N/\mathrm{d}E$ is calculated, in a manner similar to the oscillation studies, where E is either the energy of the SM neutrino E_ν, or of the HNL E_4, depending on which option is more convenient to calculate. Consider an HNL produced at location $\vec{x}_\mathrm{p}$, which then decays at $\vec{x}_\mathrm{d}$ inside the detector. The event spectrum is calculated by evaluating the integral

$$\frac{\mathrm{d}N}{\mathrm{d}E} = N_\mathrm{mod} \sum_\mathrm{T} \iiint \mathrm{d}^3\vec{x}_\mathrm{p} \iint \mathrm{d}\Omega_\mathrm{s} \frac{L^2_\mathrm{ND}}{|\vec{x}_\mathrm{p}|^2} \frac{\mathrm{d}^2\Phi}{\mathrm{d}\Omega \mathrm{d}E_\nu} \frac{\mathrm{d}E_\nu}{\mathrm{d}E} \cdot P_\mathrm{osc} \cdot \rho_\mathrm{T}(\vec{x}_\mathrm{p}) \frac{\mathrm{d}\sigma_\mathrm{T}}{\mathrm{d}\Omega_\mathrm{s}} \cdot P_\mathrm{dec} \cdot \varepsilon(p_4), \quad (5.2)$$

where $N_\mathrm{mod} = 4$ is the number of detector modules; the sum $\sum_\mathrm{T}$ is over the targets (electrons, protons, neutrons, and nuclei); the integral $\iiint \mathrm{d}^3\vec{x}_\mathrm{p}$ is over the HNL-production point; the solid-angle integral $\iint \mathrm{d}\Omega_\mathrm{s}$ is over the directions of the final-state HNL from upscattering, $(\vec{x}_\mathrm{d} - \vec{x}_\mathrm{p})/|\vec{x}_\mathrm{d} - \vec{x}_\mathrm{p}|$, which point in the direction of the detector; the differential flux $\mathrm{d}^2\Phi/(\mathrm{d}\Omega \mathrm{d}E_\nu)$ of SM neutrinos is evaluated at the distance L_ND (the near-detector baseline), whence $L^2_\mathrm{ND}/|\vec{x}_\mathrm{p}|^2$ is the geometric suppression, and $\mathrm{d}E_\nu/\mathrm{d}E$ is the density of states for the particle with energy E (either the neutrino energy, in which case the factor is just one, or the HNL energy); P_osc is the neutrino oscillation probability; $\rho_\mathrm{T}(\vec{x}_\mathrm{p})$ is the target density, normalised *per nucleon*, at $\vec{x}_\mathrm{p}$; $\mathrm{d}\sigma_\mathrm{T}/\mathrm{d}\Omega_\mathrm{s}$ is the cross section for a SM neutrino upscattering on target T; P_dec is the probability for the HNL to decay inside the detector, whose precise functional form depends on the geometrical simplifications made; and $\varepsilon(p_4)$ is the reconstruction efficiency for HNL momentum p_4. Note that here we have ignored the dependence of $\varepsilon(\,\cdot\,)$ on the direction of the photon, produced from HNL decay.

I use the two-flavour effective vacuum probability for P_osc,

$$P_\mathrm{osc} = 0.943 \cdot \sin^2\left(\frac{\Delta m^2 |\vec{x}_p|}{4E_\nu}\right), \qquad \text{where} \qquad \Delta m^2 = 2.523 \cdot 10^{-3}\,\mathrm{eV}^2, \quad (5.3)$$

which speeds up the computation compared to the full three-flavour formula; matter effects alter the probability only at the $\mathcal{O}(1\%)$ level. Note that for the near detector, oscillations can be neglected, so I set $P^\mathrm{ND}_\mathrm{osc} = 1$. I assume an homogeneous density for all cases, $\rho_\mathrm{T}(\vec{x}_\mathrm{p}) = \text{const}$. The dipole cross section $\mathrm{d}\sigma_\mathrm{T}/\mathrm{d}\Omega_\mathrm{s}$ can be found in [353, 354], and is presented explicitly in appendix B.1. The decay width γ due to the dipole operator is

$$\gamma \equiv \frac{M_4}{p_4}\Gamma_0, \qquad \text{where} \qquad \Gamma_0 = \frac{|d_\alpha|^2 M_4^3}{4\pi} \quad (5.4)$$

is the decay width in the HNL's rest frame (also found in *ibid.*). The reconstruction efficiency $\varepsilon(p_4)$ is constructed by transforming the photon reconstruction efficiency $\varepsilon_\gamma(p_\gamma)$ via the procedure described in appendix B.2, for which I am grateful to Jing-Yu Zhu. In the following sections, I detail the specific assumptions used in the cases of the outside and inside event rates, based on their different geometries.

5.3.1 Outside event rate

The outside event rate requires us to integrate over the possible production points in the Earth, which are located mostly on the off-axis parts of the neutrino beam. I obtained spectra of the flux at various off-axis angles from Laura Fields' personal webpage [370]. Unfortunately, the website is no longer publicly available, but plots of the off-axis flux can be found in [356, fig. 5.4]. In the original files provided by Fields, the spectrum of the largest angle had an extremely large number of events at very low energies. I did not use these data, and took $\theta_\mathrm{b}^\mathrm{max} = 62.72\,\mathrm{mrad}$ as the maximum beam angle. Incidentally, this is also the largest angle of *ibid.* I used GSL's bilinear-interpolation routine to obtain the differential flux as a continuous function of beam angle and neutrino energy.

Kinematics Since it is much easier to evaluate the SM neutrino's energy as a function of the HNL energy $E_\nu(E_4)$, than the other way around, $E_4(E_\nu)$, the spectrum is evaluated with $E = E_4$ in eq. (5.2), namely $\mathrm{d}N/\mathrm{d}E_4$. Simple energy-momentum conservation for two-to-two scattering, where the target particle is at rest, yields

$$E_\nu(E_4) = \frac{M_\mathrm{T} E_4 - M_4^2/2}{M_\mathrm{T} - E_4 + p_4 \cos\theta_\mathrm{s}}, \tag{5.5}$$

where M_T is the target particle's mass. In addition, the cross section $\mathrm{d}\sigma_\mathrm{T}/\mathrm{d}\Omega_\mathrm{s}$ has to be converted to the form $\mathrm{d}\sigma_\mathrm{T}/\mathrm{d}Q^2$, expressions for which are provided in appendix B.1. The factor $\mathrm{d}E_\nu/\mathrm{d}E_4$ can be combined with the cross section to yield the convenient expression

$$\frac{\mathrm{d}\sigma_\mathrm{T}}{\mathrm{d}\Omega_\mathrm{s}} \cdot \frac{\mathrm{d}E_\nu}{\mathrm{d}E_4} = \frac{1}{2\pi} \frac{\mathrm{d}\sigma_\mathrm{T}}{\mathrm{d}Q^2} \frac{\mathrm{d}Q^2}{\mathrm{d}E_\nu} \frac{\mathrm{d}E_\nu}{\mathrm{d}\cos\theta_\mathrm{s}} \frac{\mathrm{d}E_\nu}{\mathrm{d}E_4} = \frac{1}{2\pi} \frac{\mathrm{d}\sigma_\mathrm{T}}{\mathrm{d}Q^2} \cdot \frac{2 M_\mathrm{T} E_\nu^2 p_4}{M_\mathrm{T} E_4 - M_4^2/2}, \tag{5.6}$$

where $(2\pi)^{-1}$ is the probability density for the φ_s angle. (Note that a rigorous derivation would use the triple product rule, as the variables E_ν, E_4 and $\cos\theta_\mathrm{s}$ are not independent variables, however the difference is only an overall sign, which is presumably related to flipping the boundary conditions.)

Also note that E_ν depends on the target's mass M_T. This means that each quantity containing E_ν, like the flux or oscillation probability, needs to be evaluated separately for each target. In order to make this computationally efficient, I precomputed the quantities depending only on kinematics, such as the cross section and decay probability, in a table of values at fixed E_ν and Q^2.

FD geometry I took the Earth's mass density to be $2.9\,\mathrm{g/cm^3}$, which is roughly the surface density, although for the lowest depths reached by the neutrinos at $\theta_\mathrm{b}^\mathrm{max}$, the density can reach $3.375\,\mathrm{g/cm^3}$ [371]. To evaluate the integral over the point of production $\vec{x}_\mathrm{p}$, we use spherical coordinates, where $r_\mathrm{p} \equiv |\vec{x}_\mathrm{p}|$, θ_b is the polar angle (with respect to the beam axis), and φ_b is the azimuthal angle. Let the beam axis, shown in fig. 5.7 (left), be the X axis; let the perpendicular Y axis lie in the horizontal plane containing the X axis; let the Z axis be vertical; here, the origin lies at the beam source, at the surface of the Earth, and at $X = 1297\,\mathrm{km}$ is the far detector, also at the surface of the Earth. Note that the lines in shown in fig. 5.7 (left) do not represent latitudes and longitudes, and the Z axis is not parallel to the north-south axis.

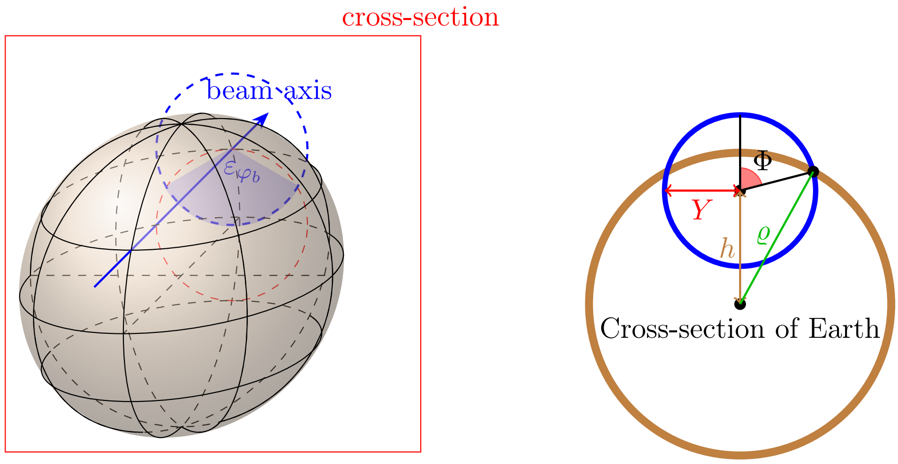

Figure 5.7: Left: 3D geometry of the outside event-rate integral for the far detector. Right: cross section of the Earth, showing the integral limits for φ_{b}. Reused from [332].

With the approximations made, the integrand of eq. (5.2) is independent of φ_{b}, which means there is a partial cylindrical symmetry that is broken by the boundary conditions imposed by the Earth (outside of which I take the mass density to be zero). Therefore, consider a specific radius r_{p} and polar angle θ_{b}, which defines the coordinate $(X, Y) = r_{\mathrm{p}} \cdot (\cos\theta_{\mathrm{b}}, \sin\theta_{\mathrm{b}})$ at $Z = 0$. The integral over φ_{b} is simply the angular size $\Delta\varphi_{\mathrm{b}} = 2(\pi - \Phi)$ that is contained in the Earth. The definition of Φ is shown in fig. 5.7, which is a cross section perpendicular to the beam axis at X. I have defined $h = \sqrt{R_\oplus^2 - (L_{\mathrm{FD}}/2)^2}$ to be the height of the horizontal plane at $Z = 0$, where $R_\oplus = 6371\,\mathrm{km}$ is the Earth's radius; Y is simply the coordinate $Y = r_{\mathrm{p}} \sin\theta_{\mathrm{b}}$; and $\varrho = \sqrt{R_\oplus^2 - (X - L_{\mathrm{FD}}/2)^2}$ is the radius of the circular boundary of the Earth within the cross-sectional plane. (Note that $|X - L_{\mathrm{FD}}/2|$ is the perpendicular distance of the cross-sectional plane to the centre of the Earth.) From these quantities, one obtains

$$\Delta\varphi_{\mathrm{b}}^{\mathrm{FD}}(r_{\mathrm{p}}, \theta_{\mathrm{b}}) = 2 \arccos\left(\frac{Y^2 + h^2 - \varrho^2}{2hY}\right). \tag{5.7}$$

Note that this assumes the existence of the triangle shown in fig. 5.7 (right), which is not the case for $Y = 0$, in which case $\Delta\varphi_{\mathrm{b}} = 2\pi$ if $X \in [0, L_{\mathrm{FD}}]$; if the argument of arccos is larger than one, then the blue circle lies entirely within the Earth (the brown circle), whence $\Delta\varphi_{\mathrm{b}} = 2\pi$; and if the argument of arccos is less than minus one, then the blue circle resides outside the Earth, and $\Delta\varphi_{\mathrm{b}} = 0$.

ND geometry The above comments for calculating eq. (5.7) do not apply for the near detector, for which $\Delta\varphi_{\mathrm{b}}^{\mathrm{ND}} = 2\pi$, as even at the maximum beam angle $\theta_{\mathrm{b}}^{\mathrm{max}}$, the SM-neutrino path lies within the Earth, taking the ND depth to be 62 m (fig. 5.5). Note that the neutrinos come from meson decay in the decay pipe, which has a non-trivial extent; this violates my assumption of a point-like source, however since I assume an effective point source at the target (MCZero), which is behind the decay pipe, accounting for the physical extent of the decay pipe will only increase the flux. However, I exclude the region around the decay pipe, setting $r_{\mathrm{p}}^{\mathrm{min}} = 270\,\mathrm{m}$, as the $1/r_{\mathrm{p}}^2$ geometric factor for the flux will not hold in that region.

Since the ND is so close to the Earth's surface, the density of the soil and rock is less than 2.9 g/cm^3, the value we used for the FD analysis. The Earth's crust has a mass density of 2.6 g/cm^3 [371], however soil has a density of 1.1 – 1.6 g/cm^3 [372], so I took an estimated average density of 2 g/cm^3.

Targets For both near and far detectors, I used the nuclei abundances in the crust from [373, §14.17], the most significant being oxygen, silicon, aluminium, iron, calcium, sodium, magnesium, potassium, and titanium. Note that the coherent scattering on nuclei attains an enhancement factor of Z^2/A, where Z is the proton number and A is the atomic mass. Therefore, heavy elements of low abundance can still be relevant due to this enhancement.

Solid-angle integral For the outside events, we make the approximation that the detector can be treated as a point, ignoring its geometry. To justify this approximation, consider incoming HNLs from the perspective of the far detector. If an HNL is created at a distance ℓ away from the detector, it has a survival probability of $e^{-\gamma\ell}$. If we ignore the variation of flux and cross section, then the number of HNLs created at a distance ℓ away from the detector scales as ℓ^2. Therefore, the number of incoming HNLs from a distance ℓ is roughly $\ell^2 e^{-\gamma\ell}$, which has a maximum at $\ell_{\text{max}} = 2/\gamma$. For energies of the GeV order, and for parameter values relevant for the outside-event exclusion curve, we have $\ell_{\text{max}} \sim 100\,\text{km}$, which provides a rough value for the typical distance an HNL travels before decaying inside the far detector. The detector size takes values 10 – 60 m, whence the angular size of the far detector from a newly created HNL is $10\,\text{m}/100\,\text{km} \sim 10^{-4}$ rad. For the far detector, this approximation is valid. For the near detector, these arguments do not work due to the small baseline; however even using the same approximations, the outside events only marginally improve the exclusion curve, so my results would not drastically change if we ignored outside events at the near detector.

When we make the approximation of a point-like detector, this also assumes that variations of the cross section, with respect to the different HNL trajectories originating from $\vec{x}_{\text{p}}$, can be neglected. Furthermore, it ignores the varying path lengths of the HNL inside the detector, which determine the locations of possible decay. The integral over the solid angle is then replaced with the solid angle

$$\Delta\Omega_{\text{s}} = \sin\theta_{\text{s}}\Delta\theta_{\text{s}}\Delta\varphi_{\text{s}} = \sin\theta_{\text{s}} \cdot 4 \arctan\left(\frac{L_{\text{d}}}{2\ell}\right) \arctan\left(\frac{L_{\text{h}}}{2\ell}\right), \tag{5.8}$$

where $L_{\text{d}} = 58.2\,\text{m}$ is the depth of the detector, $L_{\text{h}} = 12\,\text{m}$ is its height, and ℓ is the distance to the detector from production point $\vec{x}_{\text{p}}$. Elementary trigonometry yields

$$\ell = \sqrt{L_{\text{BL}}^2 + r_{\text{p}}^2 - 2L_{\text{BL}} r_{\text{p}} \cos\theta_{\text{b}}}, \tag{5.9}$$

where the baseline $L_{\text{BL}} = L_{\text{FD,ND}}$, depending on whether we are considering the near or far detector. The decay probability is

$$P_{\text{dec}} = e^{-\gamma\ell}\left(1 - e^{-\gamma L_{\text{w}}}\right), \tag{5.10}$$

where $L_{\text{w}} = 14\,\text{m}$ is the width of the detector, which I have taken to be the characteristic HNL path length inside the detector. Note that in the limit of large ℓ and small γL_{w}

(*i.e.* when we are far away from the detector, and have a long decay length with respect to the detector size),

$$P_{\mathrm{dec}} \cdot \Delta\Omega_s = e^{-\gamma\ell} \sin\theta_{\mathrm{s}} \gamma L_{\mathrm{w}} L_{\mathrm{d}} L_{\mathrm{h}}/\ell^2 \propto V_{\mathrm{det}}/\ell^2, \tag{5.11}$$

whence we see the signal scales with the detector volume and its angular size $\propto \ell^{-2}$. The angle θ_{s} can be determined as

$$\cos\theta_{\mathrm{s}} = \frac{L_{\mathrm{BL}} \cos\theta_{\mathrm{b}} - r_{\mathrm{p}}}{\ell}, \tag{5.12}$$

although the expression can violate the condition $|\cos x| \leq 1$, due to numerical artefacts resulting in the denominator being slightly smaller than the numerator; in this case I set $\cos\theta_{\mathrm{s}}$ to the sign of the numerator.

Other approximations The oscillation probability contains fast wiggles at low HNL energies E_4, as this also implies low E_ν. This can slow the integrator, which has to scan at fine intervals of r_{p} to resolve the peaks and troughs of the $\sin^2(\omega r_{\mathrm{p}})$ oscillation probability. Assuming $E_\nu \sim E_4$, I set P_{osc} to its averaged value of 1/2, when

$$E_4 < \frac{1}{4\pi} \cdot \frac{\Delta m^2 L_{\mathrm{BL}}}{4}, \tag{5.13}$$

which is the fourth trough of the oscillation probability. The interval to the next trough is $\frac{1}{4\cdot 5\cdot \pi} \frac{\Delta m^2 L_{\mathrm{BL}}}{4} \sim 6.6 \cdot 10^{-2}\,\mathrm{GeV}$.

Finally, for larger masses, which I define to be $M_4 > 10^{-2}\,\mathrm{GeV}$, I restrict the boundary values of r_{p}, as for these masses the decay length is smaller, and the HNL production occurs for $\ell < 10/\gamma$; otherwise I simply set $r_{\mathrm{p}}^{\mathrm{min}} = 0$ and $r_{\mathrm{p}}^{\mathrm{max}} = 1.5 \cdot L_{\mathrm{BL}}$. The explicit expressions for $r_{\mathrm{p}}^{\mathrm{min}}$ and $r_{\mathrm{p}}^{\mathrm{max}}$ can be found in our paper [332], eq. (C.6), however note that there is a typo: $\hat{\ell}$ should be defined as $10/(L_{\mathrm{BL}}\gamma)$, as $\ell_{\mathrm{max}} = 10/\gamma$. I also exclude the interior of the detector, namely when $Y < 15\,\mathrm{m}$, $|X - L_{\mathrm{BL}}| < L_{\mathrm{d}}$.

Final expression and result The final expression of the approximated integral for the outside-event spectrum is

$$\begin{aligned} \frac{\mathrm{d}N}{\mathrm{d}E_4} =& N_{\mathrm{mod}}\rho_{\mathrm{N}} \int_0^{\theta_{\mathrm{b}}^{\mathrm{max}}} \sin\theta_{\mathrm{b}} \mathrm{d}\theta_{\mathrm{b}} \int_{r_{\mathrm{p}}^{\mathrm{min}}}^{r_{\mathrm{p}}^{\mathrm{max}}} L_{\mathrm{ND}}^2 \mathrm{d}r_{\mathrm{p}} \times \\ & \sum_{\mathrm{T}} \left[\frac{\mathrm{d}^2\Phi}{\mathrm{d}\Omega_{\mathrm{b}} \mathrm{d}E_\nu} P_{\mathrm{osc}} \left(\frac{r_{\mathrm{p}}}{E_\nu} \right) \frac{\Delta\varphi_{\mathrm{b}}}{2\pi} \cdot \alpha_{\mathrm{T}} \frac{\mathrm{d}\sigma_{\mathrm{T}}}{\mathrm{d}Q^2} \frac{2M_{\mathrm{T}} E_\nu^2 p_4}{M_{\mathrm{T}} E_4 - M_4^2/2} \cdot P_{\mathrm{dec}} \Delta\Omega_s \varepsilon(p_4) \right], \end{aligned} \tag{5.14}$$

where ρ_{N} is the nucleon number density of the Earth's surface, and α_{T} is the abundance of target T. Note that for nucleons, $\alpha_{\mathrm{T}} = 1/2$ is already contained in eq. (B.3). A few example spectra for various masses M_4 are shown in fig. 5.8. The dashed lines indicate when the probability is replaced with its averaged-out value. Note the sharp peak at low energies for the lowest mass $M_4 = 10^{-3}\,\mathrm{GeV}$ is due to the $1/Q^2$ factor in the cross section.

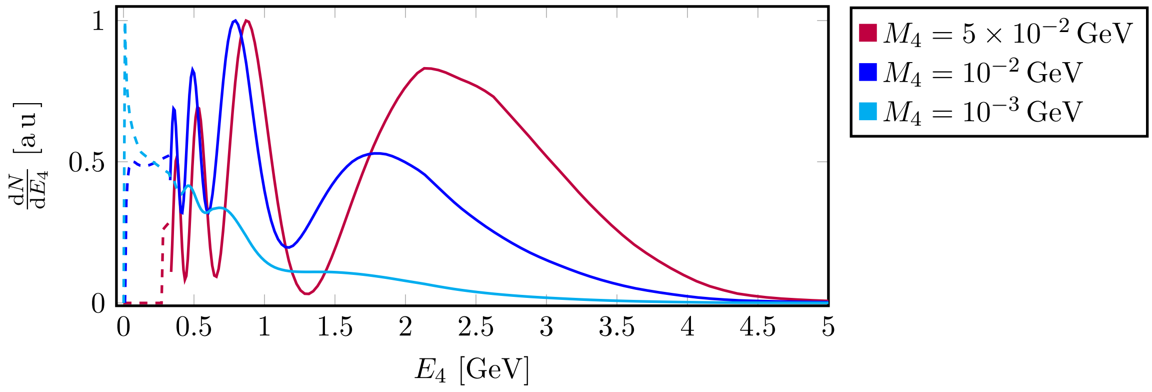

Figure 5.8: Some example spectra for outside events at the far detector, reused from [332]. The spectra have been normalised so that their peak value is at 1.

5.3.2 Inside event rate

For the inside events, I make the assumption that the flux inside the detector is collimated, as the size of the detector is very small compared to the distance to the neutrino source. This entails ignoring variations with the production point $\vec{x}_\mathrm{p}$ of the flux inside the detector. Similarly, I ignore variations in the oscillation probability, by setting $|\vec{x}_\mathrm{p}| = L_\mathrm{BL}$. This makes the flux and oscillation probability independent of the production point $\vec{x}_\mathrm{p}$; if we calculate the spectrum as a function of E_ν, we can then factorise the flux and oscillation probability outside of the integral,

$$\frac{\mathrm{d}N}{\mathrm{d}E_\nu} = N_\mathrm{mod}\frac{L_\mathrm{ND}^2}{L_\mathrm{BL}^2}\frac{\mathrm{d}^2\Phi}{\mathrm{d}\Omega\mathrm{d}E_\nu}P_\mathrm{osc}\left(\frac{L_\mathrm{BL}}{E_\nu}\right)\rho_\mathrm{N}\sum_\mathrm{T}\iiint \mathrm{d}^3\vec{x}_\mathrm{p}\iint \mathrm{d}\Omega_\mathrm{s}\alpha_\mathrm{T}\frac{\mathrm{d}\sigma_\mathrm{T}}{\mathrm{d}\Omega_\mathrm{s}}\cdot P_\mathrm{dec}\cdot\varepsilon(p_4). \quad (5.15)$$

Just like for the outside events, I assume the detector density is homogeneous; ρ_N is the nucleon number density of the detector, which is calculated by dividing the fiducial mass by the detector volume and atomic mass unit: $\rho_\mathrm{N} = M_\mathrm{fid}/(V_\mathrm{det}u_\mathrm{AMU})$. The mass density obtained this way differs slightly from the density of liquid argon, presumably due to the presence of electronics in the detector. The possible targets for this case are only electrons, nucleons, and Argon nuclei. This abundance of argon is assumed to be one: $\alpha_\mathrm{Ar} = 1$.

Kinematics Since we are evaluating the cross section at fixed E_ν, the kinematic relations have to be altered. By evaluating $Q^2 = -(p_\nu - p_4)^2 = -(p_\mathrm{T}^\mathrm{i} - p_\mathrm{T}^\mathrm{f})^2$, we can obtain

$$(E_\nu + M_\mathrm{T})E_4 - (M_\mathrm{T}E_\nu + M_4^2/2) = E_\nu p_4\cos\theta_\mathrm{s}. \quad (5.16)$$

Squaring both sides yields a quadratic equation, which can be solved to obtain $E_4(E_\nu)$. Defining

$$\begin{gathered}A_\pm = M_T + E_\nu(1\pm\cos\theta_\mathrm{s}),\quad B = M_T E_\nu + M_4^2/2,\quad E_4^0 = B/A_-,\\ \Delta = (M_4/B)^2A_+A_-,\quad C = \sqrt{1-\Delta},\quad E_4 = E_4^0\left[1-(1-C)E_\nu\cos\theta_\mathrm{s}/A_+\right],\end{gathered} \quad (5.17)$$

where E_4^0 is the HNL energy in the ultrarelativistic limit $E_4 = p_4$. One can then obtain

$$\frac{Q^2}{2M_\mathrm{T}} = E_\nu - E_4(E_\nu) = \frac{E_\nu^2(1-\cos\theta_\mathrm{s}) - M_4^2/2}{A_-} + \frac{B(1-C)}{A_+A_-}E_\nu\cos\theta_\mathrm{s}, \quad (5.18)$$

where the RHS is used in the calculation, as $E_\nu - E_4$ is numerically unstable for small four-momentum transfer $Q^2 \ll 1$, when $\cos\theta_\mathrm{s} \sim 1$. The derivative may be calculated as

$$\frac{\mathrm{d}Q^2}{\mathrm{d}\cos\theta_\mathrm{s}} = -2M_\mathrm{T}\frac{\mathrm{d}E_4}{\mathrm{d}\cos\theta_\mathrm{s}} = \frac{2M_\mathrm{T}E_\nu}{A_+}\left[\frac{2E_4E_\nu\cos\theta_\mathrm{s}}{A_-} + E_4^0C + \frac{(M_4E_\nu\cos\theta_\mathrm{s})^2}{A_-BC}\right]. \tag{5.19}$$

Note that I require $M_4 < E_4 < E_\nu$ and $\Delta \geq 0$, otherwise no such final-state energy exists. Furthermore, in the ultrarelativistic limit, there will be small quantities such as Δ in $1 - C$, which needed to be expanded to ensure numerical stability. With these expressions, we can calculate

$$\frac{\mathrm{d}\sigma_\mathrm{T}}{\mathrm{d}\Omega_\mathrm{s}} = \frac{1}{2\pi}\frac{\mathrm{d}\sigma_\mathrm{T}}{\mathrm{d}Q^2}\frac{\mathrm{d}Q^2}{\mathrm{d}\cos\theta_\mathrm{s}}. \tag{5.20}$$

Detector geometry To simplify the integration, I model the detector as a cylinder, and use cylindrical coordinates (ρ, z, θ). There is a cylindrical symmetry, as the integrand of eq. (5.15) does not depend on θ. The integral over the production point becomes then $\iiint \mathrm{d}^3\vec{x}_\mathrm{p} = 2\pi \iint \rho\mathrm{d}\rho\mathrm{d}z$, where $z \in [0, L_\mathrm{d}]$ and $\rho \in [0, r_\mathrm{d}]$, where r_d is an effective radius for the detector, which is chosen so that the area of the cylinder's cross section is the same as the detector's, $A_\mathrm{det} = \pi r_\mathrm{d}^2 = L_\mathrm{w}L_\mathrm{h}$. The probability to decay inside the detector is then

$$P_\mathrm{dec}(\gamma\ell) = 1 - \exp(-\gamma\ell), \tag{5.21}$$

where ℓ is the length of the HNL's path inside the detector. This is depicted in fig. 5.9.

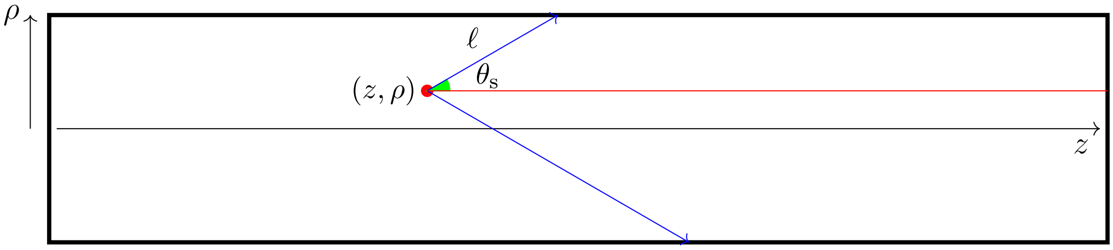

Figure 5.9: An incoming neutrino scatters at (ρ, z) in a cylindrical detector module. In blue are two possible paths for the sterile neutrinos, at constant scattering angle θ_s. In red is the trajectory of the neutrino, had it not scattered. Modified from our paper [332].

The path length ℓ depends on both scattering angles θ_s and φ_s, as well as the production point (ρ, z). In order to simplify the integral, I will use the value of ℓ at $\rho = 0$, $\ell_0 \equiv \ell(\rho = 0)$, which allows the ρ and φ_s integrals do be factorised out. (The integral over ρ will just yield the detector cross-sectional area A_det.) This approximation is actually exact if the HNL path intersects the end of the detector, instead of the side (like the paths shown in fig. 5.9), in which case $\ell = (L_\mathrm{d} - z)\sec\theta_\mathrm{s}$ for the right-hand end, and $\ell = z\sec\theta_\mathrm{s}$ for the left-hand end. To investigate the validity of this approximation, let us consider the case when the HNL path intersects the sides of the detector, as shown in fig. 5.9. In this case, ℓ is defined by the equation

$$(\ell\sin\theta_\mathrm{s}\cos\varphi_\mathrm{s} + \rho)^2 + \ell^2\sin^2\theta_\mathrm{s}\sin^2\varphi_\mathrm{s} = r_\mathrm{d}^2. \tag{5.22}$$

Solving this yields, assuming $\theta_\mathrm{s} \in (0, \pi)$,

$$\ell = \ell_0 \left[\sqrt{1 - x^2 \sin^2 \varphi_\mathrm{s}} - x \cos \varphi_\mathrm{s}\right], \qquad \text{where} \qquad x \equiv \rho / r_\mathrm{d}, \qquad \ell_0 = r_\mathrm{d} \operatorname{cosec} \theta_\mathrm{s}. \tag{5.23}$$

Averaging over φ_s,

$$\langle \ell \rangle = \int_0^{2\pi} \ell \frac{\mathrm{d}\varphi_\mathrm{s}}{2\pi} = \ell_0 \frac{2}{\pi} E(x), \tag{5.24}$$

where $E(\,\cdot\,)$ is the complete elliptic integral of the second kind,

$$E(k) = \int_0^{\pi/2} \sqrt{1 - k^2 \sin^2 \theta} \mathrm{d}\theta. \tag{5.25}$$

In the limit of small $\gamma\ell$, the decay probability simply becomes $\gamma\ell$, and we can use the above result to calculate the ratio of the exact result to our approximation,

$$\Pi \left(\gamma\ell \to 0\right) = \frac{2}{\pi} \int_0^1 2x E(x) \mathrm{d}x \approx 0.8. \tag{5.26}$$

To improve on this, I define a penalty term

$$\Pi \left(\gamma\ell_0\right) = \frac{\langle P_\mathrm{dec}(\gamma\ell)\rangle}{\langle P_\mathrm{dec}(\gamma\ell_0)\rangle} = \left[\int_0^1 \int_0^{2\pi} \left(1 - e^{-\gamma\ell}\right) \frac{\mathrm{d}\varphi_\mathrm{s}}{2\pi} 2x \mathrm{d}x\right] \Big/ \left(1 - e^{-\gamma\ell_0}\right), \tag{5.27}$$

which I multiply with the decay probability, which reduces it due to the detector geometry. I precomputed the integral and used a parameterisation for $\Pi(\,\cdot\,)$, given in appendix B.3. Note that in the limit of a large decay width, $\Pi(\gamma \to \infty) \to 1$, which implies that detector geometry becomes irrelevant for small decay length. This make intuitive sense, as the HNL decays immediately after creation, and does not probe the detector boundary.

Also note that I have calculated $\Pi(\,\cdot\,)$ with the assumption that the HNL path ends at the side of the detector; however, note that $\Pi = 1$ if the HNL path ends at the ends of the detector, whence we only underestimate the signal. Finally, we must calculate ℓ_0, taking into account the boundary conditions of the cylinder. This can simply be done by calculating the path length in both cases, when the path ends at the side of the detector, and when it ends at the end, and taking the smaller value; explicitly,

$$\ell_0 = \begin{cases} \min\left[r_\mathrm{d} \operatorname{cosec} \theta_\mathrm{s}, (L_d - z) \sec \theta_\mathrm{s}\right] & \text{if } \cos\theta_\mathrm{s} \geq 0 \\ \min\left(r_\mathrm{d} \operatorname{cosec} \theta_\mathrm{s}, z |\sec \theta_\mathrm{s}|\right) & \text{if } \cos\theta_\mathrm{s} < 0. \end{cases} \tag{5.28}$$

Final expression and result The final expression of the approximated integral for the inside-event spectrum is

$$\begin{aligned} \frac{\mathrm{d}N}{\mathrm{d}E_\nu} =& N_\mathrm{mod} \frac{L_\mathrm{ND}^2}{L_\mathrm{BL}^2} \frac{\mathrm{d}^2\Phi}{\mathrm{d}\Omega \mathrm{d}E_\nu} P_\mathrm{osc}\left(\frac{L_\mathrm{BL}}{E_\nu}\right) \rho_\mathrm{N} A_\mathrm{det} \times \\ & \sum_\mathrm{T} \int_0^{L_\mathrm{d}} \mathrm{d}z \int_{-1}^1 \mathrm{d}\cos\theta_\mathrm{s} \cdot \alpha_\mathrm{T} \frac{\mathrm{d}\sigma_\mathrm{T}}{\mathrm{d}Q^2} \frac{\mathrm{d}Q^2}{\mathrm{d}\cos\theta_\mathrm{s}} \cdot P_\mathrm{dec}(\gamma\ell_0) \Pi(\gamma\ell_0) \cdot \varepsilon(p_4). \end{aligned} \tag{5.29}$$

A few example spectra are shown in fig. 5.10. The dashed lines indicate when I replaced the oscillation probability with its averaged-out value, although this is only done for aesthetics in the case of the inside events, and the full expression is used for the calculation of the exclusion curve.

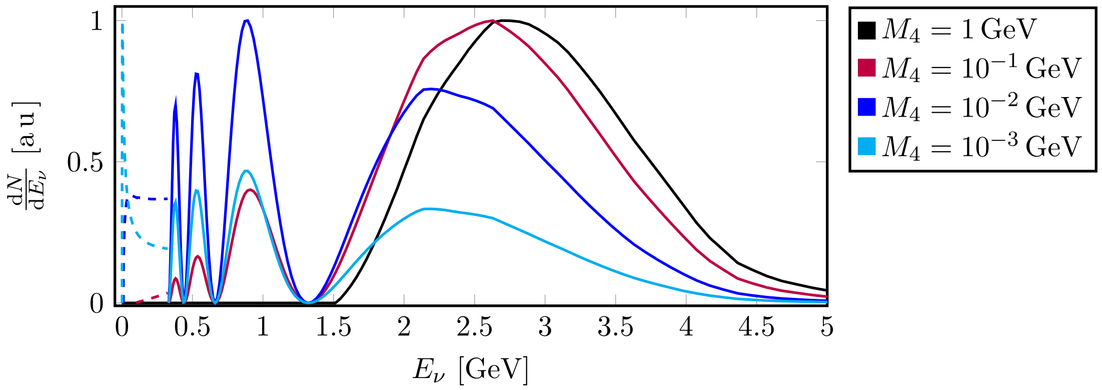

Figure 5.10: Some example spectra for inside events at the far detector, reused from [332]. The spectra have been normalised so that their peak value is at 1.

5.4 Results

In fig. 5.11, I show which types of interactions (on electrons, nucleons, or coherently on nuclei) are relevant in each area of parameter space for probing d_τ at the far detector. In dashed lines are the curves for six outside-events per year; and in solid are the curves for six inside-events per year. For the inside events, we see that coherent scattering on nuclei dominates for masses $M_4 < 0.7\,\mathrm{GeV}$, whilst for larger masses, incoherent scattering on nucleons dominates. I attribute this to the fact that larger M_4 leads to a larger Q^2, which will be suppressed by the nuclear form factor. However, the nucleon curve sharply decreases for $M_4 > 1\,\mathrm{GeV}$, due to the lack of SM neutrinos with a high enough energy to produce the HNL. For the electron, upscattering is kinematically allowed for low M_4 only, owing to its lightness, which is why the curve cuts off at $M_4 \sim 0.08\,\mathrm{GeV}$. The grey curve denotes the parameter points, where an HNL with energy 1 GeV has a decay length of 1 cm. Since the detector only has sub-centimetre resolution, parameter points to the right of this curve will not be able to resolve the unique double-bang signature of a nuclear recoil and a displaced photon. For the outside events, we see that coherent scattering always dominates, however we also see that for large moments d_τ or mass M_4, the curve disappears. This is because, as the typical decay length ℓ decreases, the allowed volume of HNL production points (such that the HNL does not decay before reaching the detector) will decrease, naïvely as ℓ^{-3}, until the number of events become negligible. Note that our approximations break down before this, as the HNLs would be able to resolve the detector geometry. In cyan, I have plotted the curve when an HNL of energy 1 GeV has a decay length of 20 m, which is roughly the size of the far detector. As we can see, it roughly matches with the upper part of the outside-events curve.

In fig. 5.12, I compare the projected sensitivity at the DUNE FD with that of SHiP. The SHiP curve was calculated by Magill, Plestid, Pospelov and Tsai [353]; the labels ECC and main refer to two types of detectors: an emulsion cloud chamber (ECC) close to the beam target, and the “main” detector. Their curve corresponds to the 95% CL sensitivity after five years of running, assuming 100 background events. The DUNE FD curves would then correspond to 10, 30, and 100 events after five years, which equate to 25, 225, and 2500 background events at 95% CL, respectively, using the relation $\text{signal} / \sqrt{\text{background}} = 2$. It’s difficult to have a full comparison of these results, without

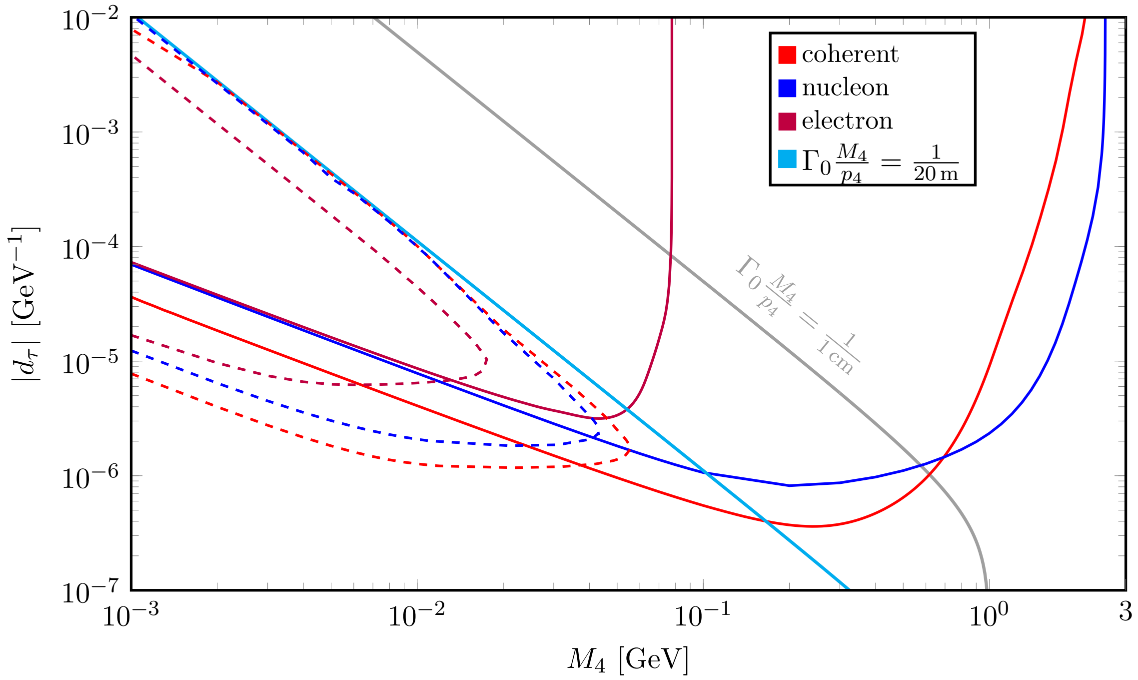

Figure 5.11: The curves for six outside- and inside-events per year, dashed and solid, respectively, at the far detector. The different colours correspond to the different types of target particles, shown in the legend. The cyan and grey lines define the points, where the typical decay length is 20 m and 1 cm, respectively, for an HNL with $E_4 = 1\,\mathrm{GeV}$. I have reused the plot in our paper [332].

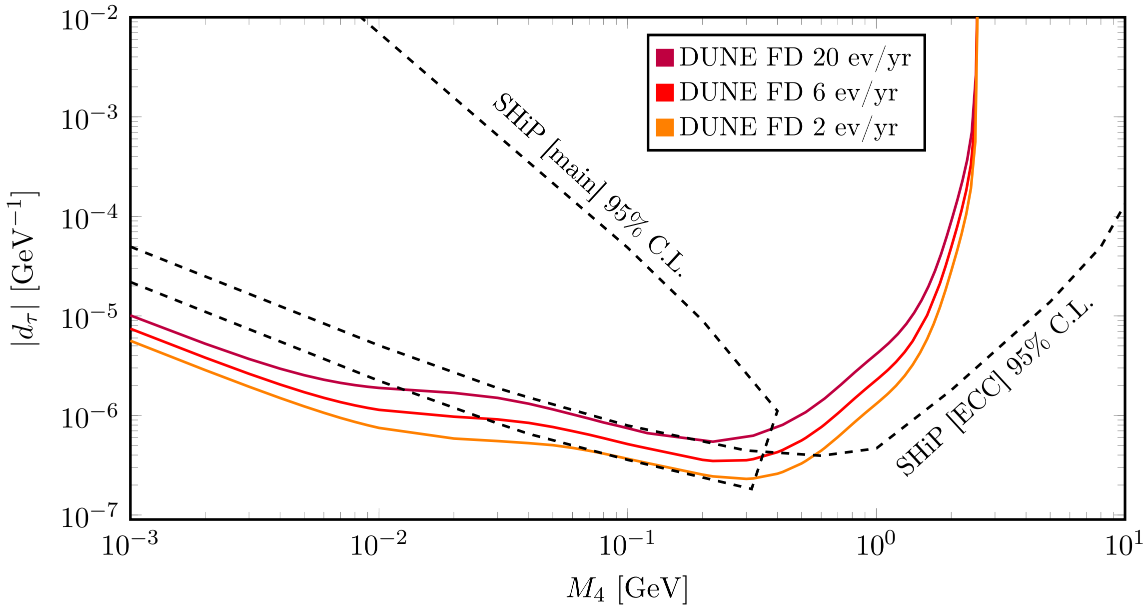

Figure 5.12: Two-, six-, and twenty-events/yr curves at the DUNE FD (orange, red, purple, respectively); and the 95% CL projected sensitivity at SHiP, from [353].

a proper background analysis as whilst DUNE will have better particle discrimination, owing to liquid argon, the beam operates at a higher POT/yr, compared with SHiP [374].

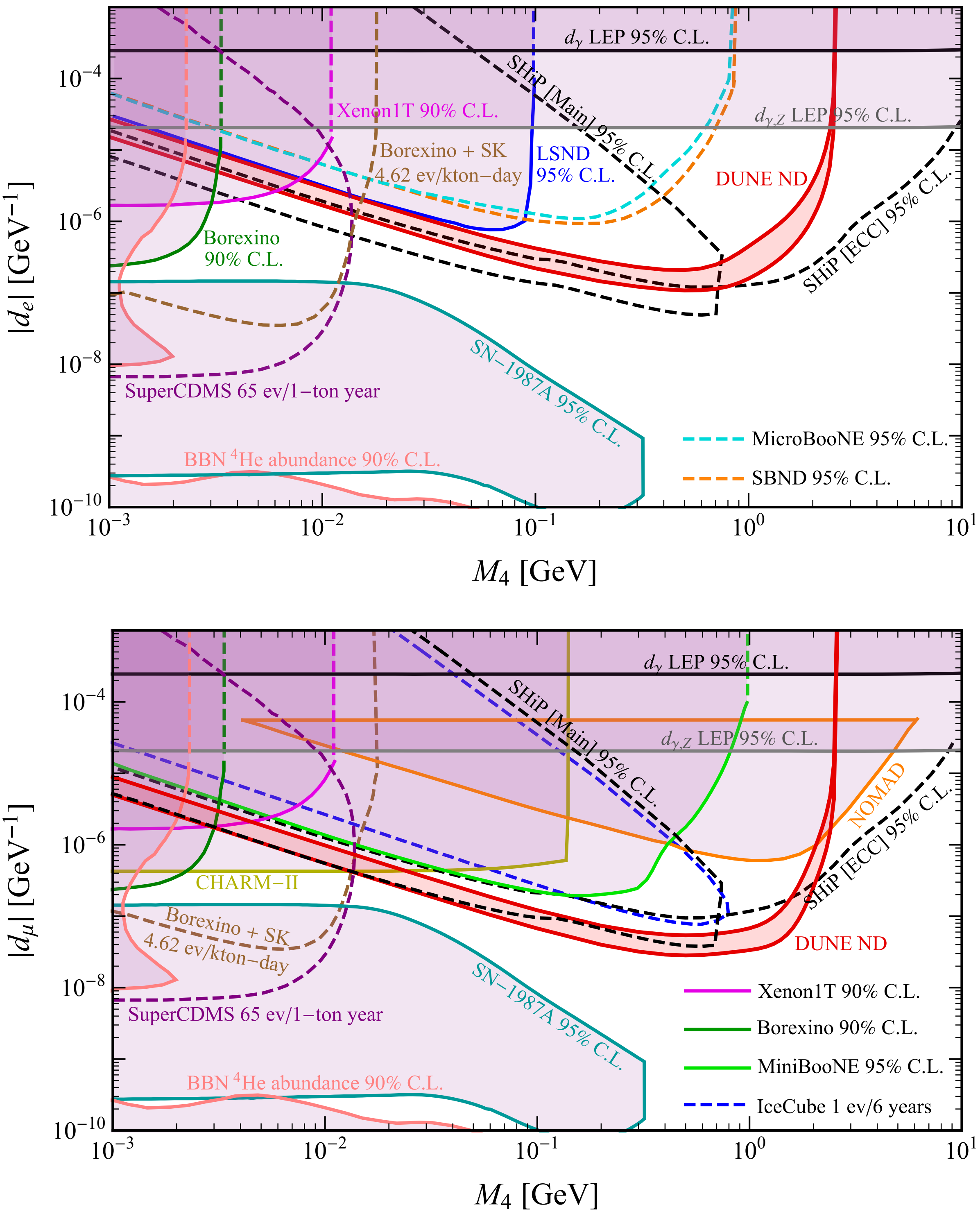

Figure 5.13: Comparison of my results (red band indicating $2-20$ events/year) for the DUNE ND, probing d_e (top) and d_μ (bottom) with existing bounds in solid, and projected or estimated ones as dashed curves (see text for details); reused from our paper [332].

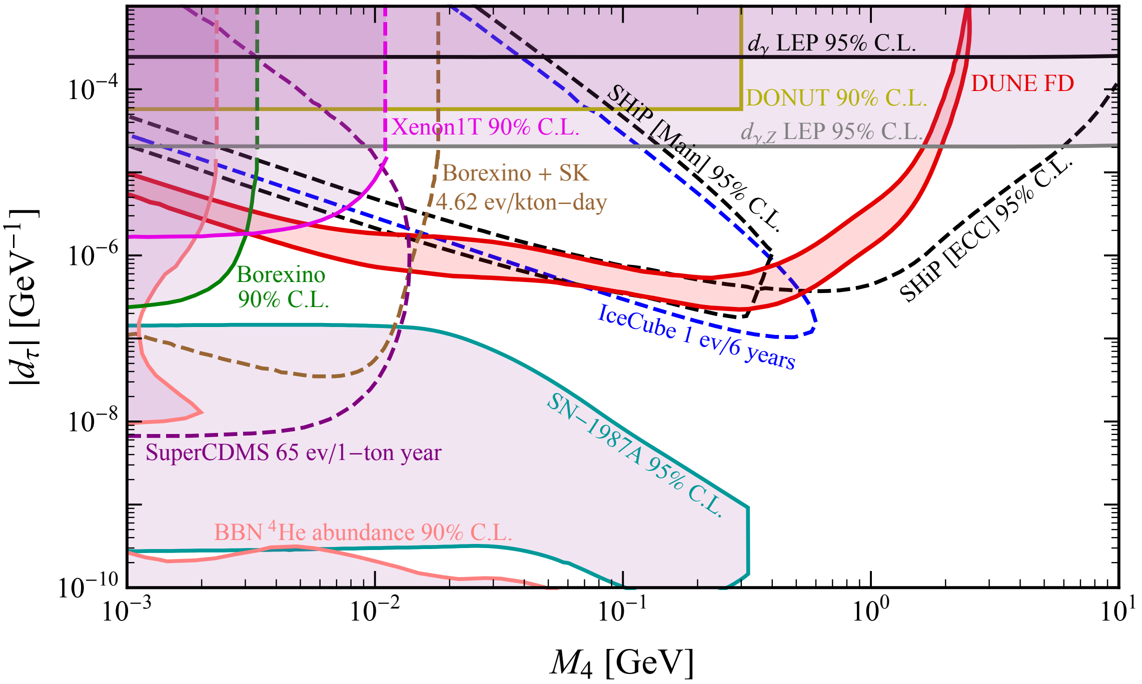

Figure 5.14: Comparison of my results (red band indicating $2-20$ events/year) with existing bounds in solid, and projected or estimated sensitivities as dashed curves (see text for details); figure reused from our paper [332].

In fig. 5.14, I show my results as a red band in the space of exclusion curves, where the band represents the region with $2-20$ events/year. At 95% CL, this would correspond to $25-2500$ background events over five years. Projected sensitivities of future experiments are plotted with a dashed curve (except for our results), as well as estimated sensitivities, which do not have a rigorous background analysis (and other experimental details like selection efficiency), and are based only on a signal rate. I am grateful to Jing-Yu Zhu for doing a literature search for all the exclusion curves, and extracting them and creating the graphics. As one can see, whilst astrophysical and cosmological probes constrain much of the parameter space at low M_4, for larger masses, only the collider bounds exist, which are relatively weak. Note that the IceCube curve is only for one event in six years of data analysed, which only corresponds to an exclusion of $1-e^{-1}\approx 63\%$, assuming no background and 100% selection efficiency. The SN1987A and LEP bounds (which are dependent on the UV completion; see the discussion in section 5.1), as well as the SHiP sensitivity are taken from [353]; Xenon1T, Borexino, BBN and ^{4}He-abundance bounds are from [354]; the estimated IceCube sensitivity (from double-bang events) is taken from [362]; the DONUT bound is actually on the SM tau-neutrino magnetic moment [375], but was reinterpreted as a bound on the transition moment at low HNL masses by [362]; the estimated sensitivity for Borexino+SK from upscattering of solar neutrinos (which partly inspired the current work) comes from [376]; and the projected sensitivity at SuperCDMS comes from [377]. The dashed lines for Borexino and Xenon1T are extrapolations of the original curves to arbitrarily large moments.

In fig. 5.13, I show my results for the sensitivity to $d_{e,\mu}$ at the DUNE ND (red band), compared with the constraints from existing data, and projections or estimations of sensitivities from other experiments, the references being the same as the d_τ case, additionally with LSND, MiniBooNE, and projections for MicroBooNE and SBND from [353]; NOMAD, originally considered in [378], and reevaluated in [353]; and the bound from CHARM-II [379], derived from the induced scattering of the muon neutrino on an electron, from [362]. As expected, the sensitivity at DUNE is much stronger for muon neutrinos, due to their dominating presence in the neutrino beam. In both cases, DUNE would be able to exclude currently unconstrained parameter space.

5.5 Conclusion and Outlook

In conclusion, the neutrino dipole portal is an interesting scenario, which may be able to explain the MiniBooNE anomaly, and which can be probed at DUNE, using both its intrinsic neutrinos at the near detector, and oscillated tau neutrinos at the far detector. DUNE can probe the transition moment for HNL masses as low as a few MeV, to a GeV. As I have already mentioned, a detailed experimental analysis for the background and selection efficiency is needed for a truly rigorous sensitivity curve. However, my results show that probing the dipole portal at DUNE is a promising venture. In addition, I did not consider HNLs that are directly produced from meson decay in the decay pipe. (This was done for the case of pure sterile-neutrino mixing for DUNE by Coloma *et al.* [380].) For example, the dipole transition moment induces HNL production from pion decay, as shown in fig. 5.15. This contribution was included in the analysis of Magill, Plestid, Pospelov and Tsai [353] via analytic methods, however a more accurate calculation would use mesons from an event generator, simulating the proton interactions on the target, and propagate them through the decay pipe, to ensure all HNLs are produced in the direction of the detector, in a calculation similar to that done here. This is the subject of ongoing work.

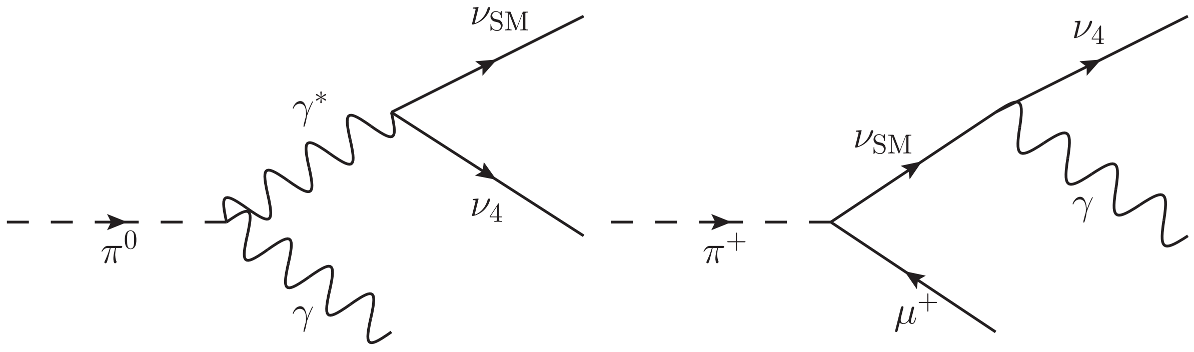

Figure 5.15: Possible decays of pions into HNLs from the dipole transition moment.

Chapter 6

Summary and Conclusion

With the completion of the theoretical development of the Standard Model of particle physics, there has been much attention and speculation on what kind of new physics lie beyond it. The phenomenon of neutrino oscillations require that the neutrinos have mass, whose generation is unknown. This work has covered phenomenological analyses of existing and future experiments in the context of neutrino oscillations and possible new physics in the neutrino sector, which I undertook during my PhD under the supervision of Prof. Thomas Schwetz-Mangold.

In chapter 3, I presented the current status of the global fit for the three-neutrino oscillation parameters. My contribution was to update the reactor analysis, using the existing code base from the previous PhD candidate Álvaro Hernández-Cabezudo. The global dataset consists of multiple opposing tendencies, with T2K and NOνA preferring different $\delta_{\rm CP}$ values in normal ordering, thus leading to their combination preferring inverted ordering, whilst the reactor data prefers normal ordering, leading to a "compromise" CP-conserving value of $\delta_{\rm CP} \approx \pi$. Despite this, the tensions within the global data set, between different experiments, are still $\leq 2\,\sigma$, using the parameter goodness-of-fit test statistic $\chi^2_{\rm PG}$. Whilst no significant tension is currently present, these opposing tendencies have continued since the previous NuFit update, and time will tell if these develop into serious tensions.

In chapter 4, I presented my work in the global FCMC statistical analysis of the sterile-neutrino hypothesis. The FCMC method is needed to evaluate the statistical significance of the sterile-neutrino hypothesis, as Wilks' theorem is violated. This method is computationally expensive, and the χ^2 routines had to be highly optimised, where analytical minimisation of pulls must be done where possible, and numerical minimisation requires a high degree of optimisation. The technical details of these aspects were presented in appendix A. In this analysis, we used the set of recent sterile-neutrino reactor experiments, as well as the limit set on the sterile mixing from solar data, to investigate the global significance of the claimed signal of new oscillations from the Neutrino-4 experiment. We found that the global significance of new oscillations is low, but that, due to the large Δm^2 of the Neutrino-4 signal, it is compatible with the other reactor experiments, but exists in a region of parameter space that is particularly difficult to probe. The CL of the exclusion curves for each experiment are generically reduced by roughly $1\,\sigma$ compared to the Wilks' theorem, indicating the importance of using a rigorous statistical method.

An analysis including the recent results from BEST, which confirmed the gallium anomaly at $> 5\,\sigma$ significance, was done with reactor data; BEST drives the significance of the evidence under the sterile-neutrino hypothesis, with it determining the mixing, and Neutrino-4 determining the mass-squared splitting. However, the gallium anomaly is in strong tension with the solar data, which is not easy to resolve. In section 4.5, I discussed possible sources of new systematic errors in the gallium experiments, which could reduce the best-fit mixing value, thus reducing the tension with solar; and also whether new physics could alleviate the solar bound. Neither avenue seems promising. With the measured ground-state gallium-neutrino cross section being highly constrained by experimental data, and with the excited-state contribution only being able to increase the theoretical prediction, relieving the gallium-solar tension remains an open question. However, there may be a case for confirming the precision of the efficiency-extrapolation method used to determine the absolute activity of the ^{51}Cr source with more direct methods that calibrate the detector efficiency and directly probe the absolute activity.

Finally, in chapter 5, I presented my results probing the neutrino dipole portal at DUNE. The dipole portal is interesting, as it provides an alternative explanation of the MiniBooNE anomaly, which is unlikely to be explained via new oscillations, as the disappearance channels from other experiments like MINOS and IceCube place strong constraints on new muon-neutrino flavour oscillations. The analysis is done assuming the domination of a single-flavour dipole transition coupling d_α of a SM neutrino of flavour α with a heavy neutral lepton. I find that DUNE will be able to explore currently unconstrained areas of the dipole parameter space, particularly at masses of hundreds of MeV, and will be competitive with other proposed experiments such as SHiP. Whilst a rigorous sensitivity curve requires a detailed analysis of experimental details like background and selection efficiency, my results show that such a search at DUNE would provide useful results. The analysis, however, ignores HNL production from meson decay in the decay pipe, and this is a future project that will explore the full potential of the DUNE ND to the dipole portal.

Appendix A

Formulae for the global FCMC sterile-neutrino analysis

A.1 DANSS

A.1.1 Covariance matrix

The explicit formula for the covariance matrix, defined in eq. (4.7), and its inverse, are

$$\begin{aligned} V_{11}^i &= \frac{R_1^i}{\Delta t_{\mathrm{T}} n_{\mathrm{T}}^i}\left(R_1^i + \frac{\Delta t_{\mathrm{T}}}{\Delta t_{\mathrm{B}}}\right), \quad V_{12}^i = \frac{R_2^i}{2\Delta t_{\mathrm{T}} n_{\mathrm{T}}^i}\left(R_1^i - \frac{\Delta t_{\mathrm{T}}}{\Delta t_{\mathrm{B}}}\right) \\ V_{22}^i &= \frac{R_2^i}{\Delta t_{\mathrm{M}} n_{\mathrm{T}}^i}\left[\frac{1}{\sqrt{R_1^i}} + \frac{R_2^i}{R_1^i}\frac{\Delta t_{\mathrm{M}}}{4\Delta t_{\mathrm{B}}} + R_2^i\frac{\Delta t_{\mathrm{M}}}{4\Delta t_{\mathrm{T}}}\right], \end{aligned} \tag{A.1}$$

and

$$\det V^i = \frac{R_2^i\sqrt{R_1^i}}{\left(n_{\mathrm{T}}^i\right)^2 \Delta t_{\mathrm{M}}\Delta t_{\mathrm{T}}}\left(R_1^i + R_2^i\sqrt{R_1^i}\cdot\frac{\Delta t_{\mathrm{M}}}{\Delta t_{\mathrm{B}}} + \frac{\Delta t_{\mathrm{T}}}{\Delta t_{\mathrm{B}}}\right), \tag{A.2}$$

$$\left(V^i\right)^{-1} = \begin{pmatrix} a_i & -b_i/2 \\ -b_i/2 & c_i \end{pmatrix}, \tag{A.3}$$

$$a_i = \frac{n_{\mathrm{T}}^i\Delta t_{\mathrm{T}}}{R_1^i}\frac{1 + \frac{R_2^i}{\sqrt{R_1^i}}\cdot\frac{\Delta t_{\mathrm{M}}}{4\Delta t_{\mathrm{B}}} + R_2^i\sqrt{R_1^i}\cdot\frac{\Delta t_{\mathrm{M}}}{4\Delta t_{\mathrm{T}}}}{R_1^i + R_2^i\sqrt{R_1^i}\cdot\frac{\Delta t_{\mathrm{M}}}{\Delta t_{\mathrm{B}}} + \frac{\Delta t_{\mathrm{T}}}{\Delta t_{\mathrm{B}}}}, \tag{A.4}$$

$$b_i = \frac{n_{\mathrm{T}}^i\Delta t_{\mathrm{M}}}{\sqrt{R_1^i}}\frac{R_1^i - \frac{\Delta t_{\mathrm{T}}}{\Delta t_{\mathrm{B}}}}{R_1^i + R_2^i\sqrt{R_1^i}\cdot\frac{\Delta t_{\mathrm{M}}}{\Delta t_{\mathrm{B}}} + \frac{\Delta t_{\mathrm{T}}}{\Delta t_{\mathrm{B}}}}, \tag{A.5}$$

$$c_i = \frac{\sqrt{R_1^i}n_{\mathrm{T}}^i\Delta t_{\mathrm{M}}}{R_2^i}\frac{R_1^i + \frac{\Delta t_{\mathrm{T}}}{\Delta t_{\mathrm{B}}}}{R_1^i + R_2^i\sqrt{R_1^i}\cdot\frac{\Delta t_{\mathrm{M}}}{\Delta t_{\mathrm{B}}} + \frac{\Delta t_{\mathrm{T}}}{\Delta t_{\mathrm{B}}}}. \tag{A.6}$$

These expressions were derived with the help of the symbolic calculator SymPy. As mentioned in the main text, these expressions are derived in the approximation of neglecting the background. In this approximation, the size of V^i is set by n_{T}^i. For the 36 bins between 1.5 − 6 MeV, the total events per day at the top baseline is $\sum_{i=1}^{36} n_{\mathrm{T}}^i = 4132.6$ events/day.

A.1.2 Minimisation over systematics

Let

$$\mathbf{D}^i \equiv \left(D_1^i \quad D_2^i\right)^{\mathrm{T}}, \qquad \mathbf{P}^i \equiv \left(P_1^i \quad P_2^i\right)^{\mathrm{T}}, \qquad \mathbf{K}^i \equiv \left(\kappa_1 P_1^i \quad \kappa_2 P_2^i\right)^{\mathrm{T}}, \tag{A.7}$$

and $\boldsymbol{\Delta}^i \equiv \mathbf{D}^i - \mathbf{P}^i$. We can then write

$$\chi^2_{\mathrm{DANSS}} = \min_{\kappa_1,\kappa_2} \left\{ \sum_{i=1}^{36} \left(\boldsymbol{\Delta}^i - \mathbf{K}^i\right) \left(V^i\right)^{-1} \left(\boldsymbol{\Delta}^i - \mathbf{K}^i\right) + \frac{\kappa_1^2 + \kappa_2^2}{\sigma^2_{\mathrm{sys}}} \right\}. \tag{A.8}$$

The minimisation over systematics can be done analytically by recognising that the problem is to minimise the degree-two multinomial

$$\sum_i \left(\sigma_k^{-2} + A\right) \kappa_1^2 - B\kappa_1\kappa_2 + \left(\sigma_k^{-2} + C\right) \kappa_2^2 - D\kappa_1 - E\kappa_2 + \chi_0^2, \tag{A.9}$$

where

$$\begin{aligned} A &= \sum_i a_i \left(P_1^i\right)^2, \quad B = \sum_i b_i P_1^i P_2^i, \quad C = \sum_i c_i \left(P_2^i\right)^2, \\ D &= \sum_i P_1^i \left(2a_i \Delta_1^i - b_i \Delta_2^i\right), \quad E = \sum_i P_2^i \left(2c_i \Delta_2^i - b_i \Delta_1^i\right), \end{aligned} \tag{A.10}$$

and χ_0^2 is the value of the χ^2 without pulls ($\kappa_1 = \kappa_2 = 0$). Then,

$$\chi^2 = \chi_0^2 - \sigma_k^2 \frac{E^2\left(1 + \sigma_k^2 A\right) + \sigma_k^2 BDE + D^2\left(1 + \sigma_k^2 C\right)}{4(1 + \sigma_k^2 A)(1 + \sigma_k^2 C) - (\sigma_k^2 B)^2}. \tag{A.11}$$

The minimum occurs at

$$\begin{aligned} \kappa_1^{\min} &= \sigma_k^2 \frac{\sigma_k^2 BE + 2(1 + \sigma_k^2 C)D}{(\sigma_k^2 B)^2 - 4(1 + \sigma_k^2 A)(1 + \sigma_k^2 C)}, \\ \kappa_2^{\min} &= \sigma_k^2 \frac{\sigma_k^2 BD + 2(1 + \sigma_k^2 A)E}{(\sigma_k^2 B)^2 - 4(1 + \sigma_k^2 A)(1 + \sigma_k^2 C)}. \end{aligned} \tag{A.12}$$

A.2 NEOS

The minimisation over the flux normalisation ξ is a simple quadratic minimisation,

$$\chi^2 = \min_{\xi} \, (\mathbf{D} - \xi\mathbf{P})^{\mathrm{T}} V^{-1} (\mathbf{D} - \xi\mathbf{P}) = c - \frac{b^2}{a} = \chi^2_{\xi=1} - \frac{(b-a)^2}{a}, \tag{A.13}$$

$$a = \mathbf{P}^{\mathrm{T}} V^{-1} \mathbf{P}, \quad b = \mathbf{P}^{\mathrm{T}} V^{-1} \mathbf{D}, \quad c = \mathbf{D}^{\mathrm{T}} V^{-1} \mathbf{D}, \quad \chi^2_{\xi=1} = (\mathbf{D} - \mathbf{P})^{\mathrm{T}} V^{-1} (\mathbf{D} - \mathbf{P}). \tag{A.14}$$

The value of ξ at which χ^2 is minimal (required to generate pseudo data) is

$$\xi_{\min} = \frac{b}{a} = 1 + \frac{\mathbf{P}^{\mathrm{T}} V^{-1} (\mathbf{D} - \mathbf{P})}{\mathbf{P}^{\mathrm{T}} V^{-1} \mathbf{P}}. \tag{A.15}$$

A.3 STEREO

A.3.1 Minimising $\xi^{\mathrm{I,II}}$

With the pull transformation eq. (4.38), $P(\alpha, \zeta)$ no longer depends on ξ, whence the ξ dependence is isolated to the pull term,

$$\operatorname{expr}\left(\alpha_l^{\mathrm{I,II}},\ \zeta_l^{\mathrm{I,II}},\ \phi_i,\ \Phi^{\mathrm{I}}\right) + \sum_{\lambda=\mathrm{I,II}} \left\{ \frac{\sum_{l=1}^{N_{\mathrm{cells}}} \left(\alpha_l^\lambda - \xi^\lambda\right)^2}{\left(\sigma_\eta^\lambda\right)^2} + \left(\frac{\xi^\lambda}{\sigma_\xi^\lambda}\right)^2 \right\}. \tag{A.16}$$

The $\xi^{\mathrm{I,II}}$-dependent part of the χ^2 function is the quadratic function

$$\left[\left(\sigma_\xi^\lambda\right)^{-2} + N_{\mathrm{cells}}\left(\sigma_\eta^\lambda\right)^{-2}\right]\xi_\lambda^2 - 2\frac{\sum_{l=1}^{N_{\mathrm{cells}}} \alpha_l^\lambda}{\left(\sigma_\eta^\lambda\right)^2}\xi_\lambda + \frac{\sum_{l=1}^{N_{\mathrm{cells}}} \left(\alpha_l^\lambda\right)^2}{\left(\sigma_\eta^\lambda\right)^2}. \tag{A.17}$$

The quadratic function $ax^2 - 2bx + c = a(x - b/a)^2 + c - b^2/a$ has a minimum value of $c - b^2/a$; this means the new pull terms for $\alpha_l^{\mathrm{I,II}}$ are

$$\frac{\sum_{l=1}^{N_{\mathrm{cells}}} \left(\alpha_l^\lambda\right)^2}{\left(\sigma_\eta^\lambda\right)^2} - \left(\frac{\sigma_\xi^\lambda}{\sigma_\eta^\lambda}\right)^2 \frac{\left(\sum_{l=1}^{N_{\mathrm{cells}}} \alpha_l^\lambda\right)^2}{\left(\sigma_\eta^\lambda\right)^2 + N_{\mathrm{cells}}\left(\sigma_\xi^\lambda\right)^2} \tag{A.18}$$

and

$$\xi^\lambda = \frac{\sum_{l=1}^{N_{\mathrm{cells}}} \alpha_l^\lambda}{N_{\mathrm{cells}} + \vartheta_\lambda}, \qquad \text{where} \qquad \vartheta_\lambda = \left(\frac{\sigma_\eta^\lambda}{\sigma_\xi^\lambda}\right)^2. \tag{A.19}$$

Equation (A.18) suffers from loss of precision in floating-point arithmetic. If we denote the pull-term for the α_l^λ by $g_\lambda(\,\cdot\,)$, then

$$\begin{aligned} g_\lambda\left(\alpha_l^\lambda\right) &= \frac{N_{\mathrm{cells}}}{\left(\sigma_\eta^\lambda\right)^2}\left\{\left\langle\alpha^2\right\rangle - \frac{N_{\mathrm{cells}}}{N_{\mathrm{cells}} + \vartheta_\lambda}\left\langle\alpha\right\rangle^2\right\} \\ &= \left(\sigma_\eta^\lambda\right)^{-2}\left\{\sum_{l=1}^{N_{\mathrm{cells}}}\left(\alpha_l^\lambda - \langle\alpha\rangle\right)^2 + \frac{1}{N_{\mathrm{cells}}^{-1} + \vartheta_\lambda^{-1}}\left\langle\alpha\right\rangle^2\right\}, \end{aligned} \tag{A.20}$$

preserves precision better than eq. (A.18), where $\langle\,\cdot\,\rangle$ represents taking the average over index l, *i.e.* $\frac{1}{N_{\mathrm{cells}}}\sum_{l=1}^{N_{\mathrm{cells}}}$.

A.3.2 Minimising Φ^{I}

With the pull transformation eq. (4.38), the Φ^{I}-dependent part is

$$\operatorname{expr}\left(\alpha_l^{\mathrm{I,II}},\ \beta_l^{\mathrm{I}},\ \zeta_l^{\mathrm{II}},\ \phi_i\right) + \left(\sigma_\zeta^{\mathrm{I}}\right)^{-2}\sum_{l=1}^{N_{\mathrm{cells}}}\left[\frac{1+\beta_l^{\mathrm{I}}}{\Phi^{\mathrm{I}}} - 1\right]^2. \tag{A.21}$$

The minimum is at

$$\sum_{l=1}^{N_{\mathrm{cells}}}\left[\frac{1+\beta_l^{\mathrm{I}}}{\Phi^{\mathrm{I}}} - 1\right]\frac{1+\beta_l^{\mathrm{I}}}{\Phi_{\mathrm{I}}^2} \propto \sum_{l=1}^{N_{\mathrm{cells}}}\left(1+\beta_l^{\mathrm{I}}\right)^2 - \left(1+\beta_l^{\mathrm{I}}\right)\Phi^{\mathrm{I}} = 0, \tag{A.22}$$

whence

$$\Phi^{\mathrm{I}}(\beta_l^{\mathrm{I}}) = \frac{\sum_{l=1}^{N_{\text{cells}}} \left(1+\beta_l^{\mathrm{I}}\right)^2}{\sum_{l=1}^{N_{\text{cells}}} \left(1+\beta_l^{\mathrm{I}}\right)}. \tag{A.23}$$

Substituting this, we have the partially minimised pull-term

$$\left(\sigma_\zeta^{\mathrm{I}}\right)^{-2} \sum_{l=1}^{N_{\text{cells}}} \left[\frac{1+\beta_l^{\mathrm{I}}}{\Phi^{\mathrm{I}}} - 1\right]^2 = \left(\sigma_\zeta^{\mathrm{I}}\right)^{-2} \left\{ N_{\text{cells}} - \frac{\left[\sum_{l=1}^{N_{\text{cells}}}\left(1+\beta_l^{\mathrm{I}}\right)\right]^2}{\sum_{l=1}^{N_{\text{cells}}}\left(1+\beta_l^{\mathrm{I}}\right)^2} \right\}. \tag{A.24}$$

This term suffers from loss of precision; to derive a form more amenable to floating-point arithmetic, first note the second term can be written as $N_{\text{cells}}(1+\langle\beta\rangle)^2/(1+2\langle\beta\rangle+\langle\beta^2\rangle)$. Defining this pull term as $h_{\mathrm{I}}(\,\cdot\,)$,

$$h_{\mathrm{I}}\left(\beta_l^{\mathrm{I}}\right) = \frac{N_{\text{cells}}}{\left(\sigma_\zeta^{\mathrm{I}}\right)^2} \cdot \frac{\langle\beta^2\rangle - \langle\beta\rangle^2}{1+2\langle\beta\rangle+\langle\beta^2\rangle} = \frac{N_{\text{cells}}}{\left(\sigma_\zeta^{\mathrm{I}}\right)^2} \frac{\sum_{l=1}^{N_{\text{cells}}}\left(\beta_l^{\mathrm{I}} - \langle\beta\rangle\right)^2}{\sum_{l=1}^{N_{\text{cells}}}(1+\beta_l^{\mathrm{I}})^2}. \tag{A.25}$$

We note that

$$\begin{aligned} h_{\mathrm{I}}\left(\beta_l^{\mathrm{I}}\right) - \sum_{l=1}^{N_{\text{cells}}}\left(\frac{\beta_l^{\mathrm{I}}}{\sigma_\zeta^{\mathrm{I}}}\right)^2 &= \frac{N_{\text{cells}}}{\left(\sigma_\zeta^{\mathrm{I}}\right)^2}\left[\frac{\langle\beta^2\rangle - \langle\beta\rangle^2}{1+2\langle\beta\rangle+\langle\beta^2\rangle} - \left\langle\beta^2\right\rangle\right] \\ &= -\frac{N_{\text{cells}}^2}{\left(\sigma_\zeta^{\mathrm{I}}\right)^2}\frac{\left(\langle\beta\rangle+\langle\beta^2\rangle\right)^2}{\sum_{l=1}^{N_{\text{cells}}}(1+\beta_l^{\mathrm{I}})^2} < 0, \end{aligned} \tag{A.26}$$

which is a good sanity check that after minimising analytically over Φ^{I}, our χ^2 value is indeed lower than it would have been otherwise.

A.3.3 Minimising ϕ_i

After the above minimisations,

$$\chi^2 = \min_{\substack{\alpha_l^{\mathrm{I,II}},\, \beta_l^{\mathrm{I,II}},\\ \phi_i}} \sum_{\lambda=\mathrm{I,II}} \left\{ \sum_{l=1}^{N_{\text{cells}}} \sum_{i=1}^{N_{\text{Ebins}}} \left[\frac{D_{l,i}^{\lambda} - \phi_i P_{l,i}^{\lambda}\left(\alpha_l^{\lambda}, \beta_l^{\lambda}\right)}{\sigma_{l,i}^{\lambda}}\right]^2 + g_\lambda\left(\alpha_l^{\lambda}\right) + h_\lambda\left(\beta_l^{\lambda}\right) \right\}, \tag{A.27}$$

where we define $h_{\mathrm{II}}\left(\beta_l^{\mathrm{II}}\right) = \sum_{l=1}^{N_{\text{cells}}}\left(\beta_l^{\mathrm{II}}/\sigma_\zeta^{\mathrm{II}}\right)^2$. Taking the derivative with respect to ϕ_i, the minimisation condition is

$$\sum_{\substack{l=1\\ \lambda=\mathrm{I,II}}}^{N_{\text{cells}}} \frac{D_{l,i}^{\lambda} - \phi_i P_{l,i}^{\lambda}}{\left(\sigma_{l,i}^{\lambda}\right)^2} P_{l,i}^{\lambda} = 0, \qquad \text{whence} \qquad \phi_i = \frac{\sum_{\substack{l=1\\ \lambda=I,II}}^{N_{\text{cells}}} D_{l,i}^{\lambda} P_{l,i}^{\lambda} / \left(\sigma_{l,i}^{\lambda}\right)^2}{\sum_{\substack{l=1\\ \lambda=I,II}}^{N_{\text{cells}}} \left(P_{l,i}^{\lambda}/\sigma_{l,i}^{\lambda}\right)^2}. \tag{A.28}$$

As I will discuss in the following sections, the energy-scale pull will change the binned prediction, by shifting the rescaled bins to the left or right. It can occur that the rescaled bins are shifted more than a bin width, in which case rescaled bins for fixed i can have a value of zero for all λ and l. In this case eq. (A.28) is no longer valid, as the denominator of the definition of ϕ_i will be zero. In this case, I simply set $\phi_i = 0$.

A.3.4 Numerical minimisation of α_i^λ and β_i^λ

It is not possible to minimise α_i^λ, β_i^λ analytically, because β_i^λ now contains the free normalisation Φ^{I}, and the energy-scale pull α_i^λ can be large (shifting the energy spectrum over one bin), preventing any simplification via series expansion. Therefore, I use a numerical algorithm, called the non-linear conjugate-gradient algorithm [293]. This is a more advanced version of the steepest decent method.

To initialise the algorithm, I set the starting point in the parameter space of pulls $\mathbf{p}_0$ to be the location of the previous pull minimum, evaluated at the previous oscillation parameters $\mathbf{p}_0 \equiv \mathbf{p}_{\min}\left(\sin^2 2\theta', \Delta m^{2'}\right)$, or if running χ^2 for the first time, $\mathbf{p}_0 \equiv \left(\alpha_l^{\mathrm{I}} = \sigma_\alpha^{\mathrm{I}}/2 \quad \beta_l^{\mathrm{I}} = \sigma_\beta^{\mathrm{I}}/2 \quad \alpha_l^{\mathrm{II}} = \sigma_\alpha^{\mathrm{II}}/2 \quad \beta_l^{\mathrm{II}} = \sigma_\beta^{\mathrm{II}}/2\right)^{\mathrm{T}}$; and I set the direction of steepest descent $\mathbf{s}_0 = -\nabla\chi^2$ to be the minimisation direction. Then, a cubic one-dimensional minimiser is used to minimise the function $f(t) = \chi^2\left(\mathbf{p}_0 + t \cdot \hat{\mathbf{s}}\right)$ (see appendix A.3.5 for details), where $\hat{\mathbf{s}} \equiv \mathbf{s}/|\mathbf{s}|$ is defined to be the unit vector in the direction of $\mathbf{s}$. One-dimensional minimality occurs when the direction of steepest descent is orthogonal to the path of minimisation, $\nabla\chi^2(\mathbf{p}_0 + t_{\min} \cdot \hat{\mathbf{s}}) \cdot \hat{\mathbf{s}} \approx 0$. Then a new direction $\mathbf{s}'$ is chosen using the Polak-Ribière method,

$$\mathbf{s}' \equiv -\nabla\chi^2\left(\mathbf{p}_{\min}\right) + \beta \cdot \mathbf{s} \quad \text{where} \quad \beta = \frac{\left[\nabla\chi^2\left(\mathbf{p}_{\min}\right) - \nabla\chi^2\left(\mathbf{p}_0\right)\right] \cdot \nabla\chi^2\left(\mathbf{p}_{\min}\right)}{\left|\nabla\chi^2\left(\mathbf{p}_0\right)\right|^2} \tag{A.29}$$

and $\mathbf{p}_{\min} \equiv \mathbf{p}_0 + t_{\min} \cdot \hat{\mathbf{s}}$. Then the algorithm repeats the line minimisation in the new direction $\mathbf{s}'$, starting at the parameter point $\mathbf{p}_0' \equiv \mathbf{p}_{\min}$.

For a quadratic function $f(\mathbf{x})$ of n variables, if the one-dimensional minimisation is exact, then the conjugate-gradient algorithm will terminate at the minimum after at most n iterations. (This is very useful for quadratic functions with many variables, as the direct method of solving the linear equations $\nabla f(\mathbf{x}) = 0$ involves the inversion of a large matrix, which is numerically unstable and computationally expensive.) For non-quadratic functions, like our $\chi^2(\mathbf{p})$, there is no guarantee of convergence. I follow the suggestion by Fletcher's textbook [293], to reset the search direction $\mathbf{s}$ to the direction of steepest descent $-\nabla\chi^2\left(\mathbf{p}_0\right)$ after $n = 4N_{\text{cells}}$ iterations (n being the dimension of the vector of pulls $\mathbf{p}$). After ten reset cycles ($40N_{\text{cells}}$ iterations), I exclusively use the direction of steepest descent, and after 1000 iterations I terminate the algorithm.

A.3.5 One-dimensional cubic minimiser

The non-linear conjugate-gradient algorithm requires one-dimensional line minimisation of the function $f(t) = \chi^2\left(\mathbf{p}_0 + t \cdot \hat{\mathbf{s}}\right)$. I first search for an interval $[t_0, t_1]$ such that $f'(t_0) < 0$ and $f'(t_1) > 0$, which guarantees that there is a local minimum in the interval. This is done by iterating over $T_k = -\operatorname{sign}[f'(0)] \cdot 2^k$ for positive integer k. Once a suitable k is found, I set $t_0 = T_{k-1}$ and $t_1 = T_k$.

I then use the function values $y_i \equiv f(t_i)$, and their derivatives $d_i \equiv f'(t_i)$, for $i = 0, 1$, to uniquely define a cubic function $F(t - t_0)$, whose minimum I take as an estimate for the minimum. With $x \equiv t - t_0$, let

$$F(x) = \alpha x^3 + \beta x^2 + \gamma x + \delta. \tag{A.30}$$

We then have $F(0) = \delta = y_0$, $F'(0) = \gamma = d_0$, and

$$F(\Delta t) = \alpha \Delta t^3 + \beta \Delta t^2 + d_0 \Delta t + y_0 = y_1, \quad F'(\Delta t) = 3\alpha \Delta t^3 + 2\beta \Delta t + d_0 = d_1, \tag{A.31}$$

where $\Delta t \equiv t_1 - t_0$. Thence, one can obtain

$$\alpha = \frac{1}{\Delta t^2}\left[\Delta d - 2\left(\frac{\Delta y}{\Delta t} - d_0\right)\right], \qquad \beta = \frac{1}{\Delta t}\left[3\left(\frac{\Delta y}{\Delta t} - d_0\right) - \Delta d\right]. \tag{A.32}$$

By solving the quadratic equation $F'(x) = 0$, one can obtain the extrema

$$x_\pm = t_\pm - t_0 = -\frac{b}{3a} \pm \sqrt{\left(\frac{b}{3a}\right)^2 - \frac{c}{3a}}. \tag{A.33}$$

From geometric considerations, (see fig. A.1), when $\alpha > 0$, the minimum is to the right, hence we take the solution with the plus sign x_+; and when $\alpha < 0$, the minimum is to the left, and we take x_- as the minimum. In the case when $3\alpha\gamma \ll \beta^2$, the cubic becomes approximately quadratic, with the minimum at

$$x = -\frac{\gamma}{2\beta}\left[1 + \mathcal{O}\left(\frac{3\alpha\gamma}{\beta^2}\right)\right]. \tag{A.34}$$

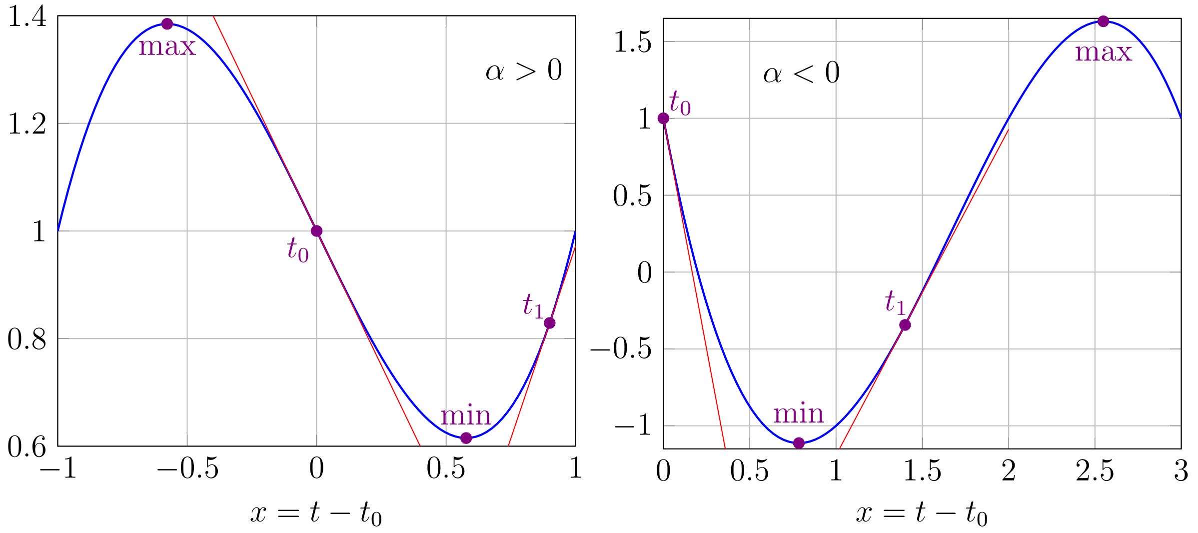

Figure A.1: Sketch of two cubics with $\alpha > 0$ (left) and $\alpha < 0$ (right) and their minima.

Having ascertained the cubic minimum's location t^*_{min}, I calculate the derivative $f'\left(t^*_{\text{min}}\right)$, in order to find out if it should replace t_0 or t_1. However, I do an additional check before replacement, as after several iterations, the cubic interpolation can become trapped in a cycle, and not converge to the real minimum, or convergence becomes slow. If I could have done better with bisection rather than cubic interpolation, I do an additional bisection. Explicitly, if $f'\left(t^*_{\text{min}}\right) < 0$ and $|t^*_{\text{min}} - t_0| < |\Delta t|/2$, or if $f'\left(t^*_{\text{min}}\right) > 0$ and $|t^*_{\text{min}} - t_1| < |\Delta t|/2$, then I do a bisection after replacement.

In the former case, when the derivative at t^*_{min} is negative, I replace t_0 by t^*_{min}; and in the latter case, when the derivative is positive, I replace t_1 by t^*_{min}. If I could have done better doing a bisection, I then set $t^* \equiv (t_0 + t_1)/2$ and replace t_0 with t^* if $f'(t^*) < 0$, and replace t_1 with t^* if $f'(t^*) > 0$.

A.3.6 Implementing the energy-scale pull

We cannot do a series expansion in the energy-scale pull, because αE_i can have a magnitude similar to the bin width ΔE. Therefore, instead of implementing the energy-scale pull in the integral over E_rec (implicit in $R^{\lambda,l}_{ij}$ in eq. (4.34)), which would require recalculating computationally expensive integrals, I instead rebin the prediction $\text{Pred}^\lambda_{l,i}$. I do so by first defining a function for the energy spectrum $S^\lambda_l(x)$, where $x \equiv (E_\text{rec} - E_0)/\Delta E \in \left[0, N^\lambda_\text{Ebins}\right]$ labels the bin as dimensionless integers, such that

$$\int_{i-1}^{i} S^\lambda_l(x)\,\mathrm{d}x = \frac{\text{Pred}^\lambda_{l,i}}{\Delta E}, \qquad \text{and} \qquad S^\lambda_l(x) \geq 0, \quad \forall x \in \mathbb{R}. \tag{A.35}$$

Rescaling the energy scale $E_\text{rec} \mapsto (1+\alpha)E_\text{rec}$ modifies the index as

$$I_i(\alpha) = \frac{E_i(1+\alpha) - E_0}{\Delta E} = i + \alpha\left(i + \frac{E_0}{\Delta E}\right), \tag{A.36}$$

whence

$$\text{Pred}^\lambda_{l,i}\left(\alpha^\lambda_l\right) \equiv \int_{I_{i-1}\left(\alpha^\lambda_l\right)}^{I_i\left(\alpha^\lambda_l\right)} S^\lambda_l(x)\,\mathrm{d}x. \tag{A.37}$$

In the implementation of `GLoBES`, the function $S^\lambda_l(\,\cdot\,)$ is taken to be piecewise constant. I found, however, that the conjugate-gradient algorithm failed to converge with this choice, as $\nabla\chi^2$ contains the function $S^\lambda_l(\,\cdot\,)$; therefore if S^λ_l is discontinuous, so is $\nabla\chi^2$, which causes problems for numerical minimisation. I therefore created a procedure to create a function S^λ_l, which interpolated between constant bin values with linear functions to create continuity, whilst still preserving non-negativity and the values in each bin as per eq. (A.35). In addition to non-negativity and area preservation, any reasonable interpolation should be monotonic between bins, so as to not introduce new local extrema (which could introduce a fake oscillation signal).

In the section below, I give the details of the interpolation procedure. Note that it is also important that not only the interpolator is continuous, but that the interpolation as a function of parameters is also continuous. This means that when the interpolation rule must change to ensure non-negativity, area preservation or monotonicity, it must be done in a continuous way.

Interpolation procedure

In this part, I will drop the indices λ and l, which are not crucial for this discussion. I define the interpolated spectrum $S(\,\cdot\,)$ piecewise in each bin,

$$S(x) = \begin{cases} S_0(x) & \text{if} \quad x < 0 \\ S_i[x-(i-1)] & \text{if} \quad x \in [i-1, i), \quad \text{for} \quad i \in \{1 \dots N\} \\ S_{N+1}(x-N) & \text{if} \quad x \geq N \end{cases} \tag{A.38}$$

where N is the total number of energy bins. Note that I have shifted each piece $S_i(\,\cdot\,)$ so as to be defined on the interval $[0,1)$. The energy-scale pull is implemented as

$$\text{Pred}_i(\alpha) = T\left[I_i(\alpha)\right] - T\left[I_{i-1}(\alpha)\right] \qquad \text{where} \qquad T(x) = \int_0^x S(x')\mathrm{d}x'; \tag{A.39}$$

I calculate $T(\,\cdot\,)$ analytically for fast χ^2 calculation.

Below I present blocks of pseudocode, with additional explanatory remarks as bullet points. Within a pseudocode block, text enclosed in braces $\{\ldots\}$ are comments. The pseudocode is only meant to be representative of my actual code.

Pseudocode block 1 First bin $i = 1$

```
let $S_1(1) = \frac{\text{Pred}_1 + \text{Pred}_2}{2}$
{Note that this guarantees the endpoint of $S_1(\,\cdot\,)$ to be non-negative.}
let $L_1(\,\cdot\,)$ be the line whose endpoint $L_1(1) = (\text{Pred}_1 + \text{Pred}_2)/2$, and whose integral,
    $$\int_0^1 L_1(x)\mathrm{d}x = \text{Pred}_1.$$
{Explicitly $L_1(x) = mx + b$ where $m = \text{Pred}_2 - \text{Pred}_1$ and $b = \text{Pred}_1 - m/2$.}
if $L_1(0) \geq 0$ then
    set $S_1$ to be $L_1$
    set $T_1(x) = \int_0^x L_1(x')\mathrm{d}x'$
else
    let $K_1(x) = m(x - x_0)$ be defined such that $K_1(1) = (\text{Pred}_1 + \text{Pred}_2)/2$ and
        $$\int_{x_0}^1 K_1(x)\mathrm{d}x = \text{Pred}_1.$$
    {Explicitly, $m = K_1(1)/(1-x_0)$ and $(1-x_0)K_1(1)/2 = \text{Pred}_1 \implies x_0 = -b/K_1(1)$.}
    set $S_1(x) = \begin{cases} 0 & \text{if } x \leq x_0 \\ K_1(x) & \text{if } x > x_0 \end{cases}$ and $T_1(x) = \begin{cases} 0 & \text{if } x \leq x_0 \\ \frac{m}{2}(x - x_0)^2 & \text{if } x > x_0 \end{cases}$    (A.40)
end if
{Notice that in the boundary case $L_1(0) = 0$, for the else statement, we would have $x_0 = 0$ and $L_1 = K_1$, as required by continuity.}
```

Pseudocode block 2 Middle bins $1 < i < N$ (part i: prelude)

```
define the function $L_i(\,\cdot\,)$ to start at $L_i(0) = S_{i-1}(1)$ (the endpoint of the previous spectrum), end at $L_i(1) = (\text{Pred}_i + \text{Pred}_{i+1})/2$ (the midpoint of the current and next bin), and let it be constant in the interval $[0.1, 0.9]$, such that its integral on the interval $[0, 1]$ is equal to $\text{Pred}_i$,
    $$L_i(x) = \begin{cases} m_0 x + b_0 & \text{if } x < 0.1 \\ Y & \text{if } x \leq 0.9 \\ m_1 x + b_1 & \text{otherwise} \end{cases}, \quad \text{where} \quad Y = \frac{\text{Pred}_i - 0.05 \cdot [L_i(0) + L_i(1)]}{0.9}. \tag{A.41}$$
```

Remarks to pseudocode block 2

- Note that fixing the start and end points of L_i with the condition of continuity fixes $m_{0,1}$, $b_{0,1}$ for a definite Y, and area preservation fixes Y.

- Non-negativity is only guaranteed heuristically, because for non-pathological cases, $\text{Pred}_i > 0.05 \cdot [L_i(0) + L_i(1)]$.
- Furthermore, monotonicity is not guaranteed and can be violated, which is dealt in the if statements in the following pseudocode block 3.

Preliminary remarks to pseudocode block 3

- Pseudocode block 3 deals with the case when the bin i is in a monotonic region, $\text{Pred}_{i-1} < \text{Pred}_i < \text{Pred}_{i+1}$ or $\text{Pred}_{i-1} > \text{Pred}_i > \text{Pred}_{i+1}$, but when the function $L_i(\,\cdot\,)$ is *not* monotonic, $Y > L_i(0), L_i(1)$ or $Y < L_i(0), L_i(1)$.
- Each $S_i(\,\cdot\,)$ is defined such that it starts and ends at the midpoint between bins,

$$S_i(0) = \frac{\text{Pred}_{i-1} + \text{Pred}_i}{2} \qquad\qquad S_i(1) = \frac{\text{Pred}_i + \text{Pred}_{i+1}}{2} \tag{A.42}$$

- If the bin i is a local maximum, $\text{Pred}_i > \text{Pred}_{i\pm1}$, I assume that $L_i(\,\cdot\,)$ also has a local maximum $Y > L_i(0), L_i(1)$. This is based on the assumption that for non-pathological cases, $Y \sim \text{Pred}_i > L_i(1)$ and $Y \sim \text{Pred}_i > S_{i-1}(1) = L_i(0)$. Analogous reasoning applies for the case of a local minimum. Therefore the following if statements handle the cases when L_i has an extremum, but Pred_i is monotonic.
- When changing our interpolation rule, it must be done in a continuous fashion. Let us consider how a local maximum is formed. First define $L_> = \max[L_i(0), L_i(1)]$ to be the higher of the two endpoints and $L_< = \min[L_i(0), L_i(1)]$ the lower. A local maximum forms when we increase Y until $Y > L_>$. The boundary between monotonicity and local maximum occurs when $Y = L_>$, at which, the function $L_i(\,\cdot\,)$ is constant on an interval of length 0.9 (instead of 0.8). Instead of increasing Y, we can fix $Y = L_>$ and increase the interval over which the function is constant, which equivalently increases its area.
- Analogous comments apply to the formation of a local minimum: instead of decreasing Y we can fix it to $Y = L_<$ and increase the interval of constancy. If we define Ξ to be the length of the interval of constancy, then the area formula for the case of $L_i(\,\cdot\,)$ being maximum and minimum, respectively, is

$$\frac{L_> + L_<}{2} + \frac{L_> - L_<}{2} \cdot \Xi \qquad \text{and} \qquad \frac{L_> + L_<}{2} - \frac{L_> - L_<}{2} \cdot \Xi. \tag{A.43}$$

- Recall that I construct the interpolation to start and end at the vertical midpoint between bins. Since we are dealing with the case when bin i is in a monotonic region, this means that $L_> > \text{Pred}_i$ and $L_< < \text{Pred}_i$. From eq. (A.43), we see $\text{area}\,(\Xi = 1) = L_> > \text{Pred}_i$ for the maximum case, which implies $\text{area}\,(\Xi) = \text{Pred}_i \implies \Xi < 1$. Similar for the minimum case, we have $\text{area}\,(\Xi = 1) = L_< < \text{Pred}_i$, which implies $\text{area}\,(\Xi) = \text{Pred}_i \implies \Xi < 1$. This is an important sanity check for our construction, as if $\Xi > 1$, the interval of constancy encroaches on the next bin; and if $\Xi = 1$ the whole interval is constant, violating continuity.

- We can see that $\Xi > 0.9$ heuristically, as when $\Xi = 0.9$, the construction is equivalent to $L_i(\,\cdot\,)$, and for $\Xi < 0.9$, the algorithm would have chosen $L_i(\,\cdot\,)$, which would satisfy the condition of monotonicity.
- The cases handled in pseudocode block 3 are displayed schematically in the four panels of fig. A.2, which regard the cases of minimum and maximum, as well as when $L_< = L_i(0)$ and $L_< = L_i(1)$.

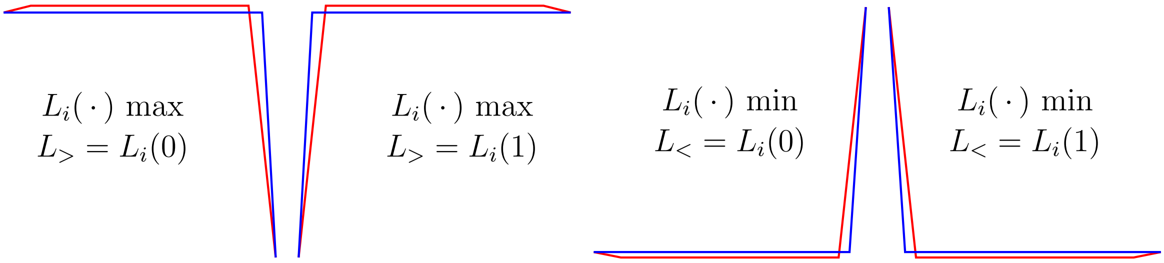

Figure A.2: The possible ways $L_i(\,\cdot\,)$ can violate monotonicity (red) and the possible replacement interpolations (blue), to scale. The start and end points of each case have height 1 or 0.1; for the first two images, $Y = 1.025$, $\text{Pred}_i = 0.9775$ and $\Xi = 0.95$, and for the latter two $Y = 0.08$, $\text{Pred}_i = 0.127$ and $\Xi = 0.94$.

Pseudocode block 3 Middle bins $1 < i < N$ (part ii: monotonicity)

```
if Pred_i is monotonic and [($L_i(\cdot)$ has max and $L_> = L_i(1)$) or ($L_i(\cdot)$ has min and $L_< = L_i(1)$)] then
    let $X = 2(L_i(1) - \text{Pred}_i)/[L_i(1) - L_i(0)]$        {In the code $X \equiv 1 - \Xi$.}
    let $m = [L_i(1) - L_i(0)]/X$
    set $S_i(x) = \begin{cases} L_i(0) + mx & \text{if } x < X \\ L_i(1) & \text{otherwise} \end{cases}$,    $T_i(x) = \sum_{j=1}^{i-1} \text{Pred}_j + \int_0^x S_i(x')\mathrm{d}x'$    (A.44)
else if Pred_i is monotonic and [($L_i(\cdot)$ has max and $L_> = L_i(0)$) or ($L_i(\cdot)$ has min and $L_< = L_i(0)$)] then
    let $X = 2(L_i(0) - \text{Pred}_i)/[L_i(0) - L_i(1)]$
    let $m = [L_i(1) - L_i(0)]/X$
    set $S_i(x) = \begin{cases} L_i(0) & \text{if } x < \Xi \\ L_i(0) + m(x - \Xi) & \text{otherwise} \end{cases}$    where $\Xi = 1 - X$    (A.45)
    set $T_i(x) = \sum_{j=1}^{i-1} \text{Pred}_j + \int_0^x S_i(x')\mathrm{d}x'$
end if
```

Remarks on the overflow bins In the case when $\alpha > 0$, $I_N(\alpha) > N$; and when $\alpha < 0$, $I_0(\alpha) < 0$. This requires interpolation for two *overflow bins*, one before the first bin, and one after the last bin, $S_{0,N+1}(\,\cdot\,)$. Due to the simplicity of $S_{0,N+1}(\,\cdot\,)$, I will not present any pseudocode. They are simply defined to interpolate the start and end points of the spectrum to zero on an interval of length 0.1. Explicitly,

$$\begin{aligned} S_0(x) &= \begin{cases} S_1(0) \cdot (10x+1) & \text{if } -x < 0.1 \\ 0 & \text{otherwise} \end{cases} \\ S_{N+1}(x) &= \begin{cases} S_N(1) \cdot (1-10x) & \text{if } x < 0.1 \\ 0 & \text{otherwise} \end{cases} \end{aligned} \tag{A.46}$$

and

$$\begin{aligned} T_0(x) &= \begin{cases} -5 \cdot S_1(0) \cdot x^2 & \text{if } -x < 0.1 \\ -0.05 \cdot S_1(0) & \text{otherwise} \end{cases} \\ T_{N+1}(x) &= \begin{cases} \sum_{i=1}^{N} \mathrm{Pred}_i + S_N(1) \cdot x(1-5x) & \text{if } x < 0.1 \\ \sum_{i=1}^{N} \mathrm{Pred}_i + 0.05 \cdot S_N(1) & \text{otherwise} \end{cases} \end{aligned} \tag{A.47}$$

Conclusion In this way I implemented an interpolation of the energy spectra, which respected the following four principles:

1. Continuity; regarding both the continuity of the interpolating function, and the continuity of the interpolation procedure as a function of the underlying binned spectrum.
2. Area preservation; the integral of the interpolating function of each bin should give the same result of the corresponding bin of the original spectrum.
3. Monotonicity; the interpolation should not introduce new local extrema into the spectrum.
4. Non-negativity; the interpolation must never be negative.

In fig. A.3 I give an example of my interpolation procedure versus the binned spectrum.

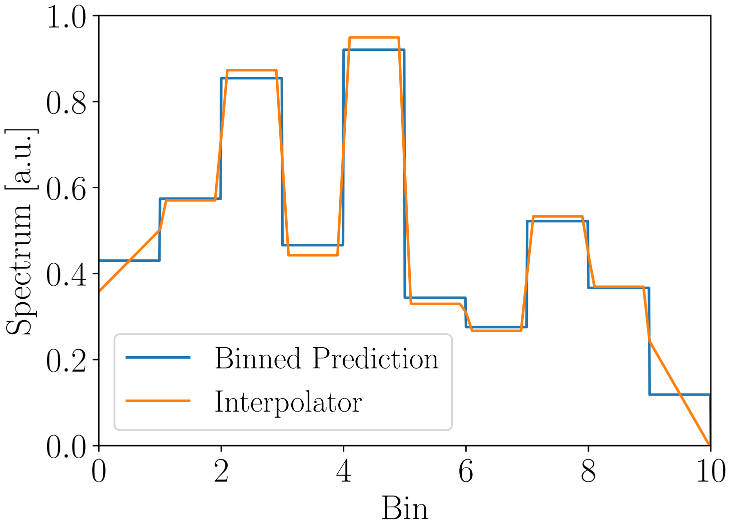

Figure A.3: Binned prediction (blue) versus interpolating function (orange).

A.3.7 Calculating $\nabla\chi^2$

In this section I detail the relevant formulae for calculating the gradient $\nabla\chi^2$. Let us denote the terms of the first line in eq. (A.27) $f_\lambda\left(\alpha_l^\lambda, \beta_l^\lambda\right)$, so that

$$\chi^2\left(\alpha_l^\lambda, \beta_l^\lambda\right) = \sum_{\lambda=\mathrm{I},\mathrm{II}} \left[f_\lambda\left(\alpha_l^{\mathrm{I},\mathrm{II}}, \beta_l^{\mathrm{I},\mathrm{II}}\right) + g_\lambda\left(\alpha_l^\lambda\right) + h_\lambda\left(\beta_l^\lambda\right)\right]. \tag{A.48}$$

To simplify the notation, let us define $\widetilde{D}_{l,i}^\lambda \equiv D_{l,i}^\lambda/\sigma_{l,i}^\lambda$, and similarly $\widetilde{P}_{l,i}^\lambda \equiv P_{l,i}^\lambda/\sigma_{l,i}^\lambda$. In f_λ, the dependence on $\alpha_l^{\mathrm{I},\mathrm{II}}$ can be isolated within ϕ_i and $\widetilde{P}_{l,i}^\lambda$, where $\phi_i\left(P_{l,i}^{\mathrm{I},\mathrm{II}}\right)$ is defined in eq. (A.28). Thus,

$$\begin{aligned}
\frac{\partial\chi^2}{\partial\alpha_l^{\mathrm{I}}} &= \sum_{i=1}^{N_{\mathrm{Ebins}}^{\mathrm{I}}} \frac{\partial f_{\mathrm{I}}}{\partial\widetilde{P}_{l,i}^{\mathrm{I}}}\frac{\partial\widetilde{P}_{l,i}^{\mathrm{I}}}{\partial\alpha_l^{\mathrm{I}}} + \frac{\partial f_{\mathrm{I}}}{\partial\phi_i}\frac{\partial\phi_i}{\partial\alpha_l^{\mathrm{I}}} + \frac{\partial f_{\mathrm{II}}}{\partial\phi_i}\frac{\partial\phi_i}{\partial\alpha_l^{\mathrm{I}}} + \frac{\partial g_{\mathrm{I}}}{\partial\alpha_l^{\mathrm{I}}} = \sum_{i=1}^{N_{\mathrm{Ebins}}^{\mathrm{I}}} \frac{\partial f_{\mathrm{I}}}{\partial\widetilde{P}_{l,i}^{\mathrm{I}}}\frac{\partial\widetilde{P}_{l,i}^{\mathrm{I}}}{\partial\alpha_l^{\mathrm{I}}} + \frac{\partial g_{\mathrm{I}}}{\partial\alpha_l^{\mathrm{I}}}\\
\frac{\partial\chi^2}{\partial\alpha_l^{\mathrm{II}}} &= \sum_{i=1}^{N_{\mathrm{Ebins}}^{\mathrm{II}}} \frac{\partial f_{\mathrm{I}}}{\partial\phi_i}\frac{\partial\phi_i}{\partial\alpha_l^{\mathrm{II}}} + \frac{\partial f_{\mathrm{II}}}{\partial\widetilde{P}_{l,i}^{\mathrm{II}}}\frac{\partial\widetilde{P}_{l,i}^{\mathrm{II}}}{\partial\alpha_l^{\mathrm{II}}} + \frac{\partial f_{\mathrm{II}}}{\partial\phi_i}\frac{\partial\phi_i}{\partial\alpha_l^{\mathrm{II}}} + \frac{\partial g_{\mathrm{II}}}{\partial\alpha_l^{\mathrm{II}}} = \sum_{i=1}^{N_{\mathrm{Ebins}}^{\mathrm{II}}} \frac{\partial f_{\mathrm{II}}}{\partial\widetilde{P}_{l,i}^{\mathrm{II}}}\frac{\partial\widetilde{P}_{l,i}^{\mathrm{II}}}{\partial\alpha_l^{\mathrm{II}}} + \frac{\partial g_{\mathrm{II}}}{\partial\alpha_l^{\mathrm{II}}},
\end{aligned} \tag{A.49}$$

where we have used that $\partial f_\lambda/\partial\phi_i = 0$ by the definition of $\phi_i(\,\cdot\,)$, by virtue of having already analytically minimised over it in eq. (A.28). The partial derivatives can be calculated as

$$\frac{\partial f_\lambda}{\partial\widetilde{P}_{l,i}^\lambda} = -2\phi_i\left(\widetilde{D}_{l,i}^\lambda - \phi_i\widetilde{P}_{l,i}^\lambda\right), \qquad \frac{\partial g_\lambda}{\partial\alpha_l^\lambda} = \frac{2}{\left(\sigma_\eta^\lambda\right)^2}\left[\alpha_l^\lambda - \frac{\langle\alpha\rangle}{1+\vartheta_\lambda/N_{\mathrm{cells}}}\right], \tag{A.50}$$

and $$\frac{\partial\widetilde{P}_{l,i}^\lambda}{\partial\alpha_l^\lambda} = \frac{1}{\sigma_{l,i}^\lambda}\cdot\frac{1+\beta_{l,i}^\lambda}{\left(1+\tilde{\zeta}_l^\lambda\right)\mathrm{Pred}_{l,i}^\lambda\left(\sin^2 2\theta = 0\right)\left[\tilde{\eta}_l^\lambda + \tilde{\xi}_l^\lambda\right]}\cdot\frac{\partial\mathrm{Pred}_{l,i}^\lambda}{\partial\alpha^\lambda}, \quad \text{where} \tag{A.51}$$

$$\begin{aligned}
\frac{\partial\mathrm{Pred}_{l,i}^\lambda}{\partial\alpha_l^\lambda} &= \left(i+1+\frac{E_0}{\Delta E}\right)S\left[I_{i+1}\left(\alpha_l^\lambda\right)\right] - \left(i+\frac{E_0}{\Delta E}\right)S\left[I_i\left(\alpha_l^\lambda\right)\right]\\
&= S(I_{i+1}) + \left(i+\frac{E_0}{\Delta E}\right)\left[S(I_{i+1}) - S(I_i)\right],
\end{aligned} \tag{A.52}$$

is calculated from differentiating eq. (A.37) using Leibniz's rule.

By the same reasoning, the dependence on $\beta_l^{\mathrm{I},\mathrm{II}}$ in $f\lambda$ can be isolated within ϕ_i and $\widetilde{P}_{l,i}^\lambda$; the derivative with respect to ϕ_i is zero be definition, whence,

$$\frac{\partial\chi^2}{\partial\beta_l^\lambda} = \sum_{i=1}^{N_{\mathrm{Ebins}}^\lambda}\frac{\partial f_\lambda}{\partial\widetilde{P}_{l,i}^\lambda}\frac{\partial\widetilde{P}_{l,i}^\lambda}{\partial\beta_l^\lambda} + \frac{\partial h_\lambda}{\partial\beta_l^\lambda}, \qquad \text{where} \qquad \frac{\partial h_{\mathrm{II}}}{\partial\beta_l^{\mathrm{II}}} = \frac{2\beta_l^{\mathrm{II}}}{\left(\sigma_\zeta^{\mathrm{II}}\right)^2}, \tag{A.53}$$

$$\begin{aligned}
\frac{\partial h_{\mathrm{I}}}{\partial\beta_l^{\mathrm{I}}} &= \frac{2}{\left(\sigma_\zeta^{\mathrm{I}}\right)^2}\frac{\sum_{m=1}^{N_{\mathrm{cells}}}\left(1+\beta_m^{\mathrm{I}}\right)}{\sum_{m=1}^{N_{\mathrm{cells}}}\left(1+\beta_m^{\mathrm{I}}\right)^2}\left[\frac{\sum_{m=1}^{N_{\mathrm{cells}}}\left(1+\beta_m^{\mathrm{I}}\right)}{\sum_{m=1}^{N_{\mathrm{cells}}}\left(1+\beta_m^{\mathrm{I}}\right)^2}\left(1+\beta_l^{\mathrm{I}}\right) - 1\right]\\
&= \frac{2}{\left(\sigma_\zeta^{\mathrm{I}}\right)^2}\frac{\sum_{m=1}^{N_{\mathrm{cells}}}\left(1+\beta_m^{\mathrm{I}}\right)}{\left[\sum_{m=1}^{N_{\mathrm{cells}}}\left(1+\beta_m^{\mathrm{I}}\right)^2\right]^2}\sum_{m=1}^{N_{\mathrm{cells}}}\left(\beta_l^{\mathrm{I}} - \beta_m^{\mathrm{I}}\right)\left(1+\beta_m^{\mathrm{I}}\right)
\end{aligned} \tag{A.54}$$

(the latter equation is less prone to loss-of-precision, but the second sum has to be computed for each bin; whereas in the former, the sums can be precomputed), and

$$\frac{\partial \widetilde{P}_{l,i}^{\lambda}}{\partial \beta_l^{\lambda}} = \frac{\mathrm{Pred}_{l,i}^{\lambda}\left(\alpha^{\lambda}\right)/\sigma_{l,i}^{\lambda}}{\left(1+\widetilde{\zeta}_l^{\lambda}\right)\mathrm{Pred}_{l,i}^{\lambda}\left(\sin^2 2\theta = 0\right)\left[\widetilde{\eta}_l^{\lambda}+\widetilde{\xi}_l^{\lambda}\right]}. \tag{A.55}$$

A.4 Minimising χ^2

Pseudocode block 4 Minimising $\chi^2(\sin^2 2\theta)$ for fixed Δm^2

```
  Input variables: $\Delta m^2$;  $\sin^2 2\theta_{1,2,3}$;  $\chi^2_{1,2,3}$;  $\varepsilon$
Require: $\sin^2 2\theta_1 < \sin^2 2\theta_2 < \sin^2 2\theta_3$ and $\sin^2 2\theta_2$ is a local minimum: $\chi^2_2 < \chi^2_1, \chi^2_3$
  repeat
    set $\Delta y_1 = \chi^2_2 - \chi^2_1$,   $\Delta y_2 = \chi^2_3 - \chi^2_2$
    set $\Delta x_1 = \sin^2 2\theta_2 - \sin^2 2\theta_1$,   $\Delta x_2 = \sin^2 2\theta_3 - \sin^2 2\theta_2$
    {Sometimes a discontinuity from numerical aberrations will prevent the conditions $|\Delta y_{1,2}| \le \varepsilon$ from being satisfied; exit the loop if the mixing interval is small.}
    if $|\Delta x_2| < 10^{-3}$ and $|\Delta x_1| < 10^{-3}$ then exit loop
    {If one of $\Delta x_{1,2}$ is much larger than the other, bisect the larger interval; otherwise use parabolic interpolation.}
    if $10\Delta x_1 < \Delta x_2$ then
      set $\sin^2 2\theta_{\text{new}} = (\sin^2 2\theta_3 + \sin^2 2\theta_2)/2$
    else if $\Delta x_1 > 10\Delta x_2$ then
      set $\sin^2 2\theta_{\text{new}} = (\sin^2 2\theta_2 + \sin^2 2\theta_1)/2$
    else
      let $ax^2 + bx + c$ be the parabola that interpolates the points $(\sin^2 2\theta, \chi^2)_{1,2,3}$
      set $\sin^2 2\theta_{\text{new}} = -b/(2a)$
      {If $\sin^2 2\theta_{\text{new}}$ is unphysical, bisect the larger interval.}
      if $\sin^2 2\theta_{\text{new}} < 0$ or $\sin^2 2\theta_{\text{new}} > 1$ then
        if $\Delta x_1 < \Delta x_2$ then
          set $\sin^2 2\theta_{\text{new}} = (\sin^2 2\theta_3 + \sin^2 2\theta_2)/2$
        else
          set $\sin^2 2\theta_{\text{new}} = (\sin^2 2\theta_2 + \sin^2 2\theta_1)/2$
        end if
      end if
    end if
    set $\chi^2_{\text{new}} = \chi^2_{\text{pseudo}}(\Delta m^2, \sin^2 2\theta_{\text{new}})$
    update point (see pseudocode block 5)
    if number of iterations > 100 then
      exit loop {Sometimes the algorithm does not converge, due to numerical aberrations. Typically, after 100 iterations, the local minimum is isolated well enough.}
    end if
  until $|\Delta y_2| \le \varepsilon$ and $|\Delta y_1| \le \varepsilon$
```

In pseudocode block 4, I present my minimisation algorithm of $\chi^2_{\text{pseudo}}(\sin^2 2\theta)$ for a fixed Δm^2. The algorithm takes a set of three graph points $(\sin^2 2\theta, \chi^2)_{1,2,3} = \mathbf{p}_{1,2,3}$, where the middle graph point is a local minimum, and reduces the size of the interval to isolate the local minimum. It is broken up into two parts: the first selects a new parameter point (pseudocode block 4), and the second updates the set of three points $(\sin^2 2\theta, \chi^2)_{1,2,3} = \mathbf{p}_{1,2,3}$ (pseudocode block 5). At termination, χ^2_2 is the minimum.

Pseudocode block 5 Update the parameter points $(\sin^2 2\theta, \chi^2)_{1,2,3} = \mathbf{p}_{1,2,3}$

```
if $\chi^2_{\text{new}} < \chi^2_2$ {The new point is lower than the existing local minimum.} then
  if $\sin^2 2\theta_{\text{new}} = 0$ {The minimum is near $\sin^2 2\theta = 0$.} then
    set $\mathbf{p}_1 = \mathbf{p}_{\text{new}}$
    {Check if the minimum is at $\sin^2 2\theta = 0$}
    while $\sin^2 2\theta_2 > 10^{-4}$ and $\chi^2_2 > \chi^2_1$ do
      set $\sin^2 2\theta_2 = 0.1 \cdot \sin^2 2\theta_2, \quad \chi^2_2 = \chi^2_{\text{pseudo}}(\Delta m^2, \sin^2 2\theta_2)$
    end while   {Ensure the middle parameter point is the minimum.}
    if $\chi^2_1 < \chi^2_2$ then set $\mathbf{p}_2 = \mathbf{p}_1$
    exit loop
  else if $\sin^2 2\theta_{\text{new}} < \sin^2 2\theta_1$ {New minimum lies outside the interval.} then
    set $\mathbf{p}_3 = \mathbf{p}_2, \quad \mathbf{p}_2 = \mathbf{p}_{\text{new}}, \quad \mathbf{p}_1 = (0, \chi^2_{3\nu})$
  else if $\sin^2 2\theta_{\text{new}} < \sin^2 2\theta_2$ {New minimum lies between $\mathbf{p}_1, \mathbf{p}_2$.} then
    set $\mathbf{p}_3 = \mathbf{p}_2, \quad \mathbf{p}_2 = \mathbf{p}_{\text{new}}$
  else if $\sin^2 2\theta_{\text{new}} < \sin^2 2\theta_3$ {New minimum lies between $\mathbf{p}_2, \mathbf{p}_3$.} then
    set $\mathbf{p}_1 = \mathbf{p}_2, \quad \mathbf{p}_2 = \mathbf{p}_{\text{new}}$
  else if $\sin^2 2\theta_{\text{new}} < 1$ {New minimum lies outside the interval.} then
    set $\mathbf{p}_1 = \mathbf{p}_2, \quad \mathbf{p}_2 = \mathbf{p}_{\text{new}}, \quad \mathbf{p}_3 = \left(1, \chi^2_{\text{pseudo}}[\Delta m^2, 1]\right)$
  else if $\sin^2 2\theta_{\text{new}} = 1$ then
    set $\mathbf{p}_3 = \mathbf{p}_{\text{new}}$
    {Check if the minimum is at $\sin^2 2\theta = 1$}
    while $\sin^2 2\theta_2 < 0.99$ and $\chi^2_2 > \chi^2_3$ do
      set $\sin^2 2\theta_2 = (1 + \sin^2 2\theta_2)/2, \quad \chi^2_2 = \chi^2_{\text{pseudo}}(\Delta m^2, \sin^2 2\theta_2)$
    end while
    {Ensure the middle parameter point is the minimum.}
    if $\chi^2_3 < \chi^2_2$ then set $\mathbf{p}_2 = \mathbf{p}_3$
    exit loop
  end if   {Update edges of interval, as $\mathbf{p}_{\text{new}}$ is larger than minimum.}
else if $\sin^2 2\theta_{\text{new}} < \sin^2 2\theta_2$ then
  set $\mathbf{p}_1 = \mathbf{p}_{\text{new}}$
else
  {$\sin^2 2\theta_{\text{new}} > \sin^2 2\theta_2$}
  set $\mathbf{p}_2 = \mathbf{p}_{\text{new}}$
end if
```

The pseudocode presented above requires the initial graph points $\mathbf{p}_{1,2,3}$ to enclose a local minimum, where $\mathbf{p}_2$ is the local minimum of the three. Below, I present pseudocode to find a local minimum of $\chi^2_{\text{pseudo}}(\sin^2 2\theta)$. There are two versions presented; one is used for the global analysis, where best-fit points occur near $\sin^2 2\theta = 0$, and another for the gallium analysis, where best-fit points occur for non-zero mixings.

Pseudocode block 6 Find local minimum of $\chi^2(\sin^2 2\theta)$, optimised for $\sin^2 2\theta_{\text{min}} = 0$

```
Input variables: $\Delta m^2$; $\sin^2 2\theta_{\text{guess}}$ {Usually $\sin^2 2\theta_{\text{guess}}$ is the previous minimum.}
let $f(x) = \chi^2_{\text{pseudo}}(\Delta m^2, x)$
if $\sin^2 2\theta_{\text{guess}} \leq 0.01$ then
    set $\mathbf{p}_1 = (0, f(0))$; $\mathbf{p}_2 = (0.01, f(0.01))$ ; $\mathbf{p}_3 = (0.1, f(0.1))$
    if $\mathbf{p}_1$ is minimal {Minimum is at $f(0)$} then
        goto Auxiliary 1 in pseudocode block 8
    else if $\mathbf{p}_3$ is minimal then
        goto Auxiliary 4 in pseudocode block 8
    end if
else if $\sin^2 2\theta_{\text{guess}} \geq 0.75$ then
    set $\mathbf{p}_1 = (0.5, f(0.5))$; $\mathbf{p}_2 = (0.75, f(0.75))$ ; $\mathbf{p}_3 = (1, f(1))$
    if $\mathbf{p}_1$ is minimal then
        goto Auxiliary 2 in pseudocode block 8
    else if $\mathbf{p}_3$ is minimal {Minimum is at $f(1)$} then
        goto Auxiliary 3 in pseudocode block 8
    end if
else
    set $\mathbf{p}_1 = (0.75 \cdot \sin^2 2\theta_{\text{guess}}, f(0.75 \cdot \sin^2 2\theta_{\text{guess}}))$; $\mathbf{p}_2 = (\sin^2 2\theta_{\text{guess}}, f(\sin^2 2\theta_{\text{guess}}))$ ;
    set $\mathbf{p}_3 = (1.25 \cdot \sin^2 2\theta_{\text{guess}}, f(1.25 \cdot \sin^2 2\theta_{\text{guess}}))$
    if $\mathbf{p}_1$ is minimal then
        goto Auxiliary 2 in pseudocode block 8
    else if $\mathbf{p}_3$ is minimal then
        goto Auxiliary 4 in pseudocode block 8
    end if
end if
run minimiser in pseudocode block 4 with $(\sin^2 2\theta, \chi^2)_{1,2,3} = \mathbf{p}_{1,2,3}$
set $\sin^2 2\theta_{\text{min}} = \sin^2 2\theta_2$; $\chi^2_{\text{min}} = \chi^2_2$
exit routine
```

Pseudocode block 7 Find local minimum of $\chi^2(\sin^2 2\theta)$, optimised for gallium

```
Input variables: $\Delta m^2$; $\sin^2 2\theta_{\text{guess}}$ {Usually $\sin^2 2\theta_{\text{guess}}$ is the previous minimum.}
let $f(x) = \chi^2_{\text{pseudo}}(\Delta m^2, x)$
set $\mathbf{p}_1 = (0, f(0))$; $\mathbf{p}_3 = (1, f(1))$ {Now we are sensitive to the whole interval, rather than focusing around a small part of it.}
if $\sin^2 2\theta_{\text{guess}} < 0.1$ then set $\mathbf{p}_2 = (0.1, f(0.1))$
else if $\sin^2 2\theta_{\text{guess}} > 0.9$ then set $\mathbf{p}_2 = (0.9, f(0.9))$
else set $\mathbf{p}_2 = (\sin^2 2\theta_{\text{guess}}, f(\sin^2 2\theta_{\text{guess}}))$
if $\mathbf{p}_1$ is minimal then goto Auxiliary 1 in pseudocode block 8
else if $\mathbf{p}_3$ is minimal then goto Auxiliary 4 in pseudocode block 8
run minimiser in pseudocode block 4 with $(\sin^2 2\theta, \chi^2)_{1,2,3} = \mathbf{p}_{1,2,3}$
set $\sin^2 2\theta_{\text{min}} = \sin^2 2\theta_2$; $\chi^2_{\text{min}} = \chi^2_2$
exit routine
```

Pseudocode block 8 Auxiliary pseudocode for pseudocode block 6

```
Auxiliary 1
while $\mathbf{p}_1$ is minimal do
  if $\sin^2 2\theta_2 < 10^{-4}$ then set $\sin^2 2\theta_{\min} = 0;\ \chi^2_{\min} = f(0)$ and exit routine
  else set $\mathbf{p}_3 = \mathbf{p}_2;\ \sin^2 2\theta_2 = 0.1 \cdot \sin^2 2\theta_2;\ \chi^2_2 = f\left(\sin^2 2\theta_2\right)$
end while
Auxiliary 2
while $\mathbf{p}_1$ is minimal do
  if $\sin^2 2\theta_1 < 0.01$ then
    if $\chi^2_1 < f(0)$ then set $\mathbf{p}_2 = \mathbf{p}_1;\ \mathbf{p}_1 = (0, f(0))$ and exit loop
    else set $\sin^2 2\theta_{\min} = 0;\ \chi^2_{\min} = f(0)$ and exit routine
  end if
  set $\mathbf{p}_3 = \mathbf{p}_2;\ \mathbf{p}_2 = \mathbf{p}_1;\ \sin^2 2\theta_1 = \sin^2 2\theta_1/2;\ \chi^2_1 = f\left(\sin^2 2\theta_1\right)$
end while
Auxiliary 3
while $\mathbf{p}_3$ is minimal do
  if $\sin^2 2\theta_2 > 0.99$ then set $\sin^2 2\theta_{\min} = 1;\ \chi^2_{\min} = f(1)$ and exit routine
  else set $\mathbf{p}_1 = \mathbf{p}_2;\ \sin^2 2\theta_2 = (1 + \sin^2 2\theta_2)/2;\ \chi^2_2 = f\left(\sin^2 2\theta_2\right)$
end while
Auxiliary 4
while $\mathbf{p}_3$ is minimal do
  if $\sin^2 2\theta_3 > 0.99$ then
    if $\chi^2_3 < f(1)$ then set $\mathbf{p}_2 = \mathbf{p}_3;\ \mathbf{p}_3 = (1, f(1))$ and exit loop
    else set $\sin^2 2\theta_{\min} = 1;\ \chi^2_{\min} = f(1)$ and exit routine
  end if
  set $\mathbf{p}_1 = \mathbf{p}_2;\ \mathbf{p}_2 = \mathbf{p}_3;\ \sin^2 2\theta_3 = (1 + \sin^2 2\theta_3)/2;\ \chi^2_3 = f\left(\sin^2 2\theta_3\right)$
end while
```

As already mentioned in section 4.3.2, I do a coarse scan of the Δm^2 grid, searching for local minima of the function

$$F(x_i) = \min_{\sin^2 2\theta} \chi^2\left(x_i, \sin^2 2\theta\right) . \tag{A.56}$$

The coarse step size is determined heuristically, depending on the dataset, and on the grid size $\Delta m^2_i - \Delta m^2_{i-1}$, which increases as the order of magnitude $\lfloor \log_{10} \Delta m^2 \rfloor$ increases. Once a local minimum is found, a routine similar to pseudocode block 4 is implemented, but for the function $F(\,\cdot\,)$ where the x values are discretised. The only differences are:

1. the boundaries of the x values are set by the extent of the grid, x_1 and x_N;
2. parabolic interpolation and bisection has to map to the nearest grid point x_i;
3. the routine must end when the interval has minimal extent $\Delta m^2_{1,2,3} = x_{i-1}, x_i, x_{i+1}$.

In the vicinity of the pseudo parameters $\left(\Delta m^2_{\text{pseudo}}, \sin^2 2\theta_{\text{pseudo}}\right)$, I also do a minimisation scan as it is likely that the best-fit point lies nearby it.

Appendix B

Formulae for neutrino dipole at DUNE

B.1 Cross Section

I took the cross-section expressions from [353, App. A] and [354, eqs. (4,5)],

$$
\begin{aligned}
\frac{\mathrm{d}\sigma(\nu_\alpha e^- \to \nu_4 e^-)}{\mathrm{d}Q^2} &= \alpha_{\mathrm{QED}} \left(\frac{|d_\alpha|}{\mathrm{GeV}^{-1}}\right)^2 \left[\frac{2}{Q^2} - \frac{1}{m_e E_\nu} + \frac{M_4^2}{2 m_e Q^2 E_\nu^2} \times \right. \\
&\left. \left(E_r - m_e - 2E_\nu + M_4^2 \frac{E_r - m_e}{Q^2}\right)\right] \times 3.894 \cdot 10^{-28}\,\mathrm{cm}^2/\mathrm{nucleon} \\
&\equiv X(m_e);
\end{aligned} \tag{B.1}
$$

$$
\frac{\mathrm{d}\sigma_{\mathrm{nucleon}}}{\mathrm{d}Q^2} = \frac{\mathrm{d}\sigma(\nu_\alpha p \to \nu_4 p)}{\mathrm{d}Q^2} + \frac{\mathrm{d}\sigma(\nu_\alpha n \to \nu_4 n)}{\mathrm{d}Q^2}; \tag{B.2}
$$

$$
\begin{aligned}
\frac{\mathrm{d}\sigma(\nu_\alpha p/n \to \nu_4 p/n)}{\mathrm{d}Q^2} &= F_{1,p/n}^2 X\left(m_{p/n}\right) + \alpha_{\mathrm{QED}} \left(\frac{|d_\alpha|}{\mathrm{GeV}^{-1}}\right)^2 \mu_{\mathrm{N}}^2 \times \\
&\left(\frac{F_2^{p/n}}{E_\nu}\right)^2 \left[2(2E_\nu - E_r)^2 - 2Q^2 + \frac{M_4^2}{m_{p/n}}\left(E_r - 4E_\nu + \frac{M_4^2}{E_r}\right)\right] \\
&\times 3.894 \cdot 10^{-28}\,\mathrm{cm}^2/\mathrm{nucleon};
\end{aligned} \tag{B.3}
$$

$$
\frac{\mathrm{d}\sigma(\nu_\alpha N \to \nu_4 N)}{\mathrm{d}Q^2} = \frac{2Z^2}{A} F_{\mathrm{nucleus}}^2 X(M_N) \tag{B.4}
$$

where $E_r \equiv \frac{Q^2}{2M_T}$ is the recoil energy and $\mu_{\mathrm{N}} \equiv \frac{e}{2m_p} \approx 0.16/\mathrm{GeV}$ is the nuclear magneton. Note that I have normalised the cross sections per *nucleon*, not nucleus. For the incoherent cross sections, I have assumed there is, on average, one proton and one neutron for every two nucleons. Also note that compared to other publications, I use $d \equiv 2\mu_{\mathrm{tr}}$. The difference here is in the definition of the magnetic moment in the Lagrangian.The relevant form factors are

$$
F_1^p = \left(1 + \frac{\eta}{1+\eta} a_p\right) G_D, \qquad F_1^n = \frac{\eta}{1+\eta} a_n G_D, \qquad F_2^{p/n} = \frac{a_{p/n}}{1+\eta} G_D, \tag{B.5}
$$

where

$$G_D = \left(1 + \frac{Q^2}{0.71\,\mathrm{GeV}^2}\right)^{-2}, \qquad a_p = \mu_p - 1, \qquad a_n = \mu_n, \qquad \eta \equiv \frac{Q^2}{4M_T^2}, \tag{B.6}$$

for the nucleon, where $a_{p/n}$ the anomalous magnetic moments of the proton/neutron: 1.793 and -1.913, respectively; note how F_1^n is suppressed by η, unlike F_1^p, as the neutron only interacts magnetically. And finally the form factor for the nucleus is

$$\begin{aligned} F_{\text{nucleus}} &= \frac{3j_1(QR_{\text{nucleus}})}{QR_{\text{nucleus}}} \exp\left[-\frac{(Qs)^2}{2}\right], \\ R_{\text{nucleus}} &= \sqrt{\left(1.23\sqrt[3]{A} - 0.6\right)^2 + \frac{7}{3}(\pi a)^2 - 5s^2}\ \text{fm}, \quad \text{where} \\ s &= 0.9\,\text{fm} \quad \text{and} \quad a = 0.52\,\text{fm} \end{aligned} \tag{B.7}$$

taken from [381, §4]. These expressions have been reproduced from appendix A of our publication [332], which I wrote.

B.2 Reconstruction Efficiency

The reconstruction efficiency for photons at DUNE, ε_γ, can be found in [369, fig. 4.26]. If we assume the distribution of the photon momenta in the rest frame on the HNL is isotropic, then we can boost this into the lab frame to obtain the function $p_\gamma(\theta_0; p_4, M_4)$, where θ_0 is the polar angle of the photon momentum in the rest frame. The reconstruction efficiency is, then,

$$\varepsilon(p_4, M_4) = \int_0^{2\pi} \varepsilon_\gamma\left[p_\gamma(\theta_0; p_4, M_4)\right] \mathrm{d}\theta_0\,. \tag{B.8}$$

Note that it is possible for the assumption of isotropy in the rest frame to be violated [382, 383], however it requires the HNL to have non-zero electric and magnetic dipole moments, and it does not significantly affect our results, so we neglect its effect. A piecewise polynomial interpolation was used to parameterise the efficiency, which was provided to me by Jing-Yu Zhu.

B.3 Penalty term

I use a parameterisation of $\Pi(\,\cdot\,)$:

$$\Pi(\lambda) = \begin{cases} (I_0 - I_1)\left|1 - \dfrac{\lambda}{\lambda_0}\right|^{2.33} + I_1; & \begin{matrix} \lambda \in [0, \lambda_0] & I_0 = \Pi(0) \\ \lambda_0 = 1.58 & I_1 = \Pi(\lambda_0) \end{matrix} \\ \displaystyle\sum_{k=0}^{5} c_k \lambda^k; & \lambda \in [\lambda_0, 10] \\ 1 - \left[C_0 - C_1 e^{-\frac{1}{(\lambda-10)}}\right] \dfrac{\lambda - 1}{\lambda^2}; & \lambda \in [10, \infty]; \quad \begin{matrix} C_0 = 0.705 \\ C_1 = 0.042 \end{matrix} \end{cases} \tag{B.9}$$

$$\begin{aligned} c_{5,4,3,2,1,0} = {} & -8.71 \cdot 10^{-6}, 2.98 \cdot 10^{-4}, -3.86 \cdot 10^{-3}, \\ & 2.22 \cdot 10^{-2}, -3.49 \cdot 10^{-2}, 8.23 \cdot 10^{-1}. \end{aligned}$$

The asymptotic form of $\Pi(\lambda \to \infty)$ is determined by evaluating eq. (5.27) in the limit of large $\gamma\ell_0$. In this limit, the denominator is estimated to be one, and we restrict the integral to near $x = 1$, as the integrand has non-negligible contributions only when the exponent is small. The exponent (eq. (5.23)) can be expanded around $x = 1 - \delta x$, assuming $\cos^2\varphi_\mathrm{s} \gg 2\delta x \sin^2\varphi_\mathrm{s}$, which yields $\delta x/\cos\varphi_\mathrm{s}$ for $\cos\varphi_\mathrm{s} > 0$, and $2|\cos\varphi_\mathrm{s}| + \delta x \cos(2\varphi_\mathrm{s})/\cos\varphi_\mathrm{s}$ for $\cos\varphi_\mathrm{s} < 0$. Since we want the exponent to be small, namely $\propto \delta x$, we ignore the latter case. Therefore, the integrand has the form $(1 - \delta x)e^{-a\cdot\delta x}$, where $a = \lambda/\cos\varphi_\mathrm{s}$. Approximating $\cos\varphi_\mathrm{s} \sim 1$ and integrating from $\delta x_\mathrm{min} = 0$ to $\delta x_\mathrm{max} = 10/\lambda$,

$$\Pi(\lambda \to \infty) = 1 - \mathrm{const} \cdot \frac{\lambda - 1}{\lambda^2}, \tag{B.10}$$

where const is determined by the averaging over $\cos^2\varphi_\mathrm{s}$. Technically, the coefficient of λ should vary slightly from one, but the difference is negligible. I approximated const as an arbitrary slowly-varying constant. In fig. B.1 I show a plot of $\Pi(\,\cdot\,)$.

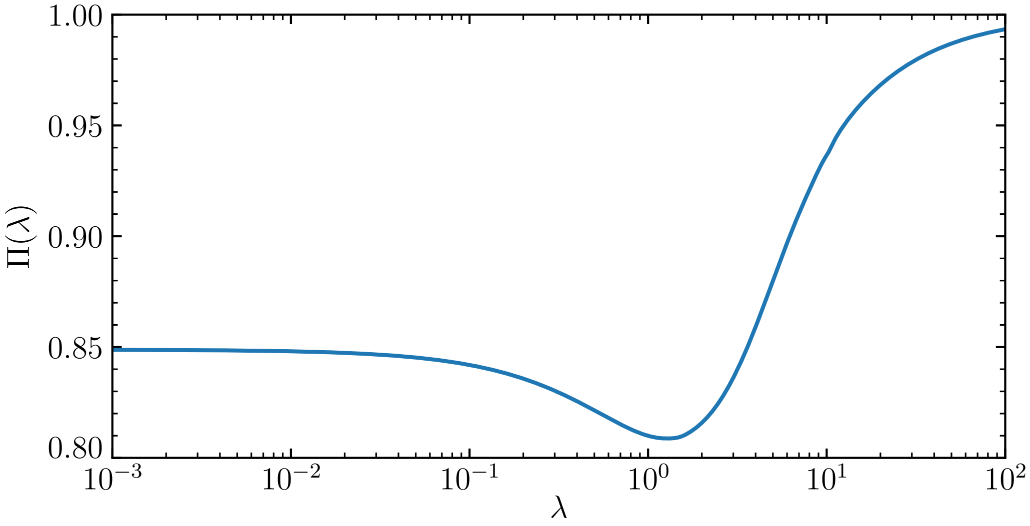

Figure B.1: A plot of $\Pi(\lambda)$.

Bibliography

[1] T. L. Carus, *De Rerum Natura.* E. P. Dutton, 1916. Translation from Latin by W. E. Leonard.

[2] S. Weinberg, *The discovery of subatomic particles.* Scientific American Books, Inc., 1983.

[3] Kelvin, *Contact Electricity and Electrolysis According to Father Boscovich*, *Nature* **56** (May, 1897) 84–85.

[4] C. N. Yang, *Elementary Particles.* Princeton University Press, 1962.

[5] D. Griffiths, *Introduction to Elementary Particles.* Wiley-VCH Verlag GmbH & Co., second, revised ed., 2008.

[6] T.-P. Cheng and L.-F. Li, *Gauge Theory of Elementary Particle Physics.* Clarendon Press, 1982.

[7] M. E. Peskin and D. V. Schroeder, *An Introduction to Quantum Field Theory.* Addison-Wesley Publishing Company, 1995.

[8] M. D. Schwartz, *Quantum Field Theory and the Standard Model.* Cambridge Univ. Press, 2014.

[9] **ALEPH, DELPHI, L3, OPAL, SLD, LEP Electroweak Working Group, SLD Electroweak Group, SLD Heavy Flavour Group**, S. Schael et al., *Precision electroweak measurements on the Z resonance*, *Phys. Rept.* **427** (2006) 257–454, [`hep-ex/0509008`].

[10] C. Giunti and C. W. Kim, *Fundamentals of Neutrino Physics and Astrophysics.* Oxford University Press, 2007.

[11] E. K. Akhmedov, *Neutrino physics*, Jan, 2000.

[12] H. Duan, G. M. Fuller, and Y.-Z. Qian, *Collective Neutrino Oscillations*, *Ann. Rev. Nucl. Part. Sci.* **60** (2010) 569–594, [`1001.2799`].

[13] F. Reines, *The neutrino: From poltergeist to particle*, *Rev. Mod. Phys.* **68** (Apr, 1996) 317–327.

[14] L. M. Brown, *The idea of the neutrino*, *Phys. Today* **31** (Sep, 1978) 23–28.

[15] E. Fermi, *Versuch einer theorie der β-strahlen. I*, *Z. Physik* **88** (Mar, 1934) 161 – 177.

[16] F. L. Wilson, *Fermi's Theory of Beta Decay*, *Am. J. Phys.* **36** (Dec, 1968) 1150 – 1160.

[17] C. L. Cowan, Jr, F. Reines, F. B. Harrison, H. W. Kruse, and A. D. McGuire, *Detection of the free neutrino: A confirmation*, *Science* **124** (Jul, 1956) 103 – 104.

[18] T. D. Lee and C. N. Yang, *Question of Parity Conservation in Weak Interactions*, *Phys. Rev.* **104** (Oct, 1956) 254 – 258.

[19] C. S. Wu, E. Ambler, R. W. Hayward, D. D. Hoppes, and R. P. Hudson, *Experimental Test of Parity Conservation in Beta Decay*, *Phys. Rev.* **105** (Feb, 1957) 1413 – 1415.

[20] E. J. Konopinski and H. M. Mahmoud, *The Universal Fermi Interaction*, *Phys. Rev.* **92** (Nov, 1953) 1045 – 1049.

[21] A. Salam, *On parity conservation and neutrino mass*, *Nuovo Cim.* **5** (1957) 299 – 301.

[22] L. Landau, *On the conservation laws for weak interactions*, *Nuclear Physics* **3** (1957), no. 1 127–131.

[23] T. D. Lee and C. N. Yang, *Parity Nonconservation and a Two-Component Theory of the Neutrino*, *Phys. Rev.* **105** (Mar, 1957) 1671 – 1675.

[24] K. M. Case, *Reformulation of the Majorana theory of the neutrino*, *Phys. Rev.* **107** (1957), no. 1 307 – 316.

[25] J. A. McLennan, *Parity Nonconservation and the Theory of the Neutrino*, *Phys. Rev.* **106** (May, 1957) 821 – 822.

[26] E. C. G. Sudarshan and R. E. Marshak, *Chirality Invariance and the Universal Fermi Interaction*, *Phys. Rev.* **109** (Mar, 1958) 1860 – 1862.

[27] J. J. Sakurai, *Mass Reversal and Weak Interactions*, *Nuovo Cim.* **7** (1958) 649 – 660.

[28] R. P. Feynman and M. Gell-Mann, *Theory of the Fermi Interaction*, *Phys. Rev.* **109** (Jan, 1958) 193 – 198.

[29] M. Goldhaber, L. Grodzins, and A. W. Sunyar, *Helicity of Neutrinos*, *Phys. Rev.* **109** (Feb, 1958) 1015 – 1017.

[30] B. Pontecorvo, *Inverse Beta Processes and Nonconservation of Lepton Charge*, *J. Exptl. Theoret. Phys.* **34** (Jan, 1958) 247 – 249.

[31] R. Davis, *Attempt to Detect the Antineutrinos from a Nuclear Reactor by the* $\mathrm{Cl}^{37}(\bar{\nu}, e^-)\mathrm{Ar}^{37}$ *Reaction*, *Phys. Rev.* **97** (Feb, 1955) 766 – 769.

[32] G. Danby, J.-M. Gaillard, K. Goulianos, L. M. Lederman, N. Mistry, et al., *Observation of High-Energy Neutrino Reactions and the Existence of Two Kinds of Neutrinos*, *Phys. Rev. Lett.* **9** (Jul, 1962) 36 – 44.

[33] G. Feinberg, *Decays of the μ Meson in the Intermediate-Meson Theory*, *Phys. Rev.* **110** (Jun, 1958) 1482 – 1483.

[34] Z. Maki, M. Nakagawa, and S. Sakata, *Remarks on the Unified Model of Elementary Particles*, *Progress of Theoretical Physics* **28** (Nov, 1962) 870–880.

[35] R. Davis, D. S. Harmer, and K. C. Hoffman, *Search for Neutrinos from the Sun*, *Phys. Rev. Lett.* **20** (May, 1968) 1205 – 1209.

[36] J. N. Bahcall, W. A. Fowler, I. Iben, Jr, and R. L. Sears, *Solar neutrino flux*, *Astrophys. J.* **137** (Jan, 1963) 344.

[37] J. N. Bahcall, *Solar Neutrinos. I. Theoretical*, *Phys. Rev. Lett.* **12** (Mar, 1964) 300 – 302.

[38] V. Gribov and B. Pontecorvo, *Neutrino astronomy and lepton charge*, *Physics Letters B* **28** (1969), no. 7 493–496.

[39] C. N. Yang and R. L. Mills, *Conservation of Isotopic Spin and Isotopic Gauge Invariance*, *Phys. Rev.* **96** (Oct, 1954) 191 – 195.

[40] J. Schwinger, *A theory of the fundamental interactions*, *Annals of Physics* **2** (1957), no. 5 407–434.

[41] S. L. Glashow, *Partial-symmetries of weak interactions*, *Nuclear Physics* **22** (1961), no. 4 579–588.

[42] J. Schwinger, *Gauge Invariance and Mass*, *Phys. Rev.* **125** (Jan, 1962) 397 – 398.

[43] P. W. Higgs, *Broken Symmetries and the Masses of Gauge Bosons*, *Phys. Rev. Lett.* **13** (Oct, 1964) 508 – 509.

[44] F. Englert and R. Brout, *Broken Symmetry and the Mass of Gauge Vector Mesons*, *Phys. Rev. Lett.* **13** (Aug, 1964) 321 – 323.

[45] G. S. Guralnik, C. R. Hagen, and T. W. B. Kibble, *Global Conservation Laws and Massless Particles*, *Phys. Rev. Lett.* **13** (Nov, 1964) 585 – 587.

[46] S. Weinberg, *A Model of Leptons*, *Phys. Rev. Lett.* **19** (Nov, 1967) 1264 – 1266.

[47] A. Salam, *Weak and Electromagnetic Interactions*, *Conf. Proc. C* **680519** (1968) 367 – 377.

[48] G. 't Hooft and M. J. G. Veltman, *Regularization and Renormalization of Gauge Fields*, *Nucl. Phys. B* **44** (1972) 189 – 213.

[49] **Gargamelle Neutrino**, F. J. Hasert et al., *Observation of Neutrino Like Interactions Without Muon Or Electron in the Gargamelle Neutrino Experiment*, *Phys. Lett. B* **46** (1973) 138 – 140.

[50] A. Benvenuti et al., *Observation of Muonless Neutrino Induced Inelastic Interactions*, *Phys. Rev. Lett.* **32** (1974) 800 – 803.

[51] M. L. Perl et al., *Evidence for Anomalous Lepton Production in* e^+- e^- *Annihilation*, *Phys. Rev. Lett.* **35** (Dec, 1975) 1489 – 1492.

[52] M. L. Perl et al., *Properties of the proposed* τ *charged lepton*, *Physics Letters B* **70** (1977), no. 4 487–490.

[53] S. Nussinov, *Solar neutrinos and neutrino mixing*, *Phys. Lett. B* **63** (Jul, 1976) 201 – 203.

[54] B. Kayser, *On the quantum mechanics of neutrino oscillation*, *Phys. Rev. D* **24** (Jul, 1981) 110 – 116.

[55] M. Beuthe, *Oscillations of neutrinos and mesons in quantum field theory*, *Phys. Rep.* **375** (2003), no. 2-3 105 – 218, [`hep-ph/0109119`].

[56] R. G. Winter, *Neutrino oscillation kinematics*, *Lett. al Nuovo Cim.* **30** (Jan, 1981) 101 – 104.

[57] C. Giunti, C. W. Kim, and U. W. Lee, *Remarks on the weak states of neutrinos*, *Phys. Rev. D* **45** (Apr, 1992) 2414 – 2420.

[58] C. Giunti, C. W. Kim, J. A. Lee, and U. W. Lee, *Treatment of neutrino oscillations without resort to weak eigenstates*, *Phys. Rev. D* **48** (Nov, 1993) 4310 – 4317.

[59] M. Beuthe, *Towards a unique formula for neutrino oscillations in vacuum*, *Phys. Rev. D* **66** (Jul, 2002) 013003.

[60] A. O. Caldeira and A. J. Leggett, *Quantum tunnelling in a dissipative system*, *Ann. Phys. (N. Y).* **149** (1983), no. 2 374 – 456.

[61] E. K. Akhmedov and A. Y. Smirnov, *Paradoxes of neutrino oscillations*, *Phys. At. Nucl.* **72** (Aug, 2009) 1363 – 1381, [`0905.1903`].

[62] E. K. Akhmedov, *Do charged leptons oscillate?*, *J. High Energy Phys.* **2007** (Sep, 2007) 116 – 116, [`0706.1216`].

[63] E. K. Akhmedov and A. Y. Smirnov, *Neutrino Oscillations: Entanglement, Energy-Momentum Conservation and QFT*, *Found. Phys.* **41** (Aug, 2011) 1279 – 1306, [`1008.2077`].

[64] E. Majorana, *Teoria simmetrica dell'elettrone e del positrone*, *Nuovo Cim.* **14** (1937) 171 – 184. Translation on INSPIRE.

[65] S. Weinberg, *Baryon- and Lepton-Nonconserving Processes*, *Phys. Rev. Lett.* **43** (Nov, 1979) 1566 – 1570.

[66] J. C. Pati and A. Salam, *Lepton number as the fourth "color"*, *Phys. Rev. D* **10** (Jul, 1974) 275 – 289.

[67] R. N. Mohapatra and J. C. Pati, *Left-right gauge symmetry and an "isoconjugate" model of CP violation*, *Phys. Rev. D* **11** (Feb, 1975) 566 – 571.

[68] H. Fritzsch, M. Gell-Mann, and P. Minkowski, *Vectorlike weak currents and new elementary fermions*, *Phys. Lett. B* **59** (Nov, 1975) 256 – 260.

[69] T. P. Cheng, *Hierarchy of lepton masses in a vectorlike theory with Majorana particles*, *Phys. Rev. D* **14** (Sep, 1976) 1367 – 1375.

[70] A. Zee, *Attempt to generate the angle between the strong and weak interactions*, *Phys. Rev. D* **9** (Mar, 1974) 1772 – 1779.

[71] A. Zee, *Cabibbo angle and quark mass spectrum*, *Phys. Rev. D* **13** (Feb, 1976) 713 – 719.

[72] T. P. Cheng and L.-F. Li, *Nonconservation of Separate μ- and e-Lepton Numbers in Gauge Theories with V+A Currents*, *Phys. Rev. Lett.* **38** (Feb, 1977) 381 – 384.

[73] T.-P. Cheng and L.-F. Li, *Muon-number-nonconservation effects in a gauge theory with V+A currents and heavy neutral leptons*, *Phys. Rev. D* **16** (Sep, 1977) 1425 – 1443.

[74] S. L. Glashow, J. Iliopoulos, and L. Maiani, *Weak Interactions with Lepton-Hadron Symmetry*, *Phys. Rev. D* **2** (Oct, 1970) 1285 – 1292.

[75] P. Minkowski, *$\mu \to e\gamma$ at a Rate of One Out of 10^9 Muon Decays?*, *Phys. Lett. B* **67** (1977) 421 – 428.

[76] M. Gell-Mann, P. Ramond, and R. Slansky, *Complex Spinors and Unified Theories*, *Conf. Proc. C* **790927** (1979) 315 – 321, [`1306.4669`].

[77] T. Yanagida, *Horizontal gauge symmetry and masses of neutrinos*, *Conf. Proc. C* **7902131** (1979) 95 – 99.

[78] T. Yanagida, *Horizontal Symmetry and Masses of Neutrinos*, *Prog. Theor. Phys.* **64** (Sep, 1980) 1103 – 1105.

[79] R. N. Mohapatra and G. Senjanović, *Neutrino Mass and Spontaneous Parity Nonconservation*, *Phys. Rev. Lett.* **44** (Apr, 1980) 912 – 915.

[80] Y. Chikashige, R. Mohapatra, and R. Peccei, *Are there real goldstone bosons associated with broken lepton number?*, *Phys. Lett. B* **98** (Jan, 1981) 265 – 268.

[81] W. Konetschny and W. Kummer, *Nonconservation of total lepton number with scalar bosons*, *Physics Letters B* **70** (1977), no. 4 433–435.

[82] G. Gelmini and M. Roncadelli, *Left-handed neutrino mass scale and spontaneously broken lepton number*, *Phys. Lett. B* **99** (Mar, 1981) 411 – 415.

[83] W. Grimus, R. Pfeiffer, and T. Schwetz, *A 4-neutrino model with a Higgs triplet*, *Eur. Phys. J. C* **13** (2000) 125 – 132, [`hep-ph/9905320`].

[84] T. P. Cheng and L.-F. Li, *Neutrino masses, mixings, and oscillations in* $\mathrm{SU}(2) \times \mathrm{U}(1)$ *models of electroweak interactions*, *Phys. Rev. D* **22** (Dec, 1980) 2860 – 2868.

[85] A. Zee, *A theory of lepton number violation and neutrino Majorana masses*, *Phys. Lett. B* **93** (Jun, 1980) 389 – 393.

[86] K. Babu, *Model of "calculable" Majorana neutrino masses*, *Physics Letters B* **203** (1988), no. 1 132–136.

[87] S. Petcov and S. Toshev, *Conservation of lepton charges, massive Majorana and massless neutrinos*, *Phys. Lett. B* **143** (Aug, 1984) 175 – 178.

[88] K. S. Babu and E. Ma, *Natural Hierarchy of Radiatively Induced Majorana Neutrino Masses*, *Phys. Rev. Lett.* **61** (Aug, 1988) 674 – 677.

[89] D. Choudhury, R. Gandhi, J. A. Gracey, and B. Mukhopadhyaya, *Two-loop neutrino masses and the solar neutrino problem*, *Phys. Rev. D* **50** (Sep, 1994) 3468 – 3476.

[90] Y. Cai, J. Herrero-García, M. A. Schmidt, A. Vicente, and R. R. Volkas, *From the trees to the forest: a review of radiative neutrino mass models*, *Front. in Phys.* **5** (2017) 63, [`1706.08524`].

[91] K. S. Babu, P. S. B. Dev, and S. Jana, *Probing Neutrino Mass Models through Resonances at Neutrino Telescopes*, `2202.06975`.

[92] R. Foot, H. Lew, X. G. He, and G. C. Joshi, *See-saw neutrino masses induced by a triplet of leptons*, *Zeitschrift für Phys. C Part. Fields* **44** (Sep, 1989) 441 – 444.

[93] E. Ma and D. P. Roy, *Heavy triplet leptons and new gauge boson*, *Nucl. Phys. B* **644** (2002), no. 1-2 290 – 302, [`hep-ph/0206150`].

[94] A. Abada, C. Biggio, F. Bonnet, M. B. Gavela, and T. Hambye, $\mu \to e\gamma$ *and* $\tau \to \ell\gamma$ *decays in the fermion triplet seesaw model*, *Phys. Rev. D* **78** (Aug, 2008) 033007, [`0803.0481`].

[95] A. Abada, C. Biggio, F. Bonnet, M. B. Gavela, and T. Hambye, $\mu \to e\gamma$ *and* $\tau \to \ell\gamma$ *decays in the fermion triplet seesaw model*, *Phys. Rev. D* **78** (Aug, 2008) 033007.

[96] S. Ashanujjaman and K. Ghosh, *Type-III see-saw: Phenomenological implications of the information lost in decoupling from high-energy to low-energy*, *Physics Letters B* **819** (2021) 136403.

[97] S. M. Barr, *New Type of Seesaw Mechanism for Neutrino Masses*, *Phys. Rev. Lett.* **92** (Mar, 2004) 101601.

[98] S. Barr and I. Dorsner, *A prediction from the type III see-saw mechanism*, *Physics Letters B* **632** (2006), no. 4 527–531.

[99] R. N. Mohapatra and A. Y. Smirnov, *Neutrino mass and new physics*, *Annu. Rev. Nucl. Part. Sci.* **56** (2006) 569 – 628.

[100] E. Ma, *Pathways to Naturally Small Neutrino Masses*, *Phys. Rev. Lett.* **81** (Aug, 1998) 1171 – 1174.

[101] S. M. Bilenky and S. T. Petcov, *Massive neutrinos and neutrino oscillations*, *Rev. Mod. Phys.* **59** (Jul, 1987) 671 – 754.

[102] S. Bilenky, J. Hošek, and S. Petcov, *On the oscillations of neutrinos with Dirac and Majorana masses*, *Phys. Lett. B* **94** (Aug, 1980) 495 – 498.

[103] M. Doi, T. Kotani, H. Nishiura, K. Okuda, and E. Takasugi, *CP violation in Majorana neutrinos*, *Physics Letters B* **102** (1981), no. 5 323–326.

[104] P. Langacker, S. Petcov, G. Steigman, and S. Toshev, *Implications of the Mikheyev-Smirnov-Wolfenstein (MSW) mechanism of amplification of neutrino oscillations in matter*, *Nuclear Physics B* **282** (1987) 589–609.

[105] J. Schechter and J. W. F. Valle, *Neutrino-oscillation thought experiment*, *Phys. Rev. D* **23** (Apr, 1981) 1666 – 1668.

[106] L. Wolfenstein, *Different varieties of massive Dirac neutrinos*, *Nucl. Phys. B* **186** (Jul, 1981) 147 – 152.

[107] C. N. Leung and S. T. Petcov, *A comment on the coexistence of Dirac and Majorana massive neutrinos*, *Phys. Lett. B* **125** (1983), no. 6 461 – 466.

[108] W. Haxton, *The Scientific Life of John Bahcall*, *Annual Review of Nuclear and Particle Science* **59** (2009), no. 1 1–20.

[109] J. N. Bahcall, *Neutrino Astrophysics.* Cambridge University Press, 1989.

[110] H. D. Holmgren and R. L. Johnston, $\mathrm{H}^3(\alpha,\gamma)\mathrm{Li}^7$ *and* $\mathrm{He}^3(\alpha,\gamma)\mathrm{Be}^7$ *Reactions*, *Phys. Rev.* **113** (Mar, 1959) 1556 – 1559.

[111] J. N. Bahcall, *Solar Neutrino Cross Sections and Nuclear Beta Decay*, *Phys. Rev.* **135** (Jul, 1964) B137 – B146.

[112] J. N. Bahcall, M. H. Pinsonneault, and S. Basu, *Solar models: Current epoch and time dependences, neutrinos, and helioseismological properties*, *Astrophys. J.* **555** (2001) 990 – 1012, [`astro-ph/0010346`].

[113] J. N. Bahcall, A. M. Serenelli, and S. Basu, *New solar opacities, abundances, helioseismology, and neutrino fluxes*, *Astrophys. J.* **621** (Mar, 2005) L85 – L88, [`astro-ph/0412440`].

[114] R. Stothers and D. Ezer, *Solar Neutrinos and the Influences of Opacity, Thermal Instability Additional Neutrino Sources, and a Central Black Hole on Solar Models*, *Astrophysical Letters* **13** (Jan, 1973) 45.

[115] D. N. Spergel and W. H. Press, *Effect of hypothetical, weakly interacting, massive particles on energy transport in the solar interior*, *Astrophys. J.* **294** (Jul, 1985) 663.

[116] W. H. Press and D. N. Spergel, *Capture by the sun of a galactic population of weakly interacting, massive particles*, *Astrophys. J.* **296** (Sep, 1985) 679.

[117] J. Faulkner and R. L. Gilliland, *Weakly interacting, massive particles and the solar neutrino flux*, *Astrophys. J.* **299** (Dec, 1985) 994.

[118] J. N. Bahcall, N. Cabibbo, and A. Yahil, *Are Neutrinos Stable Particles?*, *Phys. Rev. Lett.* **28** (Jan, 1972) 316 – 318.

[119] A. Cisneros, *Effect of neutrino magnetic moment on solar neutrino observations*, *Astrophys. Space Sci.* **10** (Jan, 1971) 87 – 92.

[120] M. Gasperini, *Testing the principle of equivalence with neutrino oscillations*, *Phys. Rev. D* **38** (Oct, 1988) 2635 – 2637.

[121] L. Wolfenstein, *Neutrino oscillations in matter*, *Phys. Rev. D* **17** (May, 1978) 2369 – 2374.

[122] S. P. Mikheyev and A. Y. Smirnov, *Resonant amplification of ν oscillations in matter and solar-neutrino spectroscopy*, *Nuovo Cimento C* **9** (Jan, 1986) 17 – 26.

[123] H. A. Bethe, *Possible Explanation of the Solar-Neutrino Puzzle*, *Phys. Rev. Lett.* **56** (Mar, 1986) 1305 – 1308.

[124] S. J. Parke, *Nonadiabatic Level Crossing in Resonant Neutrino Oscillations*, *Phys. Rev. Lett.* **57** (Sep, 1986) 1275 – 1278.

[125] W. C. Haxton, *Adiabatic Conversion of Solar Neutrinos*, *Phys. Rev. Lett.* **57** (Sep, 1986) 1271 – 1274.

[126] J. N. Bahcall, S. H. Lubow, W. F. Huebner, N. H. Magee, A. L. Merts, et al., *New Solar-Neutrino Flux Calculations and Implications Regarding Neutrino Oscillations*, *Phys. Rev. Lett.* **45** (Sep, 1980) 945 – 948.

[127] J. N. Bahcall, R. Davis, Jr, and L. Wolfenstein, *Solar neutrinos: a field in transition*, *Nature* **334** (Aug, 1988) 487 – 493.

[128] S. P. Rosen and J. M. Gelb, *Mikheyev-Smirnov-Wolfenstein enhancement of oscillations as a possible solution to the solar-neutrino problem*, *Phys. Rev. D* **34** (Aug, 1986) 969 – 979.

[129] J. N. Bahcall and H. A. Bethe, *Solution of the solar-neutrino problem*, *Phys. Rev. Lett.* **65** (Oct, 1990) 2233 – 2235.

[130] S. Hiroi, H. Sakuma, T. Yanagida, and M. Yoshimura, *Effects of Resonant Matter Oscillation in Earth on Solar Neutrino Detection*, *Prog. Theor. Phys.* **78** (1987) 1428.

[131] Y. Totsuka, *Neutrino Astronomy at Kamioka*, in *Workshop on Elementary Particle Picture of the Universe*, Feb, 1987.

[132] **Kamiokande-II**, K. S. Hirata et al., *Observation of* ^{8}B *solar neutrinos in the Kamiokande-II detector*, *Phys. Rev. Lett.* **63** (Jul, 1989) 16 – 19.

[133] **Kamiokande-II**, K. Hirata et al., *Observation of a Neutrino Burst from the Supernova SN 1987A*, *Phys. Rev. Lett.* **58** (1987) 1490 – 1493.

[134] V. A. Kuzmin, *Detection of solar neutrinos by means of the* ^{71}Ga$(\nu, e^-)^{71}$Ge *reaction*, *Zh. Eksp. Teor. Fiz.* **49** (1965) 1532 – 1534. *Sov. Phys. JETP* **22** (1966) 1051 – 1056.

[135] A. I. Abazov et al., *Search for neutrinos from the Sun using the reaction* ^{71}Ga$(\nu, e^-)^{71}$Ge *reaction*, *Phys. Rev. Lett.* **67** (Dec, 1991) 3332 – 3335.

[136] **GALLEX**, P. Anselmann et al., *Solar neutrinos observed by GALLEX at Gran Sasso*, *Physics Letters B* **285** (1992), no. 4 376–389.

[137] **GALLEX**, P. Anselmann et al., *Implications of the GALLEX determination of the solar neutrino flux*, *Physics Letters B* **285** (1992), no. 4 390–397.

[138] B. Aharmim et al., *Electron energy spectra, fluxes, and day-night asymmetries of* ^{8}B *solar neutrinos from measurements with NaCl dissolved in the heavy-water detect*, *Phys. Rev. C* **72** (Nov, 2005) 055502, [`nucl-ex/0502021`].

[139] H. H. Chen, *Direct Approach to Resolve the Solar-Neutrino Problem*, *Phys. Rev. Lett.* **55** (Sep, 1985) 1534 – 1536.

[140] **SNO Collaboration**, Q. R. Ahmad et al., *Direct Evidence for Neutrino Flavor Transformation from Neutral-Current Interactions in the Sudbury Neutrino Observatory*, *Phys. Rev. Lett.* **89** (Jun, 2002) 011301.

[141] K. Greisen, *Cosmic Ray Showers*, *Annual Review of Nuclear Science* **10** (1960), no. 1 63–108.

[142] M. Markov and I. Zheleznykh, *On high energy neutrino physics in cosmic rays*, *Nuclear Physics* **27** (1961), no. 3 385–394.

[143] C. Achar, M. Menon, V. Narasimham, P. Murthy, B. Sreekantan, et al., *Detection of muons produced by cosmic ray neutrinos deep underground*, *Physics Letters* **18** (1965), no. 2 196–199.

[144] C. Achar, M. Menon, V. Narasimham, P. Ramana Murthy, B. Sreekantan, et al., *Observation of a non-elastic cosmic ray neutrino interaction*, *Physics Letters* **19** (1965), no. 1 78–80.

[145] F. Reines, M. F. Crouch, T. L. Jenkins, W. R. Kropp, H. S. Gurr, et al., *Evidence for High-Energy Cosmic-Ray Neutrino Interactions*, *Phys. Rev. Lett.* **15** (Aug, 1965) 429 – 433.

[146] **Kamiokande-II**, K. Hirata et al., *Experimental study of the atmospheric neutrino flux*, *Physics Letters B* **205** (1988), no. 2 416–420.

[147] T. J. Haines et al., *Calculation of Atmospheric Neutrino-Induced Backgrounds in a Nucleon-Decay Search*, *Phys. Rev. Lett.* **57** (Oct, 1986) 1986 – 1989.

[148] D. Casper et al., *Measurement of atmospheric neutrino composition with the IMB-3 detector*, *Phys. Rev. Lett.* **66** (May, 1991) 2561 – 2564.

[149] **NUSEX**, M. Aglietta et al., *Experimental study of atmospheric neutrino flux in the NUSEX experiment*, *Europhys. Lett.* **8** (1989) 611 – 614.

[150] **NUSEX**, M. Aglietta et al., *Experimental study of upward stopping muons in NUSEX*, *Europhys. Lett.* **15** (1991) 559 – 564.

[151] **Fréjus**, C. Berger et al., *Study of atmospheric neutrino interactions with the Fréjus detector*, *Physics Letters B* **227** (1989), no. 3 489–494.

[152] **Fréjus**, C. Berger et al., *A study of atmospheric neutrino oscillations in the Fréjus experiment*, *Physics Letters B* **245** (1990), no. 2 305–310.

[153] **Super-Kamiokande Collaboration**, Y. Fukuda et al., *Evidence for Oscillation of Atmospheric Neutrinos*, *Phys. Rev. Lett.* **81** (Aug, 1998) 1562 – 1567.

[154] **MACRO**, C. De Marzo et al., *Macro: A Large Area Detector at the Gran Sasso Laboratory*, *Nuovo Cim. C* **9** (1986) 281 – 292.

[155] **MACRO**, M. Ambrosio et al., *Measurement of the atmospheric neutrino induced upgoing muon flux using MACRO*, *Phys. Lett. B* **434** (1998) 451 – 457, [`hep-ex/9807005`].

[156] **Soudan-2**, W. Allison et al., *The atmospheric neutrino flavor ratio from a 3.9 fiducial kiloton-year exposure of Soudan 2*, *Physics Letters B* **449** (1999), no. 1 137–144, [`hep-ex/9901024`].

[157] **Soudan-2**, W. W. M. Allison et al., *The Soudan-2 detector: The Design and construction of the tracking calorimeter modules*, *Nucl. Instrum. Meth. A* **376** (1996) 36 – 48.

[158] **Soudan-2**, W. W. M. Allison et al., *The Soudan-2 detector: The Operation and performance of the tracking calorimeter modules*, *Nucl. Instrum. Meth. A* **381** (1996) 385 – 397.

[159] **Soudan-2**, M. Sanchez et al., *Measurement of the L/E distributions of atmospheric ν in Soudan 2 and their interpretation as neutrino oscillations*, *Phys. Rev. D* **68** (Dec, 2003) 113004.

[160] F. Reines, H. W. Sobel, and E. Pasierb, *Evidence for Neutrino Instability*, *Phys. Rev. Lett.* **45** (Oct, 1980) 1307 – 1311.

[161] V. Barger, K. Whisnant, D. Cline, and R. Phillips, *Possible indications of neutrino oscillations*, *Physics Letters B* **93** (1980), no. 1 194–198.

[162] A. De Rújula, M. Lusignoli, L. Maiani, S. Petcov, and R. Petronzio, *A fresh look at neutrino oscillations*, *Nuclear Physics B* **168** (1980), no. 1 54–68.

[163] S. S. Wilks, *The large-sample distribution of the likelihood ratio for testing composite hypotheses*, *Ann. Math. Stat.* **9** (Mar, 1938) 60 – 62.

[164] N. Hata and P. Langacker, *Solar model uncertainties, MSW analysis, and future solar neutrino experiments*, *Phys. Rev. D* **50** (Jul, 1994) 632 – 660.

[165] P. I. Krastev and S. T. Petcov, *New constraints on neutrino oscillations in vacuum as a possible solution of the solar neutrino problem*, *Phys. Rev. Lett.* **72** (Mar, 1994) 1960 – 1963.

[166] **KamLAND**, K. Eguchi et al., *First Results from KamLAND: Evidence for Reactor Antineutrino Disappearance*, *Phys. Rev. Lett.* **90** (Jan, 2003) 021802, [`hep-ex/0212021`].

[167] **KamLAND**, A. Gando et al., *Reactor On-Off Antineutrino Measurement with KamLAND*, *Phys. Rev. D* **88** (2013), no. 3 033001, [`1303.4667`].

[168] T. Araki et al., *Experimental investigation of geologically produced antineutrinos with KamLAND*, *Nature* **436** (Jul, 2005) 499 – 503.

[169] **K2K**, S. H. Ahn et al., *Detection of accelerator produced neutrinos at a distance of 250-km*, *Phys. Lett. B* **511** (2001) 178 – 184, [`hep-ex/0103001`].

[170] **K2K**, M. H. Ahn et al., *Indications of neutrino oscillation in a 250 km long baseline experiment*, *Phys. Rev. Lett.* **90** (2003) 041801, [`hep-ex/0212007`].

[171] **Super-Kamiokande**, Y. Fukuda et al., *The Super-Kamiokande detector*, *Nucl. Instrum. Meth. A* **501** (2003) 418 – 462.

[172] **K2K**, E. Aliu et al., *Evidence for muon neutrino oscillation in an accelerator-based experiment*, *Phys. Rev. Lett.* **94** (2005) 081802, [`hep-ex/0411038`].

[173] **MINOS**, B. J. Rebel, *First MINOS results with the NuMI beam*, *Nucl. Phys. B Proc. Suppl.* **168** (2007) 195 – 198, [`hep-ex/0701049`].

[174] **MINOS**, P. Adamson et al., *Measurement of Neutrino and Antineutrino Oscillations Using Beam and Atmospheric Data in MINOS*, *Phys. Rev. Lett.* **110** (2013), no. 25 251801, [`1304.6335`].

[175] **OPERA**, R. Acquafredda et al., *First events from the CNGS neutrino beam detected in the OPERA experiment*, *New J. Phys.* **8** (2006) 303, [`hep-ex/0611023`].

[176] C. Bemporad, G. Gratta, and P. Vogel, *Reactor Based Neutrino Oscillation Experiments*, *Rev. Mod. Phys.* **74** (2002) 297, [`hep-ph/0107277`].

[177] **OPERA**, N. Agafonova et al., *Observation of a first ν_τ candidate in the OPERA experiment in the CNGS beam*, *Phys. Lett. B* **691** (2010) 138–145, [`1006.1623`].

[178] **OPERA**, N. Agafonova et al., *Discovery of τ Neutrino Appearance in the CNGS Neutrino Beam with the OPERA Experiment*, *Phys. Rev. Lett.* **115** (2015), no. 12 121802, [`1507.01417`].

[179] **CHOOZ**, M. Apollonio et al., *Initial results from the CHOOZ long baseline reactor neutrino oscillation experiment*, *Phys. Lett. B* **420** (1998) 397–404, [`hep-ex/9711002`].

[180] F. Boehm et al., *Search for neutrino oscillations at the Palo Verde nuclear reactors*, *Phys. Rev. Lett.* **84** (2000) 3764–3767, [`hep-ex/9912050`].

[181] **Daya Bay**, F. P. An et al., *Observation of electron-antineutrino disappearance at Daya Bay*, *Phys. Rev. Lett.* **108** (2012) 171803, [`1203.1669`].

[182] **Double Chooz**, Y. Abe et al., *Indication of Reactor $\bar{\nu}_e$ Disappearance in the Double Chooz Experiment*, *Phys. Rev. Lett.* **108** (2012) 131801, [`1112.6353`].

[183] **RENO**, J. K. Ahn et al., *Observation of Reactor Electron Antineutrino Disappearance in the RENO Experiment*, *Phys. Rev. Lett.* **108** (2012) 191802, [`1204.0626`].

[184] V. M. Lobashev et al., *Direct search for mass of neutrino and anomaly in the tritium beta spectrum*, *Phys. Lett. B* **460** (1999) 227–235.

[185] C. Kraus et al., *Final results from phase II of the Mainz neutrino mass search in tritium beta decay*, *Eur. Phys. J. C* **40** (2005) 447–468, [`hep-ex/0412056`].

[186] **KATRIN**, M. Aker et al., *Direct neutrino-mass measurement with sub-electronvolt sensitivity*, *Nature Phys.* **18** (2022), no. 2 160–166, [`2105.08533`].

[187] M. Dentler, A. Hernández-Cabezudo, J. Kopp, P. A. N. Machado, M. Maltoni, et al., *Updated Global Analysis of Neutrino Oscillations in the Presence of eV-Scale Sterile Neutrinos*, *J. High Energy Phys.* **2018** (2018) 010, [`1803.10661`].

[188] **LSND**, A. Aguilar-Arevalo et al., *Evidence for neutrino oscillations from the observation of $\bar{\nu}_e$ appearance in a $\bar{\nu}_\mu$ beam*, *Phys. Rev. D* **64** (2001) 112007, [`hep-ex/0104049`].

[189] **MiniBooNE**, A. A. Aguilar-Arevalo et al., *Updated MiniBooNE neutrino oscillation results with increased data and new background studies*, *Phys. Rev. D* **103** (2021), no. 5 052002, [`2006.16883`].

[190] S. N. Gninenko, *The MiniBooNE anomaly and heavy neutrino decay*, *Phys. Rev. Lett.* **103** (2009) 241802, [`0902.3802`].

[191] **MicroBooNE**, P. Abratenko et al., *Search for an anomalous excess of inclusive charged-current ν_e interactions in the MicroBooNE experiment using Wire-Cell reconstruction*, `2110.13978`.

[192] **MicroBooNE**, P. Abratenko et al., *Search for an anomalous excess of charged-current ν_e interactions without pions in the final state with the MicroBooNE experiment*, `2110.14065`.

[193] **MicroBooNE**, P. Abratenko et al., *Search for an Excess of Electron Neutrino Interactions in MicroBooNE Using Multiple Final State Topologies*, `2110.14054`.

[194] **MicroBooNE**, P. Abratenko et al., *Search for an anomalous excess of charged-current quasi-elastic ν_e interactions with the MicroBooNE experiment using Deep-Learning-based reconstruction*, `2110.14080`.

[195] C. A. Argüelles, I. Esteban, M. Hostert, K. J. Kelly, J. Kopp, et al., *MicroBooNE and the ν_e Interpretation of the MiniBooNE Low-Energy Excess*, `2111.10359`.

[196] **GALLEX**, W. Hampel et al., *Final results of the Cr-51 neutrino source experiments in GALLEX*, *Phys. Lett. B* **420** (1998) 114–126.

[197] **SAGE**, J. N. Abdurashitov et al., *Measurement of the response of the Russian-American gallium experiment to neutrinos from a Cr-51 source*, *Phys. Rev. C* **59** (1999) 2246–2263, [`hep-ph/9803418`].

[198] J. N. Abdurashitov et al., *Measurement of the response of a Ga solar neutrino experiment to neutrinos from an Ar-37 source*, *Phys. Rev. C* **73** (2006) 045805, [`nucl-ex/0512041`].

[199] M. Laveder, *Unbound neutrino roadmaps*, *Nucl. Phys. B Proc. Suppl.* **168** (2007) 344–346.

[200] C. Giunti and M. Laveder, *Statistical Significance of the Gallium Anomaly*, *Phys. Rev. C* **83** (2011) 065504, [`1006.3244`].

[201] V. V. Barinov et al., *Results from the Baksan Experiment on Sterile Transitions (BEST)*, `2109.11482`.

[202] T. A. Mueller et al., *Improved predictions of reactor antineutrino spectra*, *Phys. Rev. C - Nucl. Phys.* **83** (2011), no. 5 1–17, [`1101.2663`].

[203] P. Huber, *Determination of antineutrino spectra from nuclear reactors*, *Phys. Rev. C* **84** (Aug, 2011) 024617, [`1106.0687`].

[204] G. Mention, M. Fechner, T. Lasserre, T. A. Mueller, D. Lhuillier, et al., *Reactor antineutrino anomaly*, *Phys. Rev. D* **83** (2011), no. 7 1–21, [`1101.2755`].

[205] V. Kopeikin, M. Skorokhvatov, and O. Titov, *Reevaluating reactor antineutrino spectra with new measurements of the ratio between U235 and Pu239 β spectra*, *Phys. Rev. D* **104** (2021), no. 7 L071301, [`2103.01684`].

[206] C. Giunti, Y. F. Li, C. A. Ternes, and Z. Xin, *Reactor antineutrino anomaly in light of recent flux model refinements*, `2110.06820`.

[207] B. Dasgupta and J. Kopp, *Sterile neutrinos*, *Phys. Rep.* **928** (2021) 1–63, [`2106.05913`].

[208] S. Böser, C. Buck, C. Giunti, J. Lesgourgues, L. Ludhova, et al., *Status of light sterile neutrino searches*, *Prog. Part. Nucl. Phys.* **111** (Mar, 2020) 103736.

[209] V. Mukhanov, *Physical Foundations of Cosmology.* Cambridge University Press, Nov, 2005.

[210] S. Dodelson, *Modern Cosmology.* Academic Press, 2003.

[211] G. Marx and N. Menyhárd, *Cosmic neutrino radiation*, *Science* **131** (Jan, 1960) 299–300.

[212] B. Pontecorvo and Y. A. Smorodinskii, *The Neutrino and the Density of Matter in the Universe*, *Soviet Physics JETP* **14** (Jan, 1962) 173–176.

[213] Y. B. Zel'dovich and Y. A. Smorodinskii, *On an Upper Limit on the Density of Neutrinos, Gravitons, and Baryons in the Universe*, *Soviet Physics JETP* **14** (Mar, 1962) 647–650.

[214] A. A. Penzias and R. W. Wilson, *A Measurement of Excess Antenna Temperature at 4080 Mc/s.*, *Astrophys. J.* **142** (Jul, 1965) 419.

[215] R. H. Dicke, P. J. E. Peebles, P. G. Roll, and D. T. Wilkinson, *Cosmic Black-Body Radiation.*, *Astrophys. J.* **142** (Jul, 1965) 414.

[216] G. Gamow, *Expanding Universe and the Origin of Elements*, *Phys. Rev.* **70** (Oct, 1946) 572–573.

[217] Y. B. Zel'dovich and Y. A. Smorodinskii, *On an Upper Limit on the Density of Neutrinos, Gravitons, and Baryons in the Universe*, *Pis'ma Zh. Eksp. Teor. Fiz.* **4** (Sep, 1966) 174–177. *JETP Lett.* **5** 120–122.

[218] A. Dolgov, *Neutrinos in cosmology*, *Phys. Rep.* **370** (Nov, 2002) 333–535.

[219] F. Hoyle and R. J. Tayler, *The Mystery of the Cosmic Helium Abundance*, *Nature* **203** (Sep, 1964) 1108–1110.

[220] G. Raffelt and D. Seckel, *Bounds on Exotic Particle Interactions from SN 1987A*, *Phys. Rev. Lett.* **60** (1988) 1793.

[221] G. G. Raffelt and T. Astrophysics, *Stars as Laboratories.* The University of Chicago Press, 1996.

[222] **IceCube**, M. G. Aartsen et al., *First observation of PeV-energy neutrinos with IceCube*, *Phys. Rev. Lett.* **111** (2013) 021103, [`1304.5356`].

[223] **IceCube**, R. Abbasi et al., *The IceCube high-energy starting event sample: Description and flux characterization with 7.5 years of data*, *Phys. Rev. D* **104** (2021) 022002, [`2011.03545`].

[224] **IceCube**, M. G. Aartsen et al., *Detection of a particle shower at the Glashow resonance with IceCube*, *Nature* **591** (2021), no. 7849 220–224, [`2110.15051`]. [Erratum: Nature 592, E11 (2021)].

[225] J. F. Beacom, *The Diffuse Supernova Neutrino Background*, *Ann. Rev. Nucl. Part. Sci.* **60** (2010) 439–462, [`1004.3311`].

[226] K. Møller, A. M. Suliga, I. Tamborra, and P. B. Denton, *Measuring the supernova unknowns at the next-generation neutrino telescopes through the diffuse neutrino background*, *JCAP* **05** (2018) 066, [`1804.03157`].

[227] E. Vitagliano, J. Redondo, and G. Raffelt, *Solar neutrino flux at keV energies*, *JCAP* **12** (2017) 010, [`1708.02248`].

[228] E. Vitagliano, I. Tamborra, and G. Raffelt, *Grand Unified Neutrino Spectrum at Earth: Sources and Spectral Components*, *Rev. Mod. Phys.* **92** (2020) 45006, [`1910.11878`].

[229] I. Esteban, M. Gonzalez-Garcia, M. Maltoni, T. Schwetz, and A. Zhou, *The fate of hints: updated global analysis of three-flavor neutrino oscillations*, *J. High Energy Phys.* **2020** (Sep, 2020) 178, [`2007.14792`].

[230] A. Hernández-Cabezudo, *Sterile Neutrino Searches in Neutrino Oscillation Experiments*. PhD thesis, KIT, Karlsruhe, 2020.

[231] **KamLAND**, A. Gando et al., *Constraints on θ_{13} from A Three-Flavor Oscillation Analysis of Reactor Antineutrinos at KamLAND*, *Phys. Rev. D* **83** (2011) 052002, [`1009.4771`].

[232] S. Goswami and A. Y. Smirnov, *Solar neutrinos and 1-3 leptonic mixing*, *Phys. Rev. D* **72** (2005) 053011, [`hep-ph/0411359`].

[233] H. Nunokawa, S. Parke, and R. Z. Funchal, *Another possible way to determine the neutrino mass hierarchy*, *Phys. Rev. D* **72** (Jul, 2005) 1–6, [`hep-ph/0503283`].

[234] O. Yasuda, *Three flavor neutrino oscillation analysis of the Super-Kamiokande atmospheric neutrino data*, in *Symposium on New Era in Neutrino Physics*, pp. 165–177, Jun, 1998. `hep-ph/9809205`.

[235] S. Parke, *What is Δm^2_{ee} ?*, *Phys. Rev. D* **93** (2016), no. 5 053008, [`1601.07464`].

[236] A. Cervera, A. Donini, M. B. Gavela, J. J. Gomez Cadenas, P. Hernandez, et al., *Golden measurements at a neutrino factory*, *Nucl. Phys. B* **579** (2000) 17–55, [`hep-ph/0002108`]. [Erratum: Nucl.Phys.B 593, 731–732 (2001)].

[237] M. Freund, *Analytic approximations for three neutrino oscillation parameters and probabilities in matter*, *Phys. Rev. D* **64** (Jul, 2001) 053003, [`hep-ph/0103300`].

[238] E. K. Akhmedov, R. Johansson, M. Lindner, T. Ohlsson, and T. Schwetz, *Series expansions for three-flavor neutrino oscillation probabilities in matter*, *J. High Energy Phys.* **2004** (May, 2004) 078 – 078, [`hep-ph/0402175`].

[239] J. Elevant and T. Schwetz, *On the determination of the leptonic CP phase*, *J. High Energy Phys.* **2015** (2015) 16, [`1506.07685`].

[240] O. L. G. Peres and A. Y. Smirnov, *Atmospheric neutrinos: LMA oscillations, U_{e3} induced interference and CP violation*, *Nucl. Phys. B* **680** (2004) 479 – 509, [`hep-ph/0309312`].

[241] M. C. Gonzalez-Garcia, M. Maltoni, J. Salvado, and T. Schwetz, *Global fit to three neutrino mixing: Critical look at present precision*, *J. High Energy Phys.* **2012** (2012), no. 12 [`1209.3023`].

[242] M. Maltoni and A. Y. Smirnov, *Solar neutrinos and neutrino physics*, *Eur. Phys. J. A* **52** (2016), no. 4 87, [`1507.05287`].

[243] **T2K**, K. Abe et al., *T2K neutrino flux prediction*, *Phys. Rev. D* **87** (2013), no. 1 012001, [`1211.0469`]. [Addendum: Phys.Rev.D 87, 019902 (2013)].

[244] **MINERvA**, L. Aliaga et al., *Neutrino Flux Predictions for the NuMI Beam*, *Phys. Rev. D* **94** (2016), no. 9 092005, [`1607.00704`]. [Addendum: Phys.Rev.D 95, 039903 (2017)].

[245] **NOvA**, M. A. Acero et al., *New constraints on oscillation parameters from ν_e appearance and ν_μ disappearance in the NOνA experiment*, *Phys. Rev. D* **98** (2018) 032012, [`1806.00096`].

[246] **RENO**, S.-H. Seo, *New Results from RENO and The 5 MeV Excess*, *AIP Conf. Proc.* **1666** (2015), no. 1 080002, [`1410.7987`].

[247] **RENO**, J. H. Choi et al., *Observation of Energy and Baseline Dependent Reactor Antineutrino Disappearance in the RENO Experiment*, *Phys. Rev. Lett.* **116** (2016), no. 21 211801, [`1511.05849`].

[248] **Daya Bay**, F. P. An et al., *Measurement of the Reactor Antineutrino Flux and Spectrum at Daya Bay*, *Phys. Rev. Lett.* **116** (2016), no. 6 061801, [`1508.04233`]. [Erratum: Phys.Rev.Lett. 118, 099902 (2017)].

[249] **Double Chooz**, Y. Abe et al., *Measurement of θ_{13} in Double Chooz using neutron captures on hydrogen with novel background rejection techniques*, *J. High Energy Phys.* **2016** (2016) 163, [`1510.08937`].

[250] P. Huber, *NEOS Data and the Origin of the 5 MeV Bump in the Reactor Antineutrino Spectrum*, *Phys. Rev. Lett.* **118** (2017), no. 4 042502, [`1609.03910`].

[251] **RENO**, J. Yoo, “Recent Results from RENO Experiment.” Plenary Talk from Neutrino 2020, Jun, 2020.

[252] I. Esteban Muñoz, *Leptonic CP Violation and its Origin.* PhD thesis, Barcelona U., 2020. `2010.00440`.

[253] P. Vogel and J. F. Beacom, *Angular distribution of neutron inverse beta decay,* $\bar{\nu}_e + p \to e^+ + n$, *Phys. Rev. D* **60** (1999) 053003, [`hep-ph/9903554`].

[254] **RENO**, G. Bak et al., *Fuel-composition dependent reactor antineutrino yield at RENO*, *Phys. Rev. Lett.* **122** (2019), no. 23 232501, [`1806.00574`].

[255] **Daya Bay**, F. P. An et al., *Improved Measurement of the Reactor Antineutrino Flux and Spectrum at Daya Bay*, *Chin. Phys. C* **41** (2017), no. 1 013002, [`1607.05378`].

[256] **RENO**, J. K. Ahn et al., *RENO: An Experiment for Neutrino Oscillation Parameter θ_{13} Using Reactor Neutrinos at Yonggwang*, tech. rep., RENO, Mar, 2010.

[257] **RENO**, S. H. Seo et al., *Spectral Measurement of the Electron Antineutrino Oscillation Amplitude and Frequency using 500 Live Days of RENO Data*, *Phys. Rev. D* **98** (2018), no. 1 012002, [`1610.04326`].

[258] **Daya Bay**, F. P. An et al., *Measurement of electron antineutrino oscillation based on 1230 days of operation of the Daya Bay experiment*, *Phys. Rev. D* **95** (2017), no. 7 072006, [`1610.04802`].

[259] I. Esteban, M. C. Gonzalez-Garcia, A. Hernández-Cabezudo, M. Maltoni, and T. Schwetz, *Global analysis of three-flavour neutrino oscillations: synergies and tensions in the determination of θ_{23}, $\delta_{\rm CP}$, and the mass ordering*, *J. High Energy Phys.* **2019** (Jan, 2019) 106, [`1811.05487`].

[260] **RENO**, D. Lee, "Updated results on reactor antineutrino oscillation amplitude and frequency for 2900 days at RENO." Poster at Neutrino 2020, 2020.

[261] G. L. Fogli, E. Lisi, A. Marrone, D. Montanino, and A. Palazzo, *Getting the most from the statistical analysis of solar neutrino oscillations*, *Phys. Rev. D* **66** (2002) 053010, [`hep-ph/0206162`].

[262] I. Esteban, M. C. Gonzalez-Garcia, M. Maltoni, I. Martinez-Soler, and T. Schwetz, *Updated fit to three neutrino mixing: exploring the accelerator-reactor complementarity*, *J. High Energy Phys.* **2017** (2017) 087, [`1611.01514`].

[263] **Super-Kamiokande Collaboration**, "SK Atmospheric Oscillation Analysis 2020 (preliminary) results." `https://indico-sk.icrr.u-tokyo.ac.jp/event/5517/`, 2020.

[264] M. Maltoni, T. Schwetz, M. A. Tortola, and J. W. F. Valle, *Ruling out four neutrino oscillation interpretations of the LSND anomaly?*, *Nucl. Phys. B* **643** (2002) 321–338, [`hep-ph/0207157`].

[265] M. Maltoni and T. Schwetz, *Testing the statistical compatibility of independent data sets*, *Phys. Rev. D* **68** (2003) 033020, [`hep-ph/0304176`].

[266] C. Giunti, M. Laveder, Y. F. Li, Q. Y. Liu, and H. W. Long, *Update of Short-Baseline Electron Neutrino and Antineutrino Disappearance*, *Phys. Rev. D* **86** (2012) 113014, [`1210.5715`].

[267] J. Kopp, P. A. N. Machado, M. Maltoni, and T. Schwetz, *Sterile neutrino oscillations: the global picture*, *J. High Energy Phys.* **2013** (May, 2013) 50, [`1303.3011`].

[268] S. Gariazzo, C. Giunti, M. Laveder, and Y. F. Li, *Updated Global 3+1 Analysis of Short-BaseLine Neutrino Oscillations*, *J. High Energy Phys.* **2017** (2017) 135, [`1703.00860`].

[269] M. Dentler, A. Hernández-Cabezudo, J. Kopp, M. Maltoni, and T. Schwetz, *Sterile neutrinos or flux uncertainties? — Status of the reactor anti-neutrino anomaly*, *J. High Energy Phys.* **2017** (Nov, 2017) 99, [`1709.04294`].

[270] S. Gariazzo, C. Giunti, M. Laveder, and Y. F. Li, *Model-independent* $\bar{\nu}_e$ *short-baseline oscillations from reactor spectral ratios*, *Phys. Lett. B* **782** (2018) 13–21, [`1801.06467`].

[271] M. Dentler, A. Hernández-Cabezudo, J. Kopp, P. Machado, M. Maltoni, et al., *Updated global analysis of neutrino oscillations in the presence of eV-scale sterile neutrinos*, *J. High Energy Phys.* **2018** (Aug, 2018) 10, [`1803.10661`].

[272] J. M. Berryman, P. Coloma, P. Huber, T. Schwetz, and A. Zhou, *Statistical significance of the sterile-neutrino hypothesis in the context of reactor and gallium data*, *J. High Energy Phys.* **2022** (Feb, 2022) 55, [`2111.12530`].

[273] A. Serebrov, *Observation of sterile antineutrino oscillation in Neutrino-4 experiment at SM-3 reactor*, 2020. Plenary Talk from Neutrino 2020.

[274] P. Coloma, P. Huber, and T. Schwetz, *Statistical interpretation of sterile neutrino oscillation searches at reactors*, *Eur. Phys. J. C* **81** (2021), no. 1 1–12, [`2008.06083`].

[275] A. P. Serebrov et al., *Search for sterile neutrinos with the Neutrino-4 experiment and measurement results*, *Phys. Rev. D* **104** (2021), no. 3 032003, [`2005.05301`].

[276] G. J. Feldman and R. D. Cousins, *A Unified approach to the classical statistical analysis of small signals*, *Phys. Rev. D* **57** (1998) 3873–3889, [`physics/9711021`].

[277] M. Danilov, *Review of sterile neutrino searches at very short-baseline reactor experiments*, `2203.03042`.

[278] M. Galassi et al., *GNU Scientific Library Reference Manual.* GNU, `http://www.gnu.org/software/gsl/`, 3rd ed.

[279] I. Alekseev et al., *DANSS: Detector of the reactor AntiNeutrino based on Solid Scintillator*, *JINST* **11** (2016), no. 11 P11011, [`1606.02896`].

[280] **DANSS**, M. Danilov, "New Results from the DANSS experiment." Presented at EPS-HEP 2021 Virtual Conference, (July 27, 2021) [`https://indico.desy.de/event/28202/contributions/105957/`].

[281] **DANSS**, M. Danilov, *Sensitivity of the DANSS detector to short range neutrino oscillations*, *Nuclear and Particle Physics Proceedings* **273-275** (2016) 1055–1058, [`1412.0817`]. 37th International Conference on High Energy Physics (ICHEP).

[282] **NEOS**, Y. J. Ko et al., *Sterile Neutrino Search at the NEOS Experiment*, *Phys. Rev. Lett.* **118** (2017), no. 12 121802, [`1610.05134`].

[283] **RENO, NEOS**, Z. Atif et al., *Search for sterile neutrino oscillation using RENO and NEOS data*, `2011.00896`.

[284] **NEOS**, Y. Oh, "NEOS result and reactor SBL-ν project." Contributed to the 26^{th} International Workshop on Weak Interactions and Neutrinos (WIN2017), [`https://indico.fnal.gov/event/9942/contributions/116777/`].

[285] **NEOS**, Y. Ko et al., *Sterile neutrino search at the NEOS experiment*, *PoS* **NuFact2017** (2018) 042.

[286] **PROSPECT**, M. Andriamirado et al., *Improved short-baseline neutrino oscillation search and energy spectrum measurement with the PROSPECT experiment at HFIR*, *Phys. Rev. D* **103** (2021), no. 3 032001, [`2006.11210`].

[287] P. Huber, M. Lindner, and W. Winter, *Simulation of long-baseline neutrino oscillation experiments with* `GLoBES` *(General Long Baseline Experiment Simulator)*, *Comput. Phys. Commun.* **167** (2005) 195, [`hep-ph/0407333`].

[288] P. Huber, J. Kopp, M. Lindner, M. Rolinec, and W. Winter, *New features in the simulation of neutrino oscillation experiments with GLoBES 3.0: General Long Baseline Experiment Simulator*, *Comput. Phys. Commun.* **177** (2007) 432–438, [`hep-ph/0701187`].

[289] X. Qian, A. Tan, J. J. Ling, Y. Nakajima, and C. Zhang, *The Gaussian* $\mathrm{CL_s}$ *method for searches of new physics*, *Nucl. Instrum. Meth. A* **827** (2016) 63–78, [`1407.5052`].

[290] **STEREO**, H. Almazán et al., *Improved sterile neutrino constraints from the STEREO experiment with 179 days of reactor-on data*, *Phys. Rev. D* **102** (2020), no. 5 052002, [`1912.06582`].

[291] **STEREO**, *Improved sterile neutrino constraints from the STEREO experiment with 179 days of reactor-on data*, 2020.

[292] L. Bernard, *Recherche d'un neutrino stérile avec l'expérience STEREO : détermination des spectres neutrinos et caractérisation du bruit de fond.* PhD thesis, LPSC, Grenoble, 2019. [`https://inspirehep.net/literature/1787164`].

[293] R. Fletcher, *Practical Methods of Optimization*, ch. 4, pp. 80–94. John Wiley & Sons, Ltd, 2000.

[294] **NEUTRINO-4**, A. P. Serebrov et al., *First Observation of the Oscillation Effect in the Neutrino-4 Experiment on the Search for the Sterile Neutrino*, *JETP Lett.* **109** (2019), no. 4 209 – 218, [`1809.10561`].

[295] M. Danilov, *Searches for sterile neutrinos at very short baseline reactor experiments*, *J. Phys. Conf. Ser.* **1390** (2019), no. 1 012049, [`1812.04085`].

[296] C. Giunti, Y. F. Li, C. A. Ternes, and Y. Y. Zhang, *Neutrino-4 anomaly: oscillations or fluctuations?*, *Phys. Lett. B* **816** (2021) 136214, [`2101.06785`].

[297] M. V. Danilov and N. A. Skrobova, *Comment on "Analysis of the Results of the Neutrino-4 Experiment on the Search for the Sterile Neutrino and Comparison with Results of Other Experiments" (JETP Letters 112, 199 (2020))*, *JETP Lett.* **112** (2020), no. 7 452 – 454.

[298] **PROSPECT, STEREO**, M. Andriamirado et al., *Note on arXiv:2005.05301, 'Preparation of the Neutrino-4 experiment on search for sterile neutrino and the obtained results of measurements'*, `2006.13147`.

[299] F. Kaether, W. Hampel, G. Heusser, J. Kiko, and T. Kirsten, *Reanalysis of the GALLEX solar neutrino flux and source experiments*, *Phys. Lett.* **B685** (2010) 47–54, [`1001.2731`].

[300] E. P. Veretenkin, V. N. Gavrin, S. N. Danshin, T. V. Ibragimova, A. A. Kalashnikova, et al., *Calorimetric system for high-precision determination of activity of the* ^{51}Cr *neutrino source in the BEST experiment*, *J. Phys. Conf. Ser.* **798** (2017), no. 1 012140.

[301] V. N. Gavrin, T. V. Ibragimova, J. P. Kozlova, V. A. Tarasov, E. P. Veretenkin, et al., *Measurement of neutrino source activity in the experiment BEST by calorimetric method*, *JINST* **16** (2021), no. 04 P04012, [`2105.05120`].

[302] V. P. Chechev and N. K. Kuzmenko, $^{51}_{24}\mathrm{Cr}_{27}$, in *Table de Radionucléides*, vol. 8 of *Monographie BIPM-5*. Bureau International des Poids et Mesures, Pavillon de Breteuil, F-92310 Sèvres, France, 2014.

[303] J. N. Bahcall, *Gallium solar neutrino experiments: Absorption cross-sections, neutrino spectra, and predicted event rates*, *Phys. Rev.* **C56** (1997) 3391–3409, [`hep-ph/9710491`].

[304] J. Kostensalo, J. Suhonen, C. Giunti, and P. C. Srivastava, *The gallium anomaly revisited*, *Phys. Lett. B* **795** (2019) 542 – 547, [`1906.10980`].

[305] S. V. Semenov, *Cross Section of Neutrino Absorption by the Gallium-71 Nucleus*, *Phys. Atom. Nucl.* **83** (2020), no. 11 1549 – 1552.

[306] M. A. Acero, C. Giunti, and M. Laveder, *Limits on* ν_e *and* $\bar{\nu}_e$ *disappearance from Gallium and reactor experiments*, *Phys. Rev. D* **78** (2008) 073009, [`0711.4222`].

[307] **GALLEX**, T. Kirsten, *Status report on the 'Gallex' solar neutrino project*, in *6th Moriond Workshop: Massive Neutrinos in Particle Physics and Astrophysics*, pp. 119 – 129, 1986.

[308] K. Goldhagen, M. Maltoni, S. E. Reichard, and T. Schwetz, *Testing sterile neutrino mixing with present and future solar neutrino data*, *Eur. Phys. J. C* **82** (2022), no. 2 116, [`2109.14898`].

[309] N. Vinyoles, A. M. Serenelli, F. L. Villante, S. Basu, J. Bergström, et al., *A new Generation of Standard Solar Models*, *Astrophys. J.* **835** (2017), no. 2 202, [`1611.09867`].

[310] **LSND**, L. B. Auerbach et al., *Measurements of charged current reactions of ν_e on* ^{12}C, *Phys. Rev. C* **64** (2001) 065501, [`hep-ex/0105068`].

[311] B. Armbruster et al., *KARMEN limits on $\nu_e \to \nu_\tau$ oscillations in two-neutrino and three-neutrino mixing schemes*, *Phys. Rev. C* **57** (1998) 3414 – 3424, [`hep-ex/9801007`].

[312] **KATRIN**, M. Aker et al., *Improved eV-scale sterile-neutrino constraints from the second KATRIN measurement campaign*, *Phys. Rev. D* **105** (2022), no. 7 072004, [`2201.11593`].

[313] V. P. Chechev and N. K. Kuzmenko, ^{51}Cr — *Comments on evaluation of decay data*, in *Table de Radionucléides*, vol. 8 of *Monographie BIPM-5*. Bureau International des Poids et Mesures, Pavillon de Breteuil, F-92310 Sèvres, France, 2014.

[314] S. A. Fisher and R. L. Hershberger, *Branching ratios for EC decay of* ^{7}Be *and* ^{51}Cr, *Nucl. Phys. A* **423** (1984) 121 – 129.

[315] P. Yalçin and Y. Kurucu, *Emission probabilities of K X- and γ-rays following* ^{51}Cr *and* ^{67}Ga *decay*, *Applied Radiation and Isotopes* **62** (2005), no. 1 63–67.

[316] D. S. Moreira, M. F. Koskinas, I. M. Yamazaki, and M. S. Dias, *Determination of* ^{51}Cr *and* ^{241}Am *X-ray and gamma-ray emission probabilities per decay*, *Applied Radiation and Isotopes* **68** (2010), no. 4 596–599. The 7th International Topical Meeting on Industrial Radiation and Radio isotope Measurement Application (IRRMA-7).

[317] C. Bobin, *Primary standardization of activity using the coincidence method based on analogue instrumentation*, *Metrologia* **44** (2007) S27–31.

[318] E. Funck and A. Larsen, *The Influence from Low Energy x-Rays and Auger Electrons on $4\pi\beta$-γ Coincidence Measurements of Electron-capture-decaying Nuclides*, *The International Journal of Applied Radiation and Isotopes* **34** (1983), no. 3 565–569.

[319] W. Van Wyngaardt and B. Simpson, *Absolute activity measurement of the electron-capture-based radionuclides* ^{139}Ce*,* ^{125}I*,* ^{192}Ir *and* ^{65}Zn *by liquid scintillation coincidence counting*, *Applied Radiation and Isotopes* **64** (2006), no. 10 1454–1458. Proceedings of the 15th International Conference on Radionuclide Metrology and its Applications.

[320] A. Charig, J. Blake-Haskins, and E. Eigen, *Anomalous liquid scintillation counting of chromium-51*, *Analytical Biochemistry* **151** (1985), no. 2 428–430.

[321] C. W. Kim and W. P. Lam, *Some Remarks on Neutrino Decay via a Nambu-Goldstone Boson*, *Mod. Phys. Lett. A* **05** (Feb, 1990) 297 – 299.

[322] M. Hostert and M. Pospelov, *Constraints on decaying sterile neutrinos from solar antineutrinos*, *Phys. Rev. D* **104** (2021), no. 5 1 – 14, [`2008.11851`].

[323] **Borexino**, M. Agostini et al., *Comprehensive measurement of pp-chain solar neutrinos*, *Nature* **562** (Oct, 2018) 505 – 510.

[324] N. Vinyoles, A. M. Serenelli, F. L. Villante, S. Basu, J. Bergström, et al., *A New Generation of Standard Solar Models*, *Astrophys. J.* **835** (Jan, 2017) 202, [`1611.09867`].

[325] J. N. Bahcall, *The Be-7 solar neutrino line: A Reflection of the central temperature distribution of the sun*, *Phys. Rev. D* **49** (1994) 3923 – 3945, [`astro-ph/9401024`].

[326] R. Helmer and E. Schönfeld, $^{7}_{4}$Be$_3$, in *Table de Radionucléides*, vol. 1 of *Monographie BIPM-5.* Bureau International des Poids et Mesures, Pavillon de Breteuil, F-92310 Sèvres, France, 2004.

[327] S. Palomares-Ruiz, S. Pascoli, and T. Schwetz, *Explaining LSND by a decaying sterile neutrino*, *J. High Energy Phys.* **2005** (2005), no. 9 1 – 23, [`hep-ph/0505216`].

[328] S. Bashinsky and U. Seljak, *Neutrino perturbations in CMB anisotropy and matter clustering*, *Phys. Rev. D* **69** (2004) 083002, [`astro-ph/0310198`].

[329] F. Forastieri, M. Lattanzi, and P. Natoli, *Cosmological constraints on neutrino self-interactions with a light mediator*, *Phys. Rev. D* **100** (2019), no. 10 1 – 14, [`1904.07810`].

[330] J. Venzor, G. Garcia-Arroyo, A. Pérez-Lorenzana, and J. De-Santiago, *Massive neutrino self-interactions with a light mediator in cosmology*, `2202.09310`.

[331] J. Orloff, A. N. Rozanov, and C. Santoni, *Limits on the mixing of tau neutrino to heavy neutrinos*, *Phys. Lett. B* **550** (2002) 8 – 15, [`hep-ph/0208075`].

[332] T. Schwetz, A. Zhou, and J.-Y. Zhu, *Constraining active-sterile neutrino transition magnetic moments at DUNE near and far detectors*, *J. High Energy Phys.* **2021** (Jul, 2021) 200, [`2105.09699`].

[333] K. Sakurai, *Quasi-biennial variation of the solar neutrino flux and solar activity*, *Nature* **278** (Mar, 1979) 146 – 148.

[334] K. Sakurai, *Quasi-biennial periodicity in the solar neutrino flux and its relation to the solar structure*, *Solar Phys.* **74** (1981), no. 1 35 – 41.

[335] J. N. Bahcall, G. B. Field, and W. H. Press, *Is Solar Neutrino Capture Rate Correlated with Sunspot Number?*, *Astrophys. J. Lett.* **320** (Sep, 1987) L69.

[336] L. B. Okun, *On the Electric Dipole Moment of Neutrino*, *Sov. J. Nucl. Phys.* **44** (1986) 546.

[337] M. B. Voloshin, M. I. Vysotkiĭ, and L. B. Okun', *Neutrino electrodynamics and possible consequences for solar neutrinos*, *Zh. Eksp. Teor. Fiz.* **91** (1986) 754 – 765. *Sov. Phys. JETP* **64** 446 – 452.

[338] L. B. Okun', M. B. Voloshin, and M. I. Vysotkiĭ, *Electromagnetic Properties of Neutrino and Possible Semiannual Variation Cycle of the Solar Neutrino Flux*, *Yad. Fiz.* **44** (1986) 677 – 680. *Sov. J. Nucl. Phys.* **44** 440.

[339] M. B. Voloshin and M. I. Vysotkiĭ, *Neutrino Magnetic Moment and Time Variation of Solar Neutrino Flux*, *Yad. Fiz.* **44** (1986) 845 – 846. *Sov. J. Nucl. Phys.* **44** 544.

[340] B. W. Lee and R. E. Shrock, *Natural suppression of symmetry violation in gauge theories: Muon- and electron-lepton number nonconservation*, *Phys. Rev. D* **16** (1977) 1444.

[341] K. Fujikawa and R. Shrock, *The Magnetic Moment of a Massive Neutrino and Neutrino Spin Rotation*, *Phys. Rev. Lett.* **45** (1980) 963.

[342] M. Fukugita and T. Yanagida, *A Particle Physics Model for Voloshin-Vysotskii-Okun Solution to the Solar Neutrino Problem*, *Phys. Rev. Lett.* **58** (1987) 1807.

[343] K. S. Babu and V. S. Mathur, *Magnetic Moments of Dirac and Majorana Neutrinos*, *Phys. Lett. B* **196** (1987) 218–222.

[344] M. A. Stefanov, *Magnetic moment of a neutrino in a model with a flavor lepton symmetry*, *Pis'ma Zh. Eksp. Teor. Fiz.* **47** (Jan, 1988) 3 – 5. *JETP Lett.* **4** 1 – 4.

[345] R. Barbieri and G. Fiorentini, *The Solar Neutrino Puzzle and the* $\nu_{\mathrm{L}} \to \nu_{\mathrm{R}}$ *Conversion Hypothesis*, *Nucl. Phys. B* **304** (1988) 909–920.

[346] J. Pulido and J. Ralston, *Neutrino Masses and the Voloshin-Vysotskii-Okun Solution to the Solar Neutrino Problem*, *Phys. Rev. D* **38** (1988) 2864.

[347] M. B. Voloshin, *On Compatibility of Small Mass with Large Magnetic Moment of Neutrino*, *Yad. Fiz.* **48** (1988) 804 – 810. *Sov. J. Nucl. Phys.* **48** (1988) 512.

[348] K. S. Babu and R. N. Mohapatra, *Model for Large Transition Magnetic Moment of the ν_e*, *Phys. Rev. Lett.* **63** (1989) 228.

[349] K. S. Babu, S. Jana, and M. Lindner, *Large Neutrino Magnetic Moments in the Light of Recent Experiments*, *J. High Energy Phys.* **2020** (2020) 040, [`2007.04291`].

[350] **XENON**, E. Aprile et al., *Excess electronic recoil events in XENON1T*, *Phys. Rev. D* **102** (2020), no. 7 072004, [`2006.09721`].

[351] **Muon g-2**, B. Abi et al., *Measurement of the Positive Muon Anomalous Magnetic Moment to 0.46 ppm*, *Phys. Rev. Lett.* **126** (2021), no. 14 141801, [`2104.03281`].

[352] K. S. Babu, S. Jana, M. Lindner, and V. P. K, *Muon $g-2$ anomaly and neutrino magnetic moments*, *J. High Energy Phys.* **2021** (2021) 240, [`2104.03291`].

[353] G. Magill, R. Plestid, M. Pospelov, and Y.-D. Tsai, *Dipole Portal to Heavy Neutral Leptons*, *Phys. Rev. D* **98** (2018), no. 11 115015, [`1803.03262`].

[354] V. Brdar, A. Greljo, J. Kopp, and T. Opferkuch, *The Neutrino Magnetic Moment Portal: Cosmology, Astrophysics, and Direct Detection*, *JCAP* **01** (2021) 039, [`2007.15563`].

[355] **MicroBooNE**, P. Abratenko et al., *Search for Neutrino-Induced Neutral-Current Δ Radiative Decay in MicroBooNE and a First Test of the MiniBooNE Low Energy Excess under a Single-Photon Hypothesis*, *Phys. Rev. Lett.* **128** (2022), no. 11 111801, [`2110.00409`].

[356] **DUNE**, B. Abi et al., *Deep Underground Neutrino Experiment (DUNE), Far Detector Technical Design Report, Volume I Introduction to DUNE*, *JINST* **15** (2020), no. 08 T08008, [`2002.02967`].

[357] E. Gramellini, "Liquid Argon TPCs for Neutrino Detection." Keynote Talk at Light Detection In Noble Elements 2021, Sep, 2021.

[358] **NOνA**, A. Himmel, "New Oscillation Results from the NOνA Experiment." Plenary Talk from Neutrino 2020, Jul, 2020.

[359] **DUNE**, A. Abed Abud et al., *Deep Underground Neutrino Experiment (DUNE) Near Detector Conceptual Design Report*, *Instruments* **5** (2021), no. 4 31, [`2103.13910`].

[360] S. Sangiorgio et al., *First demonstration of a sub-keV electron recoil energy threshold in a liquid argon ionization chamber*, *Nucl. Instrum. Meth. A* **728** (2013) 69–72, [`1301.4290`].

[361] P. Agnes et al., *Measurement of the liquid argon energy response to nuclear and electronic recoils*, *Phys. Rev. D* **97** (2018), no. 11 112005, [`1801.06653`].

[362] P. Coloma, P. A. N. Machado, I. Martinez-Soler, and I. M. Shoemaker, *Double-Cascade Events from New Physics in Icecube*, *Phys. Rev. Lett.* **119** (2017), no. 20 201804, [`1707.08573`].

[363] C. Rubbia et al., *Underground operation of the ICARUS T600 LAr-TPC: first results*, *JINST* **6** (2011) P07011, [`1106.0975`].

[364] **ArgoNeuT**, R. Acciarri et al., *Measurement of ν_μ and $\bar{\nu}_\mu$ neutral current $\pi^0 \to \gamma\gamma$ production in the ArgoNeuT detector*, *Phys. Rev. D* **96** (2017), no. 1 012006, [`1511.00941`].

[365] **MicroBooNE**, C. Adams et al., *First measurement of ν_μ charged-current π^0 production on argon with the MicroBooNE detector*, *Phys. Rev. D* **99** (2019), no. 9 091102, [`1811.02700`].

[366] X. Zhang and B. D. Serot, *Can neutrino-induced photon production explain the low energy excess in MiniBooNE?*, *Phys. Lett. B* **719** (2013) 409–414, [`1210.3610`].

[367] E. Wang, L. Alvarez-Ruso, and J. Nieves, *Photon emission in neutral current interactions at intermediate energies*, *Phys. Rev. C* **89** (2014), no. 1 015503, [`1311.2151`].

[368] G. T. Garvey, D. A. Harris, H. A. Tanaka, R. Tayloe, and G. P. Zeller, *Recent Advances and Open Questions in Neutrino-Induced Quasi-Elastic Scattering and Single Photon Production*, *Phys. Rept.* **580** (2015) 1–45, [`1412.4294`].

[369] **DUNE**, B. Abi et al., *Deep Underground Neutrino Experiment (DUNE), Far Detector Technical Design Report, Volume II: DUNE Physics*, `2002.03005`.

[370] L. Fields, "CP Optimized Beam, Neutrino Mode." Retrieved from `https://home.fnal.gov/~ljf26/DUNEFluxes/OptimizedEngineeredNov2017_offaxis/`. Accessed June 2020.

[371] A. M. Dziewonski and D. L. Anderson, *Preliminary reference earth model*, *Phys. Earth Planet. Interiors* **25** (1981) 297–356.

[372] R. L. Donahue, R. W. Miller, and J. C. Shickluna, *Soils: an introduction to soils and plant growth.* Englewood, Cliffs, N.J.: Prentice-Hall, `https://archive.org/details/soilsintroductio00dona`, 4th ed., 1977.

[373] W. M. Haynes et al., eds., *CRC Handbook of Chemistry and Physics.* Taylor and Francis, 97th ed., 2016.

[374] **SHiP**, M. Anelli et al., *A facility to Search for Hidden Particles (SHiP) at the CERN SPS*, `1504.04956`.

[375] **DONUT**, R. Schwienhorst et al., *A New upper limit for the tau - neutrino magnetic moment*, *Phys. Lett. B* **513** (2001) 23–29, [`hep-ex/0102026`].

[376] R. Plestid, *Luminous solar neutrinos I: Dipole portals*, *Phys. Rev. D* **104** (2021) 075027, [`2010.04193`].

[377] I. M. Shoemaker and J. Wyenberg, *Direct Detection Experiments at the Neutrino Dipole Portal Frontier*, *Phys. Rev. D* **99** (2019), no. 7 075010, [`1811.12435`].

[378] S. N. Gninenko and N. V. Krasnikov, *Limits on the magnetic moment of sterile neutrino and two photon neutrino decay*, *Phys. Lett. B* **450** (1999) 165–172, [`hep-ph/9808370`].

[379] **CHARM-II**, D. Geiregat et al., *A New Determination of the Electroweak Mixing Angle From ν_μ Electron Scattering*, *Phys. Lett. B* **232** (1989) 539.

[380] P. Coloma, E. Fernández-Martínez, M. González-López, J. Hernández-García, and Z. Pavlovic, *GeV-scale neutrinos: interactions with mesons and DUNE sensitivity*, *Eur. Phys. J. C* **81** (2021), no. 1 78, [`2007.03701`].

[381] J. D. Lewin and P. F. Smith, *Review of Mathematics, Numerical Factors, and Corrections for Dark Matter Experiments Based on Elastic Nuclear Recoil*, *Astropart. Phys.* **6** (1996) 87–112.

[382] A. B. Balantekin, A. de Gouvêa, and B. Kayser, *Addressing the Majorana vs. Dirac Question with Neutrino Decays*, *Phys. Lett. B* **789** (2019) 488–495, [`1808.10518`].

[383] A. Baha Balantekin and B. Kayser, *On the Properties of Neutrinos*, *Ann. Rev. Nucl. Part. Sci.* **68** (2018) 313–338, [`1805.00922`].